INVESTIGATING DEGRADATION AND DEFORMATION MECHANISMS IN CYLINDRICAL LI-ION BATTERIES

DISSERTATION
submitted in partial fulfilment
of the requirements for the degree of
Doctor of Philosophy
at University College London

by
Anmol Jnawali

Department of Chemical Engineering
University College London

2023

DECLARATION

I, Anmol Jnawali confirm that the work presented in this thesis is my own. Where information has been derived from other sources, I confirm that this has been indicated in the thesis.

Signature

07 November 2023

ACKNOWLEDGEMENTS

Firstly, I would like to thank Paul for giving me the opportunity to work on this project within the big and warm group, EIL. I would also like to give a big thanks to Toby for making sure I didn't blow my hands off, and Francesco for all his sage advice on all things X-rays. I would also like to thank Matt, without whom a large part of this thesis would not be possible.

Special thanks to Keenan, Alice, Emanuele, Alex and Martin for the friendship and for keeping things interesting. To Anand, a massive thank you for the *whiteon* and for all his help in his short time in the group. To Ami, thank you for being there, and the same to my mum for the support and love over the years.

A very special thank you to my dog, Bella, for being the best!

RESEARCH PAPER DECLARATION FORM

1. For a research manuscript that has already been published (if not yet published, please skip to section 2)**:**		
a) Where was the work published? (e.g. journal name)	Journal of Power Sources	
b) Who published the work? (e.g. Elsevier/Oxford University Press):	Elsevier	
c) When was the work published?	15/04/2022	
d) Was the work subject to academic peer review?	Yes	
e) Have you retained the copyright for the work?	No	
[If no, please seek permission from the relevant publisher and check the box next to the below statement]: ☒ *I acknowledge permission of the publisher named under 1b to include in this thesis portions of the publication named as included in 1a.*		
2. For a research manuscript prepared for publication but that has not yet been published (if already published, please skip to section 3)**:**		
a) Has the manuscript been uploaded to a preprint server? (e.g. medRxiv):	Please select.	**If yes, which server?** Click or tap here to enter text.
b) Where is the work intended to be published? (e.g. names of journals that you are planning to submit to)	Click or tap here to enter text.	
c) List the manuscript's authors in the intended authorship order:	Click or tap here to enter text.	
d) Stage of publication	Please select.	
3. For multi-authored work, please give a statement of contribution covering all authors (if single-author, please skip to section 4)**:**		
Anmol Jnawali: Conceptualization, Investigation, Writing – original draft. **Anand N.P. Radhakrishnan:** Methodology, Software, Writing – review & editing. **Matt D.R. Kok:** Methodology, Software. **Francesco Iacoviello:** Investigation. **Daniel J.L. Brett:** Supervision. **Paul R. Shearing:** Supervision, Writing – review & editing, Funding acquisition.		

4. In which chapter(s) of your thesis can this material be found?			
Chapter 5: Motion-enhancement Assisted Digital Image Correlation of Lithium-ion Batteries during Lithiation			
5. e-Signatures confirming that the information above is accurate (this form should be co-signed by the supervisor/ senior author unless this is not appropriate, e.g. if the paper was a single-author work):			
Candidate:		**Date:**	16/01/2023
Supervisor/ Senior Author (where appropriate)**:**		**Date:**	14/02/2023

1. For a research manuscript that has already been published (if not yet published, please skip to section 2)**:**		
f) Where was the work published? (e.g. journal name)	Click or tap here to enter text.	
g) Who published the work? (e.g. Elsevier/Oxford University Press):	Click or tap here to enter text.	
h) When was the work published?	Click or tap to enter a date.	
i) Was the work subject to academic peer review?	Please select.	
j) Have you retained the copyright for the work?	Please select.	
[If no, please seek permission from the relevant publisher and check the box next to the below statement]: ☐ *I acknowledge permission of the publisher named under 1b to include in this thesis portions of the publication named as included in 1a.*		
2. For a research manuscript prepared for publication but that has not yet been published (if already published, please skip to section 3)**:**		
e) Has the manuscript been uploaded to a preprint server? (e.g. medRxiv):	No	**If yes, which server?** Click or tap here to enter text.

f) Where is the work intended to be published? (e.g. names of journals that you are planning to submit to)	Journal of Power Sources
g) List the manuscript's authors in the intended authorship order:	Anmol Jnawali, Matt D.R. Kok, Francesco Iacoviello, Daniel J.L. Brett, Paul R. Shearing
h) Stage of publication	Submitted

3. For multi-authored work, please give a statement of contribution covering all authors (if single-author, please skip to section 4**):**

Anmol Jnawali: Conceptualization, Investigation, Writing – original draft. **Matt D.R. Kok:** Methodology, Software. **Francesco Iacoviello:** Investigation, Writing – review & editing. **Daniel J.L. Brett:** Supervision. **Paul R. Shearing:** Supervision, Writing – review & editing, Funding acquisition.

4. In which chapter(s) of your thesis can this material be found?

Chapter 6: Examining the effects of silicon based additives on the long-term cycling capabilities of cylindrical cells

5. e-Signatures confirming that the information above is accurate (this form should be co-signed by the supervisor/ senior author unless this is not appropriate, e.g. if the paper was a single-author work):

Candidate:	Click or tap here to enter text.	**Date:**	12/04/2023
Supervisor/ Senior Author (where appropriate)**:**		**Date:**	12/04/2023

1. For a research manuscript that has already been published (if not yet published, please skip to section 2)**:**	
k) Where was the work published? (e.g. journal name)	Click or tap here to enter text.
l) Who published the work? (e.g. Elsevier/Oxford University Press):	Click or tap here to enter text.

m) When was the work published?	Click or tap to enter a date.	
n) Was the work subject to academic peer review?	Please select.	
o) Have you retained the copyright for the work?	Please select.	

[If no, please seek permission from the relevant publisher and check the box next to the below statement]:

☐ *I acknowledge permission of the publisher named under 1b to include in this thesis portions of the publication named as included in 1a.*

2. For a research manuscript prepared for publication but that has not yet been published (if already published, please skip to section 3)**:**

i) Has the manuscript been uploaded to a preprint server? (e.g. medRxiv):	No	**If yes, which server?** Click or tap here to enter text.
j) Where is the work intended to be published? (e.g. names of journals that you are planning to submit to)	Journal of The Electrochemical Society	
k) List the manuscript's authors in the intended authorship order:	Anmol Jnawali, Matt D.R. Kok, Muthu Krishna, Mina Abedi Varnosfaderani, Daniel J.L. Brett, Paul R. Shearing	
l) Stage of publication	Not yet submitted	

3. For multi-authored work, please give a statement of contribution covering all authors (if single-author, please skip to section 4)**:**

Anmol Jnawali: Conceptualization, Investigation, Writing – original draft. **Matt D.R. Kok:** Methodology, Software. **Muthu Krishna:** Investigation, Writing – review & editing. **Mina Abedi Varnosfaderani:** Investigation, Writing – review & editing. **Daniel J.L. Brett:** Supervision. **Paul R. Shearing:** Supervision, Writing – review & editing, Funding acquisition.

4. In which chapter(s) of your thesis can this material be found?

Chapter 7: Investigating the Deformation Mechanisms in Ni-rich 21700 cells

5. e-Signatures confirming that the information above is accurate (this form should be co-signed by the supervisor/ senior author unless this is not appropriate, e.g. if the paper was a single-author work):

Candidate:	Click or tap here to enter text.	**Date:**	12/04/2023
Supervisor/ Senior Author (where appropriate)**:**	Click or tap here to enter text.	**Date:**	19/04/2023

ABSTRACT

There has been a great focus on the study of the microstructure of lithium-ion (Li-ion) batteries in order to elucidate the effect of changing morphology on performance. However, just as important is the need to understand the macroscopic structural changes during battery cycling, and the effect of the changes.

This work has focused on characterising the changes in the internal structure of Li-ion batteries as a function of cycling. Investigations into how differing geometries and internal structure affect the dynamic changes within electrode rolls were also conducted. Extending this into a quasi-4D *in-situ* study, the magnitude of the changes occurring during individual charge cycles was elucidated. Finally, the effect of these macro-structural changes on battery performance was discussed.

Jelly rolls of cylindrical cells experience volume changes during each charge and discharge, which accumulates into irreversible changes over long periods, resulting in a collapse. The collapse is generally located at existing points of weaknesses in the electrode rolls. Also, variability in the internal structures of the cells (resulting from manufacturing variability) manifests as minor differences in deformation characteristics. Other influencing factors have a profound effect on the jelly roll deformation, for example, it was made clear that deformation is accelerated at lower temperatures and for cells containing silicon additives (SiO_x).

Identifying characteristics to qualify cells at a rapid pace in production lines and more accurately predict the lifetime of batteries is essential in meeting the increasing demand on Li-ion battery production. The effectiveness of X-ray computed tomography combined with image analysis tools such as the ones developed in or adapted to this work (virtual unrolling and optical flow), have been proven in characterising and quantifying macro-structural changes within batteries leading to failure. With some improvements and augments, these techniques could readily be developed into tools for quality assurance and cell life prediction.

IMPACT STATEMENT

Li-ion batteries are currently the most promising energy conversion devices for utilisation in electric vehicles. However, they are limited by the fact that once the batteries degrade in health, or performance, to 80%, they are considered unusable in electric vehicles. There are many causes for the degradation of batteries, and one of them is thought to be large scale changes in the internal cell components. The exact cause of these changes and the consequence on battery performance is not well understood.

Investigations into why these changes occur, and how they progress, as well as the effect of the macro cell design and cell format will be investigated. The impact of these changes on a battery's performance and the effect of silicon-based additives, will also be tested. Although focus will be on cell level changes, some investigations at different length and time scales will be conducted.

The findings have and will predominantly be disseminated through open-access journal publications, as well as a mixture of conference talks and poster presentations. The results may impact further research, via the utilisation of the same techniques and the vast amount of electrochemical data on numerous different cell types may be used for computational modelling of batteries. Ultimately, the results may be used to inform design optimisation, the implications of which will be seen from cell manufacture to operation. Therefore, the dissemination of this work could extend from academia to the commercial sector.

The aim of this work is to employ non-destructive X-ray CT to study the evolution in the macrostructure of commercial Li-ion batteries during operation and at different points in their cycle life, with a focus on cells that are likely to be employed in electric vehicles. This involves the use of lab-based X-ray machines with pixel resolutions ranging from a few micrometres to tens of micrometres to extract various qualitative and quantitative information on the mechanical changes in the cell and the impact of cell architecture.

A summary of the specific aims are as follows:

- To perform X-ray CT experiments on commercial cylindrical cells of varying geometries that were cycled at different conditions to elucidate the impact of cell format and cycling temperature on cell deformation and performance.

- To perform a large scale image analysis on a large batch of commercially relevant cells to obtain statistical information on variances within cells of the same batch and to further elucidate the impact of cell design and electrode composition on cell performance.

- To conduct a quantitative analysis on the changes occurring within commercial cylindrical cells with differing form factors *in-situ* using suitable 3D imaging and image registration tools.

STATEMENT OF CONTRIBUTIONS

The work presented in this thesis would not have been possible without the contributions of many brilliant people, to whom I am very grateful. All experiments in this thesis were conceived and designed by my PhD supervisor, Professor Paul R. Shearing, and I, with additional input from the other investigators for the particular experiments they contributed to.

In the following I state the contribution of other people to the data presented by chapter:

Chapter 4: Dr. Matt D. R. Kok developed the image analysis technique 'virtual unrolling'. Dr. Francesco Iacoviello assisted with the X-ray image acquisitions.

Chapter 5: Dr. Anand N. P. Radhakrishnan developed the image registration and correlation techniques. Dr. Matt D.R. Kok developed the image analysis technique 'virtual unrolling'. Dr. Francesco Iacoviello assisted with the X-ray image acquisitions.

Chapter 6: Dr. Matt D. R. Kok developed the image analysis technique 'virtual unrolling'.

Chapter 7: Dr. Matt D. R. Kok developed the image analysis technique 'virtual unrolling'. Industrial collaborators assisted with providing cell cycling data.

CONTENTS

ILLUSTRATIONS

TABLES

ABBREVIATIONS

Abbreviations	*Meaning*
Li-ion	Lithium-ion
CT	Computed tomography
NMC	Nickel manganese cobalt oxide ($NiMnCoO_2$)
LCO	Lithium cobalt oxide ($LiCoO_2$)
EC	Ethylene carbonate
PC	Propylene carbonate
DMC	Dimethyl carbonate
SOC	State of charge
SOH	State of health
EV	Electric vehicle
OCV	Open-circuit voltage
ANN	Artificial neural network
ECM	Equivalent circuit model
VRLA	Valve-regulated lead acid
BMS	Battery management system
CE	Coulombic efficiency
CC	Constant-current
CV	Constant-voltage
EKF	Extended Kalman filter
RC	Resistor-capacitor
ANFIS	Adaptive network-based fuzzy inference system
EIS	Electrochemical impedance spectroscopy
GPR	Gaussian process regression
RUL	Remaining useful life
LiPO	Lithium polymer
DRT	Distribution of relaxation times
3D	Three-dimensional
CT	Computed tomography
FIB-SEM	Focused ion beam–scanning electron microscopy
2D	Two-dimensional
PSD	Particle size distribution
NCA	Nickel cobalt aluminium
4D	Four-dimensional
LFP	Lithium-iron phosphate ($LiFePO_4$)
FOV	Field of view
MCMB	Meso-carbon micro-bead
EDX	Energy-dispersive X-ray spectroscopy
TOF-SIMS	Time-of-Flight Secondary Ion Mass Spectrometry
XRD	X-ray diffraction
DIC	Digital image correlation
DVC	Digital volume correlation
SEM	Scanning electron microscopy
LiPO	Lithium-ion polymer
EOL	End-of-life
DOD	Depth of discharge
1D	One dimensional

1 INTRODUCTION

1.1 BACKGROUND

The commercialisation of lithium-ion batteries has undergone a rapid expansion over the past two decades due to the flexible nature of the battery and its inherent advantages over alternative cell chemistries. Lithium-ion (Li-ion) batteries have high power and energy density, high capacity, long cycle life, fast response time, and can be manufactured into various form factors [1–3]. This makes them the battery of choice for applications in power tools, portable devices, and for energy storage applications. The superior capabilities of Li-ion batteries compared to other cells is demonstrated by Figure 1. Li-ion batteries have also entered the automotive industry, and there has been much effort put into making Li-ion batteries viable for such an application, such as investigating the use of new electrode types and improvement of existing electrode materials. There are many reviews discussing recent advances and the key issues facing the development of Li-ion batteries, such as the need for material development towards higher capacity anodes like Silicon in order to meet higher energy demands [4,5]. For electric vehicle applications, the ability to charge the batteries at a rapid rate is a must. Zhang [6] states that fast charging is limited by lithium plating mechanisms and instability of the cathode, and discusses potential solutions such as reducing internal resistance by surface modification of graphite and improving cathode stability through doping. In the current environmental landscape, there is a big push towards sustainability, with one of the research focus being directed towards eliminating the use of toxic and expensive materials. Deviation from nickel cobalt manganese based

chemistries to materials such as $LiNi_{0.5}Mn_{1.5}O_4$ [7] which eliminates Cobalt, and $LiMn_2O_4$ [8] which further removes nickel have gained increasing traction. Furthermore, there is also increasing research into alternative battery chemistries altogether, such as sodium-ion [9] based batteries to circumvent the increasing cost due to depleting reserves associated with lithium. Another sustainability strategy being relatively newly explored in greater depth is recyclability of batteries [10], and *'second life'* applications which is using batteries for alternative applications after they reach 80% reversible capacity and are considered no longer fit for electric vehicle applications. One of the major issues regarding recycling is the lack of clear labelling on batteries and a lack of transparency on the exact compositions of the batteries. Although the exploration of alternate chemistries and sustainability issues is besides the scope of this work, it is important to keep such issues in mind.

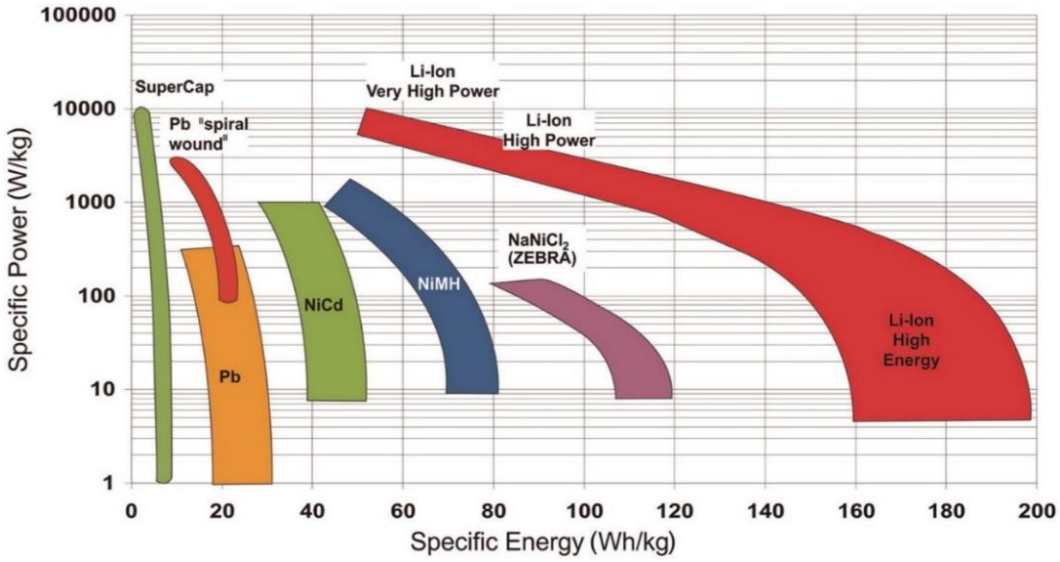

Figure 1: Ragone plot showing the energy and power densities of various battery technologies. Reprinted with permission from [11] © 2013 IMechE.

The materials for rechargeable lithium batteries were first discovered in the late 1970s [12], and were commercialised by Sony around 1990 with the introduction of a graphite//lithium cobalt oxide cell [13]. Secondary (rechargeable) Li-ion batteries require at least three components to function: positive electrode (cathode), negative electrode (anode), and an electrolyte. The safe operation of a battery requires many

more components, some of which shall be discussed later. Li-ion batteries work by the principle of intercalation and de-intercalation of Li^+ ions in the cathode and anode. Lithiated transition metal host structures are commonly used as cathodes for Li-ion batteries. The host structure is considered fully lithiated when it is fully populated with alkali metal atoms [14]. During the charging process, the positive electrode undergoes oxidation, and the Li^+ ions migrate through the electrolyte towards the anode. Electrons pass through an external electrical circuit, by way of current collectors, towards the anode. The positive Li^+ ions diffuse towards the anode due to electrical and chemical driving forces – a more comprehensive explanation can be found in [15]. The Li^+ ions then diffuse through the ion conducting electrolyte and insert themselves between the layers of the anode. This process causes an increase in the volume of the anode depending on the material – for conventional graphite anodes this is ca. 10 vol%, whilst silicon alloying-type electrodes undergo a volume expansion of up to 300% [2,16,17]. This changes the oxidation state of the material, however it is generally not by a whole number as intercalation materials are nonstoichiometric [15]. The electro-neutrality of the material must be preserved, and so the electrons from the external circuit are used to form a lithiated anode. The reverse occurs during discharge.

A working battery contains more than just the base functional components, such as current collecting tabs, mandrels, and safety devices e.g. a positive temperature coefficient switch which protects against high temperature and pressure. Whilst the microstructural evolution of batteries during cycling can have a big impact on the lifetime of a cell, such as particle fracture resulting from the expansion and contraction due to Li^+ ion de/intercalation, the other components could also have similar impacts. Various avenues have been utilised to study the impact of cell architecture on the large scale, macro, or bulk changes within Li-ion cells and on their impact on performance, such as: modelling the strain and inhomogeneity in Li-ion cells [18,19]; using high precision equipment to measure strain and changes in architecture [20]; using XRD-based techniques to measure strain inside cells [21]; using X-ray computed tomography (CT) to observe mechanical changes within cells impacted by the internal structure of the cells [22,23], and quantifying such mechanical changes with digital volume correlation (DVC) or digital image correlation (DIC) [24].

There is an ever-increasing need for higher-power, higher-energy batteries for automotive applications, which drives an increasing need for better understanding of certain factors affecting battery performance. However, it is difficult to isolate the interconnected mechanisms that are involved in the operation of a cell, hence it is difficult to ascertain exactly which factor may cause cell failure. There is a lack of literatures bridging the gap between cell design, cell defects, mechanical defects and performance. This work outlines some methods used to try to understand aspects of cell architecture that might be influencing the rate of degradation in the performance of cells. More specifically, this work tries to understand the impact of aspects such as jelly roll imperfections as a result of manufacturing conditions, cell design (location and number of tabs, inclusion/exclusion of mandrels), and mechanical deformations on the electrochemical performance and degradation of batteries in order to inform design principles for better and potentially safer batteries.

1.2 ELECTROCHEMISTRY BASICS

For basic functionality, an electrochemical cell needs only a cathode, anode, and an electrolyte. The electrodes are required for charge transfer (lithiation/delithiation), in order to create a circuit of electron flow. The electrolyte enables the transfer of ions between the electrodes. However, a battery requires many more components for effective operation, some of which are: separator, current collector, casing, and certain safety and structural features. Some of the basic components have been illustrated in Figure 2. The performance of a lithium-ion (Li-ion) battery is greatly dependent upon the effectiveness of these constituents.

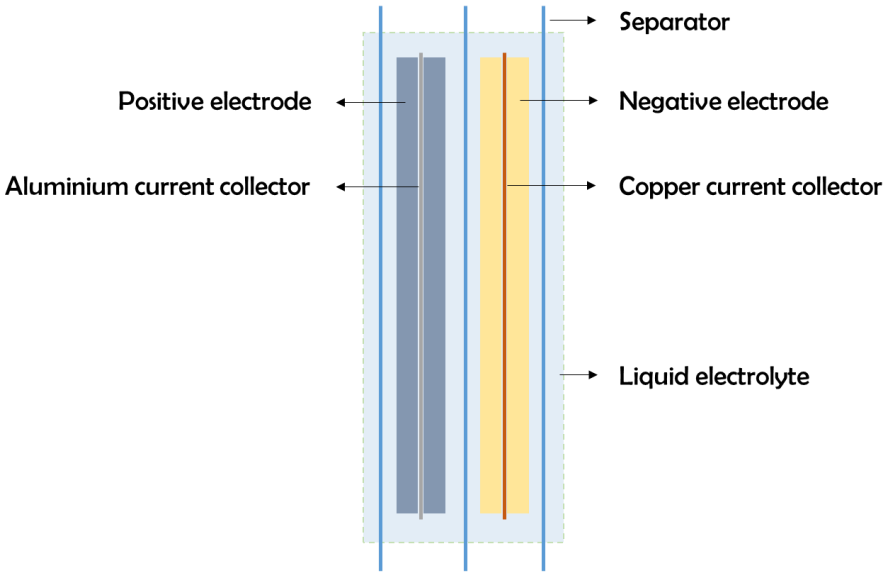

Figure 2: Schematic of some of the components present in a standard Li-ion battery.

In an electrochemical cell, chemical reactions occur at the electrodes when an ionic conductor is present [15]. During a charge operation, an oxidation reaction occurs at the positive electrode and the Li^+ ions are transported through the separator in the electrolyte and are inserted between the interstitial spaces between the negative electrode layers. The separator is electrically insulating, so electrons are transported through an external circuit. An example of the reactions at the two electrodes of a Li-ion cell containing a lithiated $Ni_yMn_zCo_{1-y-z}O_2$ (NMC) positive electrode and a graphite (C_6) negative electrode are given below.

The positive electrode half reaction is

$$xLi^+ + Li_{1-x}Ni_yMn_zCo_{1-y-z}O_2 + xe^- \rightleftharpoons LiNi_yMn_zCo_{1-y-z}O_2 \qquad 1$$

The negative electrode half reaction is

$$Li_xC_6 \rightleftharpoons xLi^+ + C_6 + xe^- \quad (2)$$

The current collectors in Li-ion batteries ensure a uniform distribution of current throughout the electrodes. The current collecting materials must not react with the electrode active materials to form alloys, and there must be potential stability between the electrodes and current collector during operation. Of course, the materials must also have a high electronic conductivity. Braithwaite *et al.* [25] studied the corrosion behaviour of aluminium and copper current collectors in excess electrolyte at ambient temperatures. They found that the aluminium current collector showed pit-like corrosion (independent of metallurgical purity) within a few hundred cycles. The copper current collector was found to be susceptible to environmental cracking only when specific metallurgical conditions existed, such as work hardening and large grain size. In some batteries, a current collector can provide structural support, such as when employing nanowires and thin films composites [26]. Copper is used for the anodes due to its stability at lower voltages, and aluminium is used for the cathode for its stability at higher voltages and its ability to form a passivating layer with common electrolyte components such as PF_6^- [25]. Aluminium is also lighter and relatively cheaper than copper, contributing to higher energy densities and lower cost.

The cell casing is used to hermetically seal the battery and protect the internal components from damage. Therefore, it should be rigid enough to maintain the shape of the battery and must not react with the electrode active materials and form an alloy [27]. Some battery casings have integrated safety mechanisms, such as pressure vents. These allow gases and molten battery materials to escape during battery failure, preventing rupture, and potential explosions [28].

1.3 BASIC COMPONENTS IN A BATTERY

1.3.1 Electrodes

The relatively slow deployment and adoption of electrical vehicles has been attributed to the lack of suitable electrode materials [29]. A Li-ion electrode must fulfil several requirements to be a good host material: good electrical conductivity; minimal structural change during de-intercalation of ions; minimal volume expansion during ion intercalation; stability with electrolyte over the operational voltage range [14]. A typical composite electrode is composed of three components: the active material, which participates in the electrochemical process; an additive to increase the electronic conductivity of the electrode; and a binder, which ensures that the electrode components adhere to each other, and to the current collector. The percentage (by mass) of the three components in the electrode is an important factor when balancing operational capability and structural integrity – too much binder material can adversely affect cycling life [30].

1.3.1.1 Negative Electrode (Anode)

Lithium metal anodes form dendrites during charge cycling, which can cause electrical shorts and initiate a thermal runaway. Therefore, research and development of secondary anode materials is necessary. Anodes are divided by the types of reactions that occur at the electrode: intercalation, conversion, and alloying [5]. Conversion reactions involve a complete change in the structure and chemical identity of the reactants [5], and alloying is occurs when elements electrochemically alloy and form compound phases with lithium [4].

The most prominent intercalation anode material is graphite. It has high Coulombic efficiency and good cycling performance. The reason for its good performance is the small volume expansion (of ca. 10% [31]) which enables it to maintain charge capacity

over many cycles. However, graphite has a relatively low specific capacity of only 372 mAh g^{-1} [32,33] when compared to other possible anode materials. There have also been studies on the performance of graphene nanocomposites as anode materials. Zhou *et al.* [34] found that their graphene–wrapped Fe_3O_4 nanosheets retained a specific capacity of 580 mAh g^{-1} after 100 cycles at currents of 700 mA g^{-1}, while Lian *et al.* [35] demonstrated reversible capacity of 1048 mAh g^{-1} at the 90th cycle at various current densities with their Fe_3O_4–graphene nanocomposite.

Conversion reactions occur with transition metal oxide (TMO) electrodes, such as CoO, Fe_2O_3, and CuO. These materials show reversible lithium storage capabilities. There will not be further discussion on them, as they are not widely used and are beyond the scope of this thesis.

Silicon is among the high capacity alloying elements that have garnered a significant amount of research interest. Silicon has significantly greater theoretical specific capacity (4200 mAh g^{-1}) than graphite [16]. However, silicon electrodes exhibit many issues that prevent their widespread application, such as significant solid electrolyte interphase (SEI) formation and cracking of the active material particles due to large volume expansions [16,17]. Silicon micro- and nano- particles show more favourable performance. For example, Lee *et al.* [26] prepared a silicon nanoparticles–graphene paper composite anode and found that it had a storage capacity of 1500 mAh g^{-1} after 200 cycles.

1.3.1.2 Positive Electrode (Cathode)

Cathode intercalation compounds can be divided into several groups by their crystal structures, such as layered ($LiCoO_2$), spinel ($LiMn_2O_4$), olivine ($LiFePO_4$), and tavorite ($LiFeSO_4F$). There have been many developments in cathode materials in order to improve battery performance, such as increasing capacity retention, improving cycling performance and life, and expanding the operating voltage range. Some examples are: development of composite electrodes with the combination (intermixed, layered, or coated) of two electrode materials [36–41]; doping of the cathode material using

transition metals and other elements such as zinc, titanium, zirconium, aluminium, and magnesium [42–49].

Transition metal oxides are the most commonly used positive electrode materials. Lithium cobalt oxide (LCO, $LiCoO_2$) is prolific as a cathode material. However, cobalt is relatively expensive compared to manganese and iron, and it can also undergo performance degradation or failure more easily (due to the formation of water impurities) when overcharged [50–53]. The partial substitution of manganese and nickel has proven an effective method for improving the electrochemical performance of the cells [54]. $LiNi_{1/3}Mn_{1/3}Co_{1/3}O_2$ (NMC-111) cells have high rate capability and stability, greater discharge capacity and a higher operating voltage range at steady-state compared to $LiCoO_2$ [5]. There is a trend towards higher Ni content (such as $LiNi_{0.8}Mn_{0.1}Co_{0.1}O_2$) in positive electrodes due to the increasing demand for higher energy batteries. However, it is important to balance the content of the cobalt and nickel, as increasing cobalt increases capacity retention, but decreasing nickel content decreases capacity [54].

1.3.1.3 Electrolyte

The electrolyte provides a conductive path for the Li^+ cations to propagate between the two electrodes. During the first charge/discharge cycle of a cell, the electrolyte undergoes decomposition and forms the 'solid electrolyte interphase' (SEI) layer on the negative electrode. A cathode electrolyte interphase (CEI) is also formed on the surface of the cathode. These layers protect the electrolyte from further decomposition and from unwanted reduction or oxidation by the electrodes [29]. It also causes a significant irreversible loss of capacity as demonstrated by the sharp decrease in reversible capacity observed after the first cycle in Figure 3. The composition and morphology of the SEI layer can significantly impact the performance of a battery. A review on the factors affecting SEI, characterising SEI and analyses can be found in [55].

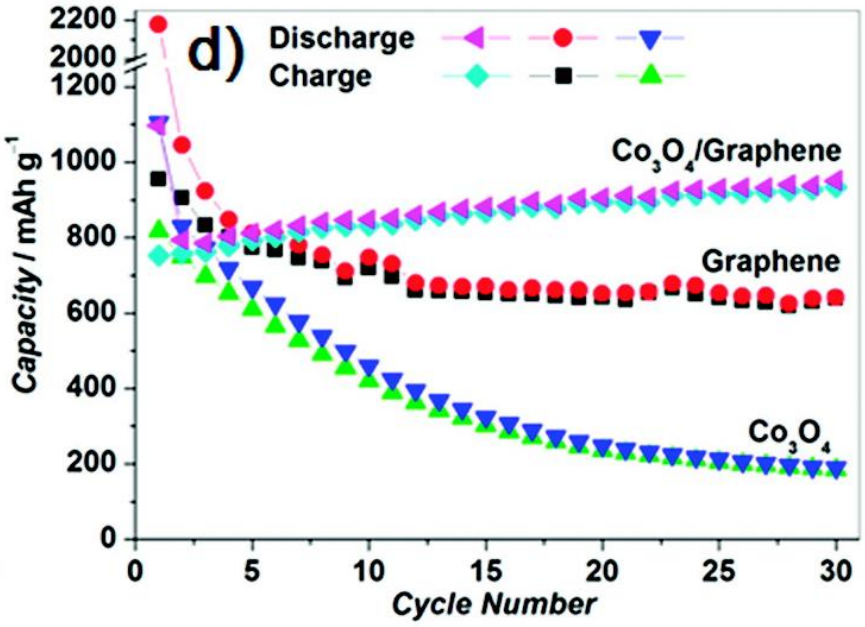

Figure 3: Demonstration of capacity loss after first cycle (significant drop in capacity between the first and second cycles) in Li-ion cells. Reprinted with permission from [56] © 2010 American Chemical Society.

The composition of the SEI layer is dependent on the composition of the electrolyte. Manthiram [57] attributes the ability of Li-ion batteries to achieve high voltages, and therefore high energy density, due to the use of non-aqueous electrolytes. In Li-ion batteries, electrolytes containing $LiPF_6$, $LiBF_4$, and $LiClO_4$ salts dissolved in ethylene carbonate (EC), propylene carbonate (PC) and dimethyl carbonate (DMC) are commonly used. Zhang [58] has reviewed electrolyte additives and their purpose for Li-ion batteries and a review on Li-ion electrolytes, and on strategies to improve electrolyte solutions for Li-ion batteries can be found in [59].

During abnormal battery operation, thermal runaway propagates due to the decomposition of the electrolyte as it reacts with the electrode [60]. Xu *et al.* [61] attempted to formulate a non-flammable electrolyte for Li-ion systems by incorporating flame-retarding additives such as alkyl phosphates and cyclophosphazene co-solvents. They discovered that even greater than 10% co-solvent content was not enough to render the electrolytes completely non-flammable. They

also found that although there was a decrease in performance due to the additives, the electrolyte containing hexamethoxycyclotri-phosphazene showed almost negligible drop in capacity over 100 cycles.

1.3.1.4 Separator

Separators are important for both the functionality of the battery as well as safety. If the electrodes within the battery come into contact, an internal short-circuit could occur, leading to potentially disastrous consequences, such as thermal runaway. Separators prevent such occurrences, and also provide a reservoir for the electrolyte. There have been great developments in separator technology over the decades, from cedar shingles to membranes [62]. Separators are required to have a wide variety of properties, including: electrochemical and mechanical stability, and large electrolyte uptake [60,63]. Additionally, they must be porous in order to allow ions to permeate, but the pores must be narrow enough that the crystals/components in the electrodes do not pass through. Lee *et al.* [64] suggest that separators for Li-ion batteries must generally have a pore size less than 1 μm, and they also provide a review of different separator types and composition for Li-ion batteries. Modern separators have safety features and are referred to as 'shutdown separators': the separator shutdown process involves softening of the separator from excess heat generated, leading to closing of the pores and the effective cessation of ionic current flow [27], however, Belov & Yang [65] have found that the shutdown mechanism is not effective in conditions where the rate of heat generation is too great. Venugopal *et al.* [63] characterised the properties of some commercially available Li-ion battery separators – they found that separators containing polyethylene were more efficient at preventing thermal runaway. Lagadec *et al.* [66] have conducted a thorough review of separator characteristics and performances.

1.4 THESIS OUTLINE

This thesis is organised in the following manner:

Chapter 2 provides a review on the techniques to diagnose the state of charge and state of health using techniques that measure electrochemical data. It also provides a review on the investigation of battery architecture, morphology, and health using imaging techniques and correlation techniques that make use out of the images obtained.

Chapter 3 covers the methods and instruments used to carry out the experiments in this thesis. It contains information on the electrochemical testing procedures, X-ray image acquisition, and image correlation techniques.

Chapter 4 demonstrates the impact of mechanical changes on the degradation of different batteries, as well as the impact of storage and cycling conditions.

Chapter 5 illustrates the combination of imaging and image correlation techniques to investigate strain gradients in cells with different internal structures.

Chapter 6 investigates the impact of silicone on the mechanical properties of the jelly roll and the degradation of the cells.

Chapter 7 presents a large scale investigation into the structural changes in 21700 EV cells as a function of long term cycling.

Chapter 8 provides conclusions drawn throughout the thesis and also provides some suggestion on the future work that can be carried in order to improve upon the results and techniques discussed.

2 LITERATURE REVIEW

2.1 ELECTROCHEMICAL DIAGNOSTIC TECHNIQUES

2.1.1 Introduction

During a standard charge/discharge cycle, both potentiostatic and Galvanostatic modes are used in order to accurately control the flow of current and the voltage of a battery. Cell cycling is typically carried out in reference to '*C-rates*'. It is a normalisation of cycling rates against the cells' capacities, and the numerical value of *C* is dependent on the cell type and model. If a cell has a rated capacity of *k Ampere-hours* (where *k* is a constant), then 1C will be equivalent to *k Amperes*. The time it takes to fully charge or discharge a cell is inversely proportional to the C-rate used. An example is provided in Table 1.

The state of charge (SOC) of a battery indicates how much energy is remaining in a battery, and the state of health (SOH) is a characterisation of the extent of degradation experienced by the cell at a point in its cycle life. It is critical to be able to accurately and precisely measure or estimate these two factors both in operation in electric vehicles (EVs) and for testing cells for experimental purposes. Some of the principle diagnostic techniques for the measurement and estimation of SOC and SOH based on battery electrochemistry will be discussed in this section.

Table 1: Theoretical charge or discharge times for a cell with a rated capacity of 5 Ah.

C-RATE	CURRENT (A)	CHARGE/DISCHARGE TIME (H)
1C	5	1
3/5C	3	1.67
2C	10	0.5

2.1.2 Voltage Method

The voltage method is relatively simple to use in that a known discharge curve can be used to derive the relationship between the voltage and the SOC of the cell. However, voltage is greatly impacted by factors such as current and temperature (*T*). The agitation caused by the electrochemical kinetics while the cell is under a load distorts the voltage and so it is not an accurate representation of the true SOC. This can be compensated for by taking the measurements while the cell is not under any load. Lookup tables or a data bank could be created for open-circuit voltage (OCV) vs. SOC, or OCV vs. T. However, interrupting operation and resting the cell for periods ranging from one hour to several hours in order to achieve OCV [67–69] can be impractical for most applications.

For this reason, literature in the past decade with a focus primarily on the voltage method as a stand-alone technique is limited. It is mostly applied as a supplement to other techniques, such as for initial calibration of Coulomb counting methods. For such applications of the voltage method, the SOC-OCV relationship is obtained in data banks, and where it's not available, it can be obtained experimentally, typically by discharging the cell at low rates with intermittent rest periods [70].

Naha *et al.* [71] propose a technique of determining a battery's SOH using a differential voltage-based feature. The technique requires offline training of an artificial neural network (ANN), but would enable online SOH estimations. They use features generated utilising the terminal voltage, current, and the cell's internal resistance for

the SOH estimation with the ANN framework. They were able to estimate SOH with errors of less than 1%. Deng *et al.* [72] have promoted an improved OCV method for a magnesium acid lithium battery which reduces the OCV incubation time, based on an equivalent circuit model (ECM). Qurthobi *et al.* [73] pursued the correlation between the OCV in a valve-regulated lead acid (VRLA) battery to its voltage in a loaded condition. They measured the resulting voltage difference between the OCV and the measured voltage when loaded at different SOCs during the discharge to obtain a correlation parameter which was then used to estimate the OCV at any point during loaded conditions.

2.1.3 Coulomb Counting

The Coulomb counting method is a technique in which the current flowing through a cell is integrated to obtain the total energy, providing the capacity of the battery in *Ah*. The charge or discharge capacity during a cycle, *q*, can be obtained from Equation 3 [74] and the SOC from Equation 4.

$$q = \sum I \cdot \Delta t \tag{3}$$

$$SOC(t) = SOC(t_0) + \frac{1}{q_r}\int_{t_0}^{t} I\, dt \tag{4}$$

where, *I* is the current and *t* is the duration of the charge or discharge, q_r, is the nominal or rated capacity of the battery, $SOC(t_0)$ is the initial SOC, at time $t = 0$. The obtained capacity can then be used to calculate the SOH of a cell:

$$SOH = \left(\frac{q_r - q}{q_r}\right) \times 100 \tag{5}$$

Coulombic efficiency (CE), also called Faradaic efficiency or current efficiency, is the ratio of the total charge extracted from the battery to the total charge put into the battery over a full cycle [52], as defined by Equation 6.

$$CE = \left(\frac{q_d}{q_c}\right) \times 100 \qquad 6$$

where, q_d is the discharge capacity, and q_c is the charge capacity. The energy available from a cell is always less than what is delivered onto the cell due to losses, therefore this method provides a simple and elegant solution for evaluating the performance of batteries by comparing columbic efficiencies.

The simplest way of evaluating battery performance and the decrease in effectiveness of a cell is to measure the capacity of a battery as it is cycled. This analysis can be used to appraise the operational efficacy of experimental cells to aid material selection and advancement: Qie *et al.* [33] exhibited the capacity and rate capability of Nitrogen-doped porous carbon nanofiber anodes for use in Li-ion cells; Komaba *et al.* [75] studied the difference in cyclability and capacity retention of SiO anode produced using different polymer binders – they resolved that the electrode performance is dependent on the binder and found poly(acrylic acid) to perform better than poly(vinyl alcohol), sodium carboxymethyl-cellulose, and conventional poly(vinylidene fluoride) binders; and Zhou *et al.* [76] compared the electrochemical performance of a hybrid anode material to find that graphene/carbon-coated Si nanoparticles displayed better long term cycle performance than graphene-Si hybrids or pristine Si. The performance of individual cells can impact the utilisation in battery packs and modules and can also result in increased degradation through overcharge and/or over-discharge. Coulomb counting can also be used to assess the performance of individual commercial cells at different cycling rates: Petzl *et al.* [77] carried out capacity fade analyses to determine the capacity retention of commercial Li-ion cells at different rates and found that higher rates leads to higher capacity loss. They also determined that there is decreased capacity fade after an initial period of rapid fade, at *'progressed degradation states'*.

Additionally, the technique can be used to determine or model pack capacity loss. Zheng *et al.* [78] represent pack capacity evolution by the *'electric quantity'* of the cells within a pack, which constrain the pack during the charge or discharge process, respectively. They present that the pack capacity does not necessarily depend on the individual cells' state of charge or capacity.

Accurately estimating the SOC and/or SOH of batteries is paramount in battery packs in order to accurately determine the energy levels in cells and also to determine remaining life of cells. This is however made difficult in battery packs due to the small variances in the initial states of batteries: electrode loading; electrolyte volume; resistance; minor structural differences due to the electrode calendering process. These variations cause the cells to age at different rates, and the differences become more accentuated over the course of the cells' life, complicating the estimation of pack SOC and SOH. In summary, the main issues with the sole use of the Coulomb counting method is that it is dependent on the initial SOC value, which is required to be accurate as otherwise there will be an increasing accumulation of errors, and that it needs to be recalibrated in order to account for ageing effects [79]. Therefore, novel methodology, and computational aid must be utilised.

Coulomb counting is often combined with OCV curves for calibration as cells age [80,81]. In that vein, Liu *et al.* [82] proposed a novel method in which the discharge process is divided into two modes based on the level of variation between the cells. Simply, SOC is estimated using an *'average cell'* for low inconsistencies, where the estimated OCV of the average cell is mapped to obtain the average SOC, whereas for a pack with higher inconsistencies, SOC is measured for all cells using the same method as before but also implementing Ampere-hour integrals and the pack SOC is determined by the cell with the *'poorest SOC cell'*. A point to note with this method is the computational load as the SOC of each individual cell has to be established. In [83], Zhang *et al.* replace the voltage axis in a differential capacity analysis with SOC as a way of calibrating the initial SOC value. In another paper [84], the same authors pose the use of the Coulomb counting method combined with differential voltage analysis as a workaround to the computational and data burdens placed on model-based and

data-driven approaches to calculating SOH. They used discrete analysis to identify two feature points in a dV/dQ vs. SOC plot in order to derive the measurement times. Then, the SOC, initial capacity, and current (which can be measured in real time) along with the obtained measurement times are used to calculate the battery SOH during discharge with errors limited to 0.5%. Data compression and computational efficiency is obtained through capturing real time parameters such as current and voltage based on *'events'* and not periodically in [85]. These events are predefined thresholds based on the current waveform dynamics and the measurements are used to obtain real time SOC using a Coulomb counting algorithm. Wu & Moo [86] attempt to increase the accuracy of SOC estimation through Coulomb counting by taking into account the degrading capacity of the cell – the change in SOH – where the SOC is defined based on the percentage of the estimated capacity relative to the present full capacity.

Garmendia *et al.* [87] propose utilising different SOC estimation modes depending on what state of cycling the battery is in: Coulomb counting method for constant-current (CC) charge/discharge states, mapping the SOC vs. constant-voltage (CV) values for the CV state, and mapping OCV vs. SOC for the rest state. For BMS integration they propose carrying out three SOC estimations simultaneously, for the cells with the lowest, highest, and average voltage in a module, in order to obtain the range within which the battery pack is operating and represent the average SOC of the pack. He and a colleague [88] tout a 90% reduction in computational time compared to models such as extended Kalman filter (EKF) by employing Coulomb counting in conjunction with a 2nd order resistor-capacitor (RC) battery model for real time error correction. Firstly, battery state is determined by the model by defining the divergence degree of the '*dynamic voltages´* from steady state. Then, Coulomb counting is used to obtain the cell SOC during the unsteady states. The model is used to identify parameters and the SOC-OCV curve offline, and is used to obtain the SOC at the steady states which is used as a correction.

Even though battery models and intelligent algorithms may carry heavy computational loads, and may also require extensive offline testing of batteries for parameter estimation, they may not accurately predict SOC as they do not necessarily account for

environmental factors or the need for real-time estimation. Sometimes experimental data is used for more than validation purposes; a mixed technique approach is utilised to determine SOC and SOH using models in order to reduce computational load or to increase reliability. Sarrafan & colleagues [89] propose a mix of Coulomb counting method and a model-based approach which takes into account battery cycling conditions and environmental and traffic conditions. Chao-Tsung [90] proposed a hybrid adaptive network-based fuzzy inference system (ANFIS) Coulomb counting method to increase the reliability of real-time SOC estimation. This intelligent algorithm is used to learn the non-linear mapping relationships between the SOC and characteristic parameters such as temperature and cycling rates, and simulate the SOC, while the Coulomb counting method is used in parallel to verify and increase reliability. Ganeshan and a friend [91] utilised a mixed algorithm of a back propagation neural network and Coulomb counting. The neural network is first trained using data (voltage, current, temperature) obtained from the cycling of a cell at constant and variable loads. Once trained, it is implemented into a microcontroller and the neural network determines the SOC and Coulomb counting is used to obtain the cell capacity and calculate SOH. Zhao *et al.* [92] proposed the use of Columbic efficiency to minimise the cumulative errors involved with the Coulomb counting method using a least-squares based algorithm. A formula for determining Coulombic efficiency that accounts for current, temperature, SOC and SOH would prove too heavy a burden computationally, therefore to reduce the load they have assumed SOH has little influence on efficiency on the short term, and that efficiency remains relatively unchanged when limiting the discharge cut-off to be 25% SOC. Similarly, Gonzalez *et al.* [93] present the inclusion of cyclic efficiency, along with the battery's self-discharge rate in order to improve the precision of the SOC estimation through Coulomb counting. They also proposed the use of a trapezoidal rule for the current integration with a width equal to the step time between the current recordings, however an error analysis in comparison to the rectangular method was beyond the scope of their study. Xie *et al.* [94] also utilise Columbic efficiency during the charging process and a modified Peukert equation to determine SOC. Through this, they were able to account for the rate and temperature dependency of the columbic efficiency by more accurately determining the SOC of cells.

Simply monitoring the capacity of a cell or pack as it undergoes degradation has limited practical relevance. In order for the technique to be of benefit, both for operational and safety reasons, it needs to be able to predict cell behaviour, degradation, and potentially, failure. Leow and colleagues [74] used the OCV method to determine the initial capacity of their cell for on-line SOC and SOH monitoring of cells in grid energy storage systems. As well as using the Coulomb counting method to determine SOC, they used the integral of current over time to determine SOH as a ratio of the calculated discharge capacity over the initial battery capacity. They were also able to conduct a lifetime analysis of their cell by extrapolating their SOH data over 50 cycles in order to predict when the cell would reach effective failure (80% of initial capacity).

Depending on the location, EV battery packs could experience temperatures ranging below 0 °C and above 40 °C. Besides leading to increased degradation, non-standard temperatures have an inherent effect on a cell's capacity [95]. Decreasing temperature leads to increasing internal resistance of the battery, reducing chemical reaction rate, therefore the maximum and minimum voltages are reached earlier, effectively reducing the available capacity [96–98]. At higher temperatures, the internal resistance decreases, leading to higher chemical activity and may result in, for example, self-discharge [95,96]. Simple Coulomb counting methods do not account for these losses, therefore in order to increase accuracy and decrease the cumulative errors involved, improvements need to be added to account for temperature effects as demonstrated in [90–92]. Feng *et al.* [99] estimated the SOC of cells at different ambient temperatures using an enhanced Coulomb counting method which employs Coulombic efficiency, and the OCV method for initialisation. They noticed that increasing current leads to a greater decrease in Coulombic efficiency at lower temperatures.

2.1.4 Electrochemical Impedance Spectroscopy

Electrochemical impedance spectroscopy (EIS) is a non-invasive technique for characterising cell resistance and state. The internal resistance of a battery is composed of Ohmic resistance and ionic resistance. Ionic resistance is a measure of the resistance

to current flow due to electrochemical factors, such as the conductivity of the electrolyte and the electrode surface area. Ohmic resistance is the resistance of an electrical circuit to current flow.

Impedance can be determined by applying an AC sinusoidal current or voltage perturbation over a range of frequencies and observing the corresponding voltage or current response. A lower internal resistance is indicative of a healthier cell, and increasing internal resistance suggests degradation of the cell. The impedance, as a function of the frequency, can be determined by the Ohm's law for an AC circuit:

$$Z(\omega) = \frac{E(\omega)}{I(\omega)} \qquad 7$$

where, E is voltage, I is the current, Z is impedance, and ω is the frequency. The mathematics behind the derivation of the equation and the determination of the impedance can be found in [100].

Figure 4 shows an ideal EIS response of a Li-ion cell (formation of two semi-circles) in the form of a Nyquist plot. The response incorporates several elements [69,101,102]: the bulk resistance, R_b, determined by the intercept at the real axis and which incorporates electric conductivity of the electrolyte and electrodes; resistance of the interface layers, R_{sei}, that is formed at the surface of the electrodes; charge transfer resistance, R_{ct}; and the Warburg impedance, W, associated with the diffusional effects of Li^+ ions on the interface of the active particles and electrolyte.

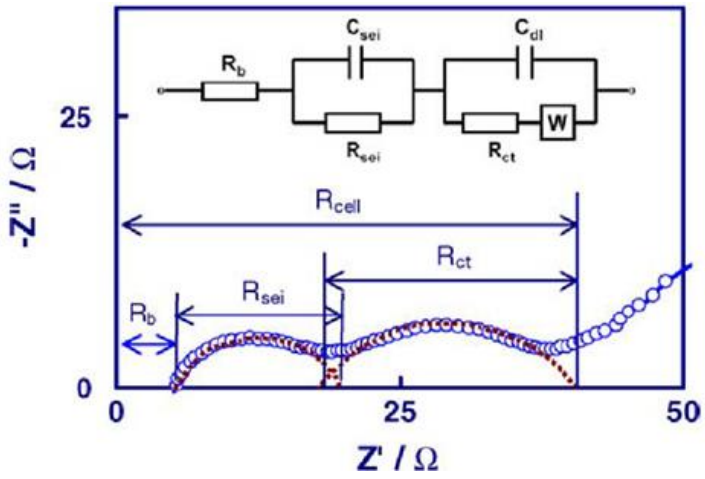

Figure 4: Typical Nyquist plot of a Li-ion cell. Reprinted with permission from [101] © 2004 Elsevier.

Hence, EIS provides useful information on the increasing resistances of batteries due to internal and external factors, and gives an indication of the state of a battery. However, it can be a very time consuming and costly method, especially when sweeping over a wide frequency range. In recent years, there have been various methods proposed for pack level, on-board EIS measurements or estimation, and in order to reduce the cost and time consumption, researchers have implemented: square waveforms followed by Fourier transforms [103]; wavelet transforms on time domain data to obtain information on the frequency domain [104]; broadband excitation signals for the measurements [105]; excitation currents generated by a motor controller [106].

Where SOH just gives the ratio between the reversible capacity and the nominal capacity, remaining useful life (RUL) tries to predict the remaining cycles until the SOH of the battery reaches 0% [107] - as such, the models must consider the dynamic parameters of the batteries which evolve as the batteries age [108]. Zhang *et al.* [109] obtained over 20,000 EIS spectra on LCO cells at a wide range of frequencies, temperatures, and SOC for their machine learning process, adopting Gaussian process regression (GPR). They use rest periods of 15 mins and use this technique to predict the capacity and RUL of cells. However, their accuracy is dependent on the

temperature staying constant and for cells cycled at the same rates as the training data was obtained on. Guha & Patra [110] propose online estimation of RUL based on the estimation of EIS through a fractional-order ECM. The parameters for the EIS estimation were obtained through processing of voltage and current measurements using least-squares technique. The internal resistance growth trend obtained from the EIS spectra were used to predict the RUL of the cells. In another paper [111], the authors combined the internal resistance growth model with a battery capacity degradation model to develop a model for RUL estimation. Similarly, Galeotti *et al.* [112] have used ECM parameters and the relationship between ohmic resistance and capacity to evaluate SOH in a lithium polymer (LiPO) cell.

Guo *et al.* [113] apply EIS to determine the SOH of cells. This was done by the deconvolution of the EIS spectra with respect to a modified distribution of relaxation times (DRT) method, considering the differential capacity of Li-ion cells. They were able to determine the SOH of various cells at different points in their cycle life with a maximum error of 1.13%. Zhou *et al.* [114] also use DRT analysis to obtain characteristic time constants. These were then used to determine characteristic frequency points where impedance contributed by the different polarisation losses, ohmic, contact and SEI, are fully developed. Then the estimation of the resistances caused by the losses can be calculated for general battery monitoring. Though they do not explore the use of the technique for determining SOC and SOH of cells, the technique is SOC-independent, so it is time and cost efficient.

Wang *et al.* [115] estimated the SOH of LFP cells by considering and calculating the growth in charge transfer resistance as compared to that at the beginning of the cell's cycle life, based on model parameters obtained from experiments at different SOC and temperatures. Rue *et al.* [116] pose a SOC estimation method for $LiFePO_4$–$Li_4Ti_5O_{12}$ (LFP-LTO) cells in which they map changes in the battery's response to perturbations. For on-board measurements and estimation, they use a binary current perturbation to simulate an on/off transient load and the EIS is obtained using a *'system identification'* method. Then they identify signature features in the EIS and map against SOC. Li [117] also made use of system identification for deriving the parameters for their EIS

estimation through an ECM designed using extended Kalman filtering (EKF), which was used for real-time estimation of cell SOC. Through experimental validation, they determined a relative error of less than 3% for their method for simulating the SOC of Li-ion cells. Westerhoff *et al.* [118] also use EIS and a simplified ECM to inform SOC estimation of Li-ion cells. By comparing the fitting parameters against the SOC derived through coulomb counting, they were able to determine a relationship between SOC and the circuit components. They estimated the SOC with a maximum touted error of 4.8% in the mid SOC ranges (20 – 80%), however their methodology has not taken battery ageing into account.

Mingant *et al.* [119] developed a novel technique to build a 'quasi-electrochemical impedance spectrum' (QEIS) for SOH estimation that makes use of only the current and voltage signals that would be easily obtained in any on-board system. The QEIS was determined by applying a Fast Fourier Transform (FTT) on the voltage and current signals for LFP modules undergoing drive cycles. The QEIS was fitted using an ECM and the fitting parameters were empirically correlated to SOH.

Lee & Choi [120] proposed another method for estimating the SOC of LiPO cells where fitting parameters are extracted using an equivalent impedance model and compared to changes at different SOCs. Their technique greatly reduces measurement time as data needs to only be collected at two frequencies. Love and colleagues [121] improve upon their previous work on single point impedance diagnostic [122] to monitor the SOH of a lithium cobolt oxide (LCO) pack. The technique hinges on finding a frequency at which there is minimal change in impedance of the LCO cells for normal SOC ranges, but at which there is a significant change during overcharge. They were able to determine the presence of an overcharged cell even though the pack was within operating limits, whilst eliminating the need to collect full impedance spectrums.

2.1.5 Summary of Electrochemical Diagnostic Techniques

To summarise: electrochemical diagnostic techniques are vital to measure the throughput of cells and their state of health and the amount of energy remaining at any given time. All the electrochemical techniques discussed in this chapter can be used for individual cells and on cell packs, though the complexity of the data processing and data management increases exponentially with the number of cells studied.

The voltage method has not experienced rapid proliferation for the estimation of SOC and SOH due to its drawbacks, such as inaccuracies introduced when applying the technique on a cell under load. This can be corrected for by obtaining correction factors between the voltage at open-circuit and under load, however, it can be time-consuming. The technique can be used for any scale of cell, from Swagelok cells containing electrodes of less than 100 μm diameter to cell modules. Voltage measurement is implemented in all electrochemical testing equipment and is used in current battery management systems (BMSs), and the measurement process is automatic.

All battery testing and monitoring systems already contain control systems to ensure safety parameters are not violated. These systems include sensors for keeping track of current input and output. As such, Coulomb counting methods for estimating SOC would be very easy to implement. However, cumulative errors and the need to accurately define the initial SOC lead to a lack of reliability of the Coulomb counting method. Researchers have attempted to implement various techniques and algorithms in order to increase reliability, decrease computational load, and reduce accumulation errors. In most cases, the initial SOC is determined using an SOC vs. OCV plot obtained through databases or experimentations. The need for offline modelling and heavy computation load is reduced by utilising a hybrid approach of Coulomb counting augmented by algorithms. There is a clear trade-off between computing load and precision, as increasing the parameters factored into the algorithms (temperature, SOH, and current rate) also increases the amount of data processing. In order to

minimise accumulating errors, researchers have factored in the SOH of the cells, recalibrating the SOC depending on the degrading capacity of the cell. In some cases, Coulomb counting has been used to predict the lifetime, and failure of cells, however the accuracy may not be up to par with other techniques.

EIS is a non-invasive technique that allows for the tracking of changes in cell resistance and SOH. Typically, however, EIS is taken at OCV and over a wide frequency range, which makes it impractical when considering on-board applications. In the past decade, there have been several techniques put forward that reduce the time and cost of the technique which make it more feasible as a diagnostic tool. EIS can be a great complementary tool alongside Coulomb counting and OCV methods for monitoring SOC and SOH in individual or pack level investigations.

2.2 BATTERY IMAGING TECHNIQUES

2.2.1 Introduction

Electrochemical diagnostic techniques are important for the *in-situ* measurement of cell characteristics and determination of SOH and SOC. However, three-dimensional (3D) methods can also be used to determine the SOH of batteries and to probe the micro- and nano-scale morphologies that affect the degradation of SOH. The use of such characterisation tools is important in order to understand the relationship between the microstructural evolution of battery materials and their performance, and an increased comprehension of the inherently three-dimensional structure of battery materials and devices would allow for the development of better performance metrics and improvement of safety/failure mechanisms. These techniques also allow for a more qualitative as well as quantitative measure of the effect of battery degradation, and enable studies of abuse testing to determine the limits of conventional utilisation and advance usage protocols and design. Although there is great potential for the implementation of the electrochemical techniques discussed previously into on-board

BMSs, 3D characterisation tools such as X-ray imaging is confined to the laboratory. However, the data obtained through 3D characterisation can easily be fed back into battery design and into battery models.

There have been many techniques employed by researchers in determining and investigating the microstructure and architecture of cells, such as optical microscopy [123–125], atomic force microscopy [123,125,126], scanning electron microscopy [127–130], and transmission electron microscopy [131–133]. Although these microscopy techniques can provide resolutions down to a few nano-meters, they typically only provide a visualisation of the surface morphology.

Tomography techniques enable the acquisition of the three dimensional configuration of objects through *'tomograms'*, which are cross-sectional images obtained through sectioning, or with the use of a penetrating beam [134]. These image slices can then be used to reconstruct the 3D volume element of the sample under consideration using various algorithms. There are many tomographic techniques available, including atom probe tomography, electron tomography, X-ray computed tomography (CT), neutron tomography, and focused ion beam–scanning electron microscopy (FIB-SEM) tomography. The application of these techniques is dependent on the desired resolution and whether it's *in-situ* and/or *operando*. Figure 5 demonstrates the feasible resolutions and acquisition periods for various X-ray machines and facilities.

X-ray CT and neutron tomography are non-invasive, whereas the other techniques are invasive, therefore the preservation of the sample is another factor to consider. The use of multiple techniques can also be beneficial depending on the property under investigation. The most common techniques used in the 3D visualisation of battery materials are X-ray CT and FIB-SEM.

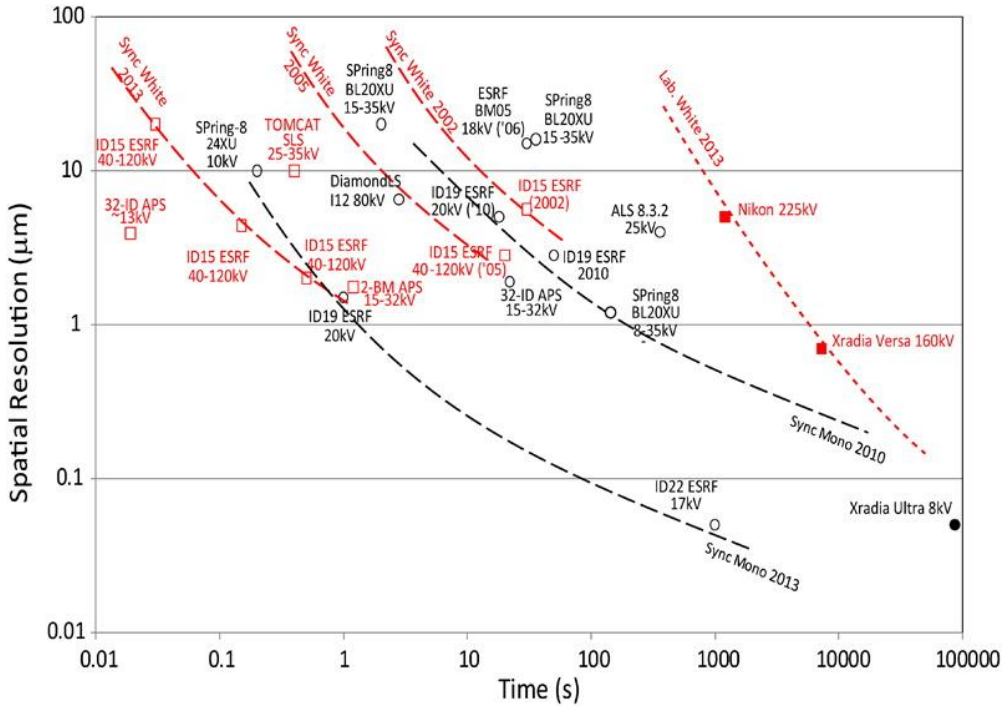

Figure 5: Plot showing achievable resolutions and rate of acquisition for different X-ray sources. Open symbols denote synchrotron sources, while filled ones represent laboratory sources, red squares denote white beam, and black circles monochromatic beam scanner. Reprinted with permission from [135] © 2014 Institute of Materials, Minerals and Mining and ASM International.

2.2.2 X-ray Computed Tomography

X-ray computed tomography is widely used in the characterisation of battery materials. It is a non-invasive technique, hence *in-situ* and *operando* investigations are possible. At the material level, the morphology and microstructural characteristics (tortuosity, porosity, average pore diameter, pore size distribution, etc.) of a porous electrode are vital for understanding ionic transport resistances and evaluate performance. X-ray CT allows for the quantitative analysis of such features, enabling optimization and design improvements.

2.2.2.1 Materials Characterisation

With the proliferation of X-ray imaging techniques, traditional methods of studying microstructural parameters of 3D materials from measurements made on two-dimensional (2D) planar sections of the material (stereology) appear limited. Taiwo *et al.* [136] conducted a comparison of 3D volume analysis versus the analysis on 2D cross-sectional image slices obtained from X-ray imaging. The 2D methodology applied in this study does not consider the 3D phase network interconnectivity which leads to significant over estimation of geometric tortuosity compared to the 3D study. However, one thing to note is that it takes less time and computing power to obtain 2D datasets compared to 3D datasets. Ebner *et al.* [137] compared the particle size distribution (PSD) of various electrode materials calculated using synchrotron X-ray CT to that obtained using laser diffraction to find the results were in agreement. Additionally, they were also able to estimate the electrode porosity from the tomography data. In another study, Gelb *et al.* [138] determined that submicron scale X-ray microscopy was insufficient to accurately investigate the porosity of a commercially available 18650 nickel cobalt aluminium (NCA) cell. They then used a nano-scale X-ray microscopy instrument to increase the resolution and confirm the nano-scale nature of the pore network.

Recent advances in laboratory-based X-ray machines have empowered researchers with the ability to conduct investigations on complex microstructural evolution in near real-time. The ability to capture a time lapse of degradation mechanisms within energy devices at increasing resolution and *in-operando* has enabled broader application of X-ray CT for material characterisation. Through the use of laboratory-based four-dimensional (4D) X-ray micro-computed tomography (CT) complemented by digital volume correlation (DVC), Paz-Garcia *et al.* [139] were able to track and image the lithiation (volume expansion) of silicon in a lithium//silicon Swagelok cell. They were also able to clearly visualise the increasing compression of the separator material due to the disproportionate expansion of the silicon compared to the decreasing volume of the lithium, as well as the cracking of the silicon particles. In another study, Tariq *et al.* [140] were able to investigate lithiation induced delamination of Si-based anodes in

a custom Li//Si/carbon cell. Tariq *et al.* [141] were able to use synchrotron nano-CT to calculate surface area, volume, connectivity, and tortuosity factors of meso-carbon micro-bead (MCMB)-based anodes and determined that the smaller particles interspersed between the larger MCMB particles caused an increase in tortuosity factors. Heenan *et al.* [142] utilised lab-based X-ray nano-CT to follow the microstructural degradation induced by thermally cycling a sample of a lithium cobalt oxide (LCO) battery electrode to elevated temperatures in order to emulate conditions that occur during thermal runaway. Through the reconstructed 3D images, they observed a reduction in the population of the smallest particles and an overall smoothing of the particle surfaces. This study also outlines the difficulties of conducting nano-scale investigations in laboratories, as there is a need to prepare very small samples (*ex-situ*) due to the small field of view (FOV) of the X-ray machines. In a different study, Lu *et al.* [143] used X-ray nano-CT to obtain a 3D model with microstructural resolution of a Li-ion battery.

2.2.2.2 Cell Level Characterisation

Although micro– and nano– scale characterisation allows researchers to study the effect of accelerated stress testing on an area of an electrode or on the particles, in most cases it requires preparation of small samples or the construction of experimental cells. It does not allow one to elucidate the interactivity of the various cell components and chemicals in a state that would be available to and used by the global consumer base. Investigations into the behaviour of readily available commercial cells has value inherently because they are those which are used by consumers and, to a great extent, by the electric vehicle manufacturers. Thus, there is much to be gained from cell level, macro investigations as well. For example, it can be used to reveal the occurrence of over-discharge in parallel assembly $LiFePO_4$ (LFP) cells [144], and to quantify separation in the layers of a lithium-ion polymer pouch cell post-mortem [145].

Cylindrical cells are widely used by electric vehicle manufacturers because of their high energy to volume ratio and due to the sturdy cell casing that prevents bulging, as is the

case with pouch cells. One of the effects of long term cycling on cylindrical cells is the deformation of the jelly roll, which is associated with the delamination of electrodes from the current collector and the resulting capacity loss [146]. Willenberg *et al.* found that in addition to jelly roll deformation, the casing is also deformed during operation, changing in diameter [20]. They monitored the change in diameter using high precision strain gauges, and noted that the change in diameter was non-linear with respect to the depth of discharge. Mussa *et al.* [147] probed prismatic cells to find that impedance increased with cycling, and hinted that an increase in the curvature leads to increased impedance rise due to the loss of contact with current collector. Carter *et al.* [144] scaled the investigations up to quasi-pack level by using X-ray CT to investigate the effect of high rate pulse discharge on cylindrical cells that were assembled in parallel and as individual cells. They discovered that parallel assembled cells exhibited over discharge, resulting in deposition of copper agglomerates. Yufit *et al.* [145] also used X-ray CT in the analysis of Li-ion cells. They were the first to apply lab-based micro-CT to quantify the electrode separation as a result of gas generation within a LiPO pouch cell. In a different paper, Carter *et al.* [23] revealed that when cycling Li-ion cells at 0 °C, jelly roll deformation occurs before Li metal plating. They also found that a mandrel suppressed both electrode roll deformation and Li plating. They, along with Waldmann *et al.* [22] also used macro scale X-ray CT to determine that cylindrical cells are less likely to undergo jelly roll deformation in the presence of a mandrel at the centre of the cell, instead of a hollow core. In a related study, Willenberg *et al.* [148] attempted to locate the origin of deformation in 18650 cells using X-ray CT combined with accelerated electrochemical testing to determine changes in geometry as a function of ageing. Pfrang *et al.* [149] observed deformations in a cell containing a mandrel using macro X-ray CT and suggested that it is likely due to the influence of the Al current collecting tab. In another paper, Pfrang *et al.* [150] expanded on their previous study and used X-ray CT of full cells to determine that geometrical inhomogeneities in the jelly roll lead to the eventual deformation of the jelly roll and also found that the anode expands at a varying rate depending on the location. In a different type of study, Sharp *et al.* [151] used full-width high-speed radiography of cylindrical cells to determine the effect of different abuse testing based on cell geometry.

With the shift in focus to larger, higher energy cells, namely the 21700 and 26650 format, studies must be conducted to determine the characteristic differences and the advantages and disadvantages. Quinn *et al.* [152] conducted a study on the differences between 18650 and 21700 cylindrical cells with the aid of X-ray CT. Waldmann *et al.* [153] took the study a step further by using X-ray images to compare the physical characteristics of 18650 and 21700 cells custom built using the same electrodes, separators and electrolytes. Pouch and prismatic cells are also of interest for higher energy and higher power applications. Shateri *et al.* [154] imaged whole Li//S pouch cells using X-ray CT to identify cycling induced gas distribution within the cell. In a similar vein, Du *et al.* [155] utilised *in-situ* X-ray imaging of pouch cells to determine the change in geometry and morphology as a result of gas distribution.

2.2.2.3 *In-situ* & *Operando* Characterisation

It is highly important to be able to observe samples in their native environments to eliminate the influence of external factors on the results and to understand the interactivity between all the components in an electrochemical system. Thus, *in-situ* and *operando* data is invaluable in elucidating the design and failure mechanisms. *In-situ* is a Latin word which indicates that something is in its original position. Zhu *et al.* [156] found that indentation of Li-ion cells lead to up to 6% decrease in capacity and attributed this to the increase in resistance due to the crushing of the graphite, cracking of current collectors, and enlarged pores in the separator through *in-situ* X-ray CT. In a similar vein, Nandini *et al.* carried out a survivability test on various commercially available 18650 Li-ion cells and found that after storing the cells below -160 °C for 14 days, there was little change in electrochemical performance and confirmed no internal damage with X-ray CT. Du *et al.* [155] used *in-situ* X-ray CT to study the impact of gas evolution of commercial Li-ion pouch cells and demonstrated the heterogeneous distribution of the gas and degradation. Vanpeene *et al.* [157] utilised a mixture of *in-situ* and *ex-situ* X-ray CT at different scales to study the volume expansion and cracking of Si-based anodes to find that the cracks expanded during charge and closed up during discharge. In another study [158], the same author used *in-situ* X-ray

CT to visualise the separation from the current collector of Si negative electrodes with micro sized particles, and the bulk cracking of the electrodes. *Operando* means that a reaction is occurring while measurements are being taken. These kinds of studies are more difficult to implement and are comparatively more rare. Choi *et al.* [159] imaged a composite Si anode during cycling with a combination of *operando* X-ray radiography and X-ray CT at sub-micron scales and tracked lithiation of Si particles using the changing attenuation of the particles, and the resulting signal intensities of the radiographs. Seitzman *et al.* [160] looked beyond present Li-ion cells with liquid electrolytes and provided insights into the Li^+ migration mechanisms in a solid-state electrolyte cell using lithium metal anodes.

The high X-ray flux achieved by synchrotron-based systems allows the tracking of temporal changes in larger samples and *operando*. Finegan *et al.* [24] were able to continuously image half of a spiral wound lithium battery while it was discharging using a synchrotron source. They were able to capture electrode swelling and cracking due to lithiation in the micrometer scale. Finegan *et al.* [161] were also the first to use high-speed synchrotron X-ray imaging complemented by thermal imaging to study the structural damage caused by induced thermal runaway reactions in an 18650 Li-ion cell. They were able to capture the propagation of thermal runaway in the cells and monitor the delamination and collapse of the electrode layers. In another study, Finegan *et al.* [162] conducted a comprehensive study of battery degradation and failure of a LCO pouch cell during overcharge-induced thermal runaway using multi-scale X-ray CT, including *operando* synchrotron X-ray computed tomography. They were able to observe delamination of the electrode layers. Furthermore, using multi-scale post-mortem CT, they were also able to show the agglomeration of the melted aluminium current collector, and the isolated Co phase on top of the $LiCoO_2$ electrode due to decomposition reactions.

2.2.3 Alternative Methods for Imaging Batteries

FIB-SEM techniques can be used to obtain high resolution 2D cross-sectional images of a sample. The time it takes to mill the surface of the sample and the quality of the milled cuts is highly dependent on the nature of the interactions between the ions and the solid being analysed. Milling occurs as a result of kinetic energy transfer between the ions of the beam and the atoms in the solid during collision. If the atom receives enough momentum to overcome the surface binding energy, it will be ejected as a *'sputtered'* particle [163]. Images can be formed through the collection of ejected atoms that become ionised, or emitted secondary electrons, however, there are drawbacks to the use of a single beam system for imaging, such as damage to the surface of interest during image acquisition. The addition of a second beam, such as an electron beam, has greatly improved the effectiveness of the technique as the secondary beam can image the sample without milling the surface and to a greater resolution. The focus point of the two beams is co-incident, so as the solid is constantly milled, the milled surface is imaged using SEM. The first dual-beam column employed a gallium source for the FIB column and an SEM, and this configuration is still commonly used. A review on the evolution of FIB and FIB-SEM tomography and its operating principles can be found in [164]. Hutzenlaub *et al.* [165] were amongst the first to apply FIB-SEM tomography to differentiate between the three phases (active material, binder, and pore phase) in a 3D reconstructed LCO cathode. In another study, Hutzenlaub *et al.* [166] were able to quantify tortuosity of the very same 3D reconstructed geometry by deriving effective diffusion through simulations. However, they found that the calculated tortuosity was inconsistent with experimental data.

Sui *et al.* [167] employed FIB-SEM imaging to compare the performance between energy-dispersive X-ray spectroscopy (EDX) and time-of-flight secondary ion mass spectrometry (TOF-SIMS) in correlative mapping of lithium content in mixed oxide Li-ion battery cathodes at various states of discharge. X-ray diffraction (XRD) is limited by its lack of sensitivity to lighter elements, whereas TOF-SIMS is able to detect ions down to the size of Li^+. Through this technique they were able to map and obtain a ratio of lithium concentration in the active material at states of full charge and

discharge. Due to the destructive limitations imposed on the sample preparation for FIB/SEM techniques, they are typically used in parallel to X-ray CT [168,169], for example, to gain a higher resolution understanding of the morphology post-mortem. For the same reasons, XRD is also used in parallel to correlate any changes in microstructural change identified with X-ray CT with crystal structure change. However, recently a technique called XRD-CT has emerged, which allows for the non-invasive phase change and heterogeneity mapping of batteries *in-situ* on a 3D scale [170–172].

Neutron imaging is another common imaging technique applied to investigate Li-ion batteries. Siegel *et al.* [173] applied neutron imaging to quantify the lithium concentration in the electrodes and the folds of a pouch cell at various SOCs. Similarly, Nie *et al.* [174] also used neutron imaging to map lithium concentrations in a full cell during charge and discharge *in-situ*. Butler *et al.* [175] imaged a commercial prismatic cell with neutron imaging and determined asymmetric volume change during discharge, and Nazer *et al.* [176] have recently taken the technique further by conducting an *operando* neutron study of a commercial cylindrical cell and observed lithium redistribution between the cathode and anode. Michalak *et al.* [177] used neutron imaging to obtain quantitative information on the gas formation from electrolyte oxidation and reduction. Unlike X-ray CT, neutron imaging is sensitive to low-Z elements and allows the visualisation of lithium concentrations and gas formations which can be used to inform rational design of cells, electrodes, electrolytes, and safety features. Ziesche *et al.* [178] have written a comprehensive review on the utilisation of neutron imaging for the investigation of Li-ion batteries, and Kardjilov *et al.* [179] provide a review on the advances in neutron imaging in general.

2.3 DIGITAL IMAGE/VOLUME CORRELATION ON LI-ION BATTERIES

Batteries undergo complex mechanical and chemical changes as they undergo electrochemical reactions. *In-situ* or *operando* experimental set-ups are one of the ways in which researchers can track changes in real time. However, computational tools can be utilised to better elucidate, and more importantly, quantify, the changes that occur during battery cycling. Typically, images of a sample that is undergoing cycling are fed into an image registration software which has the capability of tracking specific features that undergo change in space or time. Such techniques are called digital image correlation (DIC) or digital volume correlation (DVC) which allow a vectorial map of strains and displacements of volume or planar elements by comparing reference images with those in their abused or deformed states. DVC typically requires a higher computational load.

Eastwood *et al.* [180] conducted an *operando* study of the dilation caused by lithiation in the manganese oxide electrode material during charge/discharge using X-ray micro-CT. With the aid of DVC, they were able to map the spatial variation in particle dilation as a function of battery state of charge and found that it is also a function of the distance from the battery terminal. Ho *et al.* [181] also employed X-ray micro-CT in their work to quantify the inhomogeneity in the lithiation of a graphite//lithium cell. They used DVC to calculate the strain caused by the volumetric expansion of the graphite during lithiation to generate a SOC vs. strain curve and determine which area of the electrode was more lithiated than others. Finegan *et al.* [24] employed synchrotron X-ray CT to conduct DVC on a cylindrical Li-ion cell, and were able to track electrode displacement on a macro level and crack formation. Wang *et al.* [182] calculated the strain caused from tensile tests on various commercial Li-ion battery separators using a pseudo-DVC (DIC in 3 directions) technique. The displacement and strain tracking was performed by correlating spray painted speckles on the samples before and after the tests. Hao *et al.* [183] also utilised a pseudo-DVC technique for their study on the mechanical properties of Li-ion batteries. The testing was carried

out on cells that were placed under *'bending'* load at different SOC and was combined with an acoustic emission analyser. They found that electrode delamination and cracking, and interlayer slips occur as a result of failure from the bending load, and the batteries' temperature did not change by a significant amount. The DIC revealed that initially, the strain was focussed on where the bending load was applied, but became focussed at the centre as the cell casing began to crack.

DIC can be just as powerful and a useful tool as DVC in instances where the 3D displacement is not essential and where the computational load is an issue. Dai *et al.* [184] investigated the mechanical effect on the copper current collector foils and anodes of LCO cells of varying cycling rates and used DIC to obtain strain fields and displacement during electrode cracking. Similar to other works, they spray painted patterns on the samples for displacement and strain tracking, and used cameras for image acquisition. In another paper, Dai & colleagues [185] reported the strain generated during the expansion of the SiO_x//C composite electrode under various cycling parameters. They calculated the maximum strain in the in-plane direction to be 2.6% in the initial cycle, which decreased with further cycling to 0.8%. Özdogru *et al.* [186] used DIC to compare the strain evolution between sodiation and lithiation of iron-phosphate electrode materials to find that sodiation generates a greater amount of strain. In a similar vein, Yang *et al.* [187] calculated the strain generated by lithium-ion intercalation in graphite electrodes. Interestingly, they used a colour imaging technique to also determine the lithium concentration in the samples, as the colour of the graphite changes towards golden when fully lithiated. Tao *et al.* [188] used a combined approach of scanning electron microscopy and DIC to report the displacement and strain of graphite electrodes during cycling. They found that the in-plane strain distribution was much greater than the out of plane direction. Similarly, Koohbor *et al.* [189] determined the strain associated with the volumetric changes in Li-ion batteries, but with a solid state electrolyte and found that the strains were large enough to cause cracking of the electrolyte. Ahmed *et al.* also carried out DIC measurements in a solid state Li-ion cell. They conducted a study on the strains generated by stack pressure on the solid electrolyte and determined that the pressure

can enhance electrochemical performance up to a point by increasing contact between the battery components, but too much pressure leads to solid electrolyte cracking.

2.4 SUMMARY

The performance of a cell is closely linked to the structural evolution of the anode and cathode. The accelerated improvement in technology has enabled researchers to carry out investigations using X-ray CT in laboratories: the non-invasive nature of the technique allows researchers to obtain 3D volume data, enabling effortless and rapid comparison between cell types and conditions. Furthermore, *in-situ* macro– and nano–scale analyses can also be carried out, such as investigating the effects of thermal cycling on individual cathode particles, or the effects of nail penetration at the cell level. Furthermore, the data obtained by X-ray CT can be combined with other techniques and software to obtain additional microstructural data, such as porosity and tortuosity factors using the TauFactor software. Correlative techniques can be used to infer the effect of the evolving microstructure of cells on performance. Non-invasive techniques such as monitoring the reduction in cell capacity and the increase in internal resistance through EIS can be linked to the increasing growth of the solid electrolyte interphase, among other things.

There have been many studies on the micro– and nano– structural evolution of cell materials using X-ray CT in recent years, however, there is much to be discovered by studying the effect of cycling on the macro architecture of commercial cells as well. Where *'cell architecture'* incorporates mechanical design aspects of a cell. Such as: characteristics of the jelly roll (how perfect the spiral is, number of windings), electrode coating characteristics (agglomeration, pinholes, non-uniformity), welding types and defects, crimping characteristics, safety features such as positive temperature devices, pressure relief valves, etc.. The work in this thesis seeks to investigate the factors influencing the deformation in the jelly roll of cells as their health degrades, which is believed to be the primary cause of accelerated capacity fade. Primarily, investigation into the significance of cell structure, such as position and number of current collecting

tabs, and geometry of cell, as well as the temperature gradients within the cell has been carried out. Aspects relating to cathode coating, welding and safety features will not be explored. Although there have been a few studies into the cause of jelly roll deformations, as covered in this literature review, there have not been many investigations into the impact of cell architecture and cell design. This thesis hopes to build upon the previous studies and provide further insight into the cause of electrode deformation and possible ways to prevent or mitigate it through design changes. Furthermore, the studies conducted in the articles covered have been on a much smaller scale than the studies conducted here – therefore, this thesis also hopes to provide more statistically relevant results in addition.

The investigations in this thesis have been carried out primarily through electrochemical studies and X-ray CT. The most important aspect of technique selection in this thesis was the requirement for non-destructiveness for jelly roll investigations over different time scales. Although neutron imaging also allows for non-destructive characterisation of batteries, it has limitations, such as irradiation and lack of availability on a lab scale. Electrochemical data is easily obtained even as the battery is cycled in order to incite degradation within the battery for the study to occur. Furthermore, since the investigations are on individual cells and not on a battery pack scale, the electrochemical techniques do not require any modelling to monitor the health of the cells. Finally, X-ray CT allows for non-destructive investigations into the physical changes in the batteries at different length and time-scales and are more readily available in labs, and so the studies were conducted with that in mind.

3 METHODOLOGY

3.1 ELECTROCHEMICAL CYCLING

The quintessential technique for determining the state of health of a cell is monitoring its capacity as it undergoes electrochemical cycling under specific conditions which can be compared to its initial capacity. A cell for automotive applications is typically considered to be at end-of-life (EOL) once the capacity has dropped to 80% of its original capacity. For cells of comparable composition and rated capacity, the rate of decrease in capacity can be compared to gauge relative performance. Cell cycling is typically carried out in '*C*' rates. The rated capacity of a cell, *n* Ah, is equal to 1C – meaning that it will take 1 hr to fully charge or discharge the cell at *n* Amps. The time it takes to charge/discharge a cell is inversely proportional to the constant before the *C* i.e. when cycling at 0.5C (0.5*n* Amperes), it will take 2 hours to fully charge or discharge the cell. The charge cycle typically contains two regimes: a constant current (CC) phase, and a constant voltage (CV) phase. During the first phase, the current is held at a specific value while the voltage increases to a specified value, then it is held constant while the current is tapered to a lower value (usually around 3-10% of the applied current during the CC phase).

At very high temperatures (90 – 120 °C), the SEI will start to undergo exothermic decomposition [1], however, changes in the SEI and electrolyte can start at as low as 60 °C depending on the composition. At higher temperatures, exothermic reaction between the active material, SEI and electrolyte occurs, leading to decreased performance, or a thermal runaway in the worst of cases [190]. At low temperatures, diminished performance is caused by an increase in the internal resistance of cells [191]. Lithium plating and dendrite growth are also of concern when charging

below 0 °C [190], and at even lower temperatures, the cathode can break down, leading to degradation and possibly, a short [1].

Some of the factors that affect the cycle life of a cell are the operating conditions under which it is cycled, such as the depth of discharge (DOD). The depth of discharge is what voltage value the cells are discharged down to as a percentage of the cut-off voltage window. Taking the cell down to 100% DOD or higher can have an impact on the cycling performance of a battery. Firstly, discharging to the cut-off limit increases the risk of over-discharging. At low voltages (below the manufacturer's stated cut-off limit), the copper current collector in Li-ion cells may dissolve and redeposit on the negative electrode during charge, leading to potential shorts [192].

In this work, electrochemical measurements were taken using a variety of battery cycling machines: Maccor 4200 (Maccor Inc., Oklahoma, USA), Maccor 4300 (Maccor Inc., Oklahoma, USA), Bio-Logic SAS BCS-815 (BioLogic Sciences Instruments, Seyssinet-Pariset, France), and Gamry potentiostat (Gamry Instruments, Warminster, USA). Where specified (in the relevant chapters), environmental chambers were used to carry out temperature sensitive electrochemical measurements with a Maccor Temperature Chamber MTC-020 (0 to 100 °C ± 0.8 °C, Maccor Inc., Oklahoma, USA). The cycling protocols used for the cells in this work are provided in the relevant chapters. The specifications for the battery cyclers can be found in Table 2.

Table 2: Specifications of the battery cyclers

	MACCOR 4200	MACCOR 4300	BCS-815
VOLTAGE			
RANGE	0 – 5 V	0 – 5 V	0 – 9 V
ACCURACY	± 0.02% FSR	± 0.02% FSR	<±0.01% of value ±0.3 mV
CURRENT			
RANGE	300 nA to 5 A	300 nA to 5 A	1 mA - 10 A
ACCURACY	± 0.02% FSR	± 0.02% FSR	< 0.05% of value ±0.015% of FSR

3.2 X-RAY COMPUTED TOMOGRAPHY

Several different lab-based X-ray instruments were used to characterise the degradation of the battery cells used in this study. The Nikon XT H 225 (Nikon Metrology, Tring, UK) was used to scan the full (or half) width and length of the cells, and the Zeiss Xradia Versa 520 (Carl ZEISS XRM, California, USA) was used for region-of-interest scans with resolutions down to micrometres, as seen in Figure 6.

The general operation of X-ray CT is as follows: the X-ray source produces an X-ray flux, which is transmitted through the sample object. The X-ray photons are distinguished by a detector and converted to visible light by a scintillator which is then converted to digital signals for image acquisition. In this fashion, many hundreds of image slices are obtained as the sample is rotated about an axis. These images are then processed and mathematically reconstructed to obtain a 3D representation of the sample. This is represented schematically in Figure 7. The principles, design, and advances in X-ray CT can be found in [193][194].

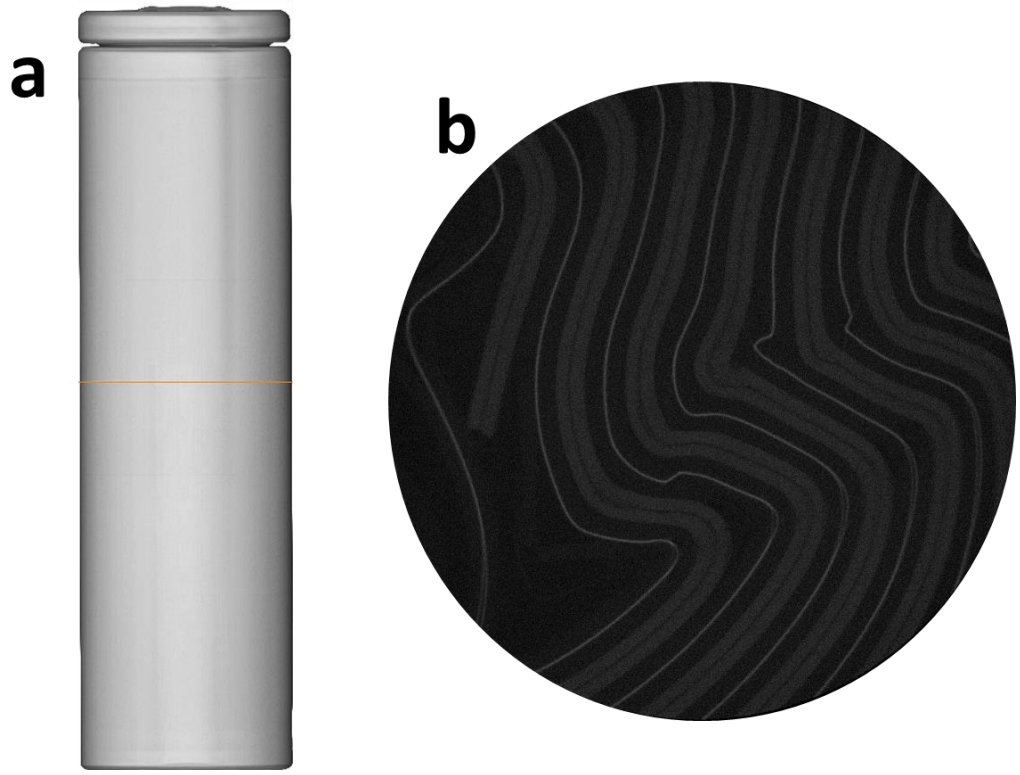

Figure 6: (a) 3D render of a full 18650 cell using Nikon XT H 225, and (b) a slice from a region of interest scan using a Zeiss Xradia Versa 520.

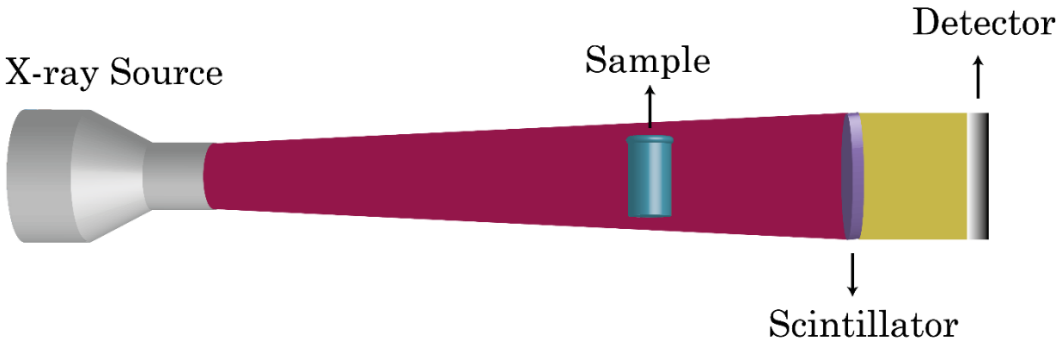

Figure 7: Schematic of an X-ray instrument set-up. The X-ray beam is transmitted through the sample and onto a scintillator. The resulting signals are picked up by the detector.

The energy of an X-ray photon can be described by the following:

$$E = h\nu = hc/\lambda \quad (8)$$

where, E is the X-ray photon energy and ν is its frequency, h is the Planck's constant, c is the speed of light, and λ is the wavelength of the X-ray. An X-ray with longer wavelengths (10 – 0.1 nm) are inappropriate for radiography as they have little penetrating power, whereas shorter wavelengths (0.1 – 0.01 nm) provide little low-contrast information [193]. Therefore, optimisation of X-ray parameters depending on the sample properties is important for diagnostic imaging.

Contrast is a measure of how well a feature can be distinguished from the surrounding background. There are two main modes of operation used for battery characterisation using X-ray CT: phase contrast and absorption contrast. X-rays are refracted and attenuated as they travel through a sample. The behaviour of X-rays as they pass through samples can be described by the below equation [195].

$$n = 1 - \delta - i\beta \quad (9)$$

where, n is the index of refraction, β describes the absorption of X-rays, and δ is the phase-shift term and incorporates refractive effects. At certain X-ray energies, the phase-shift term can be orders of magnitude greater than the absorption term, making it possible to observe phase contrast when absorption contrast does not allow sufficient distinction. The differences in the refracted rays as they pass through the sample material corresponds to producing a distorted wave front, which are picked up by the various phase contrast techniques. Low atomic number (low-Z) materials have low X-ray absorption coefficients, making them hard to characterise using conventional absorption-contrast imaging. Phase contrast was not used in this thesis and won't be discussed further.

Attenuation describes the change in the intensity of the X-ray beam as it passes through an object. Different materials absorb X-rays to different extents, creating contrast. Therefore, a radiograph can be obtained by measuring the ratio between the intensity of the attenuated beam to the incident beam [196]:

$$\frac{I}{I_0} = e^{-\mu x} \qquad 10$$

where, I is the X-ray beam's intensity after it passes through a material of thickness x, I_0 is the intensity of the incident beam, and μ is the attenuation coefficient. Thus, radiographs collected at points through which the X-rays traverse can be used to reconstruct the volume of the sample using reconstruction algorithms. The above equation describes absorption contrast, which is the principal contrast mode used in this work.

The X-ray machines employed in this work use filtered back projection algorithms to reconstruct a representation of the sample. The principle behind this reconstruction technique will be very briefly described here, but more details can be obtained in Reference [134]. When considering the example in Figure 8a with an orthonormal domain, a 1D projection, R_θ, is defined for an angle θ [134]. A projection with a position given by the radial co-ordinate ϱ along an angle θ is denoted (θ,ϱ), and its value corresponds to the attenuation undergone by the X-rays. A sinogram is a set of projections obtained as the sample is fully rotated in a 360 ° angle. The sinogram values are used to reconstruct the acquired domain as illustrated in Figure 8b, which portrays that one projection is insufficient to correctly reconstruct the original domain (as seen through the comparison between the grey shaded areas in Figure 8a & b. The more projections a sinogram contains, the more accurate the reconstruction, up to a point, depending on the size of the detector, and its position in relation to the X-ray source and sample. Hence, in general, a high number of projections are desired for a given scan. The acquisition and reconstruction involves the use of Radon and Fourier transforms and in general it follows this route: transformation of a 2D function into a

1D projection and then the back projection recovers the original function from the projections. This technique applies a ramp filter – a filter that prevents blurring to appear in the images – hence why it is referred to as the filtered back projection reconstruction algorithm.

Metallic filters of varying thicknesses were utilised in the X-ray CT conducted within this thesis. This enables the X-ray beam to penetrate batteries composed of dense transition metal oxide materials more easily as the lower energy photons are absorbed by the filter, leading to a higher average photon energy of the beam. Copper filters ranging from 0.1 to 1 mm thickness were utilised for the X-ray imaging in this work.

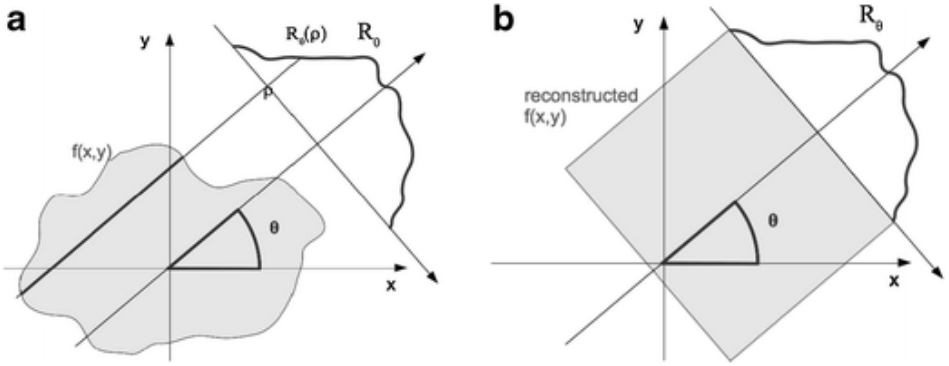

Figure 8: Diagram of X-ray image reconstruction. (a) Shows a projection line whose value corresponds to the attenuation undergone by the rays along the black line. (b) Demonstrates that one projection is not sufficient to recover the original function. Reprinted with permission from [134] © 2014 Springer Science Business Media New York.

3.3 IMAGE PROCESSING & ANALYSIS

Reconstructed images of samples were obtained as 3D volume files or 2D image stacks in the TIFF format. The 3D volume files were processed in Avizo (versions 9.0-9.5, FEI Visualization Sciences Group, Mérignac Cedex, France) to extract regions of interest and generate 3D rendered models of the samples. Fiji [197] was partially used to process the 2D image stacks and to enhance the image quality using the brightness and contrast adjusting tool. For the 16-bit TIFF images obtained from the X-ray

imaging, the toll does not change the actual pixel values. The automatic optimiser, which optimises contrast and brightness by saturating a small number of pixels in the images, was utilised. Fiji was also used to combine image slices of cells at different time scales to construct time lapse videos for motion registration, as discussed later.

3.3.1 Virtual Unrolling

Throughout the course of this research, a technique called '*virtual unrolling*' (as detailed in Kok *et al.* [146] was used for the non-destructive examination of the electrode roll for comparisons between different cells or the same cell at different stages in its life cycle using XCT imaging data. Typically, the virtual unrolling process has four steps. Firstly, the pre-processing of the XCT data: the pixel intensity of the images are normalised to range from 0 to 1. Secondly, the identification of the centre of the cell: the cell casing if determined by obtaining the longest contour within a certain greyscale threshold, and then the centre is identified by algorithmically trying out all possibilities for the centre within the cell casing that results in the least casing deformation. Thirdly, identifying the electrode roll: the boundary between the anode and cathode is increased by applying a small kernel median filter and an unsharp mask and this boundary is used to generate the unrolling plots. Median filter is a noise reduction process, where it is widely used to reduce the *'salt and pepper'* effect by replacing the value of pixels with those of the median of the neighbouring pixel values. It is effecting at preserving sharp edges while reducing noise [198], and unlike a process using an average, the selection is not significantly affected by the inclusion of an anomalous values making it good for suppressing *'spike'* noise [199]. The kernal size refers to the window that is used in determining the median values, and a small kernal size is used here in order to preserve the finer details of the images. An unsharp mask is sued to enhance the edges in the images for edge detection. It is carried out by taking the difference between the original image and a blurred version of the image (typically using a low pass filter) which is scaled and added back to the original image [200]. Finally, the boundary between the cathode and anode is translated into a Cartesian format where the cylindrical co-ordinates, are defined as below:

$$r = \sqrt{(x - x_0)^2 + (y - y_0)^2} \quad 11$$

$$\phi = arctan\left(\frac{y - y_0}{x - x_0}\right) \quad 12$$

where, the x,y co-ordinates of the centre of the cell are x_0 and y_0, respectively.

Interpretation. Virtual unrolling translates each 360° rotation of the cathode spiral into a separate layer in the unrolling plot. Figure 9 illustrates the generation of an unrolling plot from a slice of a cylindrical cell. The electrode roll has been split into two sections due to the presence of the current collecting tab at the middle of the jelly roll. The repeating cathode layers are highlighted in blue and green for the two sections. For illustration purposes, the first cathode layer next to the cell casing is highlighted in orange and the start is denoted by the yellow arrow, and the end of the 360° layer is indicated by the green arrow in Figure 9a. The translation of that same layer into an unrolled orientation can be seen in Figure 9b. It can also be seen that this cell contains a pre-existing inflection point in the jelly roll, which is a non-uniform defect due to manufacturing and assembly processes, as highlighted by the horizontal dotted orange curve in Figure 9b. This inflection point is present throughout the whole jelly roll along the same angle, as highlighted by the vertical dotted orange line. It should be noted that this technique only allows for the investigation into the uniformity of the jelly roll of the cell, hence the rolling process of manufacturing, and not aspects regarding to safety features or electrode coating quality.

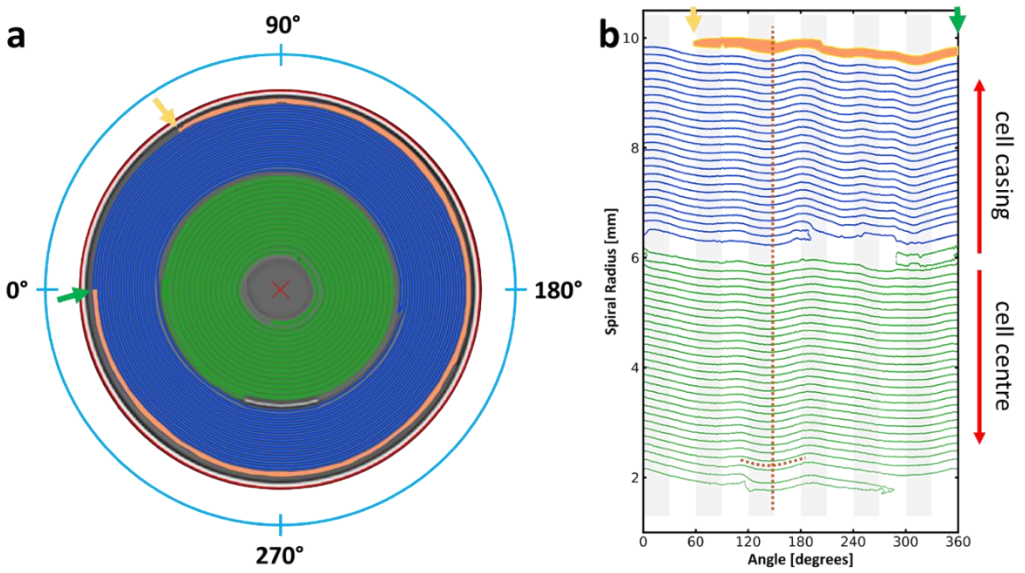

Figure 9: Illustration of the generation of a 'virtual unrolling' plot from an XCT slice of a 21700 cell. The repeating layer (cathode) is highlighted in blue and green as it has been split into two sections by the tab in the middle. The rex 'X' indicates the centre of the cell, and the red circle, the cell casing.

3.3.2 Digital Image Correlation

Digital image correlation as detailed in Jnawali *et al.* [201] was used to quantify the changes in the cell internal structure as a result of charging cells. The digital image correlation carried out in this work contained two steps: the amplification of the movement of the internal cell structures with respect to time (phase-based motion enhancement), and the optical flow-based image registration to quantify the changes.

3.3.2.1 Phase-based Video Magnification

Video magnification was carried out using the phase-based Eulerian motion processing as detailed in the paper by Wadha *et al.* [14]. The technique translates noise instead of amplifying it. In simplified terms, the motion magnification is based on complex-valued steerable pyramids, where the local phase over time is calculated. These phases

are then band passed to isolate temporal frequencies, which correspond to the motion in the various spatial scales and orientations. The movement is magnified by multiplying the band passed phases with a factor, $1+a$. The phase coefficients in each frame are then modified by this amount $(1+a)$ to enhance the motions in the video within maximum bounds, estimated from a Gaussian kernel of width = σ. 2D image slices obtained from X-ray imaging of the cells at different points in their charge cycles were used to make temporal videos in ImageJ. The MATLAB script for the video magnification was used as published by the authors (Wadha *et al.* [14]), with some changes in the processing variables: the frequency cut-offs, alpha (a) and the spatial smoothing factor, sigma (σ). The code was executed on MATLAB (version R2018a). A narrower frequency band ensures a more focused amplification and a lesser amplification of noise, but it also carries with it a risk of overlooking physical phenomenon. This step, therefore, required rigorous user supervision, where a combination of a range of a and σ values needs to be tested.

3.3.2.2 TV-L – based Image Registration (Optical Flow)

The DIC technique based on '*optical flow*' was applied to the motion-amplified videos, where each frame represented a different (de)lithiation state. Optical flow was used to elucidate the global motion of the electrodes in the magnified video at a pixel level. The process compares two frames at a time, using the first frame as reference, in order to generate movement vectors and flow fields based on pixel level changes. Movement is identified by the changes in the greyscale values of the pixels over small sub-areas in the frames. The optical flow image registration script was written on Python 3.7 using the total variation (TV) regularisation and L^1 norm algorithm as available on the Scikit-image package [202]. The TV-L optical flow method is known to be more resistant to noise and allows discontinuities in the flow field [203–205].

For accurate pixel registration, a well-defined cross-section of the images was required. It was particularly challenging to register pixels between cell-charging steps. For a video

loaded on the Python script, a marching-squares based, contour-finding algorithm was used to find the edges of the cell-casing from the last frame of the video [206], commonly applied to find perimeters of well-defined features in images without affecting feature morphology [207]. Any background pixel values outside the cell-casing were ignored in the analysis. The coordinates of the cell-casing from the last frame (after fully charging) was applied on all subsequent frames. This was crucial to ensure that the image registration step captured the overall bulging of the cell upon cycling. After 'masking' the background pixels in every frame in the video, a Sobel edge-detection step [208] was used to pick-up the interfaces between the electrodes and the electrolyte. The edge-detection step amplifies the texture of each frame, highlighting the boundaries of each material in a Li-ion cell that subsequently act as 'seeds' for the optical flow image registration step.

For a video of N frames, where each frame has a width of X pixels and a height of Y pixels, the optical flow for each frame is then calculated using the TV-L methodology. For a given frame, i, where $0 \leq i \leq N$, a displacement vector (u, v), also known as the disparity map, is calculated for each pixel at location (x, y), such that

$$image_i(x + u, y + v) = image_0(x, y) \quad (13)$$

where, $0 \leq x \leq X$ and $0 \leq y \leq Y$, and $image_0$ ($i = 0$) is the first frame of the video. The (u, v) vector field represents the Euclidean distance map between two pixels identified as similar between the two frames based on their pixel intensities. From the horizontal and vertical displacement vectors, (u, v), the total displacement magnitude was calculated from the square root of their squared sums, $\sqrt{(u^2 + v^2)}$. The total displacement magnitude was then plotted as a colour map overlaid on the corresponding frames. The colour map scaled from purple to yellow, where purple indicates no displacement, $\sqrt{(u^2 + v^2)} = 0$, and yellow denotes the maximum displacement, which is a scaled factor of the original pixel intensities. To show the direction of displacements, the (u, v) vector field have been plotted as a 2D field of arrows, where the length of the arrows is the displacement magnitude (normalised by

the largest magnitude to aid visualisation). The base of the arrows are at (x, y) and point towards ($x+u$, $y+v$).

3.4 POTENTIAL ERRORS

There are various potential errors and factors influencing raw results or interpretation of the results during the data acquisition and processing steps. Firstly, during the data acquisition period, there are potential measurement errors due to the resolution of the battery cycling machines. This is negligible due to the high sensitivity of modern machines, and all the cells would be equally affected. Additionally, fluctuation in X-ray energies as the filament ages, leading to differences in the image quality across different cells and cycle lives of the cells was not accounted for nor measured. This is unlikely to have a major impact on the results as the interest of these studies is not on microstructural features, but additional noise could lead to minor accumulating errors during image processing over time. Similarly, the potential damage to cells from the X-rays was also not accounted for, although this is believed to be negligible. There are also potential errors that may arise from the image processing steps, such as the smoothing caused by the median filter and the unsharp mask which may lead to shifts in boundaries. Additionally, although the motion enhancement algorithm used in chapter 5 is touted to be less sensitive to noise, it could certainly enhance noise, leading to mischaracterisation of physical phenomena.

The measurement and investigation of some of these aspects that may introduce error are further discussed in the Future Work chapter, section 8.5.

3.5 SUMMARY

In this chapter, the primary techniques used for the image acquisition used in later chapters to evaluate the performance of batteries were presented. The image

processing and analysis techniques used to quantify the bulk changes in the internal cell architecture were also discussed.

4 INVESTIGATION OF DEFORMATION MECHANISMS IN CYLINDRICAL CELLS

4.1 INTRODUCTION

Since their commercialisation, lithium-ion (Li-ion) batteries have experienced a surge in usage for a variety of applications such as mobile phones, laptops, and electric vehicles due to their high energy and power density and for their high cycle life. However, their continued adoption requires a more comprehensive evaluation of ageing and failure mechanisms. The 'when and how' in the functional degradation of batteries is a topic of great interest, as gaining a deeper understanding of the mechanisms will ultimately lead to better and safer manufacturing designs. Electrochemical data on its own is insufficient in assessing the damage caused by cycling conditions and battery design. Imaging and image analysis techniques including X-ray imaging, can be used in correlation to infer the cause of failure or to inspect the extent of damage caused.

For the applications mentioned above, the batteries are, in the majority of cases, left in a partial state of charge throughout their life, leaving them open to parasitic reactions which lead to increased internal resistance and loss of capacity over time – self-discharge. The kinetics vary depending on the battery type and battery chemistry, material purity, state-of-charge (SOC) and storage temperatures. Although Li-ion batteries exhibit relatively lower self-discharge rates compared to other battery types [52], it is still a factor which reduces the calendar life of the cells. It is observed in literature that lithium-ion cells show greater deformation once they hit 80% residual capacity [209]. Under open-circuit storage, it is believed that lithium loss from the graphitic positive electrode occurs due to parasitic side reactions between the

intercalated lithium and electrolyte [210]. Pistoia *et al.* [211] suggest that there are three processes occurring during self-discharge: (a) electrolyte decomposition; (b) spontaneous Li^+ reinsertion due to instability of the delithiated cathodes; (c) solubility by corrosion. There have been efforts into investigating the effects of electrolyte additives and their reactivity to understand and reduce self-discharge in lithium-based cells [5], and into grasping the contribution of graphitic anodes on the mechanisms behind self-discharge [6]. It is observed [7] that cells stored at elevated temperatures show a greater reduction in performance. However, there are few literatures on the mechanisms of self-discharge of Li-ion cells in general, and very little analysis on cells stored at ambient temperatures and physical changes to the cells caused by self-discharge.

This section will first present the results obtained from the electrochemical cycling of cylindrical batteries of two different models, with differing geometries, and, using the correlative image analysis technique *"Virtual Unrolling"*, hypotheses will be provided for possible trends in the capacity fade exhibited by the cells and the causes of the deformations in the jelly rolls of the cells. Additionally, the results of whether the storage of a selected type of cylindrical cell at 80% state-of-charge causes a decay in open-circuit voltage of the cells is given.

4.2 MATERIALS & METHODOLOGY

4.2.1 Cells, Cell Cycling & X-ray CT

M50 Cells. Four spiral wound M50 21700 cells (INR21700, LG Chem, Seoul, South Korea) of 5 Ah rated capacity, consisting of NMC-811 ($LiNi_{0.8}Mn_{0.1}Co_{0.1}O_2$) cathode and mixed graphite/Si (SiO_x) anode, were cycled between 2.5 – 4.2 V. The cycling of the cells was carried out at ambient conditions (23 ± 3 °C), using Maccor Model 4200 (Maccor Inc., Oklahoma, USA) and Bio-Logic SAS BCS-815 (BioLogic Sciences Instruments, Seyssinet-Pariset, France). The charging was carried out at 0.7C using a

CC/CV regime, tapering the current to 119 mA, followed by a 10 minutes rest step before discharging. The discharging was carried out at 1C constant current followed by a 20 minutes rest step. The initial voltage profiles for all four cells are provided in Figure 10. The cells were cycled continuously for a certain number of cycles (called a set) before being imaged using X-ray CT. A table containing information on these cells can be found in Table 3.

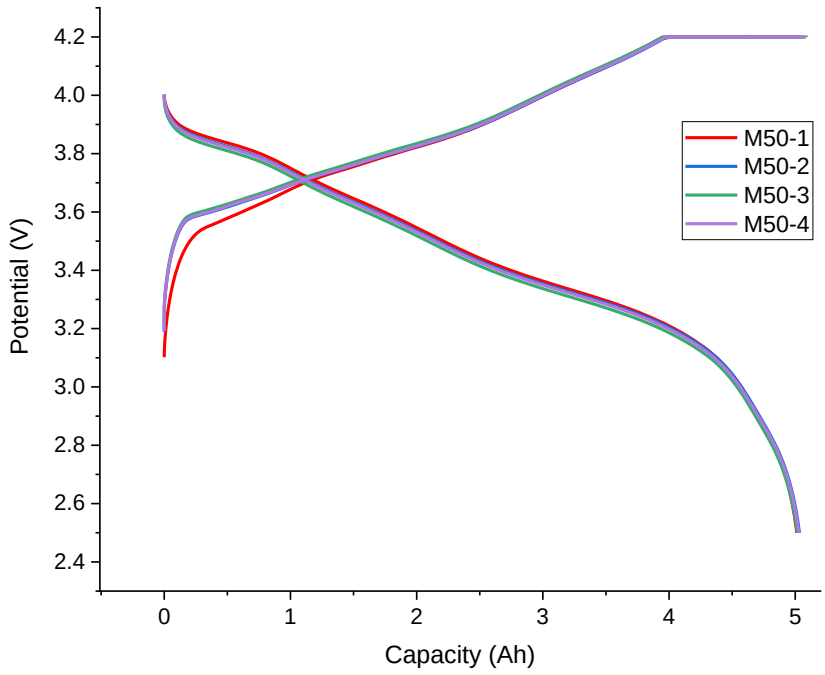

Figure 10: Initial voltage profile of the M50 cells cycled at ambient temperatures.

Four additional M50 cells were cycled at elevated and low temperatures utilising the Maccor Model 4200 cycler and Maccor Temperature Chamber MTC-020 (Maccor Inc., Oklahoma, USA) environmental chambers. The same cycling regime as above was used for the two cells cycled at 45 °C. For the two cells at 0 °C, the maximum rates specified by the manufacturer – 0.3C and 0.5C for charge and discharge, respectively – were used. A table listing the cells used in this study, their given names, chemistry,

and cycling regimes are given in Table 3, and the initial voltage profiles of the cells are provided in Figure 11.

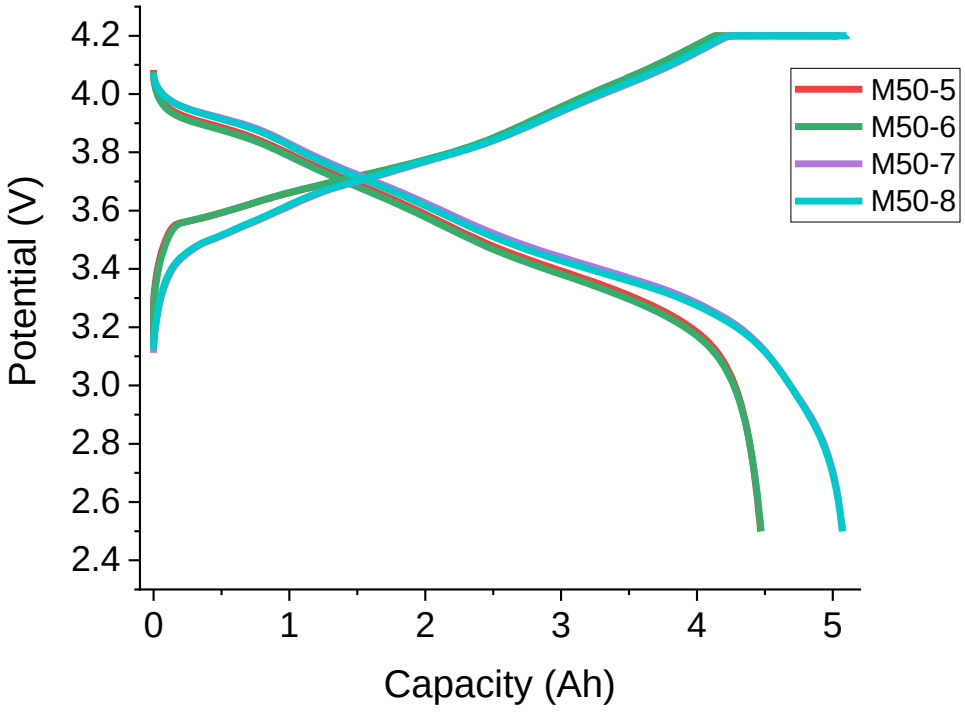

Figure 11: Initial voltage profiles of M50 cells cycled at elevated and low temperatures. M50-5 & 6 were cycled at 0 °C, and M50-7 & 8 were cycled at 45 °C.

The cells were imaged in their pristine state (before any cycling had begun) after being discharged to their lower voltage cut-off limit. Acquisition of tomographies was conducted using a Nikon XT H 225 (Nikon Metrology, Tring, UK) machine, operating between 170 – 200 kV and 80 – 215 μA. Over 1400 projections were obtained as the samples were rotated 360° about an axis, employing an exposure time of 1s. A voxel size of 39 μm was achieved for the M50 cells. The tomograms were then reconstructed using a proprietary reconstruction algorithm (CT Pro 3D, Nikon Metrology).

MJ1 Cells. Four MJ1 18650 cells (INR18650, 3.5 Ah, LG Chem, Seoul, South Korea) also containing NMC cathode and mixed graphite/Si anode were cycled using a

Maccor Model 4200. They were cycled in an environmental chamber (Maccor Temperature Chamber MTC-020) set to 25 (± 3) °C. They were charged using a CC/CV regime from 2.5 V to 4.2 V at 1.5 A, tapering the current to 100 mA, and discharged using a constant current of 4 A. The rest periods were 10 minutes after charge and 20 minutes after discharge. The initial voltage profiles for all four cells are provided in Figure 12.

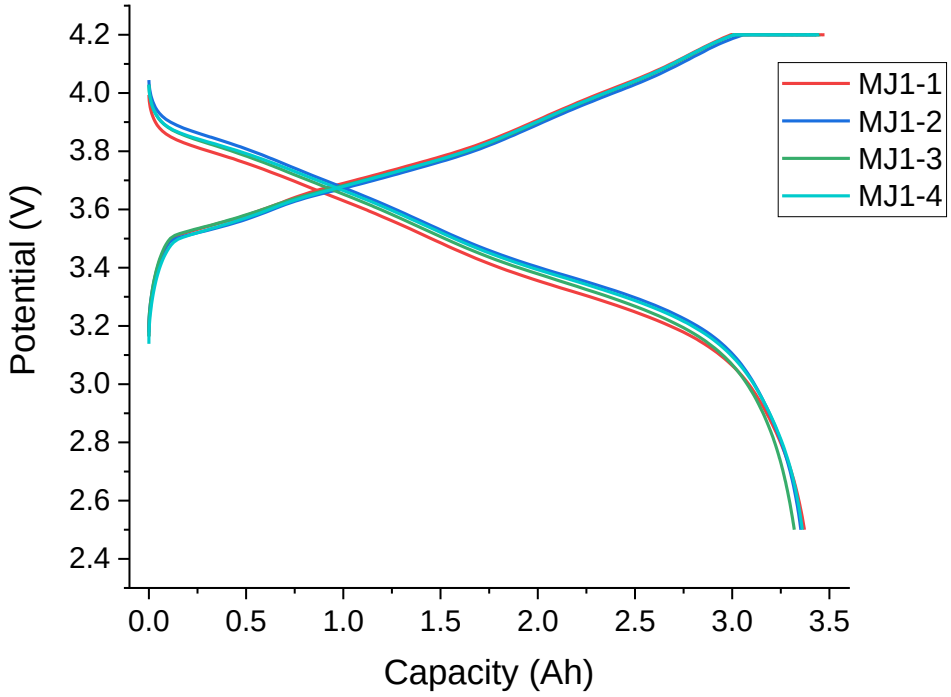

Figure 12: Initial voltage profiles of the MJ1 cells.

Whereas the M50 cells were scanned using X-ray instruments at regular intervals after a set number of cycles, the MJ1 (INR18650, 3.5 Ah, LG Chem, Seoul, South Korea) cells were scanned when their capacity faded by a certain percentage, irrespective of the number of cycles required. Table 3 provides details on these cells and imaging criteria. These capacity thresholds were chosen in order to investigate the microstructural and electrochemical behaviour of the cells as their capacity approach, converge, and exceed the accepted end-of-life state for automotive cells (80%

reversible capacity). Before any cycling of the cells had commenced, all the cells were discharged and scanned, then the cells were scanned when the capacity faded to 90% of nominal capacity, and then every 2% decrease in capacity thereafter. These cells were imaged using the Nikon XT H 225 machine. Operating between 170 – 200 kV and 80 – 215 μA, over 1400 projections were obtained employing an exposure time of 1s. A voxel size of 36 μm was achieved for the MJ1 cells.

Table 3: A summary of the cells studied in this chapter. All the cells have a SiO_x/C//NMC chemistry.

CELL	GEOMETRY	NOMINAL CAPACITY (AH)	TEMPERATURE (°C)	CHARGE (CV)	DISCHARGE	SET *	# OF CYCLES
M50-1	21700	5	23	0.7 C (119 mA)	1C	50 cycles	1000
M50-2							498
M50-3							500
M50-4							500
M50-5			0	0.3C (45 mA)	0.5C	25 cycles	150
M50-6							150
M50-7			45	0.7 C (119 mA)	1C		150
M50-8							150
MJ1-1	18650	3.5	25	1.5 A (100 mA)	4A	2% capacity fade	687
MJ1-2							1141
MJ1-3							1077
MJ1-4							1106

* A set is the number of cycles or capacity retention (%) between every X-ray scan of the cell.

Virtual unrolling. Image analysis using virtual unrolling on the X-ray CT data was carried out as outlined in the Methodology chapter, section 3.3.1.

4.2.2 M50 Storage Conditions

X-ray CT Acquisition & Storage. Five M50 21700 (INR21700, 5 Ah, LG Chem, Seoul, South Korea) cells were discharged to their lower cut-off voltage limit of 2.5 V before being scanned on the Nikon (XT H 225, Nikon Metrology, Tring, UK) for X-ray CT acquisition. It was operated between 165 – 185 kV and 100 – 210 μA, and captured over 1500 projections at 1s exposure as the cells were rotated 360° about an axis. The tomograms were then reconstructed using a proprietary reconstruction algorithm (CT Pro 3D, Nikon Metrology). The same parameters were used to obtain scans at various periods during the battery storage period for image analysis to track structural changes using virtual unrolling.

Three M50 cells (A, B, C) were charged to 80% (3.86 V) of the upper and lower voltage cut-off window using a constant current-constant voltage (CC-CV) regime at 0.2C, tapering the current to 33 mA. The remaining two cells (D, E) were charged to 80% (4 Ah) of their rated capacity at 0.2C – a CV step was not utilised for this charging regime. Storage was carried out at ambient conditions (23 ± 3 °C). The OCV of the cells were recorded at various periods during the storage period.

A summary of the M50 cells used in this study, their chemistry, and cycling regimes, as well as imaging parameters are given in Table 4.

Differential Capacity. Differential capacity profiles for the cells in the storage study were obtained by first discharging the cells, and then charging and discharging them to obtain data on a full cycle. The cells were cycled at C/20 using only a CC cycling regime. Almost 2500 data points were recorded for each cycle. In order to reduce the noise involved with acquiring data at these low rates and to accentuate the peaks, the data was smoothed using the Savitzky-Golay method in OriginPro (2018b, OriginLab Corporation, United States). Other methods average out the peak height and width, whereas Savitzky-Golay seeks to preserve the overall profile of the data, hence its utilisation. A window size of 30 points was used for the data smoothing.

Virtual unrolling. Image analysis using virtual unrolling on the X-ray CT data was carried out as outlined in the Methodology chapter, section 3.3.1.

Table 4: Tabulation of the LG M50 cells used in the 80% SOC storage study, including the cycling and scanning parameters.

GIVEN NAME	CHEMISTRY	CHARGE RATE (CC)	CHARGE RATE (CV)	CHARGE TO	X-RAY PARAMETERS
A	NMC SiO_x/graphite	0.2C (1 A)	33 mA	3.86 V	165 – 185 kV 100 – 210 μA 1s exposure
B					
C					
D			-	4 Ah	
E					

4.3 INVESTIGATION OF M50 CELLS CYCLED AT AMBIENT CONDITIONS

M50-1 has undergone the greatest number of electrochemical cycles (1145 cycles) – the capacity fade profile is provided in Figure 13, along with those of M50-2 – 4. After 100 cycles, Gulsoy *et al.* [212] observed a capacity fade of 5.2% in their M50 cells charged at 1C. Even though the M50 cells in this study were charged at 0.7C at the same temperature of 25 °C as their cells, the lowest capacity fade observed after 100 cycles was 6.20% (M50-1), while the highest was 8.70% (M50-4). Visible changes to the jelly roll of M50-1 were observed after as little as 50 cycles but the first significant deformation of the jelly roll can be seen after 150 cycles. In the timeline (Figure 14) of the progression of deformation inside M50-1, it can be seen that it initiates opposite the inner current collecting tab and continues to propagate until 350 cycles, at which point a second deformation triggers in line with the inner tab. It's also observed that the electrode layers are collapsing towards the hollow core of the cell. In an article by

Waldmann *et al.* [22], it was observed that the evolution of deformations due to cycling started in line with the inner Al-current collecting tab for three different types of 18650 cells. In their case, it was hypothesised that it may be due to the higher specific resistance of Al compared to Cu resulting in a higher temperature due to ohmic heating of the Al-current collector and tabs during discharging of the cell. It can indeed be seen in Figure 14 that the deformations are occurring in-front of and opposite the inner Al-current collector, however, Ohmic heating is unlikely to be the only cause of the deformation. To ascertain possible causes for the difference in the behaviour of the M50 cell, virtual unrolling (VU) was utilised. Figure 15 shows the unrolled jelly rolls of M50-1 in its pristine state and after 50 cycles along with the corresponding X-ray slices. The *x*-axis in the VU figure shows the angular co-ordinate of the cylindrical cell, and the *y*-axis shows the radial coordinate. The edge of the cathode layer was identified, and each 360° loop of the electrode was translated into a 2D orientation such that the outer current collecting tab is always located at 270° – as illustrated by the green arrow and yellow boxes in Figure 15a & c. It can be seen that the pristine cell has pre-existing '*defects*', or '*inflection points*' in the jelly roll along the areas highlighted by the red and green rectangles in Figure 15c – the area corresponding to the red box in the jelly roll of the cell has been marked in Figure 15b, and the defect is identified as a depressed curve in the unrolled figure. This is attributed to the electrode rolling process during manufacturing. These inflection points compromise the structural integrity of the electrode roll, providing headway for the propagation of structural collapse, portrayed by the changes to the jelly roll occurring primarily along those imperfections.

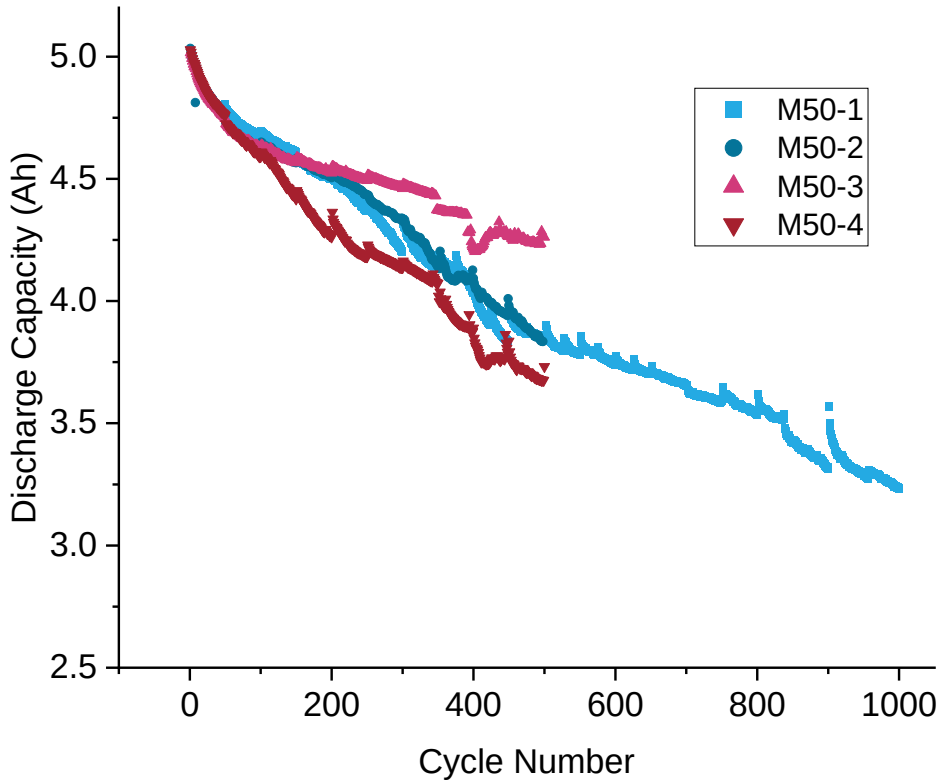

Figure 13: Discharge capacity fade profile of M50 cells cycled at ambient conditions.

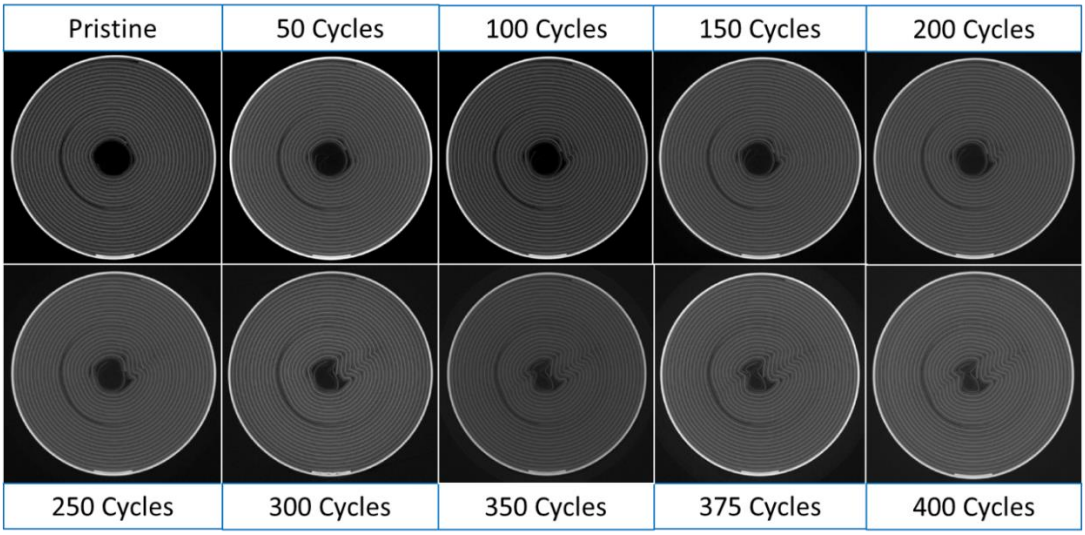

Figure 14: Progression of the deformation of the jelly roll of M50-1 in the first 400 cycles. The cell is 21 mm in diameter.

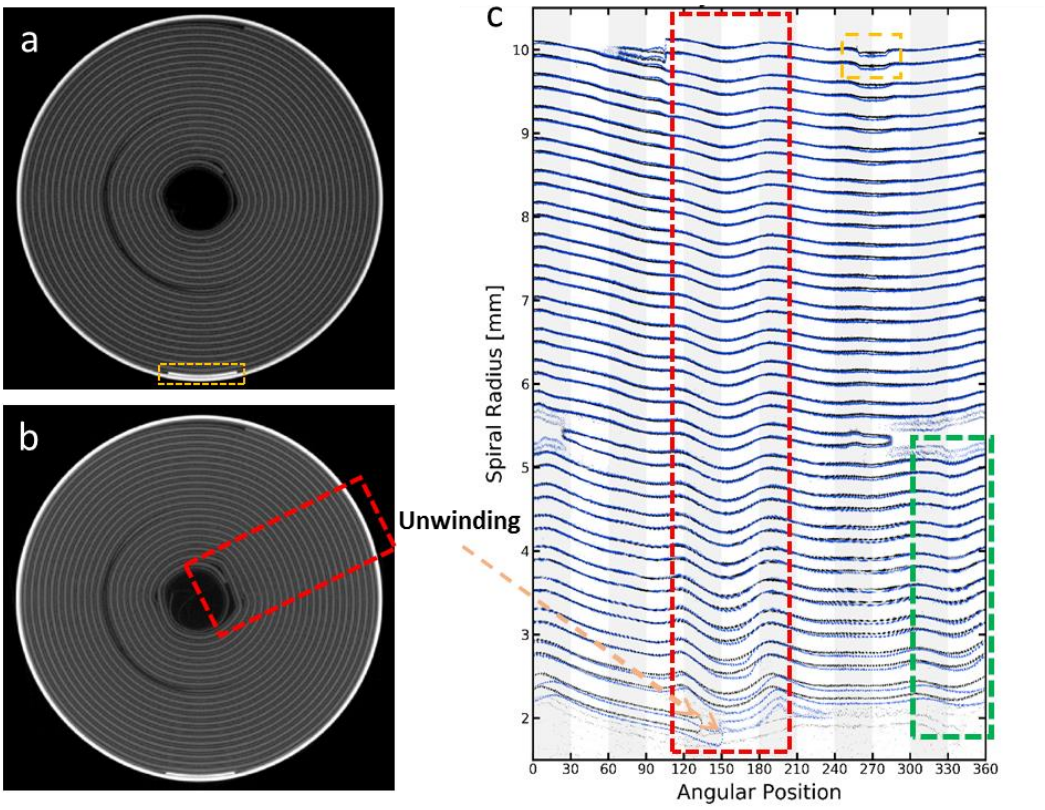

Figure 15: a) A slice of the pristine M50-1, b) after 50 cycles, and c) unrolled jelly rolls of both states superimposed onto a singular chart, black lines represent the pristine state and blue lines the cycled state. The red and green boxes represent pre-existing defects in the windings of the jelly roll that have started to deform. The cell is 21 mm in diameter.

The extent of jelly roll deformation appears to be closely linked to the outer negative tab, as there is less or no deformation in the absence of the current collecting tab towards the positive cell terminal, as demonstrated by Figure 16. It is possible that the stress afflicted by the outer Cu-current collecting tab may be transferring to other parts of the cell due to several factors: there are small gaps where the positive electrode begins and around the two current collecting tabs for the electrode to expand into, as highlighted in Figure 17, alleviating the stress on those sides. Hence, the quadrant without any structural leeway to alleviate the stress shows the greatest deformation. Furthermore, the location at which the positive electrode ends might also play a role

on the location of deformation. Whereas other parts of the electrode roll are quasi-secured in place due to the tight packing of the electrode rolls, the positive electrode end is relatively unsecured. This is demonstrated by the shift in the positive electrode evident in Figure 15, implying that the electrodes are '*unwinding*' from the inside. Thus, it is the location at which the least amount of force would be required to buckle the electrodes. Since the jelly roll is not constrained by a mandrel in this case, and since the electrodes cannot expand outwards due to the cell casing, the electrodes buckle inwards, towards the hollow centre. The discussed factors may be combining with the effects of the Al-tab as discussed by Waldmann *et al.* [22] in determining the starting location of the deformation in the jelly roll. Sonwane *et al.* [213] conducted tensile investigations into the electrodes of M50 cells and found that the electrodes were more mechanically robust in z-direction (height), so that could be another reason for less deformations at different z locations.

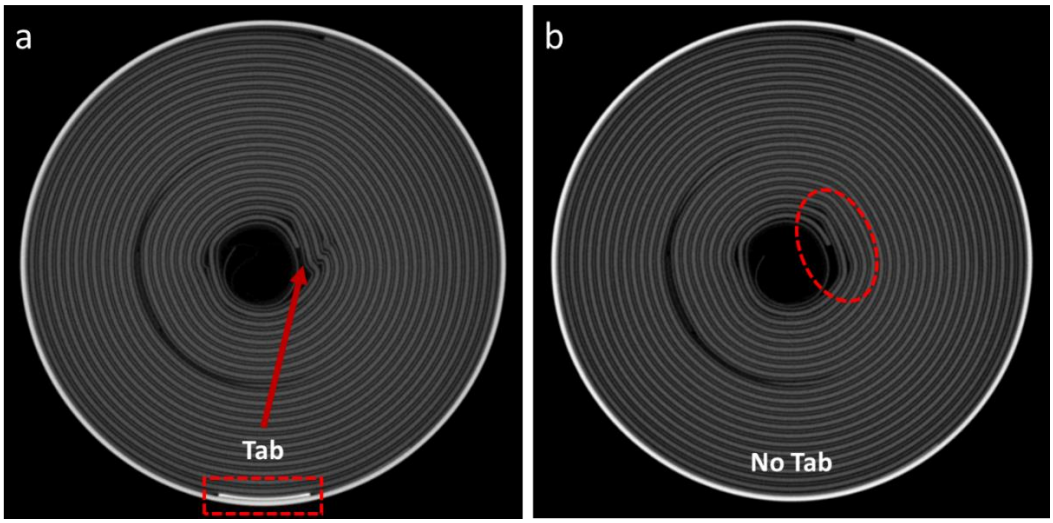

Figure 16: Slices of M50-1 after 100 cycles, a) showing deformations in the jelly roll in the presence of the outer negative tab, and b) showing the jelly roll towards the positive end without the outer tab. The cell is 21 mm in diameter.

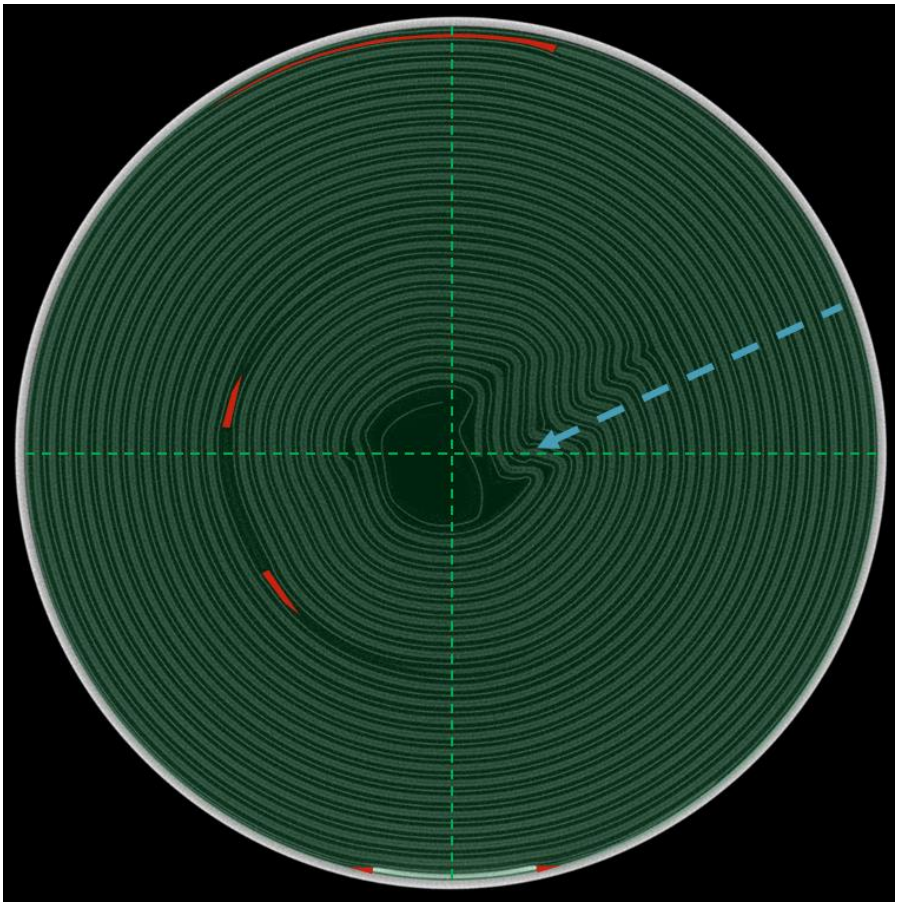

Figure 17: Structural arrangement of M50-1 allowing for stress relief on certain sides of the cell – highlighted in red. Cell is 21 mm in diameter.

Initially, M50-1 was cycled for sets of 50 cycles before being imaged using X-ray CT. The sets were then reduced to 25 cycles after the cell had undergone 350 cycles, which was then increased back to 50 cycles after the 600 cycles mark in order to accelerate the cell's descent beyond end-of-life. The reduction was performed in order to focus on the deformation mechanisms as the cell approached 80% reversible capacity, as can be seen in Figure 13. The highest rate in capacity fade was indeed observed around that point. Between cycles 375 and 425, the discharge capacity faded from 4.19 Ah to 3.9 Ah, however, when inspecting the corresponding slices in Figure 18, after 375, 400, and 425 cycles, significant differences could not be distinguished. The corresponding VU figure shows no difference either.

After 375 cycles, a higher resolution region-of-interest (ROI) scan was taken of M50-1. The ROI scan was conducted using the Zeiss Xradia Versa 520 (Carl ZEISS XRM, California, USA). Using 4X optical magnification and 45 s exposure time, 1601 projections were taken with a voxel size of 2.04 μm. The operating conditions were 159 kV and 63 μA, and the reconstruction was carried out using a filtered back-projection reconstruction algorithm (XM Reconstructor, ZEISS). Delamination of the cathode and the anode, as well as the disfiguration of the copper current collector can be seen in Figure 19. The subsequent sharp decrease in the capacity may be attributed to that, however, it is difficult to determine when exactly delamination of the electrodes initiated.

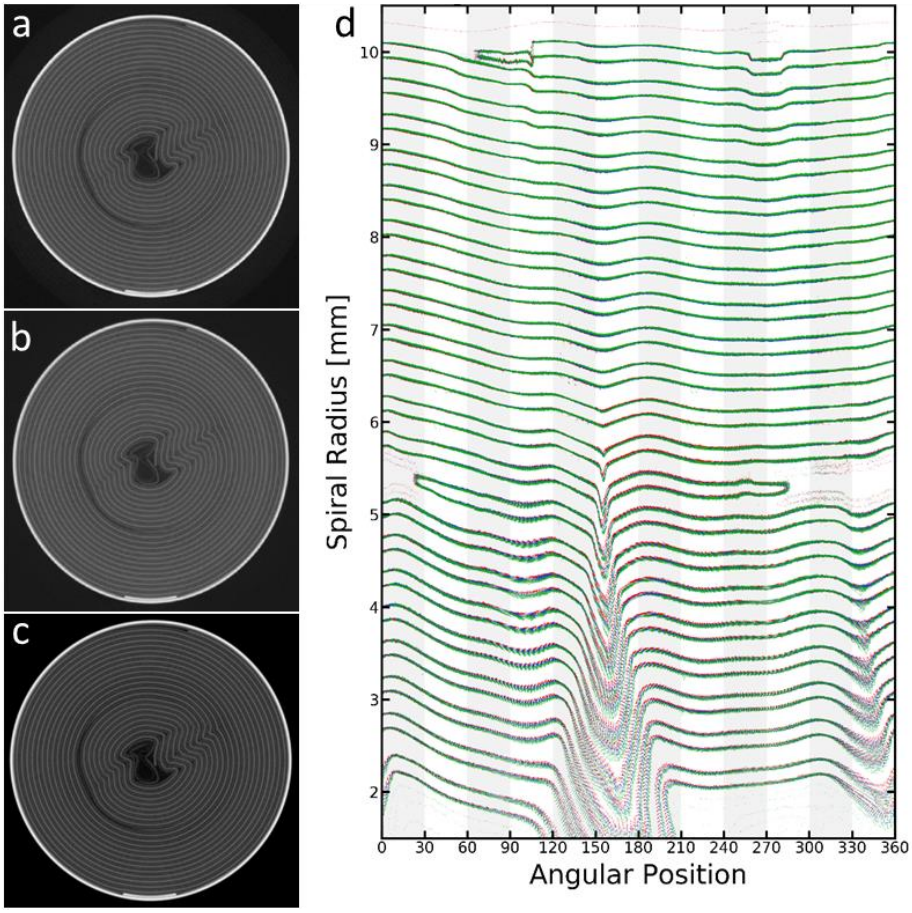

Figure 18: a-c) Slices of M50-1 after 375, 400, and 425 cycles, respectively, and d) the corresponding VU figure, red, blue, and green correspond to 375, 400 and 425 cycles, respectively. Cells are 21 mm in diameter.

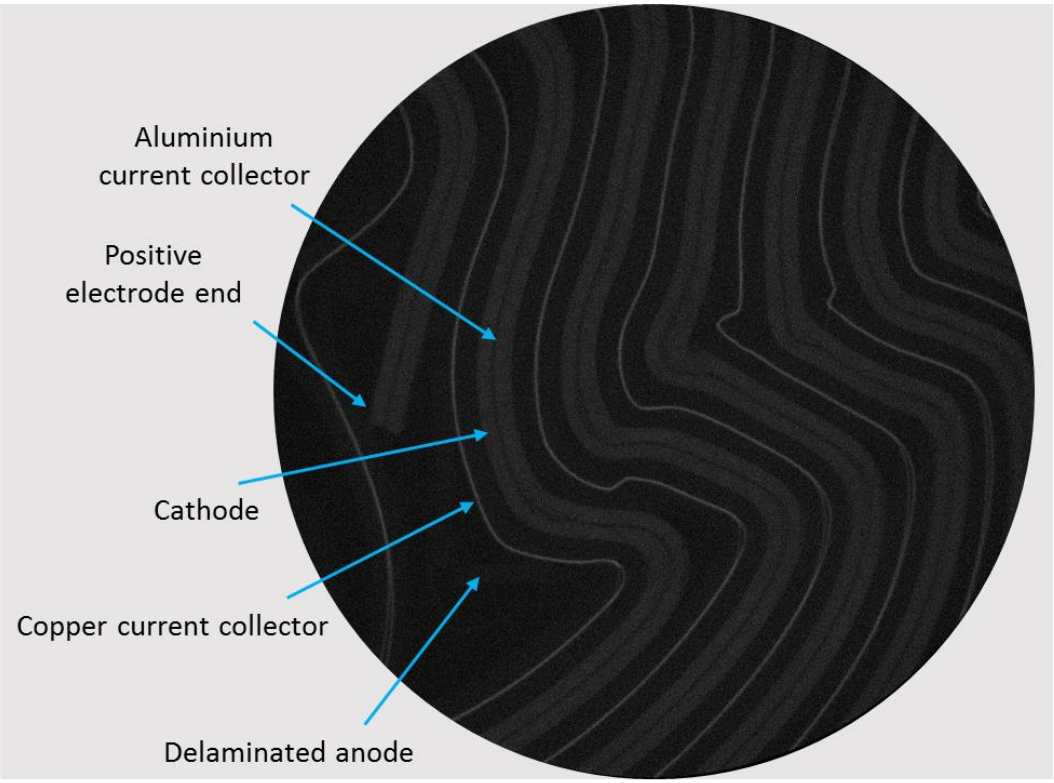

Figure 19: A region-of-interest scan of M50-1 after 375 cycles showing the deformation of the positive and negative electrodes and their current collectors, and the delamination of the negative electrode.

M50-1 reaches 80% capacity after approx. 400 cycles, after which a rapid decline in capacity fade initiates, as discussed earlier. After about 460 cycles, the capacity fade begins to stabilise, and goes into a linear phase between ca. 460 cycles to 850 cycles. Over that period there is only a further ca. 12.1% decrease in capacity. Past the 850 cycles mark, it once again begins a rapid decline in capacity fade as it heads beyond end-of-life. Figure 20 shows the unrolled jelly rolls of M50-1 between certain sets of electrochemical cycling. Similar to the previous virtual unrolling figures, it shows the displacement of electrodes after a number of cycles in reference to a previous state, but it more clearly shows the concentration of strain gradients causing the changes in the physical state of the jelly roll. It can be seen that at the start of the linear phase of capacity degradation (between 450-500 cycles, Figure 20a), there is still a significant change occurring within the jelly roll. This is likely due to the remaining effects of the

fast degradation phase between ca. 375 – 425 cycles. It can also be seen that towards the end of the linear phase (750-800 cycles, Figure 20b) the jelly roll stabilises, and there is little movement in the electrode roll. At the end of the cell's life, after 800 cycles (Figure 20c & d), there is once again a larger shift in the electrodes, which results in increased degradation, however, it is not as significant as between 450 – 500 cycles. This is likely due to there being very little space at the centre of the cell due to excessive deformation of the jelly roll, as seen in the inset of an X-ray slice after 1000 cycles in Figure 20d. After 1000 cycles, M50-1 had ca. 64.7% nominal reversible capacity remaining.

M50-2, 3 and 4 were also cycled at ambient conditions at the same rate as M50-1 and imaged every 50 cycles in order to investigate any potential variability in the mechanisms of deformations between cells. The discharge profiles of the cells can be found in Figure 13 and the associated changes to the jelly rolls after ca. 500 cycles can be found in Figure 21. It is observed that, similar to M50-1, these also exhibit a rapid decrease in capacity initially, followed by a decrease in the rate of degradation. When comparing the rate of capacity fade of the cells to the changes in the jelly rolls of the cells, it can be seen that the greatest deformation is experienced by the cell with the lowest capacity: M50-4 with ca. 3.6 Ah remaining discharge capacity after around 500 cycles. The nucleation of deformation in M50-3 is in a location that is different to the other M50 cells studied. It has nucleated next to the inner tab, instead of opposite. This could be due to the greater Ohmic heating experienced by this cell due to cell level variances within *"same batch cells"*. However, despite the difference in locations, when comparing the virtually unrolled jelly rolls of M50-1 and M50-3 in Figure 15 and Figure 22, changes are occurring at the same structural bearings for both cells (and in fact for all four cells cycled at ambient conditions): pre-existing inflection points. However, M50-3 appears to have a bigger inflection in the jelly roll in line with the inner tab than M50-1, so that, in combination with the effect of the Al-current collecting tab, may have caused the deformation to initiate in line with the tab. All the changes in the jelly roll of these three cells are occurring where the points of inflections are located, hence the hypothesis that the pre-existing imperfections in the jelly roll are the primary contributors to the location of deformation becomes stronger.

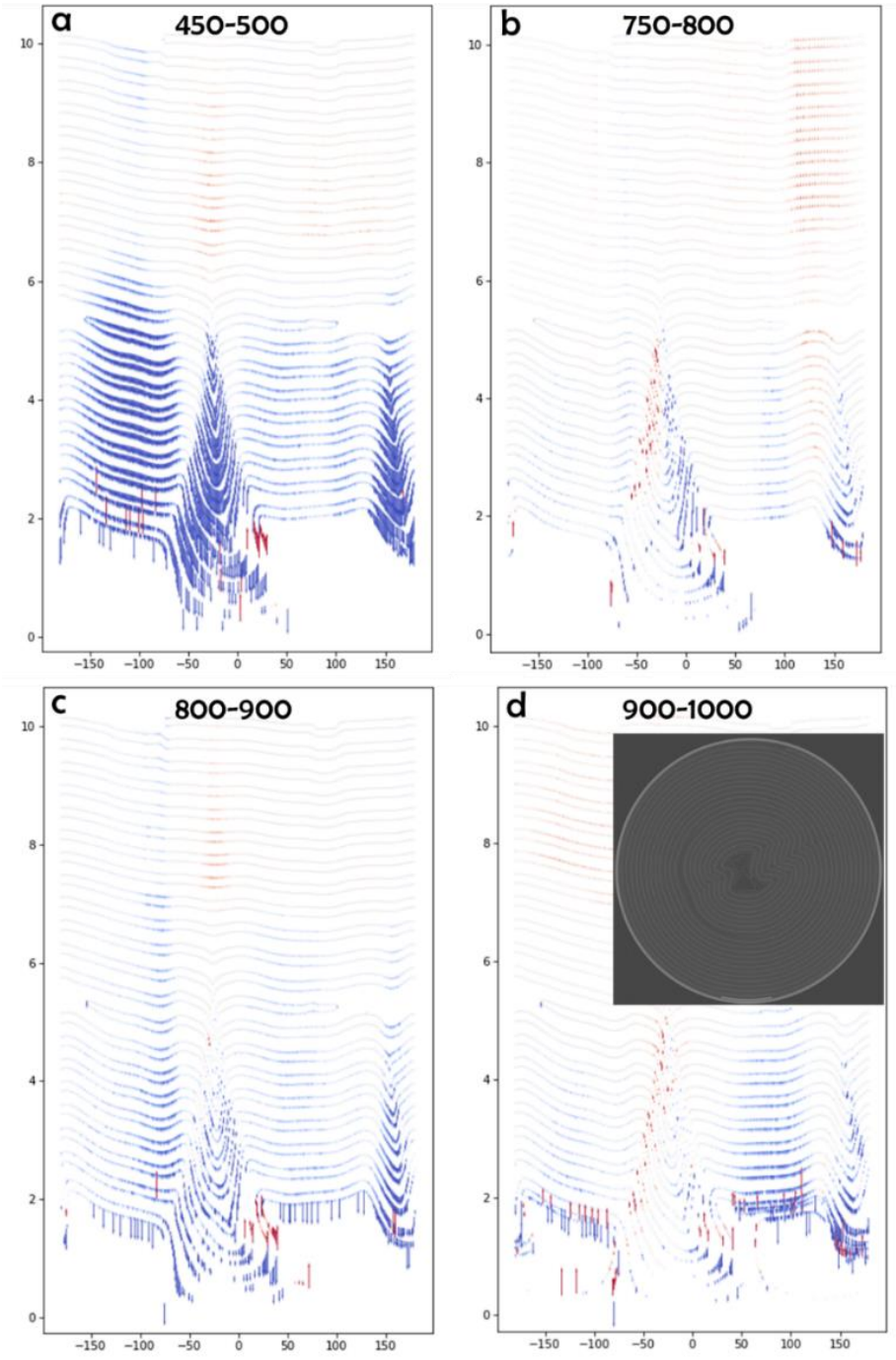

Figure 20: Unrolled jelly roll of M50-1 showing the displacement of electrodes between sets of electrochemical cycling. The cycle numbers are provided above the unrolled figures. The blue represents a shift of the electrodes towards the centre of the cell, and the red represents a shift towards the cell casing. The inset in (d) shows an X-ray slice of M50-1 after 1000 cycles.

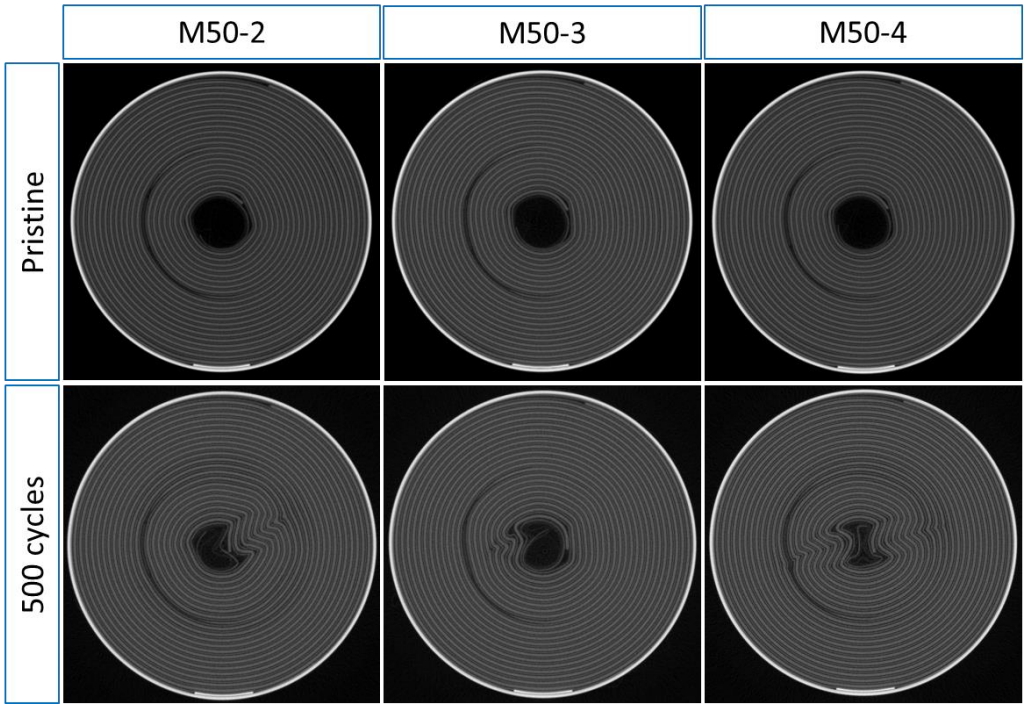

Figure 21: Slices of M50-2, M50-3, M50-4, in their pristine state and after ca. 500 cycles. The cells are 21 mm in diameter.

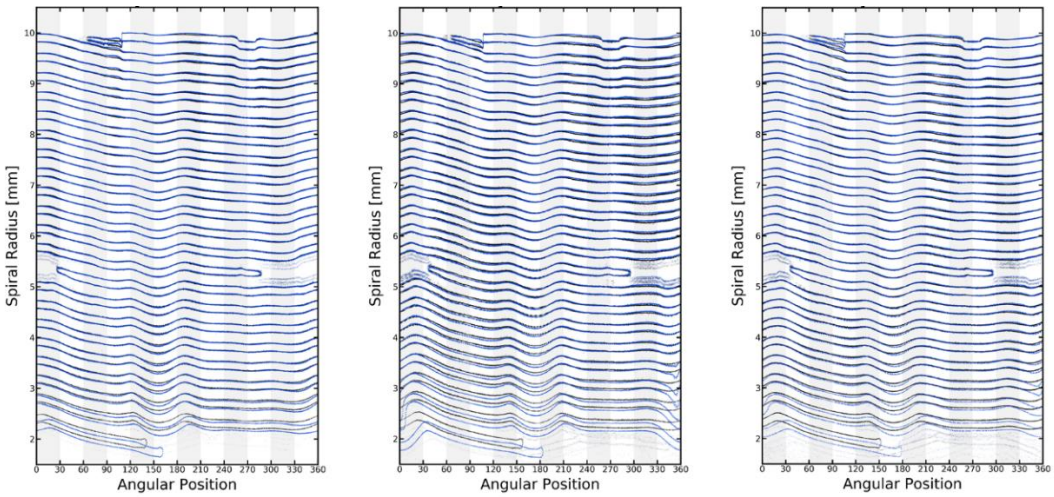

Figure 22: Left to right: unrolled jelly rolls of M50-2, M50-3, M50-4, respectively, demonstrating the nucleation of cell level changes. Black lines represent the pristine state, and blue lines once they had undergone 100 cycles.

It can be seen from Figure 13 that M50-2 follows the most similar capacity fade profile to M50-1. The progression of deformation within M50-2 can be seen in Figure 23, and it can be seen that although the capacity fade profiles are very similar, the deformation time is quite different. Whereas electrode buckling could clearly be viewed through visual inspection on M50-1 after just 150 cycles, it takes around 300 cycles for the same to occur in M50-2. Clearly there are other factors at work here, such as the microstructural morphology of the electrodes and also chemical aspects, aside from just the influence of pre-existing inflections on the nucleation and progression of deformation. M40-4 shows a greater rate of capacity fade than M50-1, and also exhibits a greater rate of deformation, with deformations at two locations after just 200 cycles (as seen in Figure 24), compared to M50-1 which showed two deformations after 350 cycles.

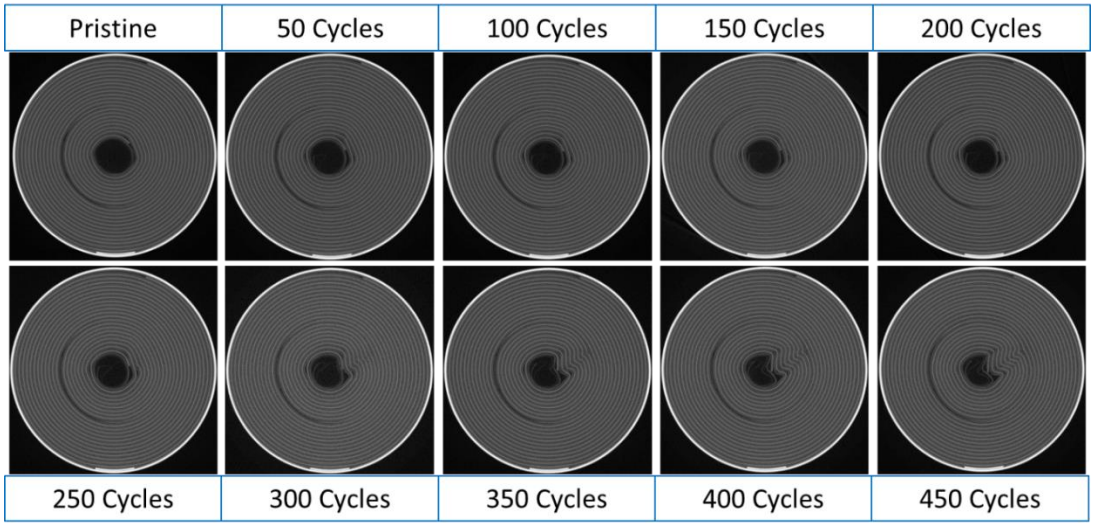

Figure 23: Progression of the deformation of the jelly roll of M50-2 over 450 cycles. The cell is 21 mm in diameter.

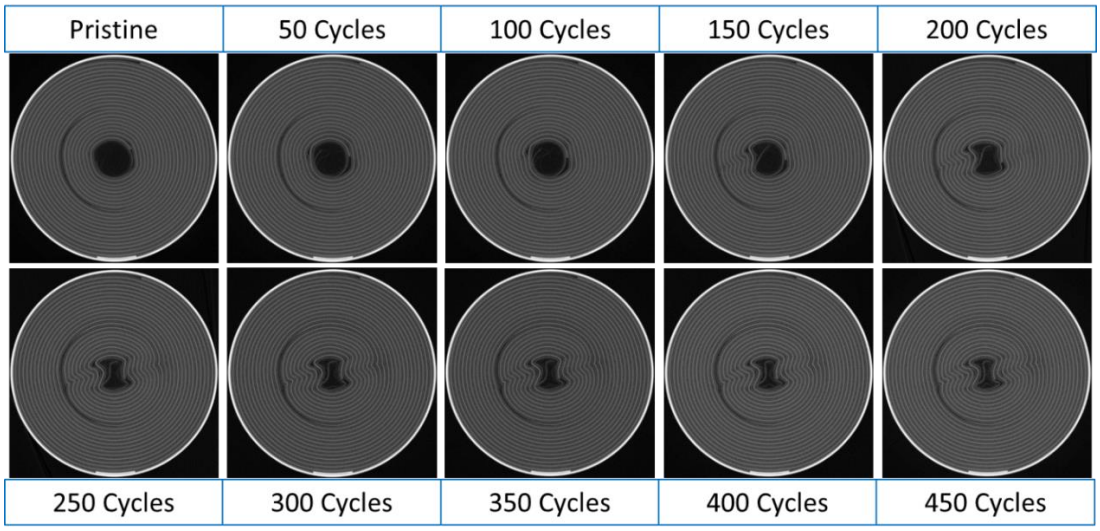

Figure 24: Progression of the deformation of the jelly roll of M50-4 over 450 cycles. Cell is 21 mm in diameter.

4.4 INVESTIGATION OF M50 CELLS CYCLED AT NON-AMBIENT CONDITIONS

Four additional M50 cells were cycled at elevated or low temperatures. This investigation was carried out in order to elucidate the effects of cycling under temperatures deviating from ambient, on the rate of deformation of the jelly rolls, and on the capacity fade. The discharge capacity profiles of M50-5 and 6, which were cycled at 0 °C, and M50-7 and 8, which were cycled at 45 °C, are provided in Figure 25. The sudden increase in the capacity of the cells cycled at 0 °C at cycles 76 and 77 is due to an increase in the temperature of the environmental chamber to 30 °C as a result of a malfunction. Similarly, the variation in the capacity at around 150 cycles is due to slight temperature fluctuations. The capacity fade after 150 cycles of cells M50-5 – 8 is 9.1%, 29.1%, 9.7%, and 10.3% of their initial discharge capacity, respectively. The greater degradation observed for M50-6 is attributed to the greater deformation experienced by the cell as seen in Figure 26. Due to the cell being cycled at 0 °C, the deposition of lithium dendrites on the carbon negative electrode surface might be another cause of

the greater capacity fade. The general point at which the deformation in M50-5 and M50-6 initiates can be inferred by comparing the capacity fade profiles and the X-ray CT data. Figure 27 shows the difference in the jelly rolls of M50-5 after 100 and 125 cycles, and of M50-6 after 50 and 75 cycles. Visible deformation of the jelly rolls occurs during those cycles, which corresponds to an increase in the capacity fade as observed in Figure 25. After 125 cycles, M50-5 had a capacity retention of ca. 94.0% compared to its first discharge capacity, and M50-6 had a capacity retention of 92.2% after 75 cycles. The deformation for both cells is occurring at very similar capacity fade values, although one sustains a greater collapse of the jelly roll than the other. After the appearance of the deformation, M50-6 continues to degrade at a greater rate than M50-5, in proportion to the extent of deformation observed in the cells comparatively. Such a sudden increase in capacity decay is not observed for the cells at 45 °C, even after the deformation of the jelly roll. These results are also likely to be in part due to the increased internal resistances as temperature decreases [101,214], hence, the increase in cell resistance caused by loss of electrode contact due to deformation is liable to be more pronounced at lower temperatures.

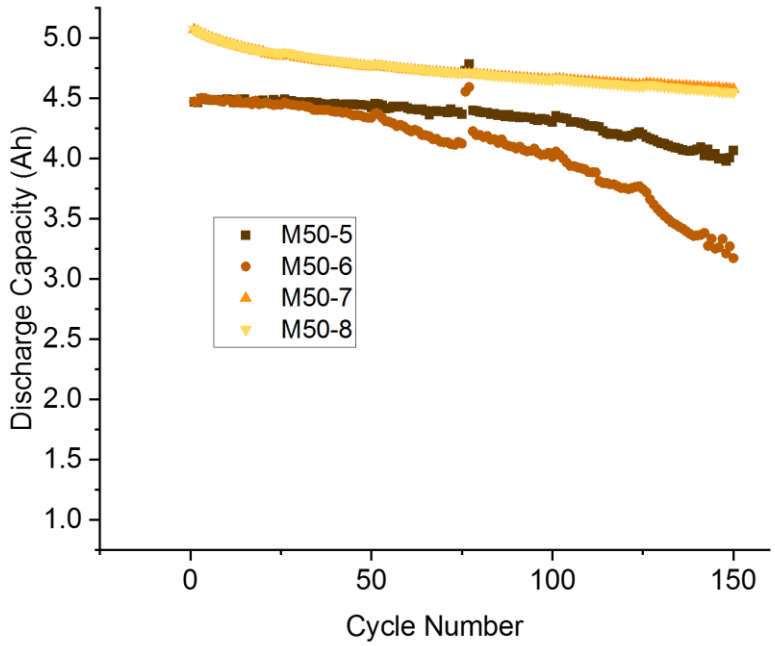

Figure 25: Discharge profiles of M50-5 & M50-6 (0 °C), M50-7 & M50-8 (45 °C).

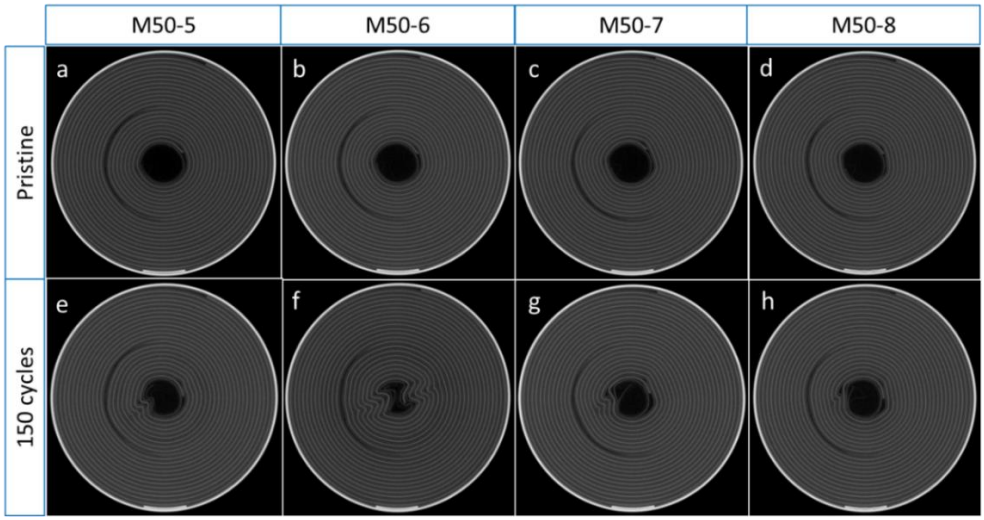

Figure 26: Slices of M50-5 & M50-6 (0 °C), M50-7 & M50-8 (45 °C), in their pristine state and after 150 cycles, respectively. The cells are 21 mm in diameter.

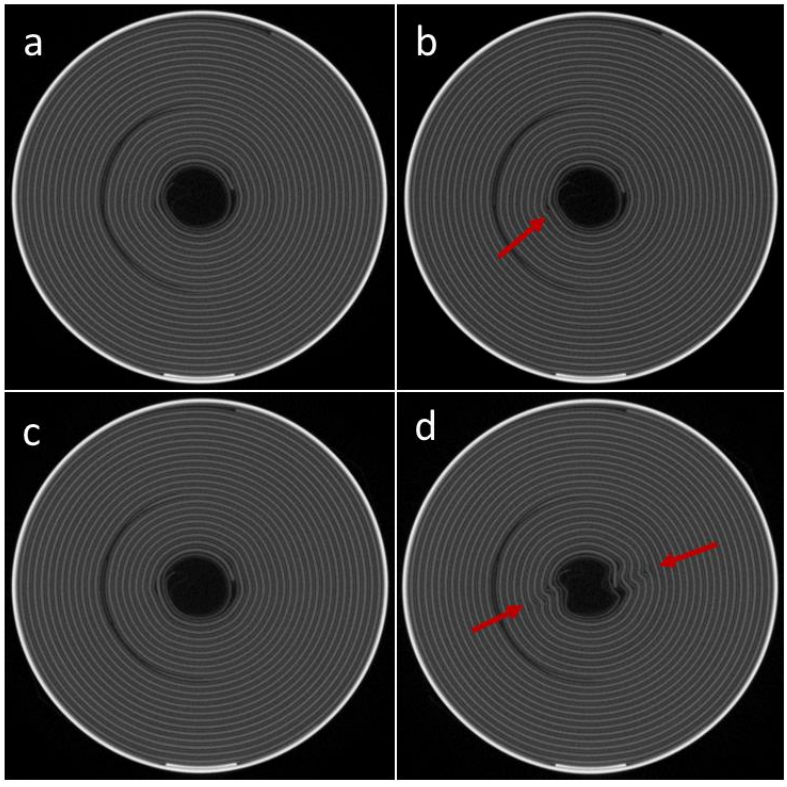

Figure 27: a-b) Slice of M50-5 after 100 cycles and after 125 cycles, respectively, and c-d) slice of M50-6 after 50 and 75 cycles, respectively. The cells are 21 mm in diameter.

Once again, when looking at the virtually unrolled jelly rolls in Figure 28, it can be seen that the deformations are occurring at pre-existing inflection points. However, even when the magnitude of inflection is relatively small compared to some of the other cells investigated above, the extent of deformation is still great within M50-5 and M50-6 cycled at 0 °C. Additionally, although it is not noticeable in Figure 27, it can be seen in Figure 28 that, similar to M50-6, M50-5 also contains a secondary deformation which is located between 150-180°. It would appear that as well as increased capacity fade, cycling at a lower temperature also accentuates the effect of the pre-existing imperfections on the rate of deformation. Another factor could be that cycling at a lower rate may be causing a greater rate of deformation.

It can be observed from Figure 26 that the position of the inner Al tab is slightly inconsistent between the M50 cells. This could be one of the factors causing slight differences in the location and rate of deformation. A comparison of the discharge capacity fade between M50-1 and the cells cycled at 45 °C can be found in Figure 29. It can be seen that the increase in cycling temperature from about 23 °C to 45 °C has not resulted in a significant increase in degradation in the 150 cycles studied. Overall, decreased temperature seems to have a more adverse effect on both the rate of capacity fade and on the amount of capacity available, within the temperature range presented here.

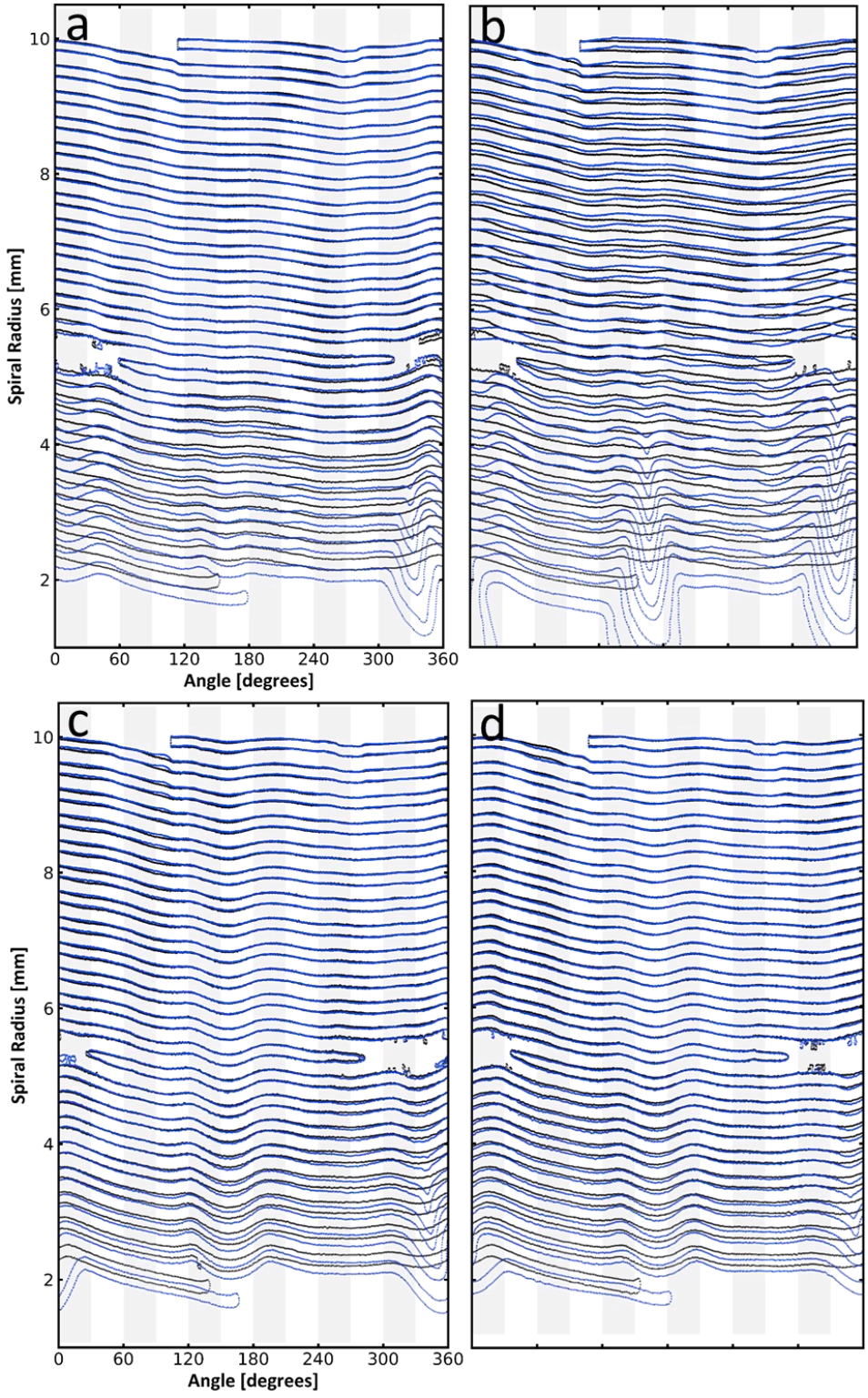

Figure 28: Left to right: unrolled jelly rolls of (a) M50-5, (b) M50-6, (c) M50-7, and (d) M50-8. The black lines represent the pristine state, and blue lines after 150 cycles.

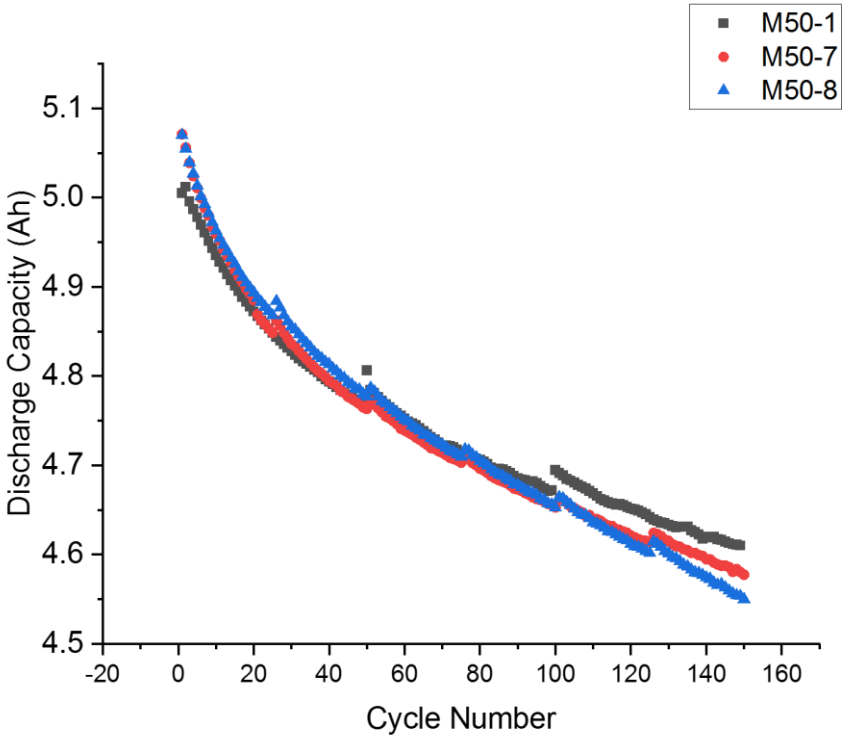

Figure 29: Comparison of the discharge profiles of M50-1, M50-7, and M50-8.

4.5 STORAGE OF M50 CELLS AT 80% SOC

Electric vehicle manufacturers consider lithium-ion cells to have reached end-of-life once their capacity retention deteriorates to below 80% as they tend to exhibit greater degradation from approximately that point. Figure 30a shows the capacity fade profile of the first 375 cycles of an M50 cell's cycle life that was charged at 3.5 A and discharged at 5 A. It passed the 80% capacity fade mark after 212 cycles. In order to identify the *'knee-points'* in the degradation behaviour of the cell, the differential capacity of the capacity profile with respect to the cycle numbers was performed, as shown in Figure 30b. The data was smoothed for a clearer representation of the trend. It can be seen that the capacity fade exhibits three distinct phases. The first phase demonstrates the initial sharp loss in capacity when first cycling cells. The second phase shows a

small bell curve of a temporary increase in capacity fade, followed by a decrease. The temperature of the cell as obtained from thermocouple attached at the cell surface was within the expected range, therefore, the behaviour was not the cause of a fluctuation in the ambient temperature, as such, the possible cause is unknown. The third phase exhibits a steady increase in capacity fade with no signs of it decreasing again. This key point in the capacity profile is likely to be the actual knee-point. In this case, the knee-point starts ca. 30 cycles before the cell's capacity fades to 80%.

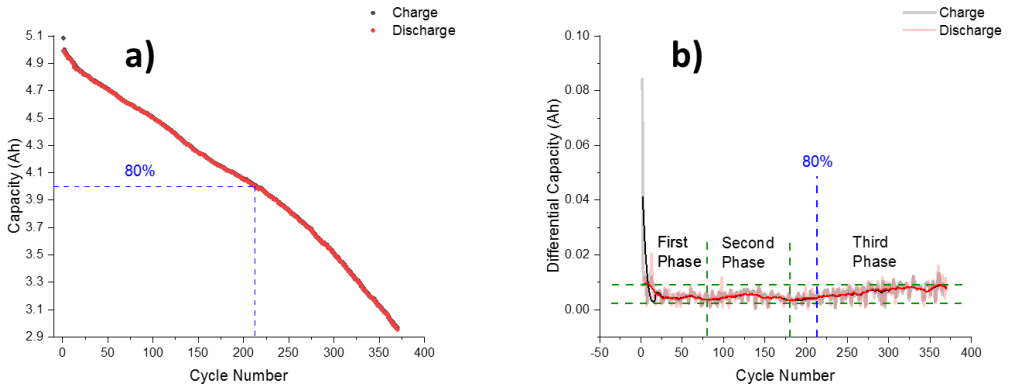

Figure 30: a) Capacity fade profile of an M50 cell, b) differential capacity with respect to cycle numbers - the transparent lines represent the actual data, and the solid overlays represent the smoothed data.

The open-circuit voltage decay of the 5 cells for the first hour of relaxation and then at specific points in their storage thereafter can be viewed in Figure 31. It can be seen from Figure 31 that the cells charged to 80% of their rated capacity achieved a higher voltage than the ones taken to 80% of the voltage window. Moreover, during the initial period right after charging was complete, those cells exhibit greater open-circuit voltage drop. During the first hour, the voltage of A, B, and C decayed by 0.055%, 0.051%, and 0.079%, respectively, whereas, D and E stabilised after decaying by 0.911%, and 0.874%, respectively. This voltage relaxation behaviour is observed in Li-ion cells when switching from charge/discharge to open-circuit voltage [215], and will not be computed as part of the voltage decay caused by the storage of the cells.

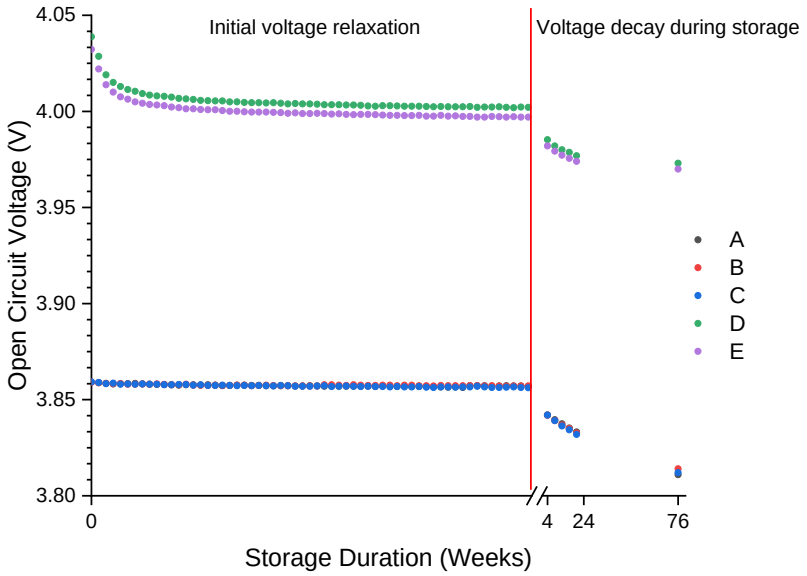

Figure 31: Open-circuit voltage decay of the cells stored at 80% SOC. For cells A, B, and C, SOC was defined using the voltage window (2.5 – 4.2 V), and for D and E, SOC was defined using their rated capacity, 5 Ah.

A summary of the relative voltage decay after the voltage had stabilised is provided in Table 5. The capacity achieved by A, B, and C after charging to 3.86 V is between 3.175 – 3.192 Ah. Hence, C and D, which were charged to 4 Ah would have more lithium intercalated into the graphite and more available lithium to engage in parasitic reactions on the anode side. The expectation would be that C and D would therefore demonstrate a greater voltage decay during storage. In the initial 20 weeks, it can be seen that the greatest voltage decay occurred during the first 4 weeks, more so than the decrease that occurred between 4 – 20 weeks. Within that time frame, it was indeed observed that one of the cells (D) charged based on capacity showed a higher voltage decay than the others. However, over the whole 20 weeks, the same cell showed a similar voltage decay to the cells charged based on voltage window, and instead the second cell (E) charged based on capacity showed a lower rate of decay. Therefore, the difference between defining SOC by capacity and voltage window could not be explicated at that stage. Between 20 weeks to 76 weeks, the voltage decay profile shows

an entirely different trend: cells charged based on the voltage window show a much greater decay than the cells charged based on capacity. Consequently, A, B, and C display almost twice the voltage decay over the entire storage period at around 1.15%, suggesting that charging to 80% of the voltage window is closer to the knee-point where Li-ion cells display greater degradation.

In order to elucidate the subtle differences in the self-discharge observed by the cells, differential capacity profiles with respect to cell potential have been plotted in Figure 32. It can be seen that the location and height of the peaks are relatively consistent between the five cells. The M50 cells charged based on 80% of the voltage window were charged to 3.86 V and the cells charged based on 80% of the nominal capacity achieved voltages ca. 4.03 – 4.04 V. These points of interest have been marked in Figure 32a and Figure 32b, which show the charge and discharge differential capacity profiles, respectively. Plotting differential capacity profiles throughout a system's lifetime can provide insight into the behaviour of the system and can be used to conduct prognosis on cell behaviour. The peaks in the differential profiles represent a transition in the phase of the electrodes, and the peak heights and locations have been associated with degradation [216,217]. Degradation results in an increase of the internal resistance of cells, a decrease in their capacity over time, and an increase in the self-discharge of the cells. Although, here, comparisons of the profiles of the same types of cells, from the same manufacturing batch, and in the same stage in their cycle life are conducted, it can provide some information on special features which may shed insight into why varying self-discharge rates were observed. It can be seen in Figure 32 that in both the charge and discharge profiles, 3.86 V is located at a slope, very close to a peak, whereas 4.03 V is located more at a trough. The peak is indicative of a structural change during intercalation of the electrodes, therefore it could be inferred that leaving a cell in the middle of that stage for a prolonged period may cause additional degradation.

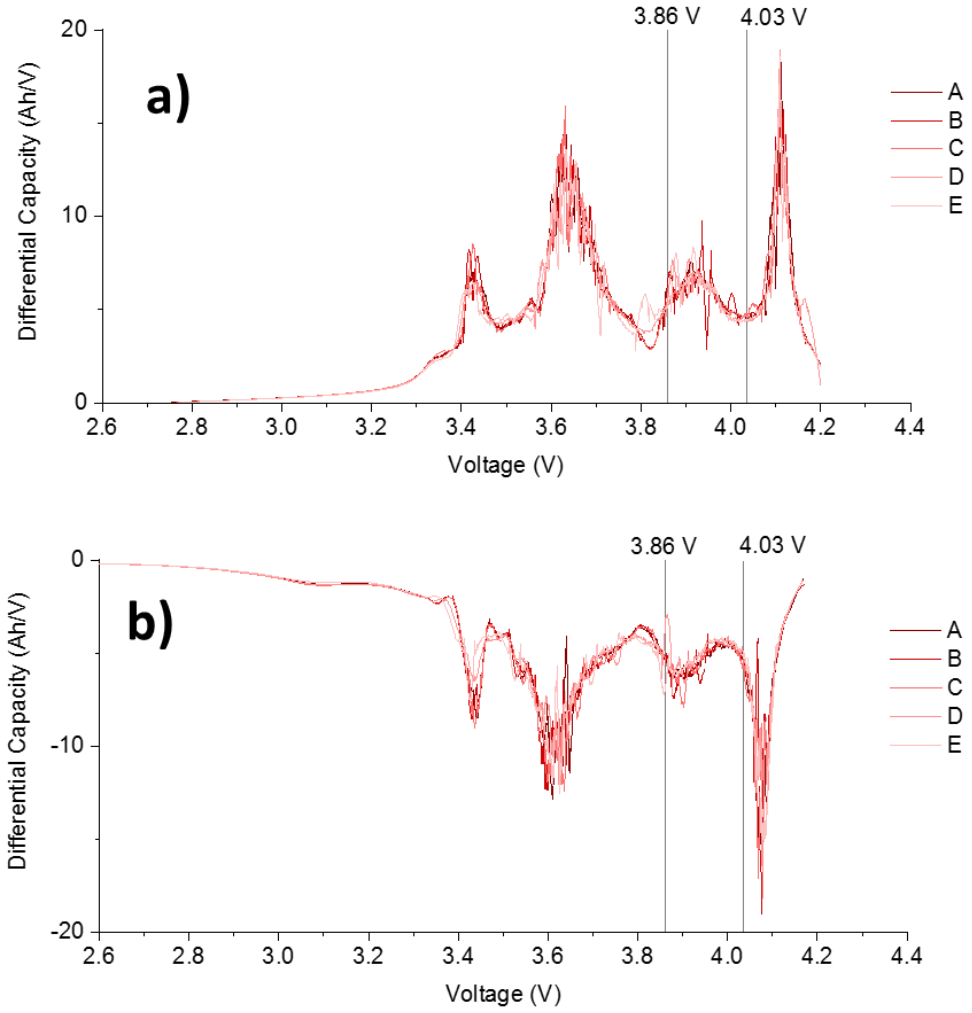

Figure 32: (a) Charge, and (b) discharge differential capacity profiles of the M50 cells.

Table 5: Open-circuit voltage decay of the cells stored at 80% SOC.

	1 HR TO 4 WEEKS (%)	1 HR TO 20 WEEKS (%)	4 WEEKS TO 20 WEEKS (%)	20 WEEKS TO 76 WEEKS (%)
A	0.387	0.616	0.230	0.579
B	0.394	0.635	0.242	0.485
C	0.368	0.629	0.261	0.520
D	0.420	0.629	0.210	0.098
E	0.376	0.576	0.201	0.101

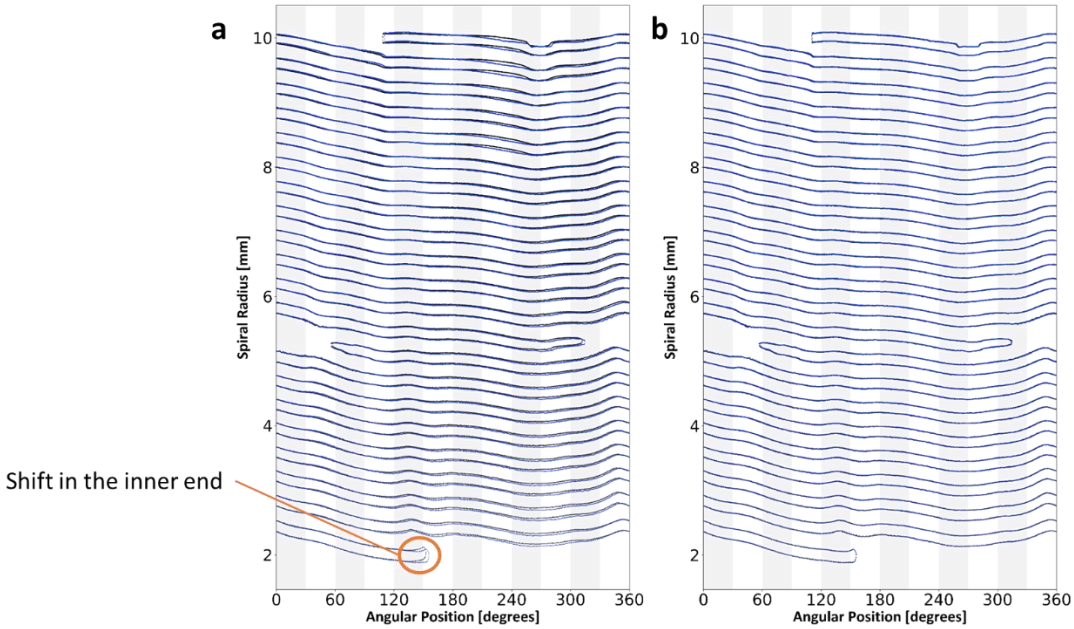

Figure 33: Unrolled jelly rolls of cell A: (a) in its pristine state (black) vs. 80% SOC (blue), and (b) 4 weeks of storage (black) vs. 76 weeks of storage (blue).

Although the stress caused from storage of NMC cells in their (quasi) charged states is associated with crystallographic changes in the NMC, architectural changes manifested from the experiment was also explored. Virtual unrolling was carried out on all five cells to determine whether storage at 80% SOC caused physical changes within the jelly rolls of the M50 cells. By superimposing the unrolled electrodes of cells at different times or states, the technique allows for the tracking of physical changes in the jelly roll. Figure 33a shows the jelly rolls of cell A in its pristine discharged state and after being charged to 80% SOC. The figure demonstrates that charging to 80% SOC from a fully discharged state causes a slight shift in the electrodes, particularly at the electrode end towards the inner coil. All cells demonstrated this behaviour when charging to 80% SOC. In other studies in this work, architectural changes during different steps in the charging of M50 cells were explored: a general increase in anode thickness was observed by [201], which leads to residual stress in the jelly roll, which is correlated by the increased displacement of the jelly roll observed in M50 cells at 3.6 – 3.9 V. Storing the cells in this state (where the electrode end is displaced) rather

than in its relaxed state may be causing additional stress within the jelly roll, contributing to the increased self-discharge behaviour for charged cells.

Virtual unrolling was then used to determine if the passive self-discharge during storage of the cells at ambient temperatures caused any physical deformations in the jelly roll. Figure 33b shows the virtually unrolled electrodes of cell A, comparing between storage after 4 weeks and storage after 76 weeks. It can be seen that ca. 1.15% self-discharge did not cause any physical shifts in the electrode of cell A. The same was the case for all other cells, whether they were charged to 80% SOC based on the voltage window or based on nominal capacity. The unrolled figures comparing the electrodes of cells B, C, D, and E between week 4 and week 76 are provided in Figure 34.

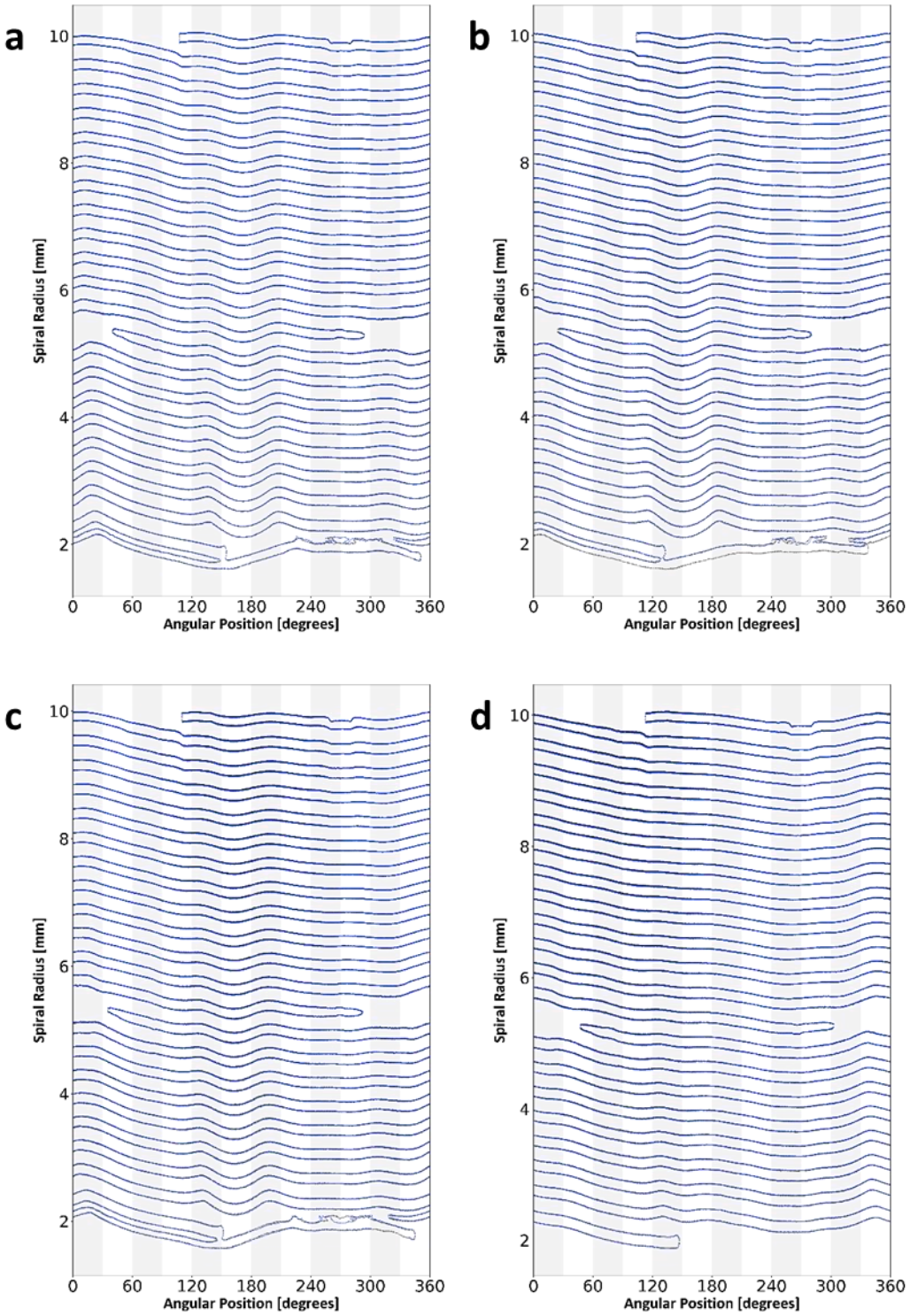

Figure 34: Unrolled jelly rolls of (a) cell B, (b) cell C, (c) cell D, and (e) cell E, between 4 weeks of storage (black) vs. 76 weeks of storage (blue).

4.6 INVESTIGATION OF MJ1 CELLS CYCLED AT AMBIENT CONDITIONS

Unlike the M50 cells, which were imaged approximately every 50 cycles, the MJ1 cells were scanned when their capacity faded to a certain threshold, irrespective of the number of cycles required. This imaging criteria was chosen in order to investigate the microstructural and electrochemical behaviour of the cells as their capacity approach, converge, and exceed the accepted end-of-life state for automotive cells (80% reversible capacity). Furthermore, unlike the M50 cells, the MJ1 cells are of the 18650 format, and their inner Al-current collector is located at the centre of the cell, not in the middle of the jelly roll. Additionally, the MJ1 cells also contain a similar NMC//Si/C chemistry to M50s, and contain a Cu-current collecting tab on the outside of the jelly roll, next to the cell casing. These features can be observed in Figure 35. Hence, the MJ1 were chosen for this investigation in order to examine the differences in deformation mechanisms and capacity fade caused by a difference in cell geometry and internal structure.

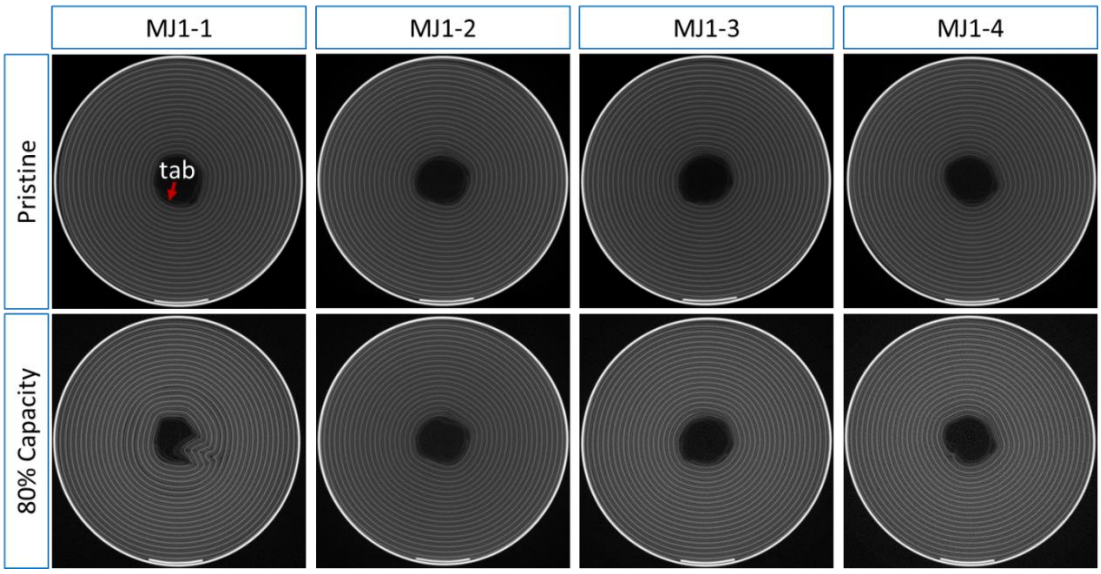

Figure 35: Slices of MJ1-1, MJ1-2, MJ1-3, and MJ1-4, in their pristine state and at 80% capacity, respectively. The cells are 18 mm in diameter.

Figure 35 shows the slices of the cycled MJ1 cells in their pristine state and after reaching 80% nominal capacity. Deformation in the jelly roll of MJ1-1, and a minor kink of the electrodes in MJ1-4 can be observed. When looking at the slices, the location of the deformations seem to be inconsistent with each other, however, they are consistent with the trends observed for the M50 cells and that observed by Kok *et al.* [146] for an MJ1 cell. When viewing the unrolled jelly-rolls in Figure 36, it can be seen that these cells studied in this project have multiple inflections. Therefore, there are shifts and deformations of the jelly roll along those inflection points in addition to the minor shifts along the outer current collecting tab. Therefore, it is not just the influence, or presence, of the outer current collecting tab that cause inflection points in the jelly roll.

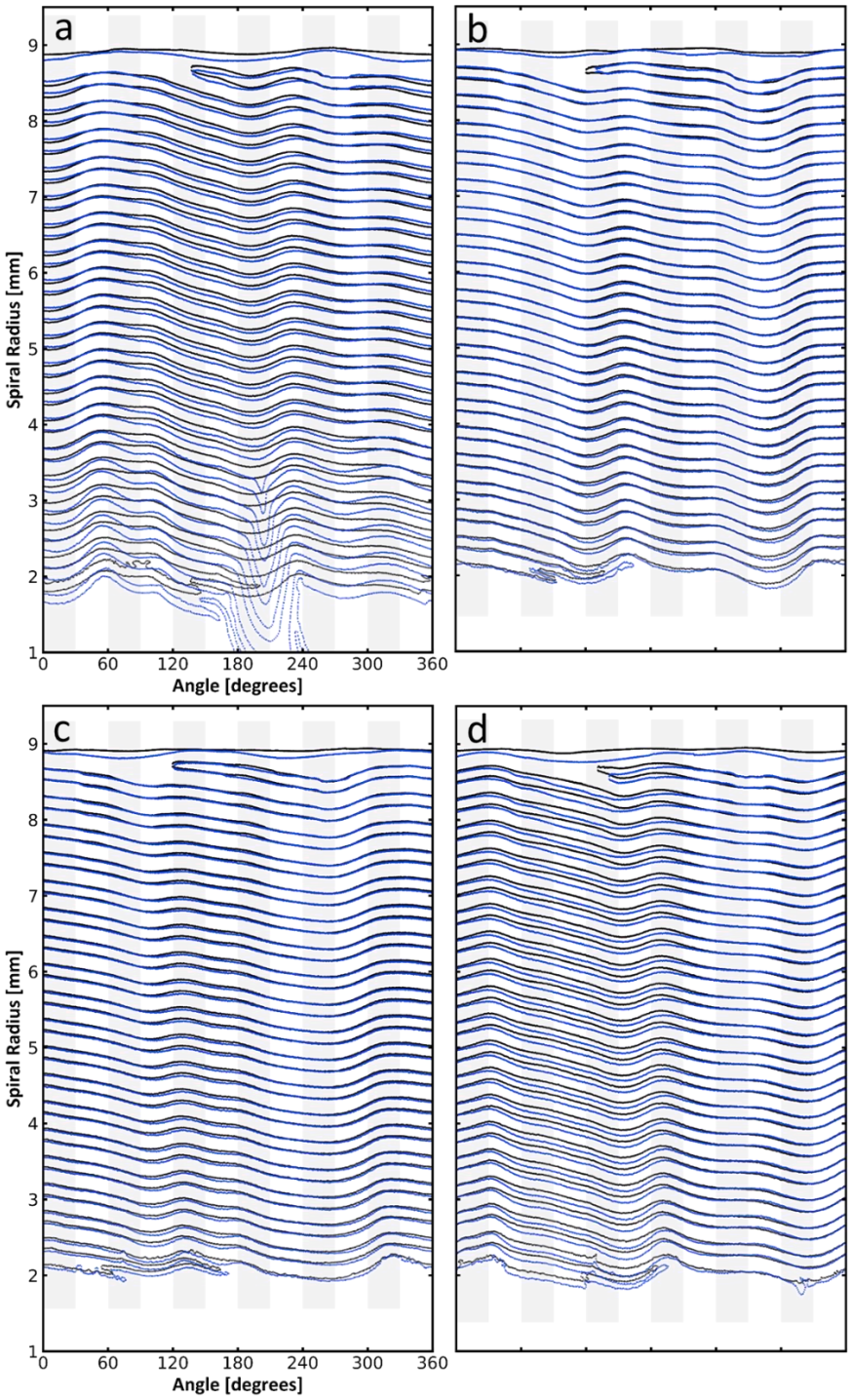

Figure 36: Left to right: unrolled jelly rolls of (a) MJ1-1, (b) MJ1-2, (c) MJ1-3, and (d) MJ1-4, respectively. Black lines represent the pristine state and blue lines once they had dropped to 80% capacity.

When observing the jelly rolls of the MJ1 cells in their pristine state it can be seen that the cells have slight variation in the location and also extent of the pre-existing inflections which is causing the deformations to initiate at different locations and at different rates. Unlike the M50s, the MJ1 cells do not contain an inner Al-current collecting tab in the middle of the jelly roll. The lack of a fixed structure which the electrodes would be bound and suppressed by, and which would provide structural support and space for electrode expansion (as discussed in the previous section), could be another explanation for the varying locations of deformation witnessed in the MJ1 cells. Furthermore, unlike in the M50s, the electrodes in the MJ1s do not end abruptly, and are instead tapered. Therefore, the space for electrode expansion that was available adjacent to the electrode end in the M50 – which would lower the prospect of deformation occurring along certain quadrants of the cylinder – is not present in the MJ1, hence, deformation could commence at a greater number of locations.

Comparing the capacity fade behaviour of the four MJ1 cells in Figure 37, it can be seen that it takes a different number of cycles to reach 80% of nominal capacity (2.8 Ah) for each cell. MJ1-1 achieves 80% capacity after 687 cycles, while MJ1-2 – MJ1-4 achieve 80% capacity after 1141, 1077, and 1106 cycles, respectively, with MJ1-1 reaching 80% at almost twice the rate of the other three cells. Proportionately, MJ1-1 shows greater deformation. Therefore, it would appear that deformation is more closely linked to the rate of capacity fade rather than the remaining reversible capacity of the cell (or perhaps, it is the deformation that causes an increase in the rate of capacity fade). However, this does not seem to be the case as MJ1-1 only shows visible deformation at 84% capacity, and not before. A comparison of note is that MJ1 cells show less deformation relative to the number of cycles and capacity fade when compared to the M50 results. This may be due to the fact that a lower equivalent C-rate was used in the charge step for MJ1s. After 800 cycles, Sørensen *et al.* [218] found that their MJ1 cells charged at 0.5C (1.75 mA) and discharged at 1C had ca. 50% capacity, demonstrating the negative effect of increasing charge rates. Another explanation could be the lack of the inner tab in the midst of the electrodes, which negates any ohmic heating effects that may have occurred, as suggested by Waldmann *et al.* [22], additionally, the inner Al tab being located at the

centre of the cell may be acting as a quasi-mandrel and suppressing deformation to an extent.

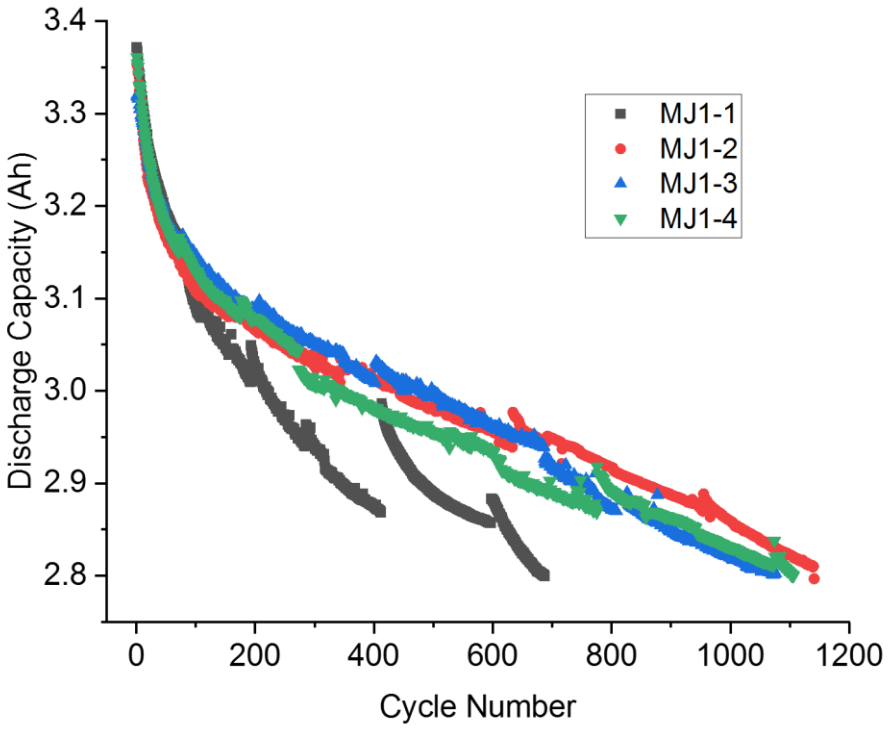

Figure 37: Discharge capacity fade of MJ1-1, MJ1-2, MJ1-3, and MJ1-4, respectively. All cells reached 80% nominal capacity after this many cycles.

4.7 CONCLUSIONS

Cylindrical cells of varying geometry and internal structures were cycled at ambient and non-ambient conditions and imaged using X-ray CT techniques to monitor the state of the jelly rolls within the cells. Buckling of the electrode rolls was observed and virtual unrolling was used to elucidate any correlations in the location of the deformation.

For the M50 cells cycled at ambient conditions, it was observed that the deformations grew in size as the cells underwent more cycles. It was also found that the deformations were initiating at pre-existing inflections in the jelly roll which provided a point of weakness for the propagation of deformation. It is likely that the rate of formation and progression of deformation is partially dependent on the degree of inflection of the pre-existing defect. The outer current collecting tab applies stress to the separator and electrode in the jelly roll, hence less deformation is observed towards the positive end of the cell, where the outer tab is absent.

Alternative cell geometries were investigated: similar to the M50s, the MJ1 cells cycled under ambient conditions also showed deformations in the electrode rolls with increasing number of cycles. When viewing the virtually unrolled figures, it was observed that the changes were happening at points of pre-existing inflections, same as the M50s. These cells also exhibited less deformation towards the positive end of the cell, where the outer current collecting tab was not present. For the MJ1 cells, less deformation is observed, partly due to the inner current-collecting tab being located at the centre of the cell, which is believed to suppress some of the stress causing deformation.

The effect of cycling temperature was studied: the M50 cells cycled at 0 °C demonstrated greater capacity fade compared to the cells cycled at 45 °C. When comparing the capacity fade profiles and the X-ray CT images, an increase in the capacity fade of the cells cycled at 0 °C was observed after the initiation of a deformation in the jelly rolls. The greater the deformation, the greater the observed capacity fade. However, the same trend could not be distinguished in the cells cycled at 45 °C. Similar to the other cells, the cells cycled at non-ambient conditions also exhibit deformations at points of pre-existing defects.

It was hypothesised that cells might show degradation if stored at 80% SOC. In order to test this, five M50 cells were charged to 80% SOC (3 based on their voltage window, and 2 based on the rated capacity of the cells) and stored at ambient conditions and their OCV was monitored. After 20 weeks, the cells showed a comparably similar

reduction in OCV (0.57 – 0.63% decrease). Additionally, any chemical changes due to storage at 80% capacity did not lead to macroscopic morphological changes.

Although potential correlations have been made between the mechanical deformations of the jelly roll and electrochemical performances of the cells, the link is not robust as the general trend in the capacity fade profiles of the cells one a quasi-linear decline that is expected of Li-ion batteries. A stronger correlation would be one where the capacity fade would take a very sharp decline once deformations appear in the jelly roll. There are potential links that may be hard to see given the way in which the data is presented, and potential ways to elucidate such links are explored in the Future Work chapter, section 8.5.

5 MOTION-ENHANCEMENT ASSISTED DIGITAL IMAGE CORRELATION OF LITHIUM-ION BATTERIES DURING LITHIATION

Work in this chapter is also presented in the following paper: "Motion-enhancement assisted digital image correlation of lithium-ion batteries during lithiation", A. Jnawali, A. N. P. Radhakrishnan, M. D. R. Kok, F. Iacoviello, D. J. L. Brett, P. R. Shearing, Journal of Power Sources, Volume 527, Copyright (2022) Elsevier.

5.1 INTRODUCTION

Lithium-ion (Li-ion) cells have many characteristics which make them desirable for use in electric vehicles (EVs), such as high power and energy density, high capacity, and long cycle life. However, in the EV industry, once cells reach 80% of their original capacity, they are generally considered to be at their end-of-life (EOL). Therefore, investigating the mechanisms behind the decrease in capacity of cells due to ageing is imperative in order to maximise cell lifetime and improve cell design.

As spiral wound cells undergo ageing, the electrode coils eventually deform, causing cracks to appear on the electrode surface and loss of contact with the current collector, leading to an irreversible capacity loss [22]. Kok *et al.* [146] have determined that the deformation of the jelly rolls occur at '*pre-existing inflection points*', which are sites of structural weaknesses that arise during the rolling process during manufacturing.

However, the mechanisms behind the deformation have not been clearly elucidated yet.

The intercalation and de-intercalation of lithium ions during cycling causes particle strain in the electrodes due to the associated volume expansions, this corresponds to around 10% and 300% in graphite [219] and silicon [16] anodes, respectively. Even the cathodes undergo volume expansions of around 4.5% for $LiNiCoAlO_2$ (NCA) [220], and 7.2% for $LiNiMnCoO_2$ (NMC) [221]. The stresses related to these volume expansions cause cracking of the electrode particles: for example, Markervich *et al.* [222] identified micro- and nano-scale cracks in graphite crystals using scanning electron microscopy; and Liu *et al.* [223] validated long term capacity loss in their experimental cell caused by cracking of NCA particles using X-ray CT.

It is believed that the lithiation/delithiation mechanism plays a part in the progression of the deformation. In this chapter, an attempt has been made to decouple the effects of (de)lithiation on the eventual deformation of the jelly roll in cylindrical cells by combining a motion enhancement technique with image registration to accentuate the motion during lithiation at the pixel level. One such digital image correlation (DIC) technique for image registration is *'optical flow'*, which indicates the apparent movement of objects in images. It operates by tracking the velocity distribution of brightness, intensity, or patterns in image sequences [224]. The combination of a motion magnification followed by the analysis of the changes in internal cell structure using an optical flow-based image registration is demonstrated in this chapter, for the first time.

5.2 MATERIALS & METHODOLOGY

Five cells of varying geometries and differing internal structures were selected for this study, as seen in Figure 38. The cells selected were at different points in cycling, with varying degrees of structural deformations of the electrodes in order to include a range of electrode behavioural patterns caused by the severity of the deformations. Information on the selected cell models can be viewed in Table 6.

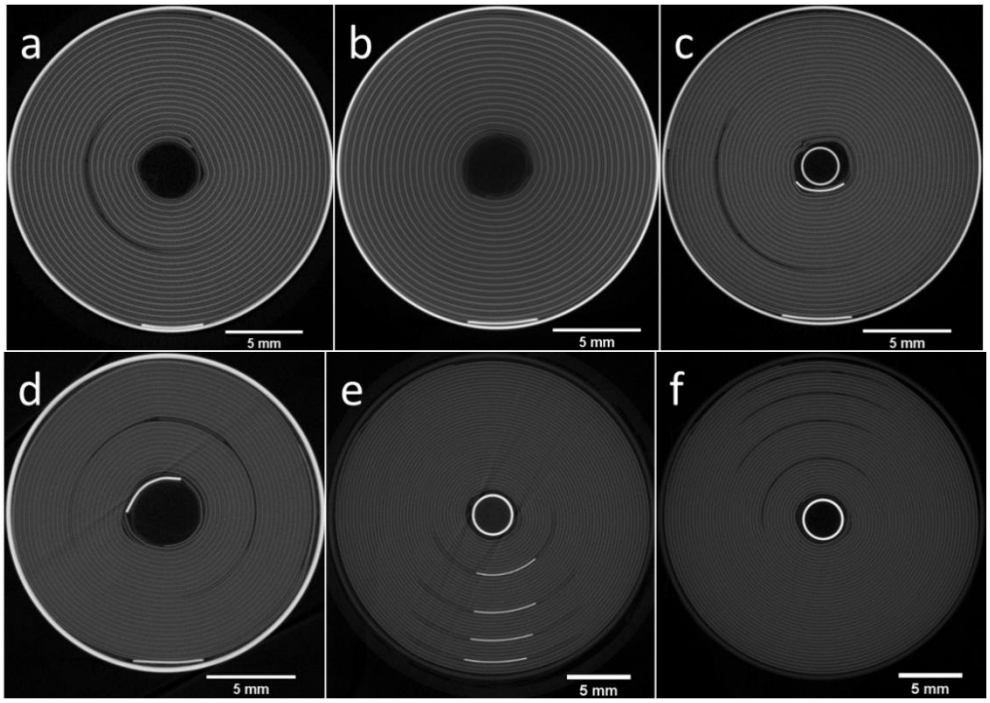

Figure 38: Cross-sectional *(xy)* slices of (a) M50; (b) MJ1; (c) VTC6; (d) HB6; (e-f) negative and positive ends of a lithium ion power cell, respectively.

Table 6: Information on the different cell types used in this study.

MODEL	MANUFACTURER	CHEMISTRY	GEOMETRY	NOMINAL CAPACITY (AH)	VOLTAGE WINDOW (V)	# OF CYCLES

M50	LG Chem.	Si/C / NMC	21700	5	2.5 – 4.2	1145
MJ1	LG Chem.	Si/C / NMC	18650	3.5	2.5 – 4.2	597
VTC6	Sony	C / NMC	18650	3.12	2.5 – 4.2	108
HB6	LG Chem.	C / NMC	18650	1.5	2 – 4.2	150
LITHIUM ION POWER CELL (LPC)	LithiumWerks	C / LFP	26650	2.6	2 – 3.6	163

a) Cell Cycling & X-ray Computed Tomography

The selected cells were discharged to their lower cut-off voltage using discharge steps with increasingly lower C-rates using a Maccor Model 4200 and Bio-Logic SAS BCS-815. The cells were then charged to their upper cut-off voltage in four charge steps using a Gamry potentiostat (Gamry Instruments, Warminster, USA). They were all charged at 1 A, current tapered to 100 mA with a CV step cut-off limit of 45 minutes. The voltage profiles during charging of the cells can be found in the 'Cell Charging Data' chapter in the Appendix. At every charge step, the cell underwent an *in situ* X-ray computed tomography (CT) scan around a region of interest in the cell using a Nikon XT H 225 (Nikon Metrology, Tring, UK) instrument. The aim was to maximise resolution, therefore half-length scans were carried out, instead of full cell scans, and the region of interest was selected to be at the centre of the cell in terms of height and width, thus the scans were truncated (a portion of the positive and negative terminals were not included in the field of view). Therefore, pixel resolutions of 13 – 14 μm were achieved for the 21700 cells, and 13 μm and 16 μm for 18650 and 26650 cells, respectively. Utilising an exposure time of 0.5 s and beam energy and current of 190 – 195 kV and 250 – 260 μA, respectively, approximately 3100 projections were acquired for the 21700s. Similarly, the settings used for the 18650s were 0.5 s, 190 kV, 210 – 220 μA, and the settings for the 26650s were 0.5 s, 190 kV, 200 μA. The

tomograms were then reconstructed using a filtered back projection algorithm (CT Pro 3D, Nikon Metrology).

A single slice from the scans at each charge step were taken from the same z-location (using the ends of the current collecting tabs as reference) in each cell, which formed sequential frames of the lithiation process. Table 7 provides some information on the voltage steps used for the various cells in this study. Automatic alignment of the stack of five slices from the different scans for each cell was carried out using the *"Align Slices"* module on Avizo (Version 9.5, Thermo Fisher Scientific). Due to the internal changes and also changes in the shape of the outer cell casing (as discussed in the *Results* portion of the chapter, section 5.3) during lithiation, the slice registration carried out by the automated process may have caused minor artefacts to be introduced in the subsequent analysis. Proper alignment is crucial, as the cell may shift in the holder slightly in between the charge steps due to user interference, as such the development of an alignment tool more robust than the automatic alignment module is of interest in the future. The contrast between the frames from the different scans were normalised, and the frames turned into a time lapse image sequence using Fiji (a distribution of ImageJ [197]). The resultant time-lapse video was exported from Fiji and are shown in *SI_Video_1[…]* – *SI_Video_5[…]* for the pristine cells and *SI_Video_11[…]* – *SI_Video_15[…]* for the cycled cells in the chapter 'Pristine and Motion Enhanced Videos of the Cells' in the Appendix.

Table 7: Information on the voltage steps used for the *in-situ* scans for the different cells, where V1 and V5 are the lower and upper manufacturer's voltage cut-off limits, respectively.

VOLTAGE STEPS (V)	M50	MJ1	VTC6	HB6	LPC
V1	2.5	2.5	2.5	2.0	2.0
V2	3.3	3.3	3.3	3.3	3.0
V3	3.6	3.6	3.6	3.6	3.2
V4	3.9	3.9	3.9	3.9	3.4
V5	4.2	4.2	4.2	4.2	3.6

b) Phase-based Video Magnification

The first step in the motion enhancement and registration technique (MERt) is to amplify the displacement of the electrodes using an established video magnification process. Video magnification was carried out using the phase-based Eulerian motion processing as detailed in the paper by Wadha *et al.* [225], and as outlined in the Methodology chapter, section 5.3.3. For example, a similar technique has been applied to amplify and track the breathing patterns of infants from low resolution video information; this is the first time that it has been applied to time-lapse X-ray data of batteries. The magnified videos are shown in *SI_Video_6[…]* – *SI_Video_10[…]* for the pristine cells and *SI_Video_16[…]* – *SI_Video_20[…]* for the cycled cells in the Appendix. The MATLAB script for the video magnification was used as published by the authors (Wadha *et al.* [225]), with some changes in the processing variables: the frequency cut-offs, alpha (*a)* and the spatial smoothing factor, sigma (σ). The code was executed on MATLAB (version R2018a). A narrower frequency band ensures a more focused amplification and a lesser amplification of noise, but it also carries with it a risk of overlooking physical phenomenon. This step, therefore, requires rigorous user supervision, where a combination of a range of *a* and σ values needs to be tested.

c) TV-L – based Image Registration (Optical Flow)

Image registration based on optical flow was carried out as outlined in the Methodology chapter, section 3.3.2.2.

d) Virtual Unrolling

The theory behind the virtual unrolling (VU) technique and its interpretation is presented by Kok *et al.*[146], and a description on how it was carried out is outlined in the Methodology chapter, section 3.3.1.

5.3 RESULTS

5.3.1 Motion Enhancement and Registration Technique (MERt)

The Motion enhancement and Registration technique (MERt) is the combination of the individual techniques: video motion enhancement and the optical flow image registration. Video motion magnification is utilised because the optical flow technique on its own is not able to precisely identify minor electrode displacements. The motion enhancement amplifies both the small and large vectors, resulting in more distinct flow fields as well as aiding in the visual presentation of the effects of lithiation, such as shifts in electrodes and casing deformation.

For the figures produced by MERt presented in this work, the arrows represent flow vectors, indicating the direction and intensity (through its size) of the movement of battery materials, and the colour map represents the displacement magnitude, with a brighter, yellow colour representing greater movement and a darker, blue colour representing no movement: the *'dead zone'*. For the analysis of Li-ion batteries using this combined technique, cells with various geometries and internal structures were selected for this study in order to elucidate the effects of the anatomy of the cells, such as the internal current collecting tabs and pre-existing points of inflection on the jelly roll, on the shift of the electrodes during lithiation. It was previously determined by Kok *et al.* [146] that all cylindrical cells contain, to varying degrees, an inflection point

in the jelly roll (as an artefact of the manufacturing process) that provides a point of weakness for the propagation of deformation.

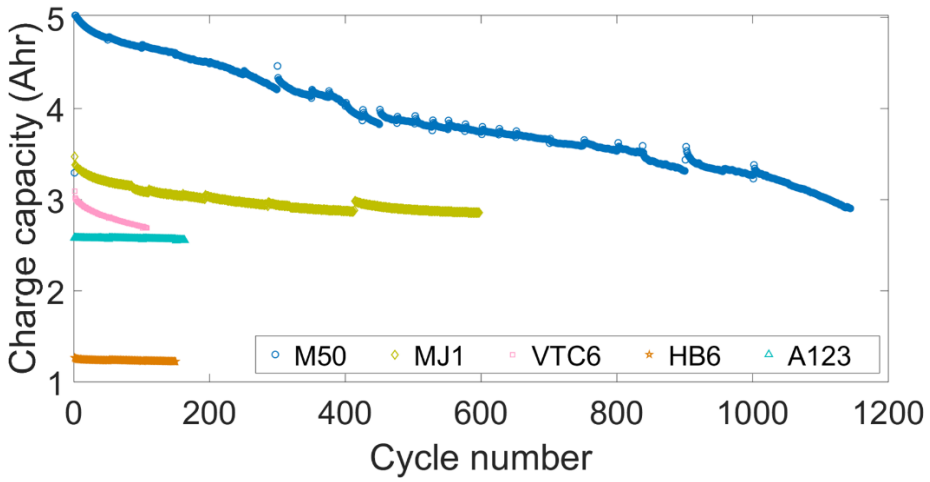

Figure 39: Charge capacities of the five cells used in this study.

The capacity fade profiles of the five cells used in this study can be found in Figure 39. It is seen that for the individually varying periods of cycling life shown in this figure, M50, MJ1, and VTC6 exhibit a greater rate of capacity fade compared to the HB6 and LPC cells. It is also observed that those very cells (M50, MJ1, and VTC6) showed to varying degrees, deformations in their jelly rolls, as opposed to the HB6 and LPC cells which showed virtually no deformations as shown in the reference images in Figure 40–Figure 44. MERt is carried out on the pristine cells, henceforth denoted by *P,* preceded by the cell model. Figure 40 shows the flow fields of the pristine M50 and MJ1 cells. The flow fields are generated by comparing the frames of the video as a pair, with the first frame as the reference frame. The flow fields for the voltage step V_2 is created by using the frame at V_1 as reference, and V_3 vs. V_1, and so on. When looking at the evolution of the flow fields for M50-*P* in Figure 40b-e, it is informative to orient the image relative to compass points, where initially there is a flow of movement from east to west. As seen from Figure 40a there is empty space on the west side of the M50-*P* where the cathode electrode roll ends, providing space for the expansion of the electrodes. There is also movement of material towards the hollow core of the cell around the location where failure is predicted to occur by virtual unrolling as discussed

below. On the west side, the electrode expands outwards, towards the cell casing. Then, from V_2, the dead zone towards the north-west starts to exert pressure inwards. At V_3 the pattern remains the same, but the movement becomes more concentrated towards the inflection point. By the end (V_4), the flow pattern on the west also changes to an inwards flow. Throughout the whole lithiation process, there is greater pressure exerted on the inflection point than elsewhere, clearly elucidating one of the causes of the deformations as a result of cell cycling.

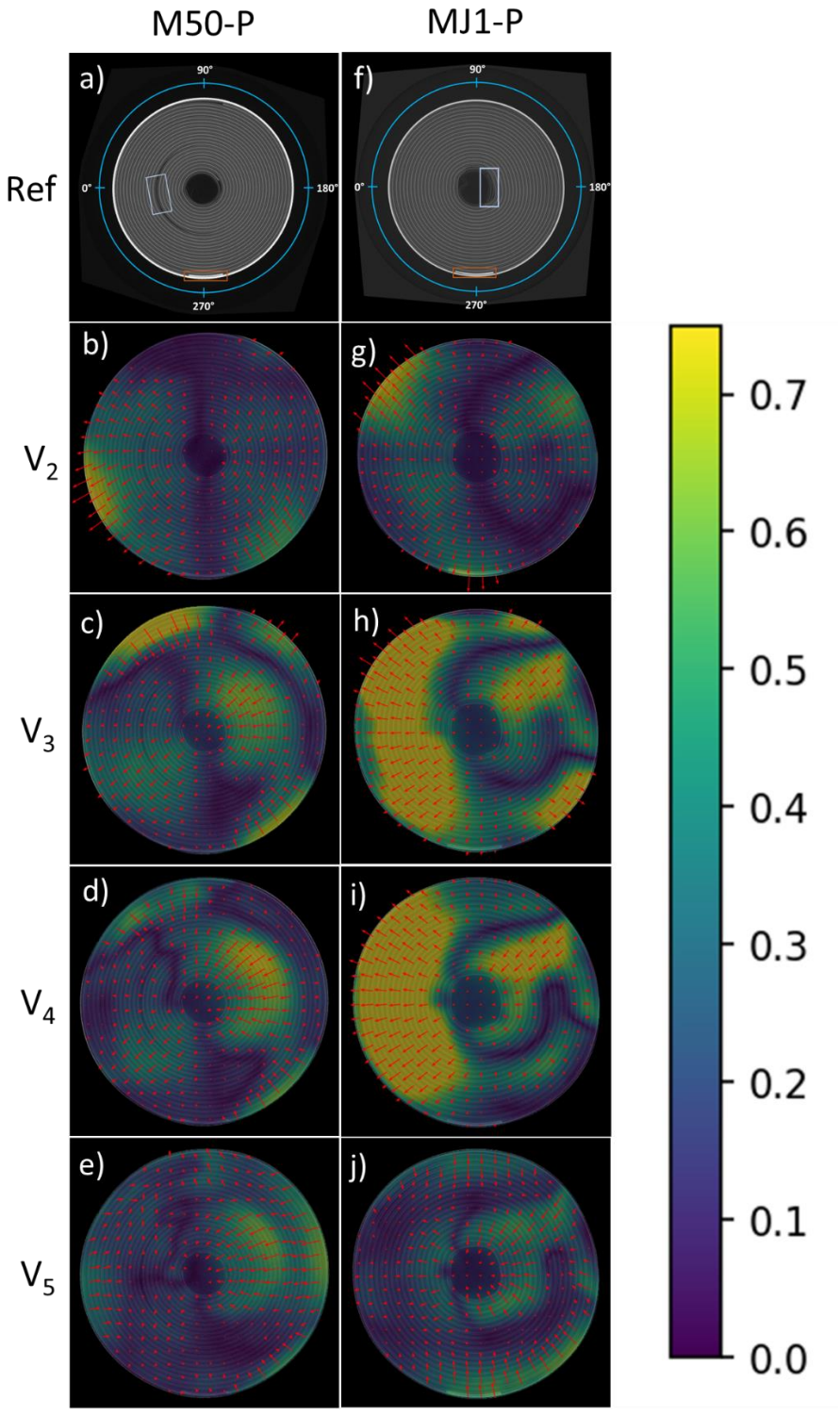

Figure 40: MERt of the pristine cells, (a-e) M50-P, (f-j) MJ1-P. A light-blue box is used to highlight the positive current collecting tabs, and a bronze box is used to highlight the negative current collecting tabs in the reference images.

Similar to the M50-*P*, the MJ1-*P* also demonstrates the exertion of pressure at the inflection point, however, it also shows a greater outwards movement on the left hand side. One possible reason for this could be that the MJ1 lacks an inner current collecting tab in the middle of the jelly roll, which the M50 has (as highlighted by the pale box in Figure 40a). The welded inner tab in the middle of M50 jelly roll may be acting as a barrier, decreasing the outwards displacement.

Part of the reason for the change in direction around the edge of the cell as the voltage increases could be that the electrodes expand in any direction where there is space as they are lithiated, but once they encounter the barrier that is the cell casing, they are forced to start expanding inwards, towards the hollow core. Another reason is that the cell casing seems to be contorting as lithiation occurs, which the MERt identifies. This may be caused by the pressure exerted by the uneven expansion of the electrode material inside the casing. The contortion of the cell casing of both M50-*P* and MJ1-*P* is more clearly visible in the enhanced videos provided in the Appendix.

MERt is conducted on aged cells of the same model as the pristine batch, henceforth denoted by *C*, preceded by the cell model. Figure 41b-e shows the flow fields of M50-*C*, a cell which had previously gone through 1144 cycles. This cell contains two deformations at the central core at opposing sides of the cell (Figure 41a). Unlike the M50-*P*, the flow sections are more evenly divided in M50-*C*. Initially there is more dead space in the centre, with outwards expansion, which then evolves into a partition of inwards compression segregated by a warped ring of dead zone from the outwards expansion zone. This pattern continues until V_5, where the movement in the outer expansion zone generally subsides and the movement at the centre of the cell continues to concentrate. Interestingly, the central flow fields are concentrated between the two deformations, more than at the deformations themselves.

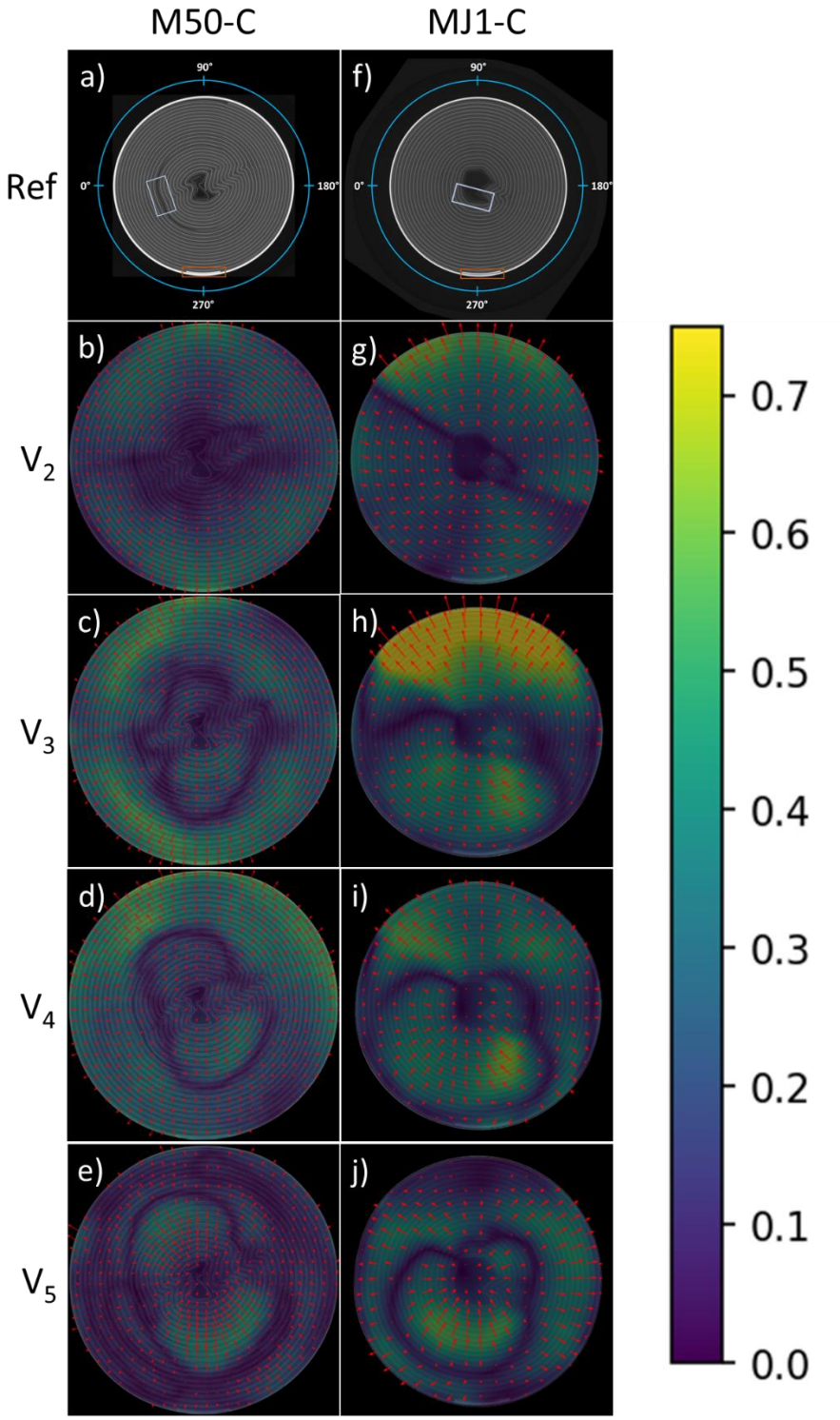

Figure 41: MERt of the cycled cells, (a-e) M50-C, (f-j) MJ1-C. A light-blue box is used to highlight positive current collecting tabs, and a bronze box is used to highlight negative current collecting tabs in the reference images.

The MJ1-*C*, which had undergone 597 cycles, also shows two different flow fields partitioned by a diagonal line of dead zone as seen in Figure 41g-j. The outwards movement observed at the top of the cell and around the edges is due to the deformation of the cell casing. At V_4, the formation of a concentrated ring of movement towards the centre of the cell separated by a ring of dead zone can be observed. The cell contains one electrode deformation, and once again, it can be seen that the movement is concentrated adjacent to the deformation, more than directly at the deformation. This suggests that initially, the nucleation point of the deformation and the concentration of electrode movement occurs at the inflection point, and as deformation reaches a critical point, the nucleation point shifts, contributing to the widening and expansion of the deformation.

The behaviour exhibited by the cell casing might have an impact on the movement of the electrodes as well: as one side of the casing compresses, limiting expansion of electrode in that direction, another side would expand, providing space for expansion. It is unclear as to the exact cause of the casing deformation, but from the magnified videos, it would seem the MJ1 is more prone this behaviour than the M50. It would be of interest to determine whether the casing deformation always takes a consistent pattern or whether it varies per cycle to more clearly determine whether it would have an effect on electrode movement, hence deformation. Willenberg *et al.* [20] were able to prove a change in the cell casing diameter of an 18650 Li-ion cell of around 10 μm using strain gauges. Furthermore, they also showed that the diameter change was non-linear during charge and discharge, which indicates that the casing might be deforming unevenly. This behaviour might also be the build-up of gases and not just the expansion/displacement of electrodes.

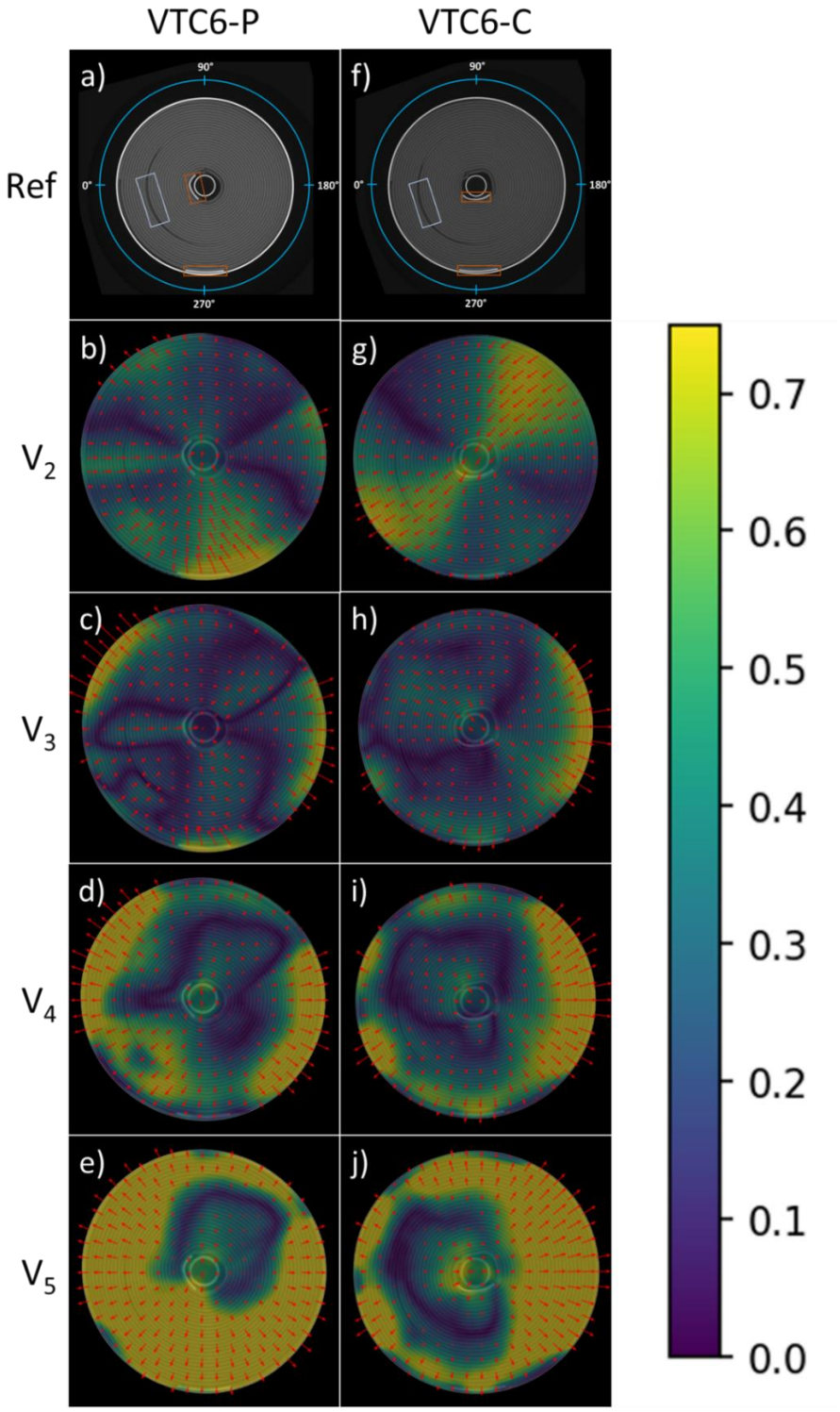

Figure 42: MERt of the pristine and cycled VTC6 cells, (a-e) VTC6-P, (f-j) VTC6-C. A light-blue box is used to highlight positive current collecting tabs, and a bronze box is used to highlight negative current collecting tabs in the reference image.

The VTC6 cell contains a mandrel as can be seen in Figure 42. This is believed to suppress the deformation of electrodes by acting as a support and limiting the space available for the deformation to occur [22]. It also contains two negative current collecting tabs, one at the edge of the cell casing and one at the centre of the cell. Initially, during charge, the pristine cell shows a flow of electrode movement from the south to the centre of the cell, and slight outward movements towards the east and north-west. Around V_4, this dynamic changes to show a greater shift of electrode towards the cell casing in all directions and also a less concentrated movement of electrode in the inner core towards the mandrel. This inner movement is occurring at a visible, pre-existing inflection point in the jelly roll as observed next to the inner negative tab in Figure 42a. This behaviour gets exacerbated as the voltage increases to V_5. Another feature in the flow field of the pristine VTC6 cell is that, in the initial few stages, there is pressure exerted by the electrodes directly towards the inner negative current collecting tab. As previously mentioned, the tab is welded and cannot move, so it is very likely that it is suppressing some of the pressure that might have resulted in jelly roll deformation. The first obvious thing that can be noticed when looking at the cycled VTC6 cell in Figure 42g-j, is that the location of the inner negative current collecting tab is different to the pristine cell. This has resulted in the formation of the deformation in a different location to the inflection observed in the pristine cell, and a difference in the movement of the electrodes. It can also be observed, that as the inflection point is located further from the inner negative tab, the pressure exerted by the electrodes reaches a higher intensity. This change also seems to have led to an initial flow field similar to that observed in MJ1-*C*. It can be seen that initially the electrodes flow in one direction, however, after reaching 3.6 V, the inwards movement of electrodes is concentrated at the deformation, and an outwards expansion surrounds the zone of inwards compression. This behaviour continues for the duration of the charge cycle, increasing in intensity. The intensity of the outwards expansion is lower towards the south and west, perhaps due to the influence of the positive and inner negative tabs.

The HB6 cells also contain two negative tabs and one positive tab, but no mandrel at the centre. Also, the location of the tabs are different to the VTC6 cells. The flow

fields of the pristine HB6 cell in Figure 43b-e shows a generally one directional flow of electrode materials. Initially, the electrodes seem to be experiencing both tensile and compressive forces from east to west around the inner negative tab, with minimal forces in the direction of the tab itself. Similarly, the outer negative tab doesn't experience much force. As the voltage increases, the expansive forces seem to be greater, and they continue to increase, now applying forces on the negative tabs as the electrodes expand towards the empty spaces between the electrode roll and the cell casing. The cycled HB6 cell in Figure 43g-j shows a similar one directional trend, however, the compressive and expansive forces are moving from west to east. One reason for this could be the large difference in the location of the inner negative and positive tabs between the pristine and cycled cells. The dead zones between the two cells are roughly mirrored, and once again, the expansive forces seem to increase as the voltage increases.

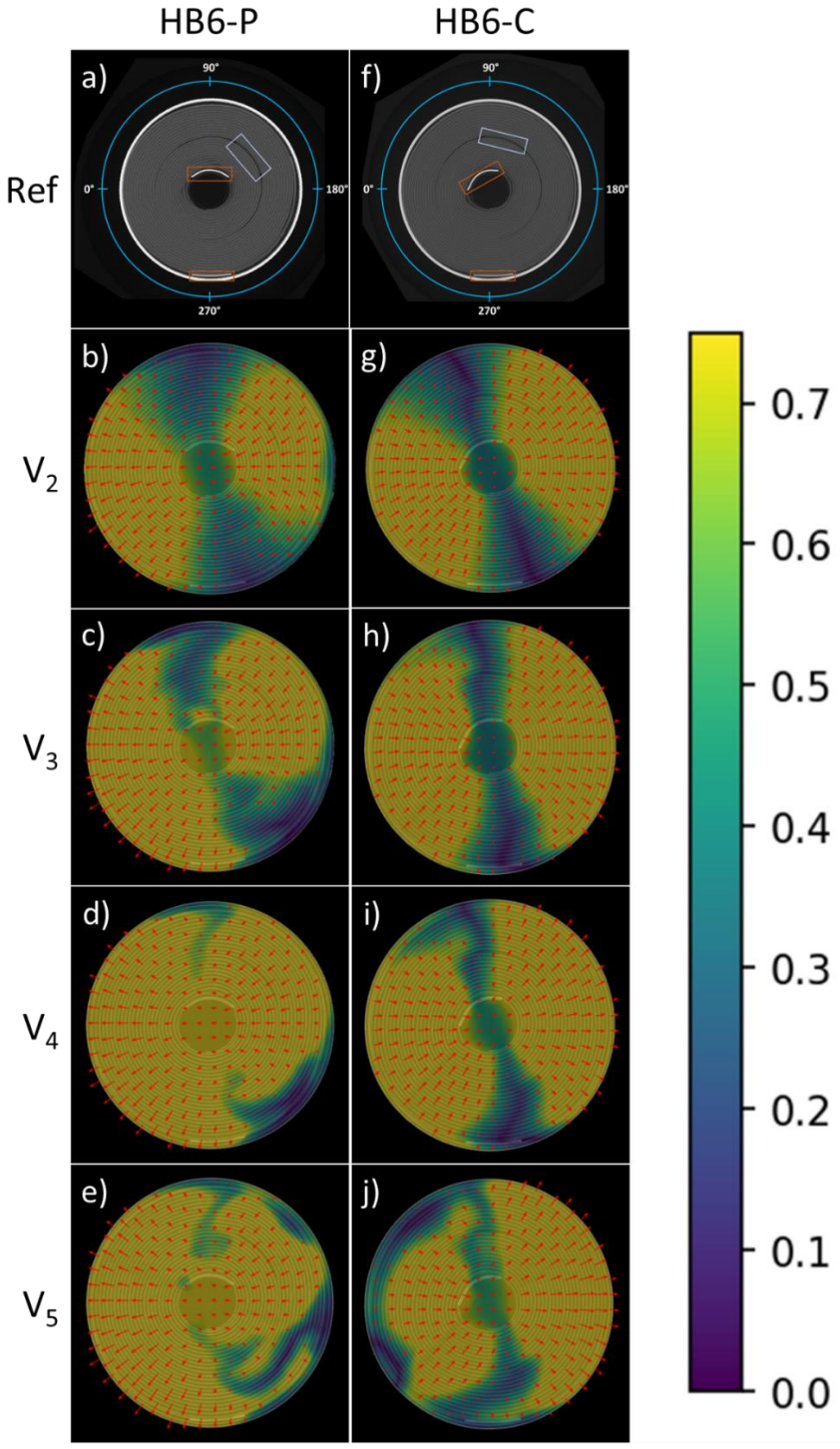

Figure 43: MERt of the pristine and cycled HB6 cells, (a-e) HB6-P, (f-j) HB6-C. A light-blue box is used to highlight the positive current collecting tabs, and a bronze box is used to highlight the negative current collecting tabs in the reference images.

Although the LPC cells contain positive and negative current collecting tabs at either ends of the tabs, they do not extend to the region of interest at the centre of the cell. The electrode displacement is expected to be different at different heights, partly due to the change in internal structure of the cell, and as such there is likely to be a vertical strain gradient. The investigation of the strain gradient along the z-axis may be of interest in future works. The only feature, or obstacle, present throughout the cell is the Mandrel. The LPC cell provides a glimpse into how a cell might behave during lithiation if it didn't contain any physical barriers amongst the jelly roll, such as current collecting tabs. Figure 44 shows the flow fields for the pristine and cycled LPC cell, which contains a mandrel and current collecting tabs at the positive and negative ends of the cell, but no tabs in the mid-section of the cell. It can be seen that without physical barriers in place, the electrodes simply shift in one direction. It is hard to say whether this is beneficial for the cycle life of the cell, however, after 163 cycles, the LPC cell has not shown any visible deformations, and as seen in Figure 39, its rate of capacity fade is low. The crystalline lattice volume change in LFP cathodes is around 6.5% [226], suggesting that LFP experiences less strain during (de)lithiation, and they generally show improved cycle life compared to NMC cells, which might explain the lack of deformations.

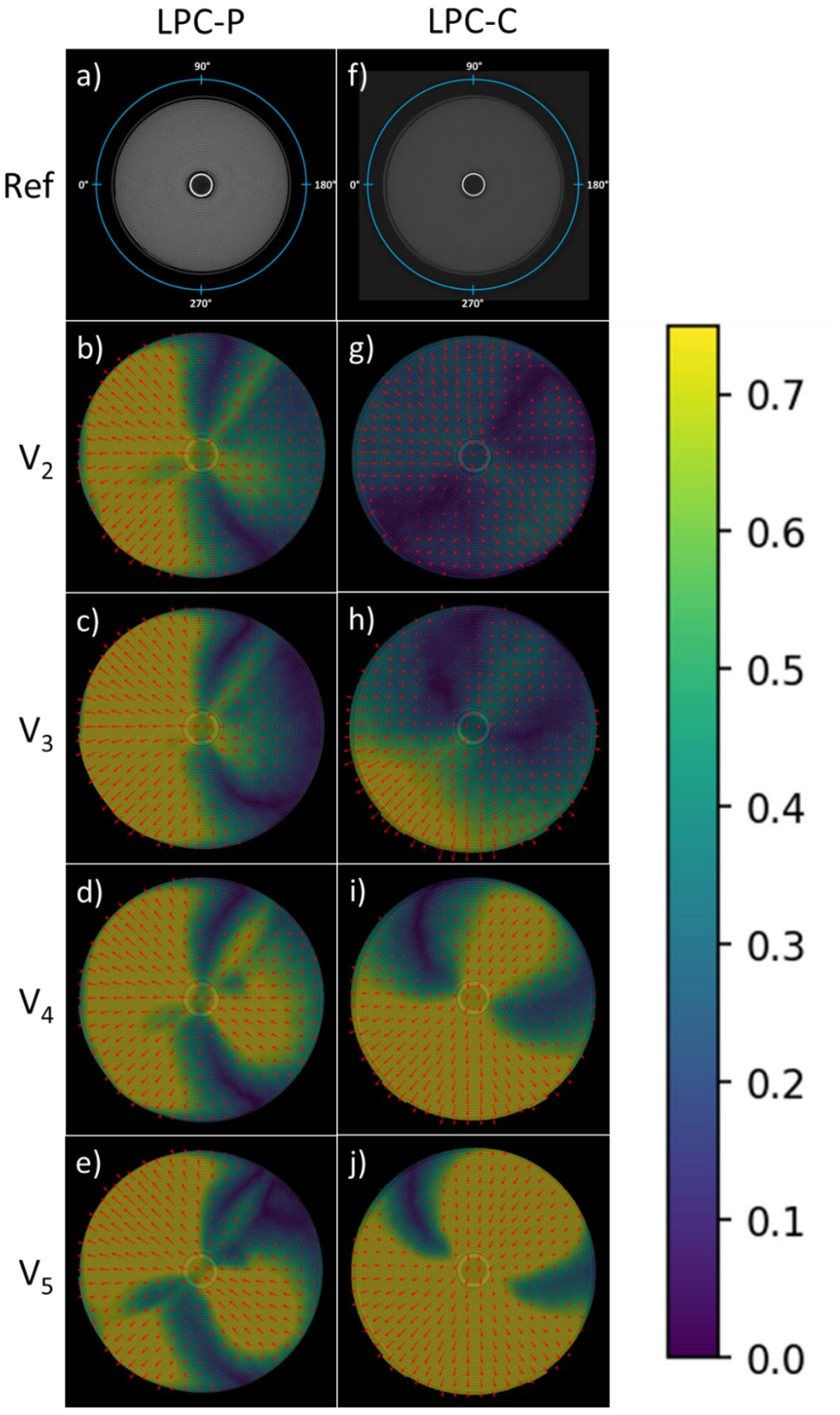

Figure 44: MERt of the pristine and cycled LPC cells, (a-e) LPC-P, (f-j) LPC-C.

5.3.2 Virtual Unrolling

Virtual unrolling was carried out on the X-ray data of the pristine and cycled cells used in this study. The orientation of the unrolling figures is the same as the orientation shown in the reference images shown in Figure 40–Figure 44 and one can use the angular co-ordinates provided in the reference images to locate features in the unrolling figure. The unrolled figures can be seen in Figure 45. In the unrolling figures for the pristine cells, pre-existing inflections in the jelly roll can be seen. These appear as crimps or curves of varying size along the electrode layers. When comparing the location of the flow fields overlaid on the frames of the motion enhanced videos of the pristine cells generated by MERt in Figure 40–Figure 44 to their counterparts in the unrolled figures in the Figure 45, it can be seen that the inwards forces are occurring at and around such pre-existing inflections as predicted by Kok *et al.* [146]. For example, it can be seen that VTC6-*P* contains two shallow inflections around 120° and 330°, and from Figure 42c-d it can be seen that compressive forces are acting around those locations. Another observation is that some of the inflections and compressive forces are located where the electrode roll ends at the inner core. Whereas other parts of the electrode roll are semi-secured in place due to the tight packing of the electrode rolls, the positive electrode end is relatively unsecured. This is also demonstrated by the shift in the electrode in the inner core in some of the enhanced videos, implying that the electrodes are *'unwinding'* from the inside. Thus, it is the location at which the least amount of force would be required to *'buckle'* the electrodes.

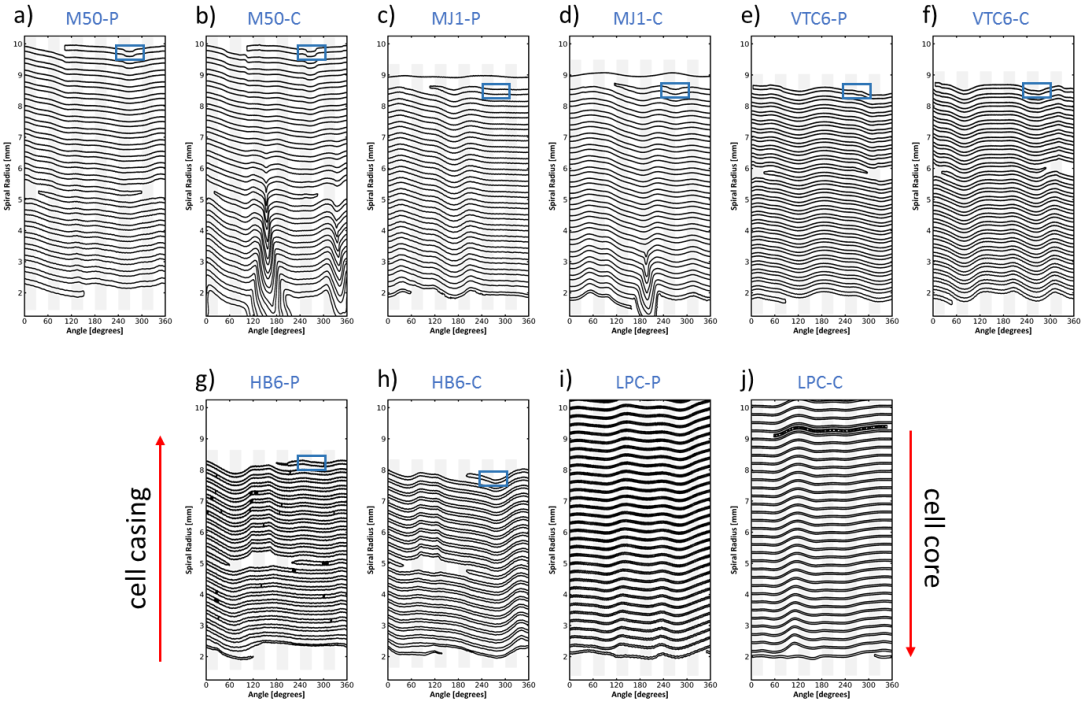

Figure 45: Virtually unrolled electrodes of (a-b) M50-P and M50-C, (c-d) MJ1-P and MJ1-C, (e-f) VTC6-P and VTC6-C, (g-h) HB6-P and HB6-C, and (i-j) LPC-P and LPC-C, respectively. The blue box indicates the location of the outer current collecting tab, if present.

As discussed previously, for cycled cells where visible deformations exist, the compressive forces act at those locations and around them. For the cycled cells that do not contain any visible deformations, virtual unrolling shows that they still contain inflections in their jelly roll that cannot be easily identified. The VTC6-*C* contains inflections at two points in the jelly roll, one around 90° and one around 270°. It can be seen from Figure 42g-j that whereas a compressive force acts at and around 90° first, a compressive force develops around 270° from V_4 onwards with a smaller magnitude. Unlike the other cells, the unrolling figure for HB6-*C* shows an upwards inflection at around 360°, as opposed to a downwards inflection. The compressive force is acting around that location, however, there is nothing in the unrolling figure to indicate the reason for such a defined split between the compressive force and the expansive force. The LPC-*C* cell shows a similar behaviour of a split between a

compressive force around the inflection at 120° and an expansive force at the opposite direction that cannot be explained by the unrolling figure.

It can be seen from the unrolling figures, that in some cases, there are inflection points located at 270°, in line with where the tab is located (if present), however it is not the case for all cells. Similarly, the inner, positive current collecting tab is identified by a disconnect in the electrode layer in the unrolling figure, and in a similar fashion, it does not always correlate to an inflection point along the angular coordinate at which the tab is located. Therefore, the exact influence of the current collecting tabs on the jelly roll is difficult to identify.

All cells contain variances, as clearly shown by the differences in the VTC6 cells and the HB6 cells in Figure 42 & Figure 43, respectively. These differences arise during the manufacturing process and lead to slight differences in the physical locations of cell internal features, such as current collecting tabs. This in turn leads to the differences in inflection points in the jelly roll and in the nucleation points of electrode shifts and deformations, which accounts for some of the variances seen in the flow fields produced by MERt of these cells. Furthermore, the observed change in the physical shape of the cells during a charge cycle due to the expansion of the cell housing and the application of an automated alignment tool causes minor artefacts in the videos, accounting for potential artefacts in the flow fields.

5.4 CONCLUSIONS

A combination of a video motion enhancement technique to magnify the motion of electrodes during the lithiation process and an image registration technique based on optical flow has been used in the analysis of batteries for the first time. The motion enhancement and registration technique, MERt, was carried out on five cell types by obtaining X-ray data at various steps in the charge cycle and converting slices from each dataset into videos. It was clearly observed that the shift of electrodes caused by the lithiation process towards the cell core is occurring at pre-existing inflection points

in the jelly roll, as revealed by virtual unrolling. Virtual unrolling also revealed that location of the inflection in the jelly roll might be influenced by the location at which the electrode roll ends at the center of the cell. For cycled cells already containing large electrode deformations, the shift was concentrated around the deformations, which is believed to contribute to the expansion of the deformations. It was also seen that the cells without large deformations showed a greater expansion of electrodes towards the outer casing, indicating that once the electrode buckles, it provides a point of weakness where the compressive forces can concentrate.

Differences in the location of internal structures such as the location of the current collecting tabs was observed between cells of the same model and batch. This difference seems to have caused differences in the flow fields between the cells, however, there isn't enough information to elucidate the exact effect of the differing internal structures.

An attempt to briefly, and systematically categorise the behaviour of the cells and their cause as observed through video enhancement and optical field flows has been made, as shown in Table 8.

Table 8: Observed changes in the cells in this study.

BATTERY	FEATURE	EFFECT
M50	Positive tab	Suppresses some outward flow of electrodes.
	Negative tab	Provides space for electrode expansion along edges.
	Positive electrode end	Where deformation initiates and the focal point of compressive electrode flow.
	Deformation	Causes increased stress alongside the point of deformation.
MJ1	Negative tab	Provides space for electrode expansion along edges.
	Positive electrode end	Where deformation initiates and the focal point of compressive electrode flow.
	Deformation	Causes increased stress alongside the point of deformation.
VTC6	Positive tab	No observable effect.
	Inner negative tab	Suppresses some inward flow of electrodes.
	Outer negative tab	Provides space for electrode expansion along edges.
	Positive electrode end	The focal point of compressive electrode flow.
	Mandrel	Suppresses some inward flow of electrodes.
HB6	Positive tab	No observable effect.
	Inner negative tab	Suppresses some inward flow of electrodes, along with the outer negative tab, forms a line of dead zone for most of the charge cycle.
	Outer negative tab	Suppresses some outward flow of electrodes, and provides space for electrode expansion along edges.
	Positive electrode end	The focal point of compressive electrode flow for the pristine cell, not for the cycled cell.
LPC	Positive electrode end	Some compressive electrode flow for the pristine cell, but not the focal point, and the focal point of compressive electrode flow for the cycled cell.
	Mandrel	Suppresses some inward flow of electrodes, and might be creating dead zones at points in the cell by dividing the inward and outward flow.

From the observed trends in Table 8, it could be concluded that the biggest driving factor for the eventual deformation of the cells is the location of the positive electrode end at the centre of the cell. In the case of the pristine HB6 cell (HB6-*P*) not following that trend: it contains a significant inflection point at where the focal point of the inwards compressive force is located. Hence it might be argued that deformation occurs in the first instance at a point of significant pre-existing inflection point (which in a lot of cases is located beside the positive electrode end). If lacking an inflection point, deformation occurs at the positive electrode end. In the case of the LPC cell, there may be factors affecting its behaviour from beyond the region of interest, such as the numerous current collecting tabs.

Lithium-ion batteries are currently the most promising energy conversion devices for utilisation in electric vehicles, however, there are still challenges in fully understanding the mechanisms that drive degradation and in optimising cell design. This chapter presents a combined approach to investigate one of the mechanisms behind cell degradation – cell deformation and electrode cracking/delamination caused by the expansion and contraction of electrodes during (de)lithiation. Utilising a method to enhance the electrode displacement that occurs during cell charging with an image registration process to create a motion enhancement and registration technique, displacement *'hotbeds'* in pristine cells were identified and correlated with observed deformations in cycled cells (if present) and also information was provided on the influence of the cell internal design on electrode displacement.

It is believed this technique, MERt, can be used in instances such as mapping the macro electrode displacement in prototype cells to inform cell design an minimise cell deformations in the long run. Another use for the technique might be to minimise the need for costly and time consuming techniques in order to achieve high resolutions for low sensitivity post-processing techniques, as this could enhance *'motion'* to make such techniques more applicable. It was not possible to test a wide array of cells, nor a large number of cells in this study, however, manufacturers would have the capacity to test a large number of cells to obtain a more statistically robust displacement map of a cell model. For the cell design and manufacturing side of the industry, the

important message would be that there is some evidence to support that current collecting tabs and mandrels seem to suppress strain leading to mechanical deformation of jelly rolls. As such, it might be prudent to increase the number of tabs and implement a mandrel. The exact number of tabs and orientation would have to be further investigated through empirical means and modelling. Another aspect to consider would be the more uniform current and heat distribution as a result of the increased number of tabs, potentially leading to longer life. The inclusion of a mandrel may not be as important of the tabs carry out a similar function to a satisfactory level (would have to be tested through comparisons between bespoke cells containing multiple tabs, and minimal tabs and a mandrel) at a lower cost, both in terms of mass and money. The increasing material cost and lower energy densities are the disadvantages, and cell engineers would be required to balance between cycle life and economic considerations. Additionally, due to the signs of casing deformations in this chapter, it may be a consideration to increase the thickness of the cell housings. This would greatly impact the energy densities of the cells, however, the change in cell diameter would have to be accounted for in pack designs so the end result may be similar in terms of volumetric densities – cost of increasing cell casing thickness would be the main concern.

6 EXAMINING THE EFFECTS OF SILICON-BASED ADDITIVES ON THE LONG-TERM CYCLING CAPABILITIES OF CYLINDRICAL CELLS

6.1 INTRODUCTION

Since the commercialisation of small lithium–manganese oxide ($Li//MnO_2$) cells inside of calculators in 1973 by Sanyo [227], there has been much interest and research efforts poured into lithium batteries to achieve higher power and energy output. Lithium-ion cells have undergone improvements in every regard, such as the doping of cathode materials leading to the commercialisation of $Li(Ni_xMn_yCo_z)O_2$ (NMC), with increased energy density and stability [228]. Similarly, anodes have also undergone change in order to get past the detrimental effects of dendritic formation in lithium metal electrodes. One of the most successful anode material is graphite, however, it has a relatively low specific capacity of 372 mAh g^{-1} [32], making it unsuitable to meet the increasing demands of electric vehicles. Out of that insufficiency, silicon (Si) has gained traction as an alternative anode material with a theoretical specific capacity of ca. 3600 mAh g^{-1} [229]. However, due to the large volume expansion experienced by Si during Li^+ ion intercalation of up to 300% [16], Si/graphite composite electrodes are more widely used commercially.

Inconsistent particle size distribution in an electrode can lead to uneven strain and uneven current distribution during operation, ultimately resulting in particle cracking and delamination. Even in small percentages, the presence of Si (or Si-based components, for example SiO_x) can be detrimental to the cycle life of a battery.

Researchers have used various techniques to study the morphology and microstructural evolution of Si-based electrodes and cells, such as the use of X-ray photoelectron spectroscopy (XPS), atomic force microscopy (AFM) & other microscopy techniques to investigate SEI formation and evolution [132,230], X-ray diffraction (XRD) & XRD computed tomography (XRD-CT) to investigate charge transfer mechanisms during lithiation, and physical displacement sensors to measure pressure and volume changes in full cells [220]. X-ray imaging techniques have also been widely used to investigate strain evolution in Si–graphite electrodes, as discussed in the Literature Review chapter, section 2.2.2.

Cylindrical Li-ion cells with NMC//Si–graphite chemistry have become popular due to their high volumetric energy density, the mechanical strength of the steel casing compared to the low strength casing of pouch cells, and cost [216]. Though there have been various studies into the effect of Si on electrochemical performance and the morphological evolution of the electrode particles, there hasn't been large scale study on commercially relevant cells. Presented in this chapter is a long term study of two types of cells with 18650 geometry where both types of cells are similar in many ways, including an NMC positive electrode, two internal current collecting tabs, and tapered electrode ends. However, one cell type (MJ1) has a Si-based component mixed in the anode, and the other (MH1) does not. With a sample size of 30 or more of each cell, analyses on their electrochemical performance, large scale physical changes and micro-scale changes in the electrodes using X-ray CT and *'virtual unrolling'* were conducted. Note that whilst the exact composition of the MJ1 commercial anode remains unknown, the short-hand Si/graphite composite is used throughout, although it is recognised that this is likely a SiO_x additive.

6.2 MATERIALS & METHODOLOGY

6.2.1 Battery Cycling and X-ray CT Acquisition

Cycling was carried out on 32 MJ1 (INR18650, 3.5 Ah, LG Chem, Seoul, South Korea) cells and 30 MH1 (INR18650, 3.2 Ah, LG Chem, Seoul, South Korea) cells. The MJ1s were charged at 1.5 A constant current (CC) to 4.2 V, following which the current was tapered to 100 mA at constant voltage (CV), following the 'high drain' protocol specified in the manufacturer's specification sheet. After 10 minutes of rest, they were then discharged to 2.5 V at 4 A CC, with a 20 minutes rest at the end of discharge. The MJ1 cells were cycled for 1200 cycles – the point at which the majority of the cells ranged 80 ±5% nominal capacity.

The MH1s were cycled to 4.2 V at 1C (3.2 A) CC, tapering current to 100 mA, and discharged to 2.5 V at 5 A CC. Rest periods of 10 minutes after charging and 20 minutes after discharging were used. Similarly to the MJ1 cells, the MH1s were cycled until most of the cells reached 80% of their nominal capacity, although this represents a spread of cycle numbers. The MH1 cells were cycled using a comparatively higher C-rate protocol but were maintained within the manufacturer's recommended limits. All cells were cycled using a Maccor battery cycler in an environmental chamber set to 25 °C. All cells were scanned using a Nikon XT H 225 (Nikon Metrology, Tring, UK) X-ray machine in their pristine state (as shipped from supplier at their nominal voltage of approximately 3.6 V) and after cycling. The pristine MJ1s were scanned using a beam energy of 220 kV, a current of 159 uA, and an exposure time of 267 ms, resulting in a pixel size of about 35 μm and 2025 projections. The cycled MJ1s were scanned at 190 kV, 210 μA, and 500 ms, to achieve a pixel size of 36 μm and 2027 projections. Both the pristine and cycled MH1s were scanned at 190 kV, 220 μA and 500 ms, achieving a voxel size of approximately 36 μm and 2027 projections. The acquired images were then reconstructed into TIFF image stacks using a filtered back projection algorithm (CT Pro 3D, Nikon Metrology).

Internal region of interest (ROI) X-ray CT was carried out on a MJ1 and MH1 cell for higher resolution acquisition of internal features. The Zeiss Xradia 620 Versa (Carl ZEISS XRM, California, USA) X-ray machine was used for the high resolution scans. The MJ1 cell was scanned using beam parameters of 150 kV, 133 μA, and 12 s exposure time, resulting in a voxel size of ca. 1 μm. The MH1 cell was scanned using 150 kV, 133 μA, and 28 s exposure time, resulting in ca. 2 μm voxel size.

6.2.2 Virtual Unrolling

Virtual unrolling on the cells was conducted as outlined in the Methodology chapter, section 3.3.2, which also describes its interpretation.

6.3 RESULTS & DISCUSSION

Thirty two MJ1 and thirty MH1 cells were investigated in this study. The cells are the same in geometry and in internal structure: 18650 cells with spirally wound electrodes, and one of each positive and negative current collecting tabs. They both also contain tapered electrode ends, and the same cathode chemistry: NMC-811 [216]. Where they differ is in the anode chemistry: where the MJ1 contains a Si–graphite anode, the MH1 does not contain any Si. For ease, the MJ1 cells have been denoted 101-132, and the MH1 cells have been denoted 01-30. The capacity profiles of the MJ1 cells can be seen in Figure 46 and the same for the MH1 cells can be viewed in Figure 47. The sudden changes in capacity of the MJ1 cells between 800 – 1100 cycles are due to a pause in the cycling due to errors in the cycling machine. The cells were cycled under different protocols, both of which were within the maximum C-rate allowed by the data sheet. The MJ1 cells were cycled for 1200 cycles according to the manufacturer's 'high-drain' protocol (1.5 A charge, 4 A discharge); at the end of the 1200 cycles carried out on the MJ1 cells, the final charge capacities ranged from ca. 69 – 81% compared to their nominal capacity, with all but three cells above 78%. The MH1s were expected to be more mechanically stable than the MJ1s, therefore, they were cycled at a higher charge

and discharge rate compared to the MJ1s but within a protocol that adhered to the acceptable boundaries from the manufacturer's cell data sheet. The MH1s were cycled at 3.2 A charge and 5 A discharge until the majority of the cells reached 80% nominal capacity or lower; the exact termination criteria varied and the final capacities ranged between ca. 75 – 84% of the nominal capacities, with 23 cells within the 80 – 81% region. This slightly more aggressive-duty cycle led to an accelerated capacity fade in the MH1 cells and the number of cycles vary between 180 – 443 cycles. The reason for the rapid capacity fade of the MH1 cell is most likely to be the higher charge rate used. Accelerated cycling rates have an adverse effect on the capacity retention of Li-ion cells [77,231], and since the MH1s were charged at more than double the C-rate of the MJ1s and were also discharged at a slightly faster rate, the rate of capacity fade observed is perhaps not unexpected. Tables of the SOH can be found in the 'SOH and Deformation Summaries' chapter in the Appendix.

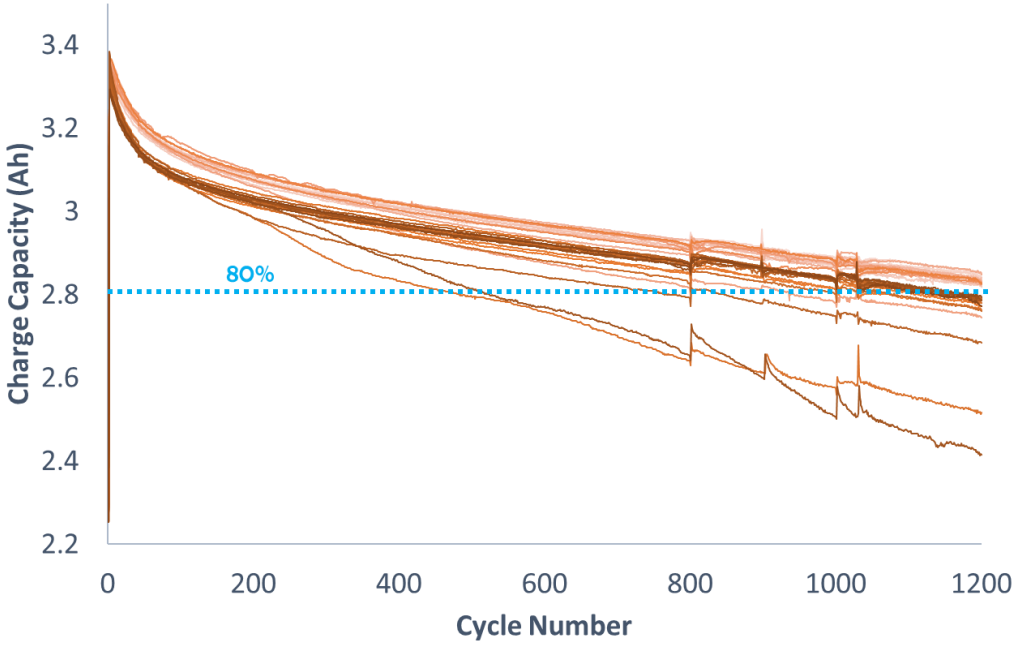

Figure 46: Charge capacity profiles of the 32 MJ1 cells.

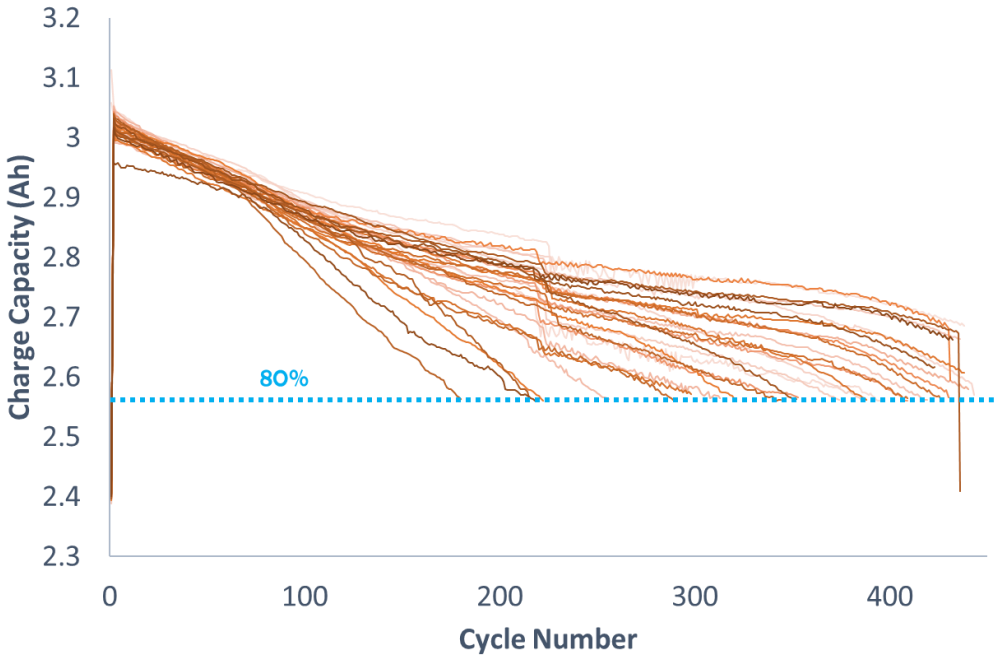

Figure 47: Charge capacity profiles of the 30 MH1 cells.

Prolonged electrochemical cycling results in the mechanical deformation of the jelly rolls within cylindrical cells [22,232]. As mentioned above, the MH1s were cycled at an accelerated rate, and in spite of their accelerated capacity fade, no significant changes to the MH1 cell architecture was observed. Consequently, the capacity loss is unlikely to be associated with morphology evolution of the electrode or cell architecture change.

By contrast, the effect of Si additives in the electrode becomes clear when you look at the mechanical changes within the cells. Figure 48 shows the X-ray CT slices of MH1-30 and MJ1-109, which are of similar SOH – 79.7% and 81%, respectively. Figure 48a shows the region of interest (ROI) micro-X-ray CT slice of MH1-30 after 432 cycles at accelerated rates, and Figure 48b shows the same for MJ1-109 after 1200 cycles. Comparing the two, it can be seen that the MH1 cell has no acutely visible deformations in its jelly roll, whereas the build-up of stress associated with the expansion and contraction of the electrodes during intercalation over 100s of cycles has resulted in a deformation of the MJ1 jelly roll, affecting several of the inner layers

of both the cathode and anode. The increased volume expansion caused by the presence of Si in the anode of the MJ1 cells is the likely cause of the cell architecture collapse. As a result of the deformation, delamination of the cathode and anode can be observed in Figure 48b, as highlighted by the red arrows. This would likely have resulted in the separation of the active material from the current collector foil, potentially leading to isolation and a loss of capacity. However, it appears that the electrode has not entirely separated from the current collector, and has maintained connection through the electrode material, therefore the capacity is not expected to have substantially dropped. However, the current pathways would have changed, as the electrons would have to travel through more of the electrode material to reach the current collector (as shown by the dashed yellow arrows in Figure 48b); at this stage of battery life, the consequences would likely have been manifested by power fade, however, if allowed to continue cycling, the inevitable delamination of electrode material would have driven accelerated capacity loss.

Although the MH1 doesn't show any visible deformations, it does not mean that the jelly has not undergone any change. From Figure 48a, it can be seen that there is a swelling of the anode (highlighted in red) which is applying pressure on the cathode layer towards the centre of the cell, revealing for the first time, the nucleation of jelly roll deformation in cylindrical cells. This makes it clear that in the first instance, jelly roll deformations are a direct result of anode swelling through the accumulation of irreversible anode expansion from the Li^+ ion (de)intercalation cycles.

Since the MJ1 cells contain Si, and since Si experiences a greater volume expansion during Li^+ intercalation, it is now clear why more deformations might be observed in those cells compared to the MH1s. Whilst in this study, Si has not impacted the capacity fade of MJ1s significantly compared to the MH1s, it may come into effect relatively suddenly with more cycling, when the delaminated portions of the electrodes lose all contact with the current collector as a result of further deformation, which could in turn lead to a *'knee point'*; inflection in the capacity fade curve. Additionally, Figure 48c-d show the X-ray CT slices of MH1-30 where the outer current collecting tab is visible. It is clear that after cycling, the current collecting tab has experienced

enough outwards expansive forces (as illustrated by the blue arrow) due to the (de)intercalation mechanism such that the tab becomes curved. However, that it is not enough stress to result in deformations. When looking at the X-ray CT slices of the pristine and cycled MJ1-109 in Figure 48e-f, it can be seen that although it contains the same number of electrode windings as the MH1, it does not contain as much space between the current collecting tab and the jelly roll, and the current collecting tab in MJ1-109 is already pressed against the cell casing even in its pristine state. Although the presence of Si plays a large role in the architectural changes, it is unlikely to be the sole cause for the deformations observed in the MJ1 cells. From these observations, it can also be concluded that during a cycle by cycle basis, when the electrodes expand, the jelly roll first fills in the available spaces between the casing and the jelly roll, and perhaps once that spacing is insufficient to accommodate the changes in the electrodes over a long period of time, it results in the buckling of the electrodes.

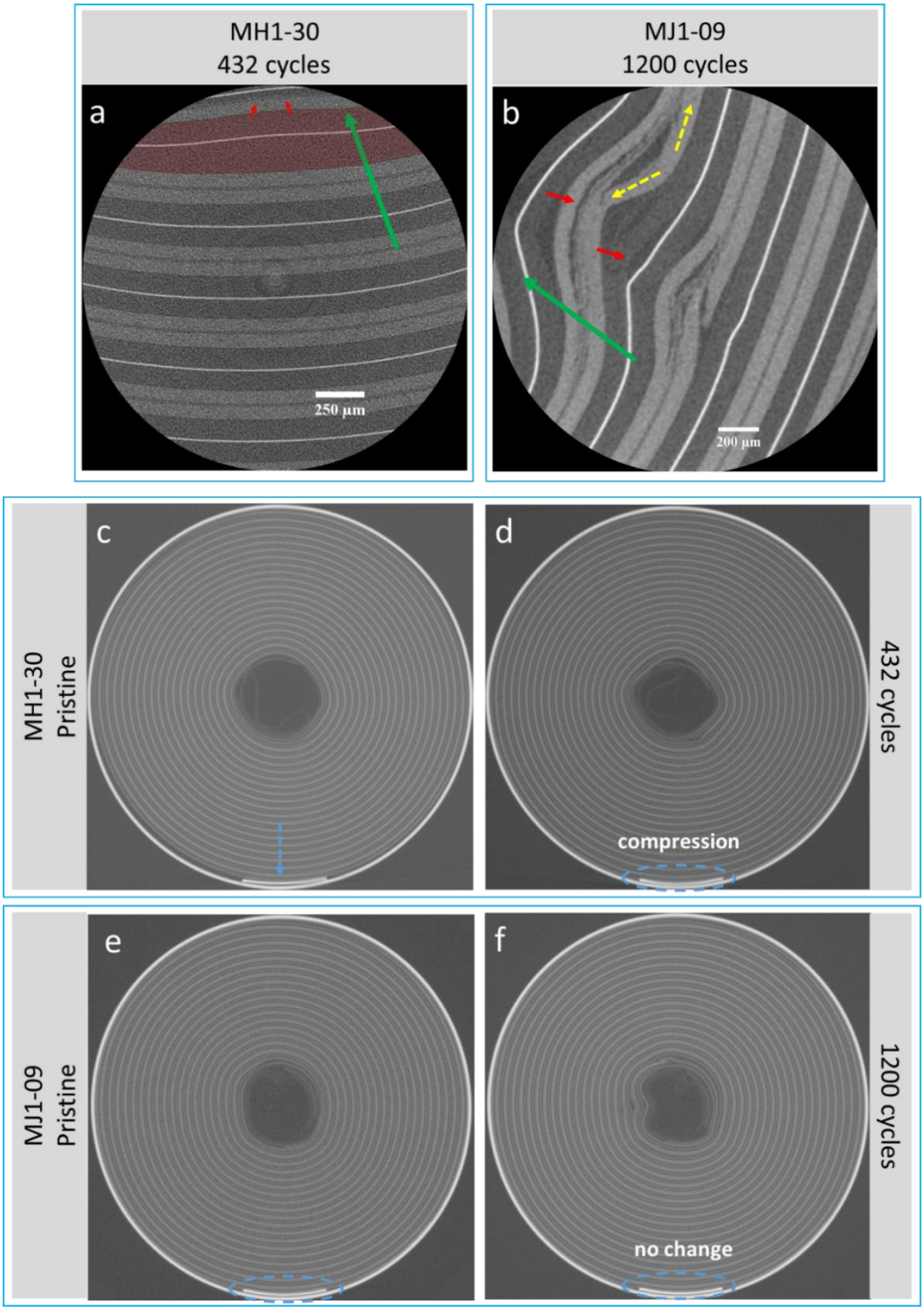

Figure 48: X-ray CT slices of a) cycled MH1 cell, b) cycled MJ1 cell, c-d) comparison of a pristine and cycled MH1 cell, respectively, e-f) comparison of a pristine and cycled MJ1 cell, respectively. The green arrows indicate the direction of the cell centre. Both types of cell are 18 mm in diameter.

When looking at all the cells in this study as a whole, the detrimental effect of Si on the architecture of the jelly roll becomes clearer. Table A 3 in the Appendix shows the number of deformations (a visible displacement or crimping of one or more electrode layers) observed in the two different cell types. It can be seen that the vast majority of MH1 cells (28 of the 30) do not contain any deformations in the jelly roll, whereas in the case of the MJ1 cells, there are only 3 cells without deformations. Furthermore, the majority of MJ1 cells (23 out of the 32) contain multiple deformations (up to three). One of the cells with three deformations (MJ1-126) can be observed in Figure 49. It shows the locations of the deformations in the cell with respect to the z-location, indicated on Figure 49a. The cell contains two very obvious deformations and a smaller deformation (as seen in Figure 49c) that is harder to observe; upon closer inspection, it can be seen that there is indeed a small *'crimping'* of the electrodes. Thus, for the purposes of clarity, it should be noted that not only the major electrode collapses are considered, but also the smaller scale crimping of the electrodes, and the noticeable separation, or delamination, of the electrode winding (as illustrated in Figure A 3 in the Appendix) as deformations. The differences in the number, severity and location of deformations between the cells in the same batch may also be cause by cell to cell variations. It would be difficult to find, demonstrate and quantify variations in the microstructure and chemical compositions of the electrodes, but one way to more easily quantify cell to cell variation is by initial capacities. Zilberman & Jossen [233] found initial capacity variance of 0.2% in the 24 MJ1 cells they studied, however, the 32 MJ1 cells in this study had a variance of 3.35%.

Also in the Appendix, Table A 1 and Table A 2 contain the number of deformations observed in each of the MH1 and MJ1 cells, respectively. Though the MH1s show little to no deformation, there is however a rearrangement of the jelly roll that is not distinct to visual inspection. The virtual unrolling of MJ1-109 and MH1-30 in Figure 50 shows the electrode displacement as a function of cycling. The black lines represent the jelly roll in the pristine state, and the blue lines represent the state of the jelly roll after cycling. It can be seen that the electrode displacement in the MJ1 is concentrated in the layers towards the centre of the cell, primarily at the location of the deformation, however, the MH1 exhibits a cell wide shift (as highlighted by the arrows in Figure

50b) with the outer electrode layers shifting towards the casing, as observed before. Figure A 4 in the Appendix contains more unrolling figures from a sample of MH1 and MJ1 cells, showing similar results.

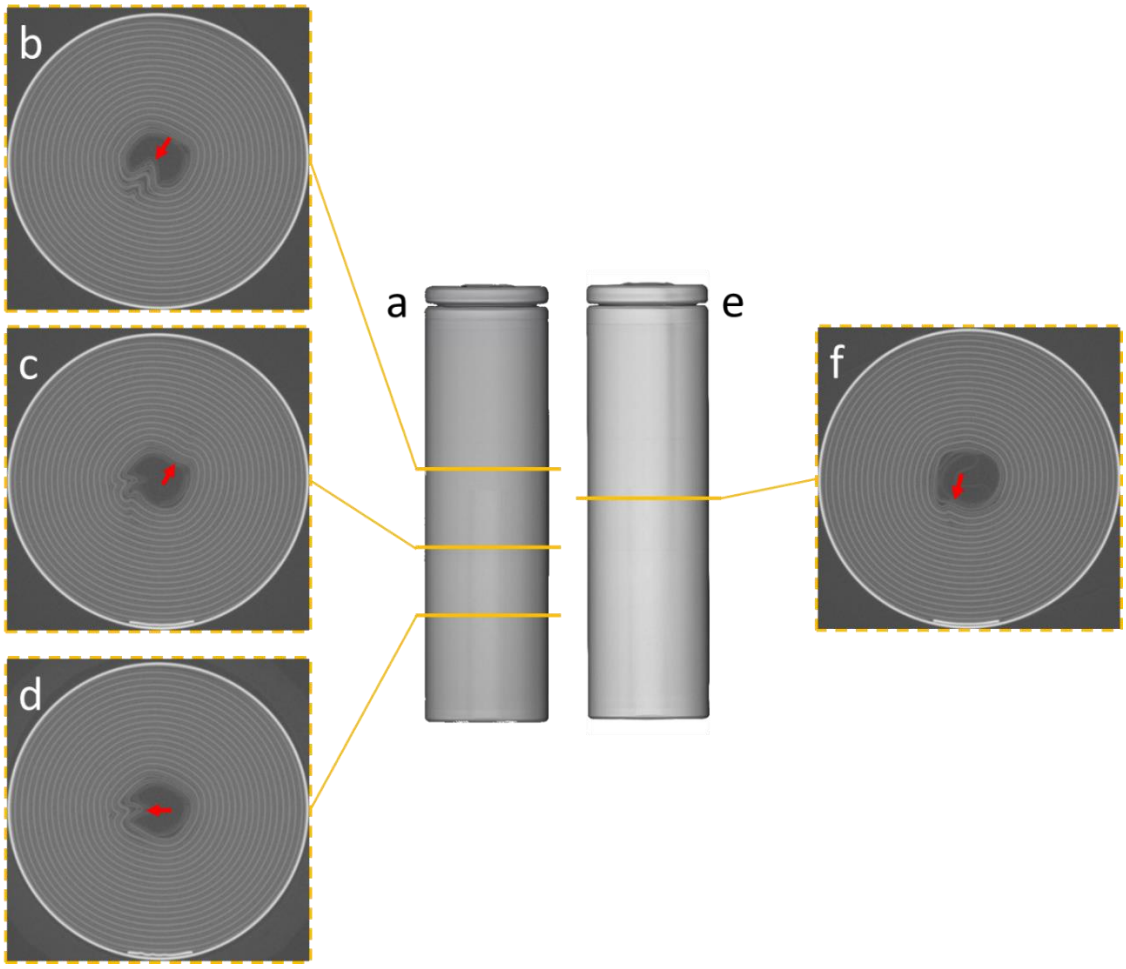

Figure 49: a) Volume rendering of MJ1-126, (b-d) X-ray CT slices showing three deformations, as indicated by the red arrows, e) volume rendering of MH1-04, f) an X-ray CT slice showing a small deformation resulting from long term cycling, as indicated by the red arrow.

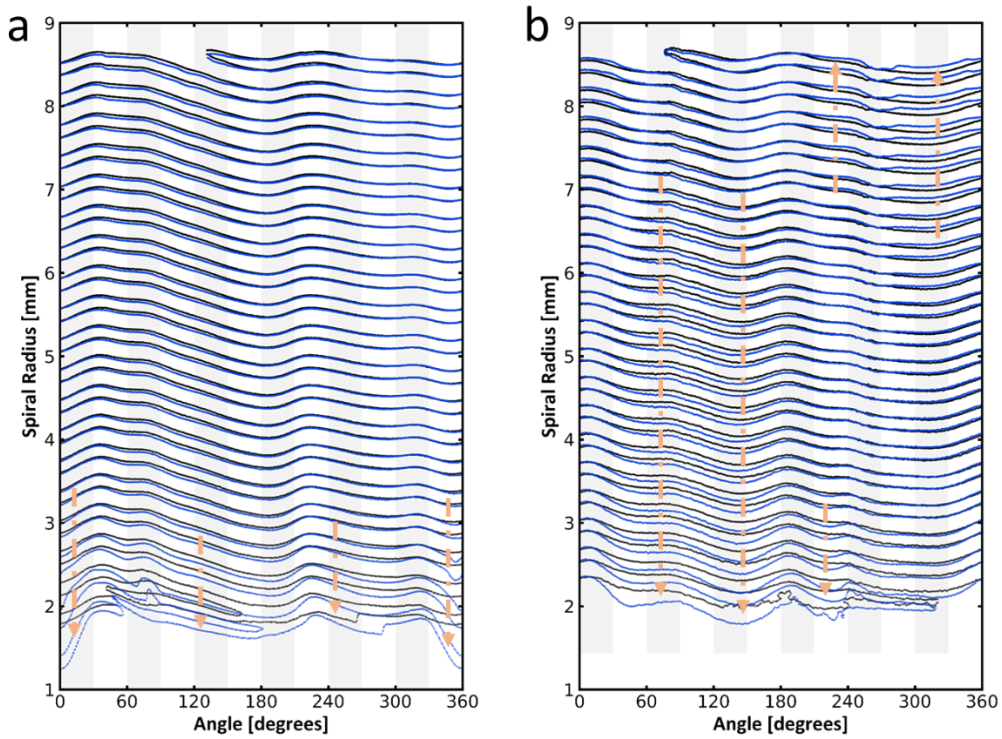

Figure 50: Virtual unrolling of a) MJ1-109 and, b) MH1-32 showing the change in the electrode position before (black lines) and after (blue lines) cycling. The arrows highlight the displacement of the electrode.

Anodes experience volume expansion as Li^+ ions intercalate into the layers of the electrode. Although this is partially reversible, over time, the irreversible changes accumulate, leading to a permanent change in the volume of the electrode layers. The change in the thickness of the anode layers in the MJ1 and MH1 cells can be seen in Figure 51a and Figure 51b, respectively. It can be seen that in the MJ1 cells, the anode layers closest to the centre of the cell have increased in thickness by up to ca. 18 µm after 1200 cycles. The increase in anode thickness observed in the MJ1 cells is similar to the nucleation of deformation, which also initiates at the centremost layers and proliferates through the outer layers. Hence, it is possible that there is greater electrochemical activity at the centremost layers, resulting in greater (de)intercalation activities, and a greater accumulation of irreversible changes, leading to particle fractures, electrode collapse, and greater volume changes. The increased activity at the centre may be due to the positive current collecting tab located there, which would

cause a non-uniform current distribution around it. On the other hand, it can be seen from Figure 51b that the anode layers in the MH1 experience significantly less increase in thickness, with a maximum of ca. 4 µm. This clearly demonstrates the greater reversibility of graphite, and the detrimental impact of Si on the morphology of the jelly roll. Both types of cell experience a decrease in the thickness of the anode layer closest to the cell casing, which is due to the expansive forces of the entire jelly roll windings compressing the outermost layer against the casing. However, given that the pixel resolution of the X-ray scans used to obtain this data was 35 µm, a degree of error is expected.

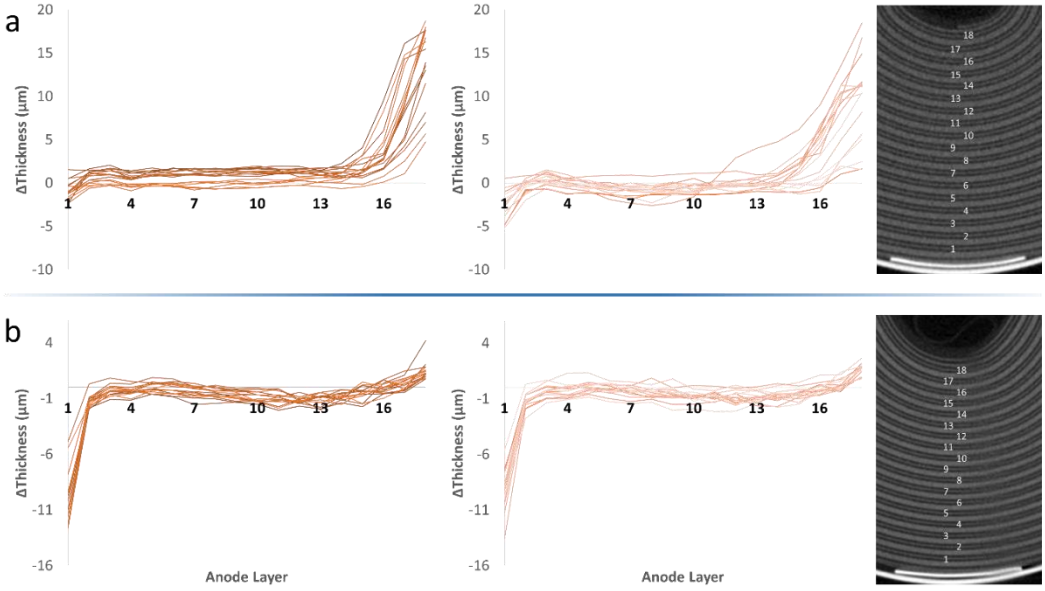

Figure 51: Change in thickness of each anode layer in a) MJ1 cells, and b) MH1 cells.

An attempt to illustrate the trend between SOH and the change in thickness of the anode layer closest to the centre of the cell (layer 18 as demonstrated in the slice containing numbered anode layers in Figure 51a) against the number of deformations observed for all the MJ1 cells can be found in Figure 52. The colours of the plot markers represent the number of deformations observed according to Table A 2, where: green is for 0 deformations; cream is for 1; orange is for 2; and dark red is for 3. It doesn't appear that there is a strong correlation between the SOH and the change in anode thickness, with respect to the number of deformations further proving that

just the appearance of deformation is insufficient to cause significant drops in capacity retention. There are expected to be small variations in the formulation of the electrodes between the cells during the manufacturing process, and one possibility for the lack of a strong trend might just be the random cracking of Si particles, forming points of weaknesses at various locations, at which the deformations subsequently nucleate.

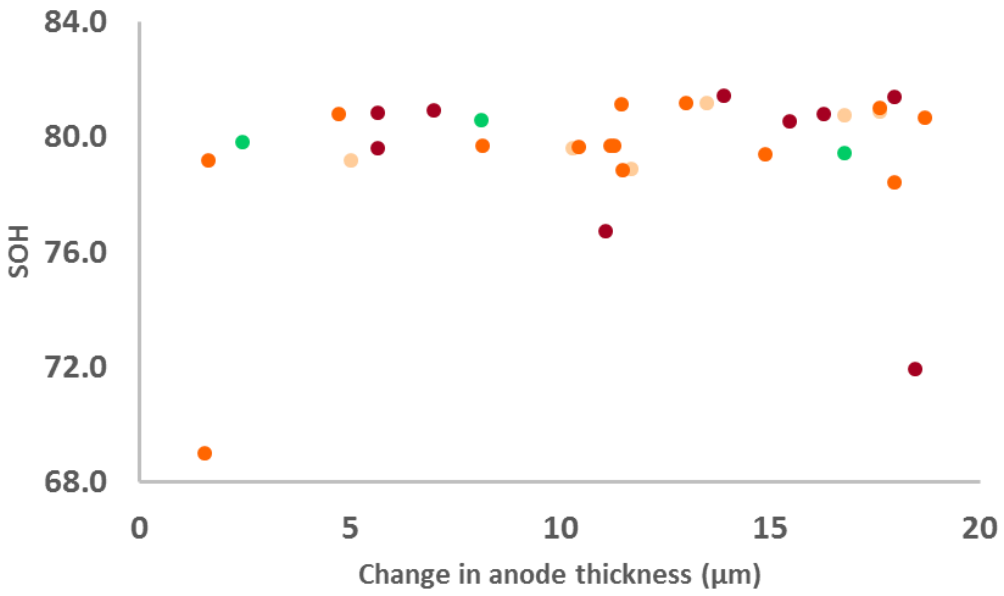

Figure 52: SOH vs. thickness change in the innermost anode layer of all the MJ1 cells. The plot markers correspond to the number of deformations observed in the cell: green for 0; cream for 1; orange for 2; and dark red for 3.

From the image and electrochemical analyses of a large batch of these commercial cells containing Si-based additives (MJ1s) and cells without Si additives (MH1s) it seems very likely that the two different modes of cell degradation have been observed in the two types of cells resulting in varying degrees of jelly roll deformation and capacity fade. The much greater capacity fade observed in the MH1 cells is unlikely to result solely from being cycled at a higher rate than the MJ1 cells. The MH1s showed very low levels of deformation of the jelly roll, therefore microstructural evolution of the electrodes is unlikely to be lifetime critical, hence, other chemical processes, such as parasitic side reactions, greater SEI formation, or inventory loss may dictate failure.

The presence of Si additives in the MJ1s causes high degree of mechanical deformation, possibly leading to power fade, and inevitable capacity loss from total electrode delamination, however, they were able to be cycled to approximately 1200 cycles before falling below the 80% SOH mark. Therefore, for the purposes of utilisation in EVs the MJ1s seem more suitable with the greater energy density that they provide. A more aggressive cycling protocol may accelerate the failure of the MJ1s, thus operation parameters for Si containing batteries require careful selection.

6.4 CONCLUSIONS

In this chapter, a large scale analysis of two types of commercially relevant cells that are similar in all regards (except that one contains Si in the anode, and the other doesn't) was carried out. The 32 MJ1 cells, which contain Si show large – and sometimes numerous – deformations of the jelly roll in all but 3 of the cells, and also show delamination of the electrodes in some cases. The nucleation of a jelly roll deformation was revealed, for the first time, to be caused by the swelling of the anode layers towards the centre of the cell. Therefore, the mechanical changes in the jelly rolls from long-term cycling is attributed to the presence of Si which experience a larger volume expansion during intercalation of Li^+ ions.

By contrast, of the 30 MH1 cells (which do not contain Si), only two of the cells show small deformations in the jelly roll; this indicates that increasing Si content is a major driving force for jelly roll collapse. The MH1 cells underwent an accelerated capacity fade, perhaps associated with the higher C-rate during cycling, although this appears to have had little impact on the jelly roll architecture. Furthermore, the addition of Si has also led to an irreversible change in anode thickness of up to ca. 18 μm in the MJ1 cells, compared to the maximum of around 4 μm in the MH1 cells due to the more limited expansion and contraction behaviour in the graphite anode.

Whilst the deformations in the MJ1s have led to the delamination of the electrodes, it has not resulted in the complete loss of current pathways to the current collecting foils.

The impact of the deformations caused by the presence of Si might come into play with further cycling as further deformations might lead to the loss of contact with the current collector in full. However, as such an occurrence has not occurred in the MJ1 cells cycled down to ca. 80% capacity, it should have little to no impact on their utilisation in electric vehicles. With the increasing demands on EVs for higher power and energy for them to take over the market as the sole choice as a transportation device, the inclusion of additives that increase battery capacity is paramount. It would be of interest to investigate the limit of Si additives in carbon anodes before it has a significant impact on long term performance, as it appears that existing commercial cells have not reached that limit, so there is room for improvement in cell capacities to meet the increasing demands on EVs.

7 INVESTIGATING THE DEFORMATION MECHANISMS IN NI-RICH 21700 CELLS

7.1 INTRODUCTION

In the face of current environmental challenges, the proliferation of electric vehicles is essential to drive changes towards net zero. The state-of-health (SOH) of a battery determines its usability in electric vehicles. In the automotive industry, once a cell reaches 80% of its initial capacity, it is generally considered to be at its end-of-life (EOL) [1], [2]. Therefore, maximising the output of a cell before it reaches EOL is critical in driving down associated costs and improving performance of electric vehicles. However, the driving forces behind battery performance loss, via cell degradation, need to be better understood. Gaining an understanding of the factors that drive cells towards EOL in lithium-ion (Li-ion) batteries is therefore critically important.

The conditions in which the cells are cycled can accelerate degradation by inducing chemical changes within the batteries. Batteries for automotive applications are expected to be able to operate at very low temperatures, however, cycling at temperatures below 0 °C can cause lithium plating on the negative electrode [234] and reduction of electrolyte by the lithium causing a decrease in ionic conductivity [77]. On the other hand, cycling at elevated temperatures leads to an increase in the growth of the solid-electrolyte interphase (SEI) layer [235], leading to an increase in the resistance of the cells [69]. Reduction in capacity is also caused by the irreversible charge consumption [236] from the increasing growth in SEI. These effects also pose a safety risk as lithium plating can lead to internal shorts, resulting in thermal runaway.

Mechanical degradation occurs in numerous forms, and can also lead to deterioration of capacity. During cycling, the intercalation and de-intercalation of Li^+ ions can cause volume changes of up to 10% in graphite [219] and 300% in silicon [16] anodes. Li-ion cathodes also experience volume changes of up to 5% by $Li[Ni_{1-a-b}Co_aAl_b]O_2$ ($0.05 < a < 0.15$ & $0.02 < b < 0.10$) (NCA) [220] and ca. 2% by $LiNi_{0.8}Mn_{0.1}Co_{0.1}O_2$ (NMC) [221,237]. The stresses associated with these volume expansions can cause electrode cracking and particle fracture. Markervich *et al.* [222] utilised SEM combined with Raman spectroscopy to demonstrate the damage to graphite crystals due to mechanical stresses from lithium insertion at the micro- and nano-scale. Liu *et al.* [223] identified cracking in NCA granules using X-ray CT and determined that this caused the observed long term capacity loss, they also observed that the electrodes with the best lifetime displayed less cracking. Particle cracking leads to loss of capacity through various mechanisms. Cracked particles expose more active material surfaces to the electrolyte, leading to formation of inorganic materials on those surfaces, increasing resistance, and consuming lithium in the formation of the passivating layer. The formation of SEI can also lead to isolation of the cracked active material as the layer forms around the displaced particles. Additionally, the number of sites suitable for reversible lithium ion accommodation may decrease due to the cracking and formation of new planes which might not be accessible to the electrolyte [222].

Ageing through electrochemical cycling can also lead to large scale mechanical deformation of the jelly roll, which is attributed to increased capacity fade and accelerated descent towards EOL. Zhao *et al.* [238] suggest that plastic deformation of particles caused by charge/discharge leads to irreversible change in the shape of the electrodes. Waldmann *et al.* [22] found that the deformations are more pronounced at higher cycling rates and initiate near the current collecting tabs, which they have partially assigned to the Ohmic heating effects at the tabs. In support of the findings by Waldmann [22], Kim *et al.* [18] found, through their simulations, that the stress experienced by the separator at the Ni-current collecting tab/separator interface was greater than the yield strength of the jelly roll, demonstrating that it's more likely for deformations to occur in line with the tabs.

The exact cause of jelly roll deformation is not yet understood. It may be that stress-induced bulk cracking of electrode particles, as discussed above, may compromise the structural integrity of the electrode rolls in a cell, leading to large-scale deformation of the jelly roll, or just the bulk expansion and contraction of the electrodes during cycling may be causing gradual irreversible change in their shape. Similarly, the exact consequence of the deformation is also not well understood, however, cell level jelly roll deformation is likely to cause delamination of the active material, resulting in uneven distribution of current and increased resistance. The delamination of the electrodes might also lead to *'dead zones'* - areas that have lost all contact to the current collector.

Cell quality assurance methods rely heavily on optical detectors [239] for checking the quality of electrodes before cell assembly, however, that does not take into account any influences arising from the assembly process. Virtual unrolling (VU) (which works provably [146], even with acquisition periods of less than two minutes) has the potential for the implementation of a non-destructive, in-line quality assurance procedure that can be carried out as a final step in the manufacturing process, and which does not rely on human input through the fast acquisition and analysis of the jelly rolls of pristine cells. This chapter will focus on cell level, macro deformations and aim to provide some insight into the how deformations occur, their progression, and the impact on the structure of the cell.

7.2 MATERIALS & METHODOLOGY

7.2.1 Cell Cycling

Forty-eight state-of-the-art commercial 21700 Li-ion cells (Ni-rich cathode, graphite/SiOx anode) were selected for this study and were split into two batches for cycling: batch A containing 45 cells numbered 01 – 45, and batch B containing the remaining three cells numbered 46 – 48. The cells from batch A were cycled between

2.5 – 4.2 V in an environmental chamber (Espec) set to 33 °C using a constant charge/constant voltage (CC/CV) regime with 10 minutes rest after both charge and discharge. The cells were cycled at 1C for both charge and discharge using Maccor (4000H series with 0 – 5 V, 100 A channels), and the current was tapered to C/20 during the CV step on charge. Every 100 cycles, these cells were subjected to reference performance tests (RPTs), which were conducted at 25 °C. The cells were charged to 4.2 V at C/3, tapering current to C/20 during the CV step on charge. After a 60 minutes rest, the cells were discharged to 2.5 V at C/3 and the measured capacities were taken as the reversible cell capacities. After a 60 minutes rest step, the cells were once again charged to 4.2 V. Additionally, direct current internal resistance (DCIR) investigations were carried out on the 46 cells using a 2C pulse over 30 seconds at 100, 80, 50 and 20% state-of-charge (SOC) as part of the RPT every 100 cycles.

The other three cells (46 – 48) were cycled using a Maccor battery cycler (Model 4200, Maccor Inc., Tulsa, USA) in an environmental chamber (Maccor Temperature Chamber MTC-020, Maccor Inc.) set to 40 °C. Similarly, these cells were also cycled at 1C charge and discharge using a CC/CV regime between 2.5 – 4.2 V.

7.2.2 X-ray Computed Tomography

All the Ni-rich 21700 cells were scanned using a Nikon X-ray machine (XT H 225, Nikon Metrology, Tring, UK) at the beginning of their life (pre-cycling) and after all the cycling had concluded. The scans were carried out using an exposure time of 0.5 s, beam energy and current of 200 kV and 210 μA, respectively. Approximately 1450 projections were taken for each cell. The image reconstruction of the acquired projections was carried out using a filtered back projection algorithm (CT Pro 3D, Nikon Metrology) resulting in a voxel size of 39 μm.

Additionally, *in-situ* truncated scans were carried out on cells 46 – 48 every 200 electrochemical cycles. The scans were carried out at six different voltage points during the charge cycle: 2.5, 3.4, 3.6, 3.8, 4.0, and 4.2 V. The charging was carried out

at 0.7C, tapering the current to 100 mA at each voltage step, with a step limit of 45 minutes for the CV process. The scans were truncated, resulting in a voxel size of 12 μm, using an exposure time of 0.5 s and beam parameters of 195 kV and 210 μA.

7.2.3 Virtual Unrolling

Virtual unrolling on the cells was conducted as outlined in Methodology, section 3.3.2. Interpretation of the figures is also provided there.

7.3 RESULTS & DISCUSSION

The forty-five cells from batch A were cycled until the knee point was visible for the majority of the cells and the three cells from batch B were cycled for 600 cycles. The capacity retention for all the cells can be seen in Figure 53. After 600 cycles, the cells from batch A have a capacity retention within the 85-90% range, however, the cells from batch B are below 84%. The greater degradation could be the impact of cycling at a slightly elevated temperature of 40 °C compared to 33 °C, leading to greater solid electrolyte interphase (SEI) build-up at the surface of the electrodes and a greater rate of active material loss. Cells from both batches show the typical accelerated capacity fade in the initial stages of cycling [56] as highlighted by the blue lines in Figure 53a-b, associated with the evolution of the interface layers at the surface of the cathode and anode. Then, a quasi-linear stage of capacity fade is observed. After 100 cycles, the cells in batch B had capacity retention ranging from 96.25% to 97.7%, and although the exact composition of the cathode in these cells is unknown, the nickel content is expected to be ≥ 0.8. Ryu *et al.* [240] investigated the degradation in Ni rich cells with Ni content ≥ 0.6. In coin cells, they found that after 100 cycles the cells had a capacity retention ranging from ca. 96% to 75% as the nickel content was increased to 100%, with 80% nickel content cells achieving ca. 95% capacity retention. The greater degradation observed by them is likely due to the use of lithium metal in the coin cells and charging to 4.3 V. A capacity *'knee-point'* is a secondary accelerated drop in capacity

retention observed in cells undergoing long term electrochemical cycling. From Figure 53b, it can be seen that the cells in batch A reach a knee-point in capacity fade at different points in their cycling, as highlighted by the red dotted lines. Six hundred cycles was not sufficient to reach the knee-point for any of the cells in batch B. The point at which the cells in batch A experience the most capacity fade can be more clearly observed when looking at the differential capacity plotted versus the number of cycles in Figure 53c. Although the differential capacity starts to increase before 1500 cycles, there is a sharp increase in the last 100 cycles of the cells' cycling period for most cells, which is the knee-point. After 2200 cycles, there are only two cells in batch A which do not experience the same rate of capacity fade as the other cells – cells 06 and 07 – and their X-ray slices after cycling can be seen in Figure 53d & e. Additionally, X-ray CT slices of the three cells with the earliest knee-point (cells 01, 24, and 43) can be seen in Figure 54. Compared to cells 06 and 07, which did not exhibit a knee-point, those cells show a more severe deformation of the jelly roll, and in some cases, multiple deformations can be observed. Figure 54 also contains X-ray CT slices for the cells in batch B after 600 cycles. It can be seen that the nucleation of deformation has occurred in the cells in batch B, but they have not progressed to the level show in batch A due to the lower number of electrochemical cycles performed. It is clear that greater electrochemical cycling leads to the formation of more severe and numerous deformations in the jelly rolls of cylindrical cells, and it is also clear that at some point the deformations reach a 'break-point' that causes a secondary, rapid decrease in capacity.

Figure 55 shows the results of the DCIR tests carried out on the cells at 100% SOC. It shows the percentage increase in the resistance at all points up to 1700 cycles compared to the initial resistance values at the pristine state. It can be seen that the spread of the increase in resistances starts to widen as the cells are cycled. Even if the cells are from the same manufacturing batch, there are small variances in active material loading and electrode arrangement causing these differences. Cell 1 consistently has the highest increase in resistance for most of the cycling period. In return, it has one of the earliest knee-point (1600 cycles) as seen in Figure 53. Additionally, cell 36 'overtakes' cell 1 to have the highest rate of increase after

1400 cycles, and it also has one of the earliest knee-points in batch A, suggesting that the cells with a greater rate of increase in DCIR are indicative of greater capacity fade. DCIR measures the Ohmic resistance resulting from the electrodes, current collectors, electrical connections, and the conductivity of the electrolyte. The connection between DCIR and the knee-point could be described by the loss in active material and the loss of contact with the current collectors due to the propagation of deformations within the jelly rolls of the cells. A feature of interest in the DCIR result is the dip in the rate of resistance increase at 1000 and 1100 cycles, which seems to split the cells into two clusters. The cause for this is unclear, however, all the cells in both clusters follow the same trend, and both clusters re-join to exhibit a uniform trend, so it is assumed to be an artefact caused by the experimental set-up.

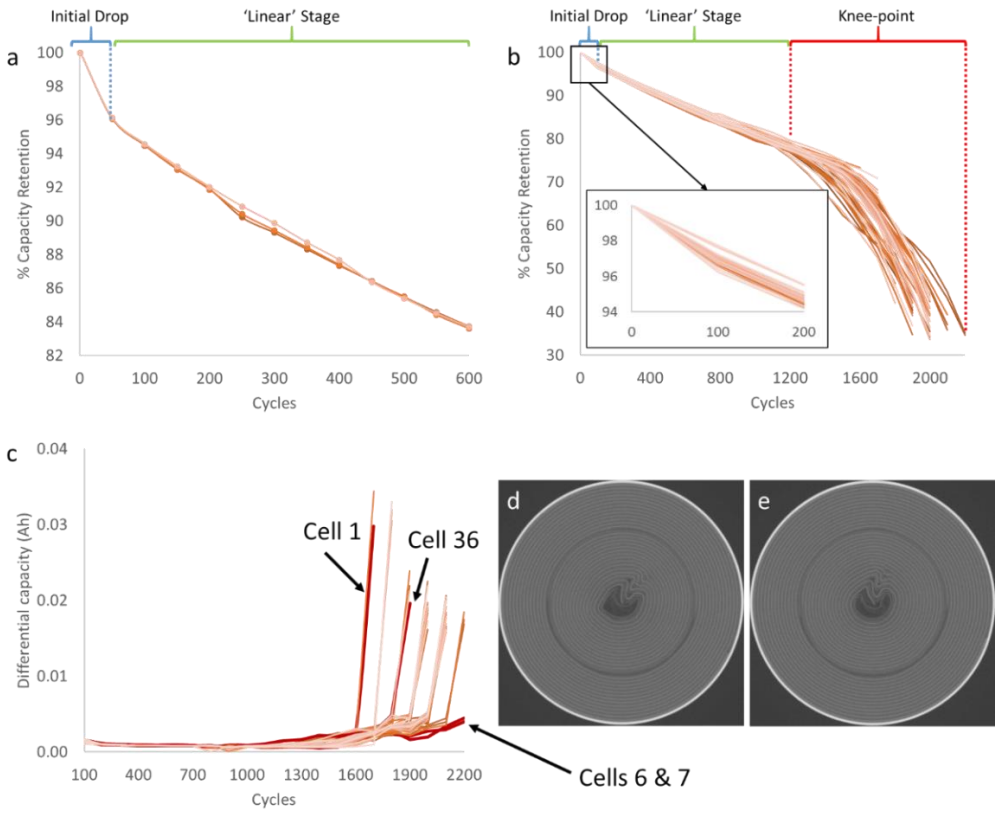

Figure 53: Capacity retention profiles of a) cells 46-48, b) cells 01-45, c) differential capacity profile against the number of cycles showing the point at which cells 01-46 enter the knee-point, and d-e) X-ray CT slices of cycled cells 06 and 07, respectively. A few data points in (c) have been highlighted for illustration purposes.

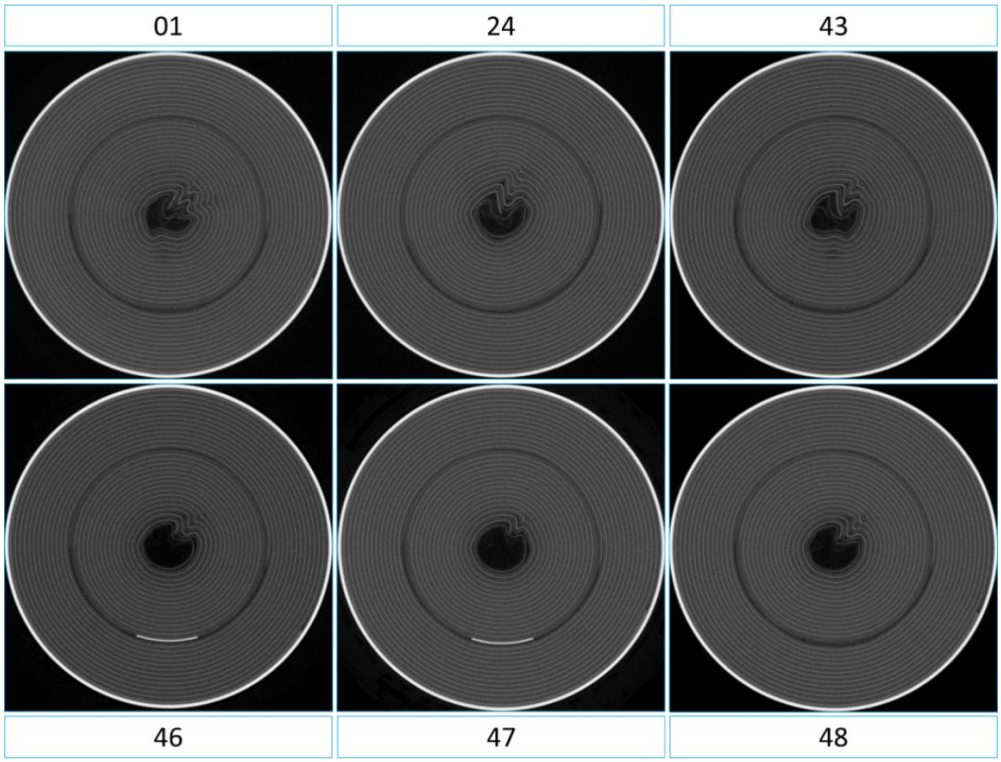

Figure 54: X-ray CT slices of cells 01, 24, 43, after 1600 – 1700 cycles, and 46, 47, 48 after 600 cycles.

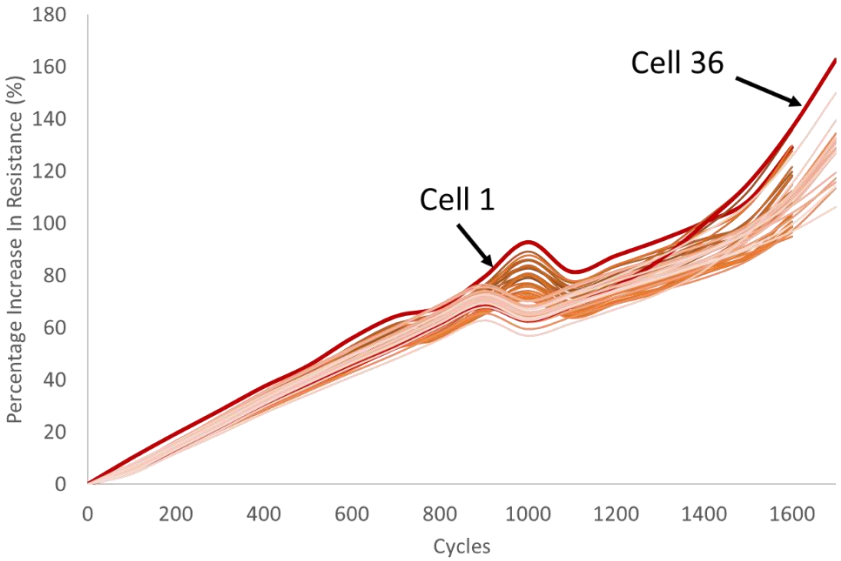

Figure 55: Percentage increase in the resistance of the cells compared to their resistance at the pristine state from the DCIR tests conducted at 100% SOC.

The change in anode thickness over the whole cycling period for batch A can be seen in Figure 56, where the *x*-axis corresponds to the numbered anode layers in the X-ray CT slice. The anode comprises of a mixture of graphite and silicon (SiO_x), and as such, the expectation would be an irreversible increase in thickness over time. However, it can be seen that for the first layer (outer) there is actually a net *decrease* in thickness, which can be assigned to the fact that the strain from the expansion of the electrodes is directed towards the cell casing [201], thus the layers closest to the casing would be compressed between the casing and the expanding inner layers. Furthermore, Kim *et al.* [18] found through their finite element model, that the greatest stress was experienced by the separator next to the current collecting tab, which was located between the tab and the cell casing. In our case, the tab is located in the middle of the casing and the cell centre, thus by extrapolation, the greatest stress might be experienced by the layers between the tab and the casing, resulting in some of the compression of the layers. All the layers experience some form of thickness change, but, the biggest increase is experienced by the centremost layers, demonstrating that the irreversible change occurs from the inside out. The current collecting tab is located between the anode layers 13 & 14, and when examining Figure 56, it would appear that the tab is suppressing some of the expansion propagating throughout the layers. The irreversible expansion of the electrodes leads to increased strain on the jelly roll, and results in electrode deformation and then delamination of the active material from the current collecting foil, leading to capacity loss. Therefore, it may be of benefit to move the current collecting tab more towards the centre of the cell to suppress the volume expansion in more layers. It has been noted that the inclusion of a mandrel also suppresses the deformation of the electrodes at the centre of the cell [22], so a combination of a mandrel and a shift of the tabs closer to the centre might lead to fewer deformations and longer cell life. However, this may inadvertently lead to suppression of the stress related to electrode expansion in both directions radially, and cause a burst of pressure at some point. Whilst the re-design of cell architectures is outside of the remit of this paper, it illustrates the possibility of using this technique to inform cell design strategies.

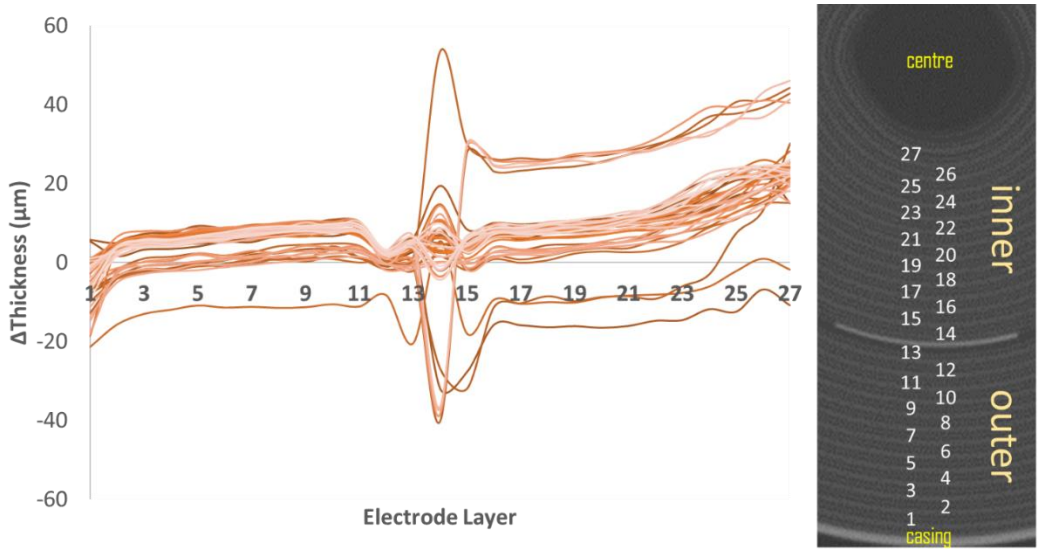

Figure 56: Anode thickness change for the cells in batch A. The *x*-axis indicates the anode layer corresponding to the labelled X-ray CT slice.

Cells 46-48 were scanned (full cell, not truncated) every 50 cycles, which allows for the examination of the internal changes in the jelly roll at a more granular temporal resolution, as shown in Figure 57. The change in thickness of the anode layers is split into two clusters, before the tab, and after. From these higher temporal resolution scans, it is clear that there is definitely a divide between the electrode layers before and after the tab (the inner and outer sections illustrated in Figure 57): the anode layers before the tab and closer to the cell casing experience compression over time, whereas the layers after the tab experience expansion, starting with the innermost layers. Furthermore, there is a wave-like pattern to the compression and expansion, which is likely due to the degree of reversibility of the electrode expansion caused by the Li^+ ion intercalation/alloying. Analysis into whether deformations cause greater thickness changes were carried out on cell 47. For consistency, all the thickness change analysis presented thus far were carried out at the same point for all cells, relative to their current collecting tab, and as such the result for cell 47 in Figure 57b shows the change in thickness of the anode layers at a point where there is no deformation. Complementary data in Figure 58a shows the thickness changes for cell 47 at a point where there is deformation. When comparing the two figures, it can be seen that in

the absence of a deformation, the initial thickness of the anode is greater (ca. 150 μm) than at the point of deformation (ca. 140 μm). However, when comparing the layers, for example, layer 27, at the point of no deformation there is little change between the initial and final anode thicknesses, whilst at the point of deformation there is an increase from ca. 150 μm to 157 μm. The difference in the initial anode thicknesses at the different points in the cell demonstrates the variance caused by standard manufacturing and assembly processes. A 3D rendering of the cell and slices at a point of deformation and at a point where there is no deformation are shown in Figure 58(b-d) for reference. Non-uniform current distribution leads to uneven utilisation of active materials and gradients in temperature and potential [241,242]. This becomes increasingly severe as the discharge progresses, and the effect is stronger closer to the negative current collecting tab [70]. It has been previously demonstrated by Zhang *et al.* [243] that a cell configuration with one positive tab produces a more non-uniform current distribution leading to poor performance. The cells contain one of each positive and negative current collecting tabs, therefore it is expected to have highly uneven current and temperature distributions throughout the electrodes. As such, there may be non-uniform active material utilisation and electrochemical activity throughout the jelly roll, which results in sections of the anode experiencing more Li^+ intercalation/alloying, and therefore more drastic expansion and contraction during electrochemical cycles, ultimately leading to electrode collapse and deformations. This explains the increased anode thickness changes observed at the deformations, and also explains the greater number of deformations observed on the bottom half of the cells in batch A (as shown in Figure A 7 in the Appendix) where the negative current collecting tab is present. For reference, the X-ray slices of all 48 cells in their pristine state can be found in Figure A 5 and Figure A 6.

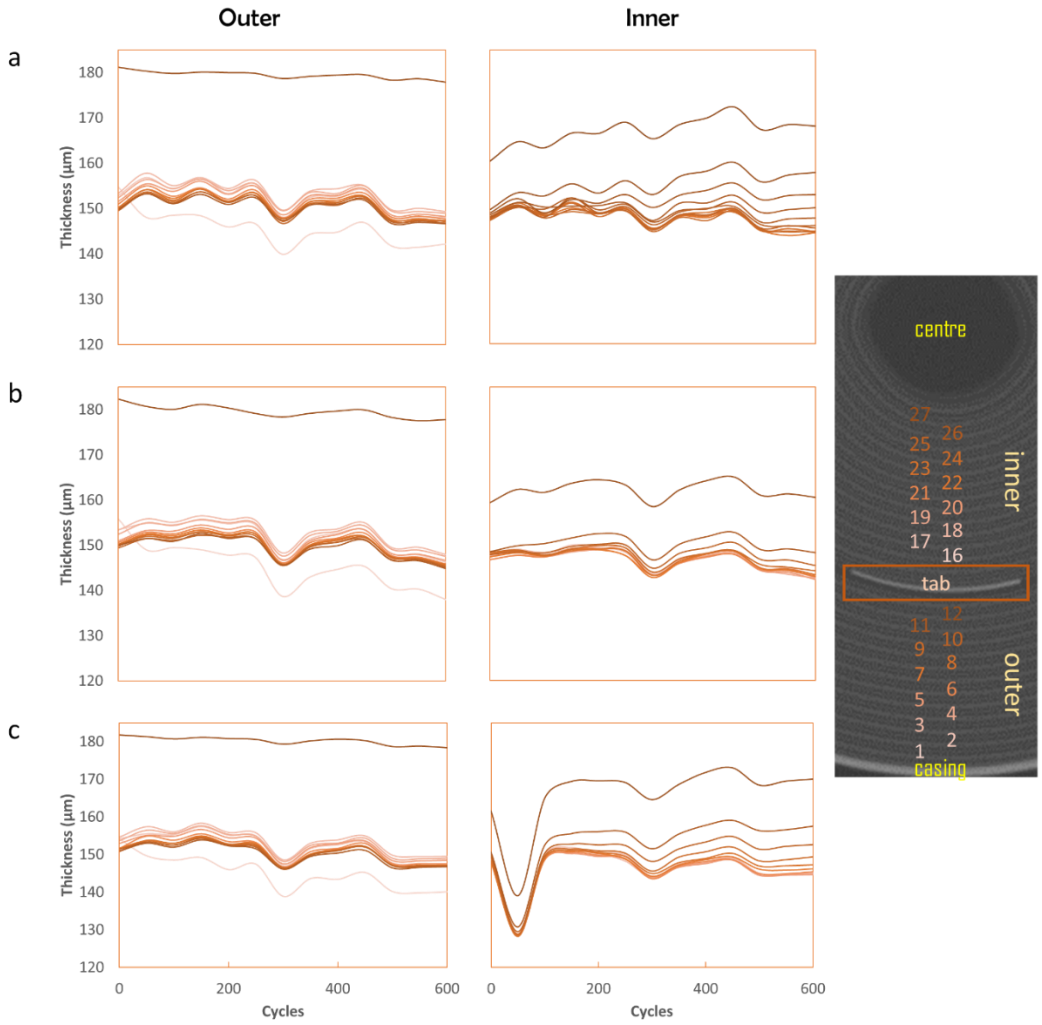

Figure 57: Anode thickness change for the cells in batch B a) Cell-46, b) Cell-47, and c) Cell-48, respectively. The *x*-axes indicate the anode layer corresponding to the labelled X-ray CT slice. The plots have been split into two: the inner section (after the tab), where the darker lines represent the layers closer to the cell centre, and the outer section (before the tab), where the darker lines represent layers closer to the cell tab.

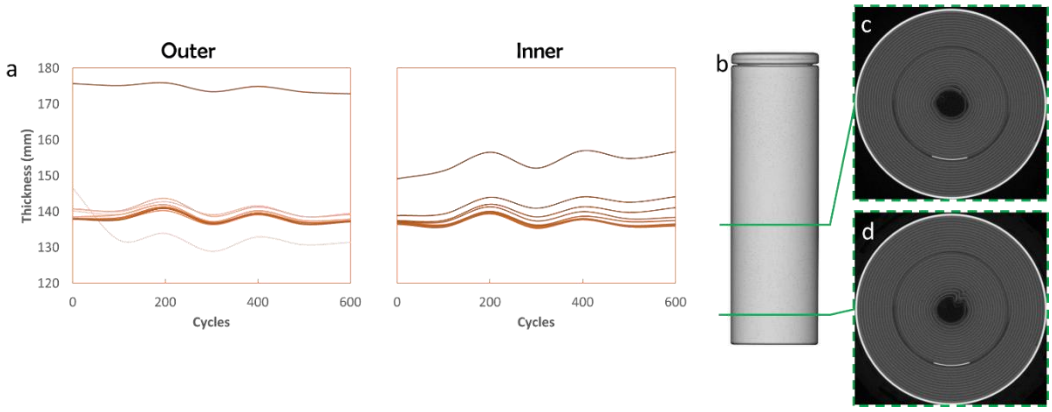

Figure 58: a) anode thickness change for Cell-47 at a point of deformation, b) a 3D render of Cell-47, c) a slice at a point where there is no deformation, and d) a slice at a point of deformation. The plots in (a) have been split into two: the inner section (after the tab), where the darker lines represent the layers closer to the cell centre, and the outer section (before the tab), where the darker lines represent layers closer to the cell tab.

Figure 59 shows the displacement of the jelly rolls of cells 46-48 as a function of cycling. The displacement show that across the cell there is a re-arrangement of the jelly roll during initial cycling – the period when the initial accelerated drop in capacity is observed. This indicates that a larger change in the jelly roll has a greater impact on the degradation of capacity. For reference, for cell 46, the decrease in discharge capacity between the first and 50th cycle was 2.50%, whereas between 50th to 200 cycles it was 4.33%. For cell 47 it was 2.45% and 4.39%, and for cell 48 it was 2.32% and 4.25%, respectively. The red sections indicate a compression of the electrodes towards the cell casing, and the blue indicates an expansion towards the cell centre. It can be seen that during the initial re-arrangement, the electrode fills out the space between the cell casing and the jelly roll. Where there is no space on the outside, the jelly roll is forced to expand towards the centre of the cell – the only other available space. In the later cycles, the strain from the expansion and contraction of the electrodes becomes focused on the inflection points in the spiral, defined as the pre-existing, non-circular (non-linear in the electrode displacement plots) arrangement of the electrode roll due to manufacturing and assembly processes. The deformations nucleate at the inflection

points and continue to expand and proliferate throughout the layers, from the centre layers to the outer layers towards the direction of the cell casing, similar to the observations with the anode thickness changes, further evidence that the swelling of the electrodes leads to the deformation.

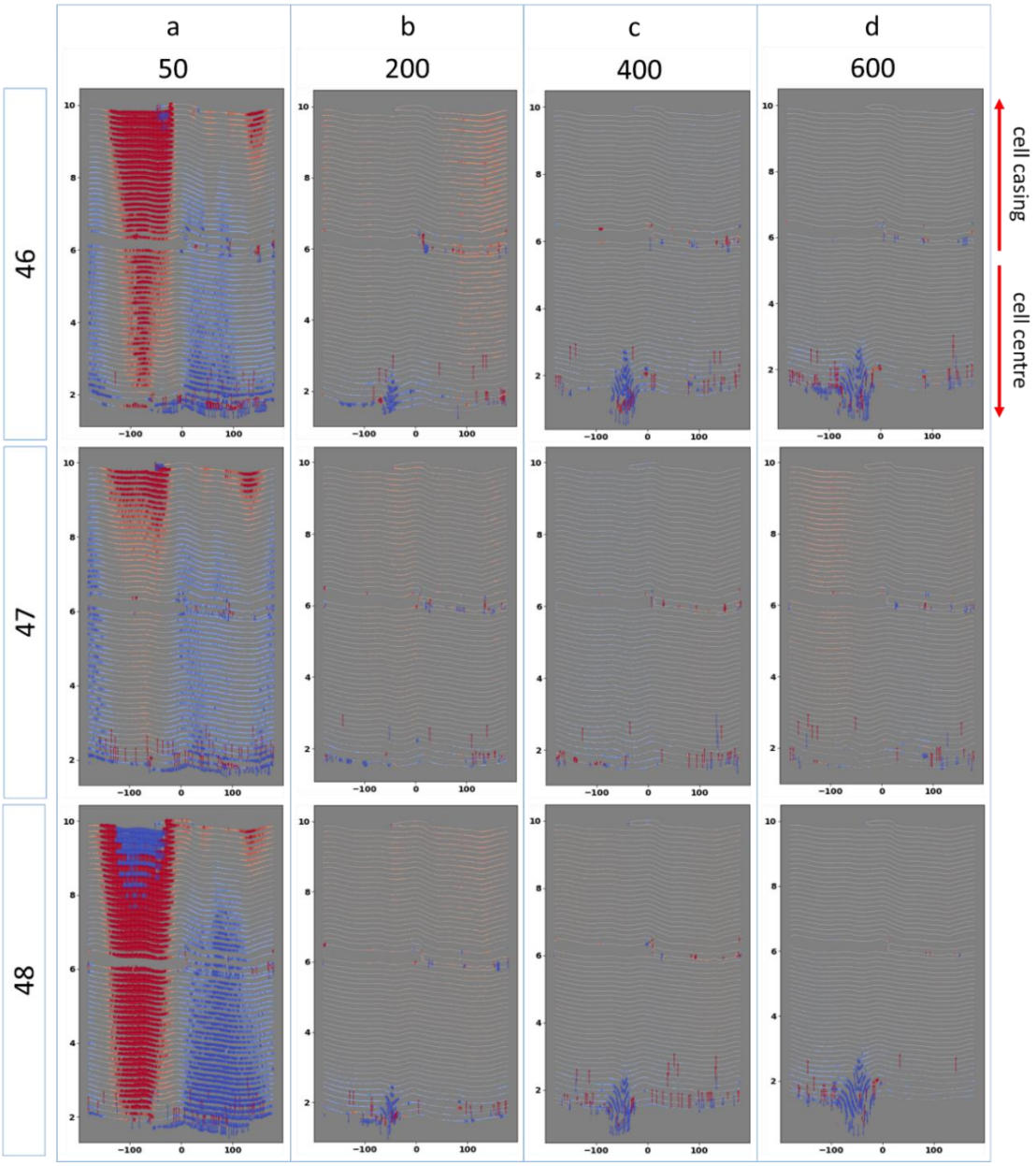

Figure 59: Electrode displacement for cells 46-48 a) pristine to 50 cycles, b) 150 cycles to 200 cycles, c) 350 cycles to 400 cycles, and d) 550 cycles to 600 cycles. The red indicates compression, and the blue, an expansion.

To investigate the effects of (de)lithiation on the mechanical changes in the jelly roll, cells 46-48 were subjected to *in-situ* scans at six different voltage steps at the beginning of life and every 200 cycles thereafter. The cells were scanned in their discharged state, and the cell was charged while mounted on the X-ray machine stage and scanned at 3.4 V and then every 200 mV thereafter up to 4.2 V. Figure 60 shows the strain distributions for cell 48 at the different voltage steps throughout its cycling period. It can be seen that the biggest rearrangement of the jelly roll occurs at the beginning of life, and afterwards the most change occurs between 3.6 V and 4.0 V, primarily at 3.6 V. A point of note is that the jelly roll deformation appears to be nucleating between the two opposing forces of outwards compression and inwards expansion. This is illustrated by comparing the strain distributions at 4.0 V at the beginning of life (Figure 60d at 000 cycles) and at the location of the deformation that appears after cycling in (Figure 60b at 200 cycles). Figure 61 shows the resulting anode thickness change for cell 48. For the outer layers, initially there is a large spread of thicknesses ca. 106 – 112 μm, and after 600 cycles, not only does the thickness of the anode layers decrease, the spread also decreases: ca. 104 – 108 μm. This change is consistent over the whole voltage range. It can also be seen that there is little change in anode thickness until the voltage reaches 3.6 V, similar to the strain distribution. As for the inner layers, the thicknesses of the anode layers have a relatively low spread, however, with cycling, the inner most layer starts to increase in thickness. Once the innermost layer reaches a thickness of ca. 106 μm, the layer before it starts to increase in thickness as well, and thus the spread in layer thicknesses starts to widen. The anode layers closer to the middle start to become thinner and the spread in thicknesses shrinks, possibly due to the crushing effect of the expansion in the inner layers. Similarly to the outer section, these changes are consistent over the whole voltage range.

From the voltage profile, it can be seen that the biggest increase in capacity occurs between 3.6 – 3.8 V (661.4 mAh – ca. 13.8% of the remaining reversible capacity), which might be the cause of the greater shift between 3.6 and 3.8 V. Also of interest is that the anode seems to contract slightly between 4.0 and 4.2 V, however, over the full course of the cycling period, the inner anode layers increase in size. The same trend is shown by the other two cells in batch B, as seen in Figure A 8 & Figure A 9 in the

Appendix. Thus, over a single charge cycle, the electrochemical processes cause changes in the thicknesses of the electrodes, causing expansion and contraction forces to spread throughout the electrode layers, and also eventually lead to the irreversible increase in the thicknesses of the anodes. Through the combination of these two effects, over the lifetime of a cell, jelly deformations nucleate at regions where the expansion and contraction forces collide and where the structural integrity of the jelly roll is compromised due to the expansion of the anode.

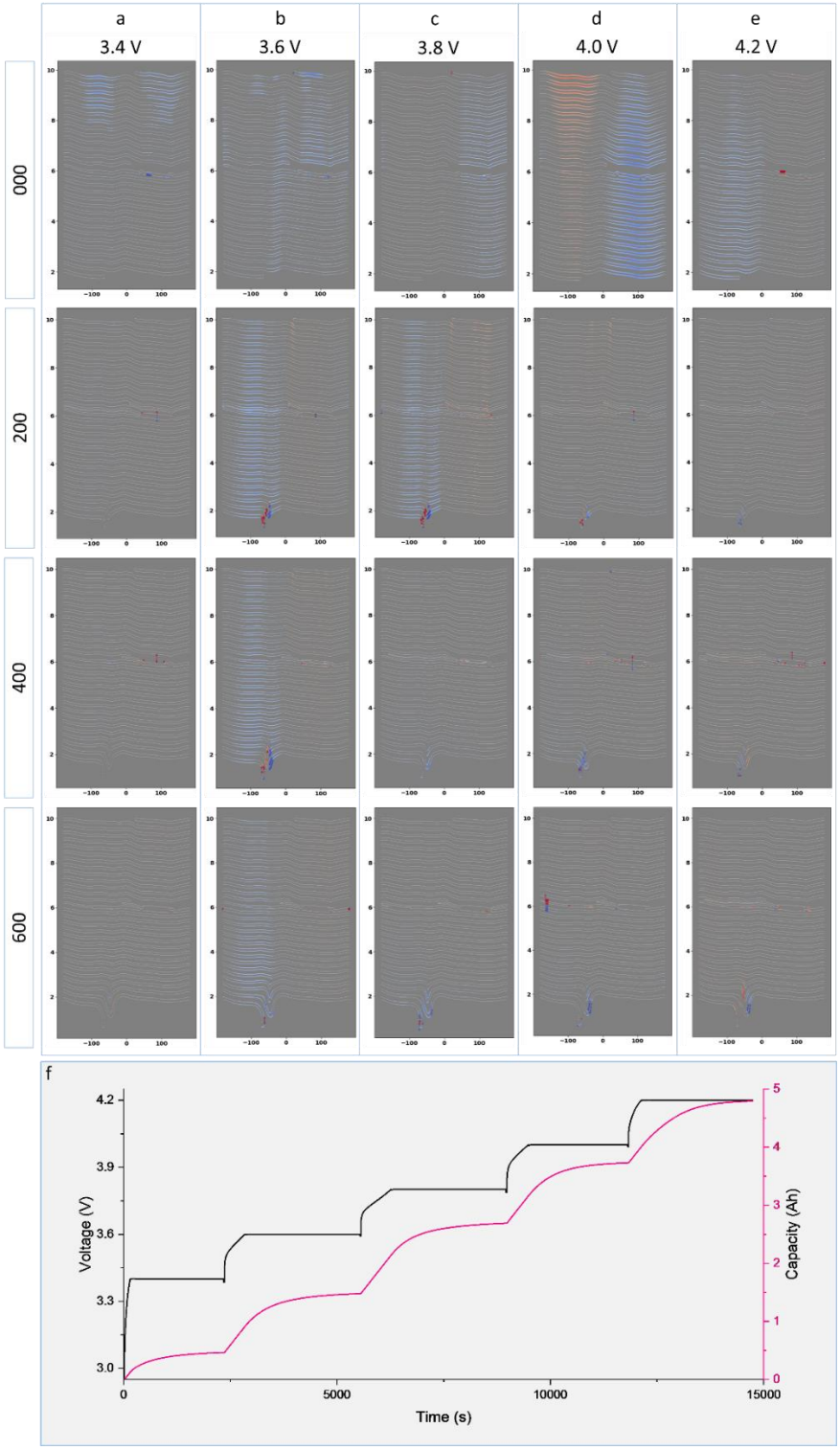

Figure 60: Electrode displacement for cell-48 a) 2.5 V to 3.4 V, b) 3.4 V to 3.6 V, c) 3.6 V to 3.8 V, d) 3.8 V to 4.0 V, and e) 4.0 V to 4.2 V. The voltage profile at the pristine state (000) is shown in (f).

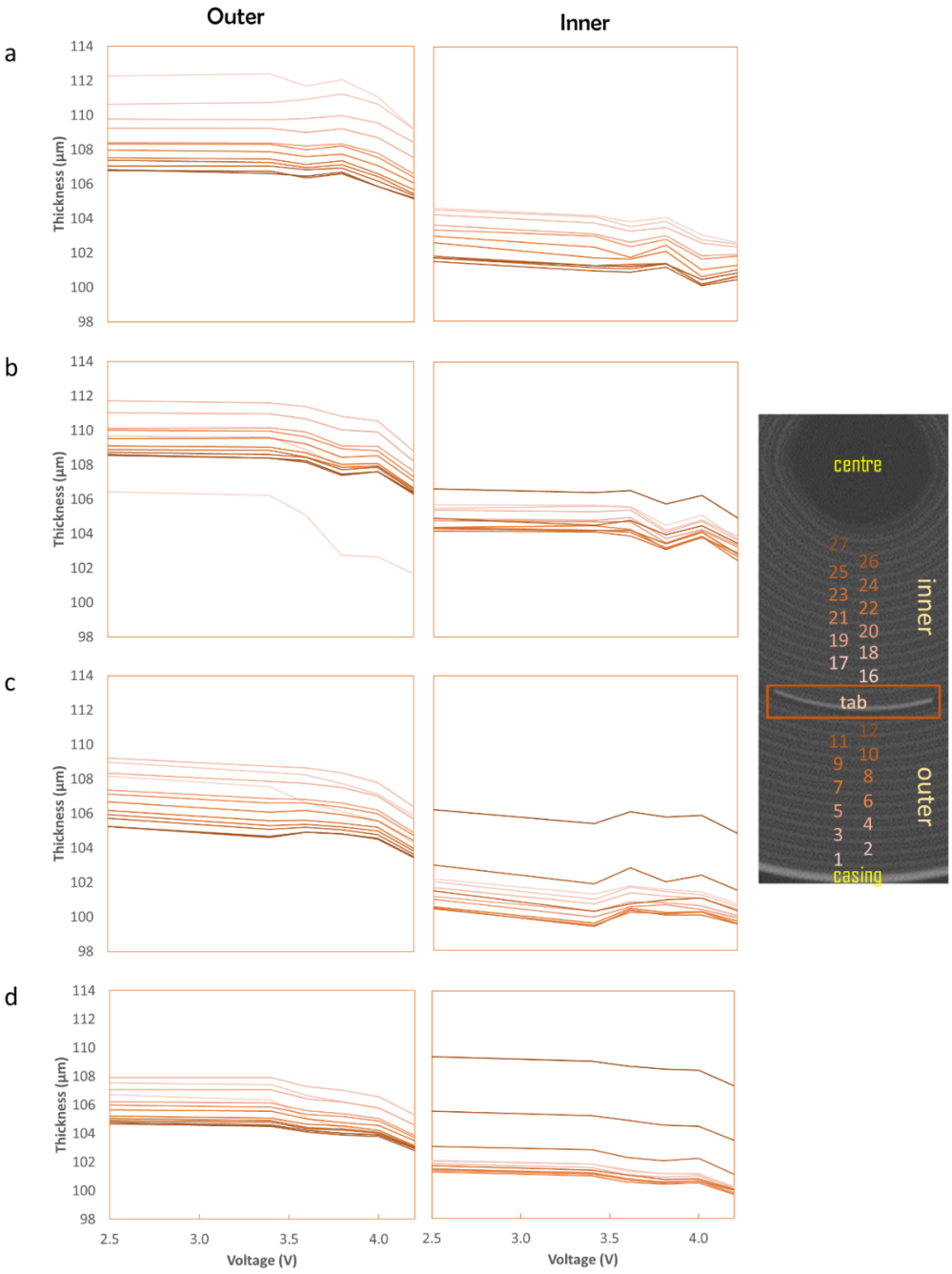

Figure 61: Anode thickness change for the Cell-48 at different voltage points a) pristine, b) 200 cycles, c) 400 cycles, and d) 600 cycles, respectively. The *x*-axes indicate the anode layer corresponding to the labelled X-ray CT slice. The plots have been split into two: the inner section (after the tab), where the darker lines represent the layers closer to the cell centre, and the outer section (before the tab), where the darker lines represent layers closer to the cell tab.

From the vast number of 21700 cells studied in this work, it has become clear that increased electrochemical cycling leads to jelly roll deformation and that DCIR may be a potential tool to differentiate the cells that are more likely to fail from the less likely to fail cells. It's also likely that the current collecting tabs suppress some of the forces causing deformation, thus it may be prudent to add additional tabs and move them closer to the centre of the cell. The increase in electrode thickness starts at the centre of the cell and propagates towards the outer layers, and data points towards the negative current collecting tab having a bigger influence on the nucleation of deformations, possibly due to uneven current distributions, thus another case for increasing the number of tabs.

7.4 CONCLUSIONS

Forty-eight commercial cells for electric vehicles were tested to gain an understanding behind the mechanisms of cell capacity fade and degradation. It was found that deformation of the jelly roll leads to a knee-point (or a secondary dip in capacity retention) which arises as a result of the thickening of the electrode in the cells. It was determined that the current collecting tabs suppress the propagation of the expansion of the electrodes and so it may be of benefit for the automotive industry to shift the tab closer to the centre of the cell and also add a mandrel to suppress deformation and potentially increase the cycle life of the cells. As a counter point, this may lead to a decrease in the safety rating of the cells as the strains behind the expansion of the electrodes might lead to pressure build-up. It would also lead to increased material cost and lower gravimetric energy densities. Additionally, it may be of benefit to increase the number of tabs in the cell to improve current distribution, as non-uniform current distribution and active material utilisation may be one of the factors causing the deformations; this is a known strategy in high power cells, but may also have lifetime benefits for energy cells.

It was also determined that there is a cell wide re-arrangement of the electrode rolls during the initial cycles, which contributes to the initial drop in capacity retention

experienced by most lithium-ion cells. Further cycling then leads to the nucleation of deformations at pre-existing inflection points caused by manufacturing processes. Therefore, improving manufacturing processes to create a more uniform (circular) jelly roll may be the most important factor for improving cell life. One option would be to taper the electrode ends, as non-tapered ends leave spaces between the cell casing and jelly roll for the shift of electrodes to occur, and the deformations appear between the two opposing strains of expansion and contraction.

8 CONCLUSIONS & FUTURE WORK

8.1 INVESTIGATION OF DEFORMATION MECHANISMS IN CYLINDRICAL CELLS

In the first instance, investigations into how the internal structure of two different types of cells changes as a function of cycling was conducted. Investigations into how cycling temperature, and storage conditions affect the physical changes to the jelly rolls were also undertaken. Buckling of the electrode rolls with electrochemical cycling was observed and virtual unrolling was used to elucidate any correlations in the location of the deformation.

Initial observations of the M50 cells showed that deformations were generally correlated with imperfections in the jelly roll (points deviating from a perfect spiral structure), and so deformations nucleated at pre-existing points of weakness (inflection points). It was thought likely that the rate of formation and progression of deformation is partially dependent on the degree of inflection of the pre-existing defect.

Similar to the M50s, the other cell type investigated, MJ1, also showed deformations in the electrode rolls with increasing number of cycles occurring at similar pre-existing inflection points. Both cells also exhibited less deformation towards the positive end of the cell, where the outer current collecting tab was not present as the tab seems to exert additional pressure on the electrode rolls. For the MJ1 cells, less deformation was observed, partly due to the inner current-collecting tab being located at the centre of the cell, which is believed to suppress some of the stress causing deformation.

The effect of cycling temperature was studied: the M50 cells cycled at 0 °C demonstrated greater capacity fade compared to the cells cycled at 45 °C, and similarly,

they also exhibited a greater deformation of the jelly roll. An increase in the capacity fade of the cells cycled at 0 °C was observed after the initiation of a deformation in the jelly rolls leading to the belief that deformations cause a drop in performance.

Finally, storing M50 cells at 80% capacity had no physical impact on their internal structure.

8.2 MOTION-ENHANCEMENT ASSISTED DIGITAL IMAGE CORRELATION OF LITHIUM-ION BATTERIES DURING LITHIATION

In the second phase of the project, the study was expanded to test a greater variety of cell geometries (18650, 21700, 26650) as well as chemical composition. Additionally, it was adapted to investigate the effect of a single charge cycle in a quasi-4D, *in-situ* experimental set-up.

A combination of a video motion enhancement technique to magnify the motion of electrodes during the lithiation process and an image registration technique based on optical flow was used for the investigation. Virtual unrolling revealed that location of the inflection in the jelly roll might be influenced by the location at which the electrode roll ends at the center of the cell, and for cycled cells already containing large electrode deformations, the shift was concentrated around the deformations, which is believed to contribute to the expansion of the deformations.

The biggest driving force for the eventual deformation of the cells seemed to be the location of the positive electrode end at the centre of the cell. Additionally, deformation of the cell casing was also observed, indicating that the stresses and strains caused by the chemical changes within the electrodes are strong enough to deform metal sheets.

Utilising a method to enhance the electrode displacement that occurs during cell charging with an image registration process to create a motion enhancement and registration technique, displacement *'hotbeds'* were identified in pristine cells and correlated with observed deformations in cycled cells.

8.3 EXAMINING THE EFFECTS OF SILICON-BASED ADDITIVES ON THE LONG-TERM CYCLING CAPABILITIES OF CYLINDRICAL CELLS

Next, the study turned to investigating the effect of Si additives in the anode and its effect on the deformation of cells. In order to do this, two very similar cells (MJ1 & MH1) were used, the former containing Si (or SiO_x). Additionally, the study was expanded to study a large array of cells for statistical significance.

The 32 MJ1 cells, which contain Si show large – and sometimes numerous – deformations of the jelly roll in all but 3 of the cells, and also show delamination of the electrodes in some cases. Through high resolution X-ray CT, the nucleation of a jelly roll deformation was revealed to be caused by the swelling of the anode layers towards the centre of the cell. Therefore, the mechanical changes in the jelly rolls from long-term cycling is attributed to the presence of Si which experience a larger volume expansion during intercalation of Li^+ ions.

By contrast, of the 30 MH1 cells (which do not contain Si), only two of the cells show small deformations in the jelly roll; this indicates that increasing Si content is a major driving force for jelly roll collapse. The MH1 cells underwent an accelerated capacity fade, but that appeared to have had little cause/effect on the jelly roll architecture. Furthermore, the addition of Si has also led to an irreversible change in anode thickness of up to ca. 18 μm in the MJ1 cells, compared to the maximum of around 4 μm in the MH1 cells due to the more limited expansion and contraction behaviour in the graphite anode.

8.4 INVESTIGATING THE DEFORMATION MECHANISMS IN NI-RICH 21700 CELLS

Finally, the project was focused back on 21700 cells (for their relevance in electric vehicle battery packs) and the study was expanded to investigate a large number of commercially relevant Ni-rich 21700 cells.

Forty-eight commercial cells for electric vehicles were tested to gain an understanding behind the mechanisms of cell capacity fade and degradation. It was found that deformation of the jelly roll leads to a knee-point (or a secondary dip in capacity retention) which arises as a result of the thickening of the electrode in the cells. It was determined that the current collecting tabs suppress the propagation of the expansion of the electrodes and so it may be of benefit for the automotive industry to shift the tab closer to the centre of the cell, and also add a mandrel to suppress deformation and potentially increase the cycle life of the cells.

It was also determined that there is a cell wide re-arrangement of the electrode rolls during the initial cycles, which contributes to the initial drop in capacity retention experienced by most lithium-ion cells. Further cycling then leads to the nucleation of deformations at pre-existing inflection points caused by the manufacturing processes. Therefore, improving manufacturing processes to create a more uniform (circular) jelly roll may be the most important factor for improving cell life.

8.5 FUTURE WORK

X-ray CT has proven to be a very powerful tool for the non-destructive investigation of batteries, and virtual unrolling (VU) has proven effective in identifying trends in cell degradation due to mechanical changes within the cells. However, more work can be done to develop the technique and to validate and correlate the observations and

results. Below are some of the work suggested in order to improve the techniques discussed in previous chapters and to obtain more conclusive data:

1. The link between degradation of capacity and mechanical changes within the batteries is not strongly linked given the data. The link could be made stronger through further data processing of the electrochemical data and additional experiments. Firstly, exploring the statistical differences between cells that showed faster degradation compared to the cells that showed slower degradation might yield some clues into the cause. Secondly, using models to generate capacity fade profiles (perhaps a model that purposely discounts the potential effects of jelly roll deformations) and comparing rates of degradation between model and empirical data might be useful. Additionally, models to obtain strain and stress values would be useful to also determine the effect of the mechanical design of batteries. Those values obtained from the models could be compared to those obtained through DIC for example in Chapter 5 (with further analysis). The electrochemical data (voltage, current, capacity, temperature) obtained on the cells in these studies could be used to implement the models. Depending on the type of model used, obtaining the parameters to feed into the models might require some cell disassembly and characterisation of electrode (thickness, area, coating uniformity, etc.), separator and electrolyte properties. Since electrolyte compositions are not revealed by manufacturers, mass spectroscopy (or similar) techniques will have to be utilised.

2. The MERt technique could be greatly improved by developing an alignment tool more robust than the current automatic alignment approaches. Similarly, investigating the strain along the z-axis instead of just the x- and y-axes would provide more information on the impact of the observed strain within the cells.

3. Additionally, the application of strain gauges, or very high resolution *operando* imaging to investigate the deformation of the cylindrical cell casings would provide information on the impact of deformations on cell behaviour and pressure build-up. The determination of whether the cell casing deformation is even or warped and the relationship between the casing deformation and jelly roll deformation might inform future cell design. This study could be coupled with a temperature study, either using experimental cells with temperature probes inside the jelly roll and on the casing, or using thermal cameras. It would be useful to gain information on whether the casing expansion is caused by temperature increases. It would also provide correlative information of the benefit of increased number of tabs on heat distribution and its impact on cycle life.

4. Additionally, it would be useful to gain information on the strain in the z-direction of the cells - especially for the variety of cells studied in Chapter 5. A lot of the cells studied have current collecting tabs that are present for only half the height of the cells, and the stress in the cell would be different at different points in the cell due to their presence (or lack of). It may be more representative to carry out operando experiments coupled with DVC techniques to explore the strains in the z-direction.

5. An *operando* nano-X-ray CT experimental set-up to correlate, or disprove, the extent of electrode expansion observed using VU would be of interest for validation purposes.

6. Exploration of the potential damage caused by X-rays to the cells would be of interest. However, the damage is likely to be negligible, so a very large sample size would be required, and even then it may be difficult to decouple differences caused by X-ray damage to differences caused by cell-to-cell variances. It may be of benefit to subject the cells to several orders of magnitude more X-rays than they would likely experience during

the accumulated periodic scans over their life cycles (as conducted in the studies in this thesis).

7. The virtual unrolling technique would prove useful for the electric vehicle manufacturing industry to detect end-of-line manufacturing defects and could also potentially be useful for cell life predictions. Further work can be carried out in order to improve the technique and understanding of the cell behaviours explored here, for example, by applying this technique to investigate cells with multiple current-collecting tabs, and *'tabless'* 4680 cells would provide valuable information on the prospective batteries of the future. The virtual unrolling technique is adaptable and would easily be transferrable to 4680 cells, and direct comparisons could be made between tabbed 21700 cells and the effect of increased size and lack of tabs could be elucidated. Comparisons could also be made with pouch cells, as the unrolling technique could be used to gauge the layer uniformity (how flat and straight the electrode layers are) and their evolution during cycling due to gas evolution and lack of a sturdy casing.

8. Aspects such as the impact of casing expansion in a module setting and the impact of differing number of tabs in heat rejection and distribution would of interest to investigate the cylindrical cells in their natural position in battery packs and modules, where they are welded to busbars and glued in position. It would not be possible to X-ray CT a module of cells, but it may be possible to emulate a module setting using 2-4 cells welded and glued down. Alternatively, other techniques such as thermal imaging could be used.

9 REFERENCES

[1] Lu L, Han X, Li J, Hua J and Ouyang M 2013 A review on the key issues for lithium-ion battery management in electric vehicles *J. Power Sources* **226** 272–88

[2] Scrosati B, Hassoun J and Sun Y K 2011 Lithium-ion batteries. A look into the future *Energy Environ. Sci.* **4** 3287–95

[3] Luo X, Wang J, Dooner M and Clarke J 2015 Overview of current development in electrical energy storage technologies and the application potential in power system operation *Appl. Energy* **137** 511–36

[4] Nitta N, Wu F, Lee J T and Yushin G 2015 Li-ion battery materials: Present and future *Mater. Today* **18** 252–64

[5] Etacheri V, Marom R, Elazari R, Salitra G and Aurbach D 2011 Challenges in the development of advanced Li-ion batteries: A review *Energy Environ. Sci.* **4** 3243–62

[6] Zhang S S 2020 Challenges and Strategies for Fast Charge of Li-Ion Batteries *ChemElectroChem* **7** 3569–77

[7] Yi T-F, Mei J and Zhu Y-R 2016 Key strategies for enhancing the cycling stability and rate capacity of LiNi0.5Mn1.5O4 as high-voltage cathode materials for high power lithium-ion batteries *J. Power Sources* **316** 85–105

[8] Thackeray M M and Amine K 2021 LiMn2O4 spinel and substituted cathodes *Nat. Energy* **6** 566–566

[9] Chayambuka K, Mulder G, Danilov D L and Notten P H L 2020 From Li-

Ion Batteries toward Na-Ion Chemistries: Challenges and Opportunities *Adv. Energy Mater.* **10** 1–11

[10] Fan E, Li L, Wang Z, Lin J, Huang Y, Yao Y, Chen R and Wu F 2020 Sustainable Recycling Technology for Li-Ion Batteries and Beyond: Challenges and Future Prospects *Chem. Rev.* **120** 7020–63

[11] Budde-Meiwes H, Drillkens J, Lunz B, Muennix J, Rothgang S, Kowal J and Sauer D U 2013 A review of current automotive battery technology and future prospects *Proc. Inst. Mech. Eng. Part D J. Automob. Eng.* **227** 761–76

[12] Whittingham M S 2004 Lithium batteries and cathode materials *Chem. Rev.* **104** 4271–301

[13] Thackeray M M, Wolverton C and Isaacs E D 2012 Electrical energy storage for transportation - Approaching the limits of, and going beyond, lithium-ion batteries *Energy Environ. Sci.* **5** 7854–63

[14] van Schalkwijk W A and Scrosati B 2002 *Advances in Lithium-Ion Batteries* (Boston, MA: Springer US)

[15] Oldham K B, Myland J C and Bond A M 2011 *Electrochemical Science and Technology* (Chichester, UK: John Wiley & Sons, Ltd)

[16] Taiwo O O, Heenan T M M, Finegan D P, Brett D J L, Shearing P R, Paz-García J M, Hall S A, Mokso R, Villanueva-Pérez P and Patera A 2017 Microstructural degradation of silicon electrodes during lithiation observed via operando X-ray tomographic imaging *J. Power Sources* **342** 904–12

[17] Taiwo O O, Loveridge M, Beattie S D, Finegan D P, Bhagat R, Brett D J L and Shearing P R 2017 Investigation of cycling-induced microstructural degradation in silicon-based electrodes in lithium-ion batteries using X-ray nanotomography *Electrochim. Acta* **253** 85–92

[18] Kim S, Lee Y S, Lee H S and Jin H L 2010 A study on the behavior of a cylindrical type Li-Ion secondary battery under abnormal conditions *Materwiss. Werksttech.* **41** 378–85

[19] Sturm J, Rheinfeld A, Zilberman I, Spingler F B, Kosch S, Frie F and Jossen A 2019 Modeling and simulation of inhomogeneities in a 18650 nickel-rich, silicon-graphite lithium-ion cell during fast charging *J. Power Sources* **412** 204–23

[20] Willenberg L K, Dechent P, Fuchs G, Sauer D U and Figgemeier E 2020 High-precision monitoring of volume change of commercial lithium-ion batteries by using strain gauges *Sustain.* **12**

[21] Yu X, Feng Z, Ren Y, Henn D, Wu Z, An K, Wu B, Fau C, Li C and Harris S J 2018 Simultaneous Operando Measurements of the Local Temperature, State of Charge, and Strain inside a Commercial Lithium-Ion Battery Pouch Cell *J. Electrochem. Soc.* **165** A1578–85

[22] Waldmann T, Gorse S, Samtleben T, Schneider G, Knoblauch V and Wohlfahrt-Mehrens M 2014 A Mechanical Aging Mechanism in Lithium-Ion Batteries *J. Electrochem. Soc.* **161** A1742–7

[23] Carter R, Klein E J, Atkinson R W and Love C T 2019 Mechanical collapse as primary degradation mode in mandrel-free 18650 Li-ion cells operated at 0 °C *J. Power Sources* **437** 226820

[24] Finegan D P, Tudisco E, Scheel M, Robinson J B, Taiwo O O, Eastwood D S, Lee P D, Michiel M Di, Bay B, Hall S A, Hinds G, Brett D J L and Shearing P R 2015 Quantifying bulk electrode strain and material displacement within lithium batteries via high-speed operando tomography and digital volume correlation *Adv. Sci.* **3** 1–11

[25] Braithwaite J W 1999 Corrosion of Lithium-Ion Battery Current Collectors *J.*

Electrochem. Soc. **146** 448

[26] Lee J K, Smith K B, Hayner C M and Kung H H 2010 Silicon nanoparticles-graphene paper composites for Li ion battery anodes *Chem. Commun.* **46** 2025–7

[27] Balakrishnan P G, Ramesh R and Prem Kumar T 2006 Safety mechanisms in lithium-ion batteries *J. Power Sources* **155** 401–14

[28] Finegan D P, Darcy E, Keyser M, Tjaden B, Heenan T M M, Jervis R, Bailey J J, Vo N T, Magdysyuk O V., Drakopoulos M, Michiel M Di, Rack A, Hinds G, Brett D J L and Shearing P R 2018 Identifying the Cause of Rupture of Li-Ion Batteries during Thermal Runaway *Adv. Sci.* **5**

[29] Armand M and Tarascon J M 2008 Building better batteries *Nature* **451** 652–7

[30] Marks T, Trussler S, Smith A J, Xiong D and Dahn J R 2011 A Guide to Li-Ion Coin-Cell Electrode Making for Academic Researchers *J. Electrochem. Soc.* **158** A51

[31] Qi Y and Harris S J 2010 In Situ Observation of Strains during Lithiation of a Graphite Electrode *J. Electrochem. Soc.* **157** A741

[32] De Las Casas C and Li W 2012 A review of application of carbon nanotubes for lithium ion battery anode material *J. Power Sources* **208** 74–85

[33] Qie L, Chen W M, Wang Z H, Shao Q G, Li X, Yuan L X, Hu X L, Zhang W X and Huang Y H 2012 Nitrogen-doped porous carbon nanofiber webs as anodes for lithium ion batteries with a superhigh capacity and rate capability *Adv. Mater.* **24** 2047–50

[34] Zhou G, Wang D W, Li F, Zhang L, Li N, Wu Z S, Wen L, Lu G Q and Cheng H M 2010 Graphene-wrapped Fe3O4anode material with improved

reversible capacity and cyclic stability for lithium ion batteries *Chem. Mater.* **22** 5306–13

[35] Lian P, Zhu X, Xiang H, Li Z, Yang W and Wang H 2010 Enhanced cycling performance of Fe3O4–graphene nanocomposite as an anode material for lithium-ion batteries *Electrochim. Acta* **56** 834–40

[36] Whitacre J F, Zaghib K, West W C and Ratnakumar B V. 2008 Dual active material composite cathode structures for Li-ion batteries *J. Power Sources* **177** 528–36

[37] Kim S B, Lee K J, Choi W J, Kim W S, Jang I C, Lim H H and Lee Y S 2010 Preparation and cycle performance at high temperature for Li[Ni0.5Co0.2Mn0.3]O2coated with LiFePO4 *J. Solid State Electrochem.* **14** 919–22

[38] Gao J and Manthiram A 2009 Eliminating the irreversible capacity loss of high capacity layered Li[Li0.2Mn0.54Ni0.13Co0.13]O2cathode by blending with other lithium insertion hosts *J. Power Sources* **191** 644–7

[39] Lim J H, Bang H, Lee K S, Amine K and Sun Y K 2009 Electrochemical characterization of Li2MnO3-Li[Ni1/3Co1/3Mn1/3]O2-LiNiO2cathode synthesized via co-precipitation for lithium secondary batteries *J. Power Sources* **189** 571–5

[40] Stewart S, Albertus P, Srinivasan V, Plitz I, Pereira N, Amatucci G and Newman J 2008 Optimizing the Performance of Lithium Titanate Spinel Paired with Activated Carbon or Iron Phosphate *J. Electrochem. Soc.* **155** A253

[41] Yi T F, Shu J, Zhu Y R, Zhou A N and Zhu R S 2009 Structure and electrochemical performance of Li4Ti5O12-coated LiMn1.4Ni0.4Cr0.2O4spinel as 5 V materials *Electrochem. commun.* **11** 91–4

[42] Chen G, Wilcox J D and Richardson T J 2008 Improving the Performance of Lithium Manganese Phosphate Through Divalent Cation Substitution *Electrochem. Solid-State Lett.* **11** A190

[43] Polo Fonseca C, Bellei M A, Amaral F A, Canobre S C and Neves S 2009 Synthesis and characterization of LiMxMn2-xO4 (M = Al, Bi and Cs ions) films for lithium ion batteries *Energy Convers. Manag.* **50** 1556–62

[44] Heo J B, Lee S B, Cho S H, Kim J, Park S H and Lee Y S 2009 Synthesis and electrochemical characterizations of dual doped Li1.05Fe0.997Cu0.003PO4 *Mater. Lett.* **63** 581–3

[45] Wang H, Xia H, Lai M O and Lu L 2009 Enhancements of rate capability and cyclic performance of spinel LiNi0.5Mn1.5O4by trace Ru-doping *Electrochem. commun.* **11** 1539–42

[46] Shenouda A Y and Liu H K 2009 Studies on electrochemical behaviour of zinc-doped LiFePO4 for lithium battery positive electrode *J. Alloys Compd.* **477** 498–503

[47] Sivaprakash S and Majumder S B 2009 Understanding the role of Zr4+cation in improving the cycleability of LiNi0.8Co0.15Zr0.05O2cathodes for Li ion rechargeable batteries *J. Alloys Compd.* **479** 561–8

[48] Zhang B, Chen G, Xu P and Li C C 2008 Effect of equivalent and non-equivalent Al substitutions on the structure and electrochemical properties of LiNi0.5Mn0.5O2 *J. Power Sources* **176** 325–31

[49] Arumugam D, Paruthimal Kalaignan G and Manisankar P 2009 Synthesis and electrochemical characterizations of nano-crystalline LiFePO4 and Mg-doped LiFePO4 cathode materials for rechargeable lithium-ion batteries *J. Solid State Electrochem.* **13** 301–7

[50] Belov D and Yang M H 2008 Investigation of the kinetic mechanism in overcharge process for Li-ion battery *Solid State Ionics* **179** 1816–21

[51] Doh C H, Kim D H, Kim H S, Shin H M, Jeong Y D, Moon S I, Jin B S, Eom S W, Kim H S, Kim K W, Oh D H and Veluchamy A 2008 Thermal and electrochemical behaviour of C/LixCoO2cell during safety test *J. Power Sources* **175** 881–5

[52] Root M 2010 *The TAB Battery Book: An In-Depth Guide to Construction, Design, and Use* (McGraw-Hill/TAB Electronics)

[53] Fergus J W 2010 Recent developments in cathode materials for lithium ion batteries *J. Power Sources* **195** 939–54

[54] Dou S and Wang W 2011 Synthesis and electrochemical properties of layered LiNi 0.5-x Mn 0.5-x Co 2x O 2 for lithium-ion battery from nickel manganese cobalt oxide precursor *J. Solid State Electrochem.* **15** 399–404

[55] Verma P, Maire P and Novák P 2010 A review of the features and analyses of the solid electrolyte interphase in Li-ion batteries *Electrochim. Acta* **55** 6332–41

[56] Wu Z, Ren W, Wen L, Gao L, Zhao J, Chen Z, Zhou G, Li F and Cheng H-M 2010 Graphene Anchored with Co3O4 Nanoparticles as Anode of Lithium Ion Batteries with Enhanced Reversible Capacity and Cyclic Performance *ACS Nano* **4** 3187–94

[57] Manthiram A 2011 Materials challenges and opportunities of lithium ion batteries *J. Phys. Chem. Lett.* **2** 176–84

[58] Zhang S S 2006 A review on electrolyte additives for lithium-ion batteries *J. Power Sources* **162** 1379–94

[59] Aurbach D, Talyosef Y, Markovsky B, Markevich E, Zinigrad E, Asraf L,

Gnanaraj J S and Kim H J 2004 Design of electrolyte solutions for Li and Li-ion batteries: A review *Electrochim. Acta* **50** 247–54

[60] Finegan D P, Darcy E, Keyser M, Tjaden B, Heenan T M M, Jervis R, Bailey J J, Malik R, Vo N T, Magdysyuk O V., Atwood R, Drakopoulos M, DiMichiel M, Rack A, Hinds G, Brett D J L and Shearing P R 2017 Characterising thermal runaway within lithium-ion cells by inducing and monitoring internal short circuits *Energy Environ. Sci.* **10** 1377–88

[61] Xu K, Ding M S, Zhang S, Allen J L and Jow T R 2002 An Attempt to Formulate Nonflammable Lithium Ion Electrolytes with Alkyl Phosphates and Phosphazenes *J. Electrochem. Soc.* **149** A622

[62] Yoshio M, Brodd R J and Kozawa A 2009 *Lithium-Ion Batteries* ed M Yoshio, R J Brodd and A Kozawa (New York, NY: Springer New York)

[63] Venugopal G, Moore J, Howard J and Pendalwar S 1999 Characterization of microporous separators for lithium-ion batteries *J. Power Sources* **77** 34–41

[64] Lee H, Yanilmaz M, Toprakci O, Fu K and Zhang X 2014 A review of recent developments in membrane separators for rechargeable lithium-ion batteries *Energy Environ. Sci.* **7** 3857–86

[65] Belov D and Yang M H 2008 Failure mechanism of Li-ion battery at overcharge conditions *J. Solid State Electrochem.* **12** 885–94

[66] Lagadec M F, Zahn R and Wood V 2019 Characterization and performance evaluation of lithium-ion battery separators *Nat. Energy* **4** 16–25

[67] Barai A, Chouchelamane G H, Guo Y, McGordon A and Jennings P 2015 A study on the impact of lithium-ion cell relaxation on electrochemical impedance spectroscopy *J. Power Sources* **280** 74–80

[68] Barai A, Guo Y, McGordon A and Jennings P 2014 An exploration of Li-ion cell relaxation using EIS *FISITA 2014 World Automot. Congr. - Proc.*

[69] Robinson J B, Darr J A, Eastwood D S, Hinds G, Lee P D, Shearing P R, Taiwo O O and Brett D J L 2014 Non-uniform temperature distribution in Li-ion batteries during discharge – A combined thermal imaging, X-ray micro-tomography and electrochemical impedance approach *J. Power Sources* **252** 51–7

[70] Zhang G, Shaffer C E, Wang C-Y and Rahn C D 2013 In-Situ Measurement of Current Distribution in a Li-Ion Cell *J. Electrochem. Soc.* **160** A610–5

[71] Naha A, Han S, Agarwal S, Guha A, Khandelwal A, Tagade P, Hariharan K S, Kolake S M, Yoon J and Oh B 2020 An Incremental Voltage Difference Based Technique for Online State of Health Estimation of Li-ion Batteries *Sci. Rep.* **10** 1–11

[72] Li K, Xue Y, Cui S and Niu Q 2014 *Intelligent Computing in Smart Grid and Electrical Vehicles* vol 463 (Springer)

[73] Qurthobi A, Pambudi A B K, Darmawan D and Iskandar R F 2018 Correlation between battery voltage under loaded condition and estimated state of charge at valve-regulated lead acid battery on discharge condition using open circuit voltage method *Int. J. Power Electron. Drive Syst.* **9** 357–64

[74] Leow Y Y, Ooi C A and Hamidi M N 2020 Performance evaluation of grid-connected power conversion systems integrated with real-time battery monitoring in a battery energy storage system *Electr. Eng.* **102** 245–58

[75] Komaba S, Shimomura K, Yabuuchi N, Ozeki T, Yui H and Konno K 2011 Study on Polymer Binders for High-Capacity SiO Negative Electrode of Li-Ion Batteries *J. Phys. Chem. C* **115** 13487–95

[76] Zhou M, Cai T, Pu F, Chen H, Wang Z, Zhang H and Guan S 2013 Graphene/carbon-coated si nanoparticle hybrids as high-performance anode materials for li-ion batteries *ACS Appl. Mater. Interfaces* **5** 3449–55

[77] Petzl M, Kasper M and Danzer M A 2015 Lithium plating in a commercial lithium-ion battery – A low-temperature aging study ed W A van Schalkwijk and B Scrosati *J. Power Sources* **275** 799–807

[78] Zheng Y, Ouyang M, Lu L and Li J 2015 Understanding aging mechanisms in lithium-ion battery packs: From cell capacity loss to pack capacity evolution *J. Power Sources* **278** 287–95

[79] Rivera-Barrera J, Muñoz-Galeano N and Sarmiento-Maldonado H 2017 SoC Estimation for Lithium-ion Batteries: Review and Future Challenges *Electronics* **6** 102

[80] Gismero A, Schaltz E and Stroe D I 2020 Recursive state of charge and state of health estimation method for lithium-ion batteries based on coulomb counting and open circuit voltage *Energies* **13**

[81] Kim J, Seo G S, Chun C, Cho B H and Lee S 2012 OCV hysteresis effect-based SOC estimation in extended Kalman filter algorithm for a LiFePO 4/C cell *2012 IEEE Int. Electr. Veh. Conf. IEVC 2012*

[82] Liu S, Wang J, Liu Q, Tang J, Liu H, Zhou Y and Pan X 2021 A Novel Discharge Mode Identification Method for Series-Connected Battery Pack Online State-of-Charge Estimation over A Wide Life Scale *IEEE Trans. Power Electron.* **36** 326–41

[83] Zhang S, Guo X, Dou X and Zhang X 2020 A data-driven coulomb counting method for state of charge calibration and estimation of lithium-ion battery *Sustain. Energy Technol. Assessments* **40**

[84] Zhang S, Guo X, Dou X and Zhang X 2020 A rapid online calculation method for state of health of lithium-ion battery based on coulomb counting method and differential voltage analysis *J. Power Sources* **479** 228740

[85] Mian Qaisar S 2020 A Proficient Li-Ion Battery State of Charge Estimation Based on Event-Driven Processing *J. Electr. Eng. Technol.* **15** 1871–7

[86] Wu T H and Moo C S 2017 State-of-Charge Estimation with State-of-Health Calibration for Lithium-Ion Batteries *Energies* **10** 987

[87] Garmendia M, Gandiaga I, Perez G, Viscarret U and Etxeberria-Otadui I 2013 Proposal and validation of a SOC estimation algorithm of LiFePO4 battery packs for traction applications *World Electr. Veh. J.* **6** 771–81

[88] He L and Guo D 2019 An Improved Coulomb Counting Approach Based on Numerical Iteration for SOC Estimation with Real-Time Error Correction Ability *IEEE Access* **7** 74274–82

[89] Sarrafan K, Muttaqi K M and Sutanto D 2020 Real-Time State-of-Charge Tracking Embedded in the Advanced Driver Assistance System of Electric Vehicles *IEEE Trans. Intell. Veh.* **5** 497–507

[90] Chao-Tsung M 2019 Design and Implementation of a Hybrid Real-Time State of Charge Estimation Scheme for Battery Energy Storage Systems *Processes* **8** 2

[91] Ganeshan A and Shanmughasundaram R 2019 Estimation of Soc and Soh Using Mixed Neural Network and Coulomb Counting Algorithm *Int. J. Innov. Technol. Explor. Eng.* **8** 2557–61

[92] Zhao L, Lin M and Chen Y 2016 Least-squares based coulomb counting method and its application for state-of-charge (SOC) estimation in electric vehicles *Int. J. Energy Res.* **40** 1389–99

[93] González I, Ramiro A, Calderón M, Calderón A J and González J F 2012 Estimation of the state-of-charge of gel lead-acid batteries and application to the control of a stand-alone wind-solar test-bed with hydrogen support *Int. J. Hydrogen Energy* **37** 11090–103

[94] Xie J, Ma J and Bai K 2018 Enhanced Coulomb Counting Method for State-of-Charge Estimation of Lithium-ion Batteries based on Peukert's Law and Coulombic Efficiency *J. Power Electron.* **18** 910–22

[95] Lu Z, Yu X L, Wei L C, Cao F, Zhang L Y, Meng X Z and Jin L W 2019 A comprehensive experimental study on temperature-dependent performance of lithium-ion battery *Appl. Therm. Eng.* **158**

[96] Lindgren J and Lund P D 2016 Effect of extreme temperatures on battery charging and performance of electric vehicles *J. Power Sources* **328** 37–45

[97] Hausmann A and Depcik C 2013 Expanding the Peukert equation for battery capacity modeling through inclusion of a temperature dependency *J. Power Sources* **235** 148–58

[98] Liao L, Zuo P, Ma Y, Chen X, An Y, Gao Y and Yin G 2012 Effects of temperature on charge/discharge behaviors of LiFePO4 cathode for Li-ion batteries *Electrochim. Acta* **60** 269–73

[99] Feng F, Lu R and Zhu C 2014 A Combined State of Charge Estimation Method for Lithium-Ion Batteries Used in a Wide Ambient Temperature Range *Energies* **7** 3004–32

[100] Choi W, Shin H-C, Kim J M, Choi J-Y and Yoon W-S 2020 Modeling and Applications of Electrochemical Impedance Spectroscopy (EIS) for Lithium-ion Batteries *J. Electrochem. Sci. Technol.* **11** 1–13

[101] Zhang S S, Xu K and Jow T R 2004 Electrochemical impedance study on the

low temperature of Li-ion batteries *Electrochim. Acta* **49** 1057–61

[102] Zhang S S 2007 Electrochemical study of the formation of a solid electrolyte interface on graphite in a LiBC2O4F2-based electrolyte *J. Power Sources* **163** 713–8

[103] Yokoshima T, Mukoyama D, Nara H, Maeda S, Nakazawa K, Momma T and Osaka T 2017 Impedance Measurements of Kilowatt-Class Lithium Ion Battery Modules/Cubicles in Energy Storage Systems by Square-Current Electrochemical Impedance Spectroscopy *Electrochim. Acta* **246** 800–11

[104] Hoshi Y, Yakabe N, Isobe K, Saito T, Shitanda I and Itagaki M 2016 Wavelet transformation to determine impedance spectra of lithium-ion rechargeable battery *J. Power Sources* **315** 351–8

[105] Al Nazer R, Cattin V, Granjon P, Montaru M and Ranieri M 2013 Broadband identification of battery electrical impedance for HEVs *IEEE Trans. Veh. Technol.* **62** 2896–905

[106] Howey D A, Mitcheson P D, Yufit V, Offer G J and Brandon N P 2014 Online Measurement of Battery Impedance Using Motor Controller Excitation *IEEE Trans. Veh. Technol.* **63** 2557–66

[107] Lipu M S H, Hannan M A, Hussain A, Hoque M M, Ker P J, Saad M H M and Ayob A 2018 A review of state of health and remaining useful life estimation methods for lithium-ion battery in electric vehicles: Challenges and recommendations *J. Clean. Prod.* **205** 115–33

[108] Ungurean L, Cârstoiu G, Micea M V. and Groza V 2017 Battery state of health estimation: a structured review of models, methods and commercial devices *Int. J. Energy Res.* **41** 151–81

[109] Zhang Y, Tang Q, Zhang Y, Wang J, Stimming U and Lee A A 2020

Identifying degradation patterns of lithium ion batteries from impedance spectroscopy using machine learning *Nat. Commun.* **11** 6–11

[110] Guha A and Patra A 2018 Online Estimation of the Electrochemical Impedance Spectrum and Remaining Useful Life of Lithium-Ion Batteries *IEEE Trans. Instrum. Meas.* **67** 1836–49

[111] Guha A and Patra A 2017 State of Health Estimation of Lithium-Ion Batteries Using Capacity Fade and Internal Resistance Growth Models *IEEE Trans. Transp. Electrif.* **4** 135–46

[112] Galeotti M, Cinà L, Giammanco C, Cordiner S and Di Carlo A 2015 Performance analysis and SOH (state of health) evaluation of lithium polymer batteries through electrochemical impedance spectroscopy *Energy* **89** 678–86

[113] Guo D, Yang G, Zhao G, Yi M, Feng X, Han X, Lu L and Ouyang M 2020 Determination of the differential capacity of lithium-ion batteries by the deconvolution of electrochemical impedance spectra *Energies* **13**

[114] Zhou X, Pan Z, Han X, Lu L and Ouyang M 2019 An easy-to-implement multi-point impedance technique for monitoring aging of lithium ion batteries *J. Power Sources* **417** 188–92

[115] Wang X, Wei X and Dai H 2019 Estimation of state of health of lithium-ion batteries based on charge transfer resistance considering different temperature and state of charge *J. Energy Storage* **21** 618–31

[116] Rue A La, Weddle P J, Ma M, Hendricks C, Kee R J and Vincent T L 2019 State-of-Charge Estimation of LiFePO 4 –Li 4 Ti 5 O 12 Batteries using History-Dependent Complex-Impedance *J. Electrochem. Soc.* **166** A4041–6

[117] Li M 2017 Li-ion dynamics and state of charge estimation *Renew. Energy* **100** 44–52

[118] Westerhoff U, Kroker T, Kurbach K and Kurrat M 2016 Electrochemical impedance spectroscopy based estimation of the state of charge of lithium-ion batteries *J. Energy Storage* **8** 244–56

[119] Mingant R, Bernard J and Sauvant-Moynot V 2016 Novel state-of-health diagnostic method for Li-ion battery in service *Appl. Energy* **183** 390–8

[120] Lee J-H and Choi W-J 2011 Novel State-of-Charge Estimation Method for Lithium Polymer Batteries Using Electrochemical Impedance Spectroscopy *J. Power Electron.* **11** 237–43

[121] Love C T, Virji M B V, Rocheleau R E and Swider-Lyons K E 2014 State-of-health monitoring of 18650 4S packs with a single-point impedance diagnostic *J. Power Sources* **266** 512–9

[122] Love C T and Swider-Lyons K 2012 Impedance Diagnostic for Overcharged Lithium-Ion Batteries *Electrochem. Solid-State Lett.* **15** A53

[123] Beaulieu L Y, Eberman K W, Turner R L, Krause L J and Dahn J R 2001 Colossal Reversible Volume Changes in Lithium Alloys *Electrochem. Solid-State Lett.* **4** A137

[124] Ni Z H, Wang H M, Kasim J, Fan H M, Yu T, Wu Y H, Feng Y P and Shen Z X 2007 Graphene thickness determination using reflection and contrast spectroscopy *Nano Lett.* **7** 2758–63

[125] Beaulieu L Y, Cumyn V K, Eberman K W, Krause L J and Dahn J R 2001 A system for performing simultaneous in situ atomic force microscopy/optical microscopy measurements on electrode materials for lithium-ion batteries *Rev. Sci. Instrum.* **72** 3313–9

[126] Jeong S K, Inaba M, Mogi R, Iriyama Y, Abe T and Ogumi Z 2001 Surface film formation on a graphite negative electrode in lithium-ion batteries:

Atomic force microscopy study on the effects of film-forming additives in propylene carbonate solutions *Langmuir* **17** 8281–6

[127] Li Z, Huang J, Yann Liaw B, Metzler V and Zhang J 2014 A review of lithium deposition in lithium-ion and lithium metal secondary batteries *J. Power Sources* **254** 168–82

[128] Wang G, Shen X, Yao J and Park J 2009 Graphene nanosheets for enhanced lithium storage in lithium ion batteries *Carbon N. Y.* **47** 2049–53

[129] Zhu Y, Murali S, Cai W, Li X, Suk J W, Potts J R and Ruoff R S 2010 Graphene and graphene oxide: Synthesis, properties, and applications *Adv. Mater.* **22** 3906–24

[130] Nie M, Chalasani D, Abraham D P, Chen Y, Bose A and Lucht B L 2013 Lithium Ion Battery Graphite Solid Electrolyte Interphase Revealed by Microscopy and Spectroscopy *J. Phys. Chem. C* **117** 1257–67

[131] Abraham D P, Twesten R D, Balasubramanian M, Kropf J, Fischer D, McBreen J, Petrov I and Amine K 2003 Microscopy and Spectroscopy of Lithium Nickel Oxide-Based Particles Used in High Power Lithium-Ion Cells *J. Electrochem. Soc.* **150** A1450

[132] Nie M, Abraham D P, Chen Y, Bose A and Lucht B L 2013 Silicon solid electrolyte interphase (SEI) of lithium ion battery characterized by microscopy and spectroscopy *J. Phys. Chem. C* **117** 13403–12

[133] Maranchi J P, Hepp A F and Kumta P N 2003 High Capacity, Reversible Silicon Thin-Film Anodes for Lithium-Ion Batteries *Electrochem. Solid-State Lett.* **6** A198

[134] Guillet J P, Recur B, Frederique L, Bousquet B, Canioni L, Manek-Hönninger I, Desbarats P and Mounaix P 2014 Review of Terahertz Tomography

Techniques *J. Infrared, Millimeter, Terahertz Waves* **35** 382–411

[135] Maire E and Withers P J 2014 Quantitative X-ray tomography *Int. Mater. Rev.* **59** 1–43

[136] Taiwo O O, Finegan D P, Eastwood D S, Fife J L, Brown L D, Darr J A, Lee P D, Brett D J L and Shearing P R 2016 Comparison of three-dimensional analysis and stereological techniques for quantifying lithium-ion battery electrode microstructures *J. Microsc.* **263** 280–92

[137] Ebner M, Geldmacher F, Marone F, Stampanoni M and Wood V 2013 X-Ray Tomography of Porous, Transition Metal Oxide Based Lithium Ion Battery Electrodes *Adv. Energy Mater.* **3** 845–50

[138] Gelb J, Finegan D P, Brett D J L and Shearing P R 2017 Multi-scale 3D investigations of a commercial 18650 Li-ion battery with correlative electron- and X-ray microscopy *J. Power Sources* **357** 77–86

[139] Paz-Garcia J M, Taiwo O O, Tudisco E, Finegan D P, Shearing P R, Brett D J L and Hall S A 2016 4D analysis of the microstructural evolution of Si-based electrodes during lithiation: Time-lapse X-ray imaging and digital volume correlation *J. Power Sources* **320** 196–203

[140] Tariq F, Yufit V, Eastwood D S, Merla Y, Biton M, Wu B, Chen Z, Freedman K, Offer G, Peled E, Lee P D, Golodnitsky D and Brandon N 2014 In-operando X-ray tomography study of lithiation induced delamination of Si based anodes for lithium-ion batteries *ECS Electrochem. Lett.* **3** 76–8

[141] Tariq F, Yufit V, Kishimoto M, Shearing P R, Menkin S, Golodnitsky D, Gelb J, Peled E and Brandon N P 2014 Three-dimensional high resolution X-ray imaging and quantification of lithium ion battery mesocarbon microbead anodes *J. Power Sources* **248** 1014–20

[142] Heenan T M M, Finegan D P, Tjaden B, Lu X, Iacoviello F, Millichamp J, Brett D J L and Shearing P R 2018 4D nano-tomography of electrochemical energy devices using lab-based X-ray imaging *Nano Energy* **47** 556–65

[143] Lu X, Bertei A, Finegan D P, Tan C, Daemi S R, Weaving J S, O'Regan K B, Heenan T M M, Hinds G, Kendrick E, Brett D J L and Shearing P R 2020 3D microstructure design of lithium-ion battery electrodes assisted by X-ray nano-computed tomography and modelling *Nat. Commun.* **11** 1–13

[144] Carter R, Huhman B, Love C T and Zenyuk I V. 2018 X-ray computed tomography comparison of individual and parallel assembled commercial lithium iron phosphate batteries at end of life after high rate cycling *J. Power Sources* **381** 46–55

[145] Yufit V, Shearing P, Hamilton R W, Lee P D, Wu M and Brandon N P 2011 Investigation of lithium-ion polymer battery cell failure using X-ray computed tomography *Electrochem. commun.* **13** 608–10

[146] Kok M D R, Robinson J B, Weaving J S, Jnawali A, Pham M, Iacoviello F, Brett D J L and Shearing P R 2019 Virtual unrolling of spirally-wound lithium-ion cells for correlative degradation studies and predictive fault detection *Sustain. Energy Fuels* **3** 2972–6

[147] Mussa A S, Lindbergh G, Klett M, Gudmundson P, Svens P and Lindström R W 2018 Inhomogeneous active layer contact loss in a cycled prismatic lithium-ion cell caused by the jelly-roll curvature *J. Energy Storage* **20** 213–7

[148] Willenberg L, Dechent P, Fuchs G, Teuber M, Eckert M, Graff M, Kürten N, Sauer D U and Figgemeier E 2020 The Development of Jelly Roll Deformation in 18650 Lithium-Ion Batteries at Low State of Charge *J. Electrochem. Soc.* **167** 120502

[149] Pfrang A, Kersys A, Kriston A, Sauer D U, Rahe C, Käbitz S and Figgemeier

E 2018 Long-term cycling induced jelly roll deformation in commercial 18650 cells *J. Power Sources* **392** 168–75

[150] Pfrang A, Kersys A, Kriston A, Sauer D U, Rahe C, Käbitz S and Figgemeier E 2019 Geometrical Inhomogeneities as Cause of Mechanical Failure in Commercial 18650 Lithium Ion Cells *J. Electrochem. Soc.* **166** A3745–52

[151] Sharp M, Darst J J, Hughes P, Billman J, Pham M, Petrushenko D, Heenan T M M, Jervis R, Owen R, Patel D, Wenjia D, Michael H, Rack A, Magdysyuk O V., Connolley T, Brett D J L, Hinds G, Keyser M, Darcy E, Shearing P R, Walker W and Finegan D P 2022 Thermal Runaway of Li-Ion Cells: How Internal Dynamics, Mass Ejection, and Heat Vary with Cell Geometry and Abuse Type *J. Electrochem. Soc.* **169** 020526

[152] Quinn J B, Waldmann T, Richter K, Kasper M and Wohlfahrt-Mehrens M 2018 Energy Density of Cylindrical Li-Ion Cells: A Comparison of Commercial 18650 to the 21700 Cells *J. Electrochem. Soc.* **165** A3284–91

[153] Waldmann T, Scurtu R-G, Richter K and Wohlfahrt-Mehrens M 2020 18650 vs. 21700 Li-ion cells – A direct comparison of electrochemical, thermal, and geometrical properties *J. Power Sources* **472** 228614

[154] Shateri N, Auger D J, Fotouhi A, Brighton J, Du W, Owen R E, Brett D J L and Shearing P R 2022 Investigation of the Effect of Temperature on Lithium-Sulfur Cell Cycle Life Performance Using System Identification and X-Ray Tomography *Batter. Supercaps* **202200035**

[155] Du W, Owen R E, Jnawali A, Neville T P, Iacoviello F, Zhang Z, Liatard S, Brett D J L and Shearing P R 2022 In-situ X-ray tomographic imaging study of gas and structural evolution in a commercial Li-ion pouch cell *J. Power Sources* **520** 230818

[156] Zhu X, Wang H, Allu S, Gao Y, Cakmak E, Hopkins E J, Veith G M and

Wang Z 2020 Investigation on capacity loss mechanisms of lithium-ion pouch cells under mechanical indentation conditions *J. Power Sources* **465** 228314

[157] Vanpeene V, Villanova J, Suuronen J P, King A, Bonnin A, Adrien J, Maire E and Roué L 2020 Monitoring the morphological changes of Si-based electrodes by X-ray computed tomography: A 4D-multiscale approach *Nano Energy* **74**

[158] Vanpeene V, Villanova J, King A, Lestriez B, Maire E and Roué L 2019 Dynamics of the Morphological Degradation of Si-Based Anodes for Li-Ion Batteries Characterized by In Situ Synchrotron X-Ray Tomography *Adv. Energy Mater.* **9** 1–13

[159] Choi P, Parimalam B S, Su L, Reeja-Jayan B and Litster S 2021 Operando Particle-Scale Characterization of Silicon Anode Degradation during Cycling by Ultrahigh-Resolution X-ray Microscopy and Computed Tomography *ACS Appl. Energy Mater.* **4** 1657–65

[160] Seitzman N, Bird O F, Andrykowski R, Robbins S, Al-Jassim M M and Pylypenko S 2021 Operando X-ray Tomography Imaging of Solid-State Electrolyte Response to Li Evolution under Realistic Operating Conditions *ACS Appl. Energy Mater.* **4** 1346–55

[161] Finegan D P, Scheel M, Robinson J B, Tjaden B, Hunt I, Mason T J, Millichamp J, Di Michiel M, Offer G J, Hinds G, Brett D J L and Shearing P R 2015 In-operando high-speed tomography of lithium-ion batteries during thermal runaway *Nat. Commun.* **6** 1–10

[162] Finegan D P, Scheel M, Robinson J B, Tjaden B, Di Michiel M, Hinds G, Brett D J L and Shearing P R 2016 Investigating lithium-ion battery materials during overcharge-induced thermal runaway: An operando and multi-scale X-ray CT study *Phys. Chem. Chem. Phys.* **18** 30912–9

[163] Giannuzzi L A and Stevie F A 2005 *Introduction to Focused Ion Beams* ed L A Giannuzzi and F A Stevie (Boston, MA: Springer US)

[164] Shore K A 2013 Nanofabrication Using Focused Ion and Electron Beams: Principles and Applications *Contemp. Phys.* **54** 140–1

[165] Hutzenlaub T, Thiele S, Zengerle R and Ziegler C 2012 Three-Dimensional Reconstruction of a LiCoO2 Li-Ion Battery Cathode *Electrochem. Solid-State Lett.* **15** A33

[166] Hutzenlaub T, Asthana A, Becker J, Wheeler D R, Zengerle R and Thiele S 2013 FIB/SEM-based calculation of tortuosity in a porous LiCoO2 cathode for a Li-ion battery *Electrochem. commun.* **27** 77–80

[167] Sui T, Song B, Dluhos J, Lu L and Korsunsky A M 2015 Nanoscale chemical mapping of Li-ion battery cathode material by FIB-SEM and TOF-SIMS multi-modal microscopy *Nano Energy* **17** 254–60

[168] Frisco S, Kumar A, Whitacre J F and Litster S 2016 Understanding Li-Ion Battery Anode Degradation and Pore Morphological Changes through Nano-Resolution X-ray Computed Tomography *J. Electrochem. Soc.* **163** A2636–40

[169] Komini Babu S, Mohamed A I, Whitacre J F and Litster S 2015 Multiple imaging mode X-ray computed tomography for distinguishing active and inactive phases in lithium-ion battery cathodes *J. Power Sources* **283** 314–9

[170] Finegan D P, Vamvakeros A, Cao L, Tan C, Heenan T M M, Daemi S R, Jacques S D M, Beale A M, Di Michiel M, Smith K, Brett D J L, Shearing P R and Ban C 2019 Spatially Resolving Lithiation in Silicon–Graphite Composite Electrodes via in Situ High-Energy X-ray Diffraction Computed Tomography *Nano Lett.* **19** 3811–20

[171] Vamvakeros A, Matras D, Ashton T E, Coelho A A, Dong H, Bauer D,

Odarchenko Y, Price S W T, Butler K T, Gutowski O, Dippel A, Zimmerman M von, Darr J A, Jacques S D M and Beale A M 2021 Cycling Rate-Induced Spatially-Resolved Heterogeneities in Commercial Cylindrical Li-Ion Batteries *Small Methods* **5** 2100512

[172] Matras D, Ashton T E, Dong H, Mirolo M, Martens I, Drnec J, Darr J A, Quinn P D, Jacques S D M, Beale A M and Vamvakeros A 2022 Emerging chemical heterogeneities in a commercial 18650 NCA Li-ion battery during early cycling revealed by synchrotron X-ray diffraction tomography *J. Power Sources* **539** 231589

[173] Siegel J B, Lin X, Stefanopoulou A G, Hussey D S, Jacobson D L and Gorsich D 2011 Neutron Imaging of Lithium Concentration in LFP Pouch Cell Battery *J. Electrochem. Soc.* **158** A523

[174] Nie Z, McCormack P, Bilheux H Z, Bilheux J C, Robinson J P, Nanda J and Koenig G M 2019 Probing lithiation and delithiation of thick sintered lithium-ion battery electrodes with neutron imaging *J. Power Sources* **419** 127–36

[175] Butler L G, Schillinger B, Ham K, Dobbins T A, Liu P and Vajo J J 2011 Neutron imaging of a commercial Li-ion battery during discharge: Application of monochromatic imaging and polychromatic dynamic tomography *Nucl. Instruments Methods Phys. Res. Sect. A Accel. Spectrometers, Detect. Assoc. Equip.* **651** 320–8

[176] Nazer N S, Strobl M, Kaestner A, Vie P J S and Yartys V A 2022 Operando Neutron Imaging Study of a Commercial Li-Ion Battery at Variable Charge-Discharge Current Densities *SSRN Electron. J.* 140793

[177] Michalak B, Sommer H, Mannes D, Kaestner A, Brezesinski T and Janek J 2015 Gas Evolution in Operating Lithium-Ion Batteries Studied in Situ by Neutron Imaging *Sci. Rep.* **5** 1–9

[178] Ziesche R F, Kardjilov N, Kockelmann W, Brett D J L and Shearing P R 2022 Neutron imaging of lithium batteries *Joule* **6** 35–52

[179] Kardjilov N, Manke I, Woracek R, Hilger A and Banhart J 2018 Advances in neutron imaging *Mater. Today* **21** 652–72

[180] Eastwood D S, Yufit V, Gelb J, Gu A, Bradley R S, Harris S J, Brett D J L, Brandon N P, Lee P D, Withers P J and Shearing P R 2014 Lithiation-induced dilation mapping in a lithium-ion battery electrode by 3D X-ray microscopy and digital volume correlation *Adv. Energy Mater.* **4** 1–7

[181] Ho A S, Parkinson D Y, Finegan D P, Trask S E, Jansen A N, Tong W and Balsara N P 2021 3D Detection of Lithiation and Lithium Plating in Graphite Anodes during Fast Charging *ACS Nano* **15** 10480–7

[182] Wang Y, Li Q M and Xing Y 2020 Porosity variation of lithium-ion battery separators under uniaxial tension *Int. J. Mech. Sci.* **174** 105496

[183] Hao W, Yuan Z, Li D, Zhu Z and Jiang S 2021 Study on mechanical properties and failure mechanism of 18650 Lithium-ion battery using digital image correlation and acoustic emission *J. Energy Storage* **41** 102894

[184] Dai C, Wang Z, Liu K, Zhu X, Liao X, Chen X and Pan Y 2019 Effects of cycle times and C-rate on mechanical properties of copper foil and adhesive strength of electrodes in commercial LiCoO2 LIBs *Eng. Fail. Anal.* **101** 193–205

[185] Dai C, Li C, Huang H, Wang Z, Zhu X, Liao X, Chen X, Pan Y and Fang D 2019 In situ strain measurements and stress analysis of SiO@C composite electrodes during electrochemical cycling by using digital image correlation *Solid State Ionics* **331** 56–65

[186] Özdogru B, Dykes H, Padwal S, Harimkar S and Çapraz Ö Ö 2020

Electrochemical strain evolution in iron phosphate composite cathodes during lithium and sodium ion intercalation *Electrochim. Acta* **353** 136594

[187] Yang W, Xie H, Shi B, Song H, Qiu W and Zhang Q 2019 In-situ experimental measurements of lithium concentration distribution and strain field of graphite electrodes during electrochemical process *J. Power Sources* **423** 174–82

[188] Tao R, Zhu J, Zhang Y, Song W-L, Chen H and Fang D 2020 Quantifying the 2D anisotropic displacement and strain fields in graphite-based electrode via in situ scanning electron microscopy and digital image correlation *Extrem. Mech. Lett.* **35** 100635

[189] Koohbor B, Sang L, Çapraz Ö Ö, Gewirth A A and Sottos N R 2021 In Situ Strain Measurement in Solid-State Li-Ion Battery Electrodes *J. Electrochem. Soc.* **168** 010516

[190] Vetter J, Novák P, Wagner M R, Veit C, Möller K-C, Besenhard J O, Winter M, Wohlfahrt-Mehrens M, Vogler C and Hammouche A 2005 Ageing mechanisms in lithium-ion batteries *J. Power Sources* **147** 269–81

[191] Sato N 2001 Thermal behavior analysis of lithium-ion batteries for electric and hybrid vehicles *J. Power Sources* **99** 70–7

[192] Arora P, Ehite R E and Doyle M 1998 Capacity Fade Mechanisms and Side Reactions in Lithium-Ion Batteries *J. Electrochem. Soc.* **145** 3647–67

[193] Hsieh J 2015 *Computed Tomography: Principles, Design, Artifacts, and Recent Advances*

[194] Stock S R 2008 Recent advances in X-ray microtomography applied to materials *Int. Mater. Rev.* **53** 129–81

[195] Fitzgerald R 2000 Phase-sensitive X-ray imaging ; New approaches that can detect X-ray phase shifts within soft tissues show promise for clinical and biological applications *Phys. Today* **53** 23–8

[196] Stock S R 1999 X-ray microtomography of materials *Int. Mater. Rev.* **44** 141–64

[197] Schindelin J, Arganda-Carreras I, Frise E, Kaynig V, Longair M, Pietzsch T, Preibisch S, Rueden C, Saalfeld S, Schmid B, Tinevez J-Y, White D J, Hartenstein V, Eliceiri K, Tomancak P and Cardona A 2012 Fiji: an open-source platform for biological-image analysis *Nat. Methods* **9** 676–82

[198] Justusson B I 2006 Median filtering: Statistical properties *Two-Dimensional Digital Signal Prcessing II: Transforms and Median Filters* pp 161–96

[199] Stewart R R 1985 Median filtering: Review and a new F/K analogue design *J. Can. Soc. Explor. Geophys.* **21** 54–63

[200] Guang Deng 2011 A Generalized Unsharp Masking Algorithm *IEEE Trans. Image Process.* **20** 1249–61

[201] Jnawali A, Radhakrishnan A N P, Kok M D R, Iacoviello F, Brett D J L and Shearing P R 2022 Motion-enhancement assisted digital image correlation of lithium-ion batteries during lithiation *J. Power Sources* **527** 231150

[202] van der Walt S, Schönberger J L, Nunez-Iglesias J, Boulogne F, Warner J D, Yager N, Gouillart E and Yu T 2014 scikit-image: image processing in Python *PeerJ* **2** e453

[203] Zach C, Pock T and Bischof H 2007 A Duality Based Approach for Realtime TV-L 1 Optical Flow *Pattern Recognition* vol 0 (Berlin, Heidelberg: Springer Berlin Heidelberg) pp 214–23

[204] Wedel A, Pock T, Zach C, Bischof H and Cremers D 2009 An Improved Algorithm for TV-L 1 Optical Flow *Lecture Notes in Computer Science (including subseries Lecture Notes in Artificial Intelligence and Lecture Notes in Bioinformatics)* vol 5604 LNCS pp 23–45

[205] Sánchez Pérez J, Meinhardt-Llopis E and Facciolo G 2013 TV-L1 Optical Flow Estimation *Image Process. Line* **3** 137–50

[206] Lorensen W E and Cline H E 1987 Marching cubes: A high resolution 3D surface construction algorithm *Proceedings of the 14th annual conference on Computer graphics and interactive techniques - SIGGRAPH '87* vol 21 (New York, New York, USA: ACM Press) pp 163–9

[207] Radhakrishnan A N P, Pradas M, Sorensen E, Kalliadasis S and Gavriilidis A 2019 Hydrodynamic Characterization of Phase Separation in Devices with Microfabricated Capillaries *Langmuir* **35** 8199–209

[208] Danielsson P-E and Seger O 1990 Generalized and Separable Sobel Operators *Machine Vision for Three-Dimensional Scenes* ed H Freeman (Academic Press, Inc.) pp 347–79

[209] Bach T C, Schuster S F, Fleder E, Müller J, Brand M J, Lorrmann H, Jossen A and Sextl G 2016 Nonlinear aging of cylindrical lithium-ion cells linked to heterogeneous compression *J. Energy Storage* **5** 212–23

[210] Wang C, Zhang X, Appleby A J, Chen X and Little F E 2002 Self-discharge of secondary lithium-ion graphite anodes *J. Power Sources* **112** 98–104

[211] Pistoia G, Antonini A, Rosati R and Zane D 1996 Storage characteristics of cathodes for Li-ion batteries *Electrochim. Acta* **41** 2683–9

[212] Gulsoy B, Vincent T A, Sansom J E H and Marco J 2022 In-situ temperature monitoring of a lithium-ion battery using an embedded thermocouple for

smart battery applications *J. Energy Storage* **54** 105260

[213] Sonwane A, Yuan C and Xu J 2021 Coupling Effect of State-of-Charge and Strain Rate on the Mechanical Behavior of Electrodes of 21700 Lithium-Ion Battery *J. Electrochem. Energy Convers. Storage* **18** 1–11

[214] Maheshwari A, Heck M and Santarelli M 2018 Cycle aging studies of lithium nickel manganese cobalt oxide-based batteries using electrochemical impedance spectroscopy *Electrochim. Acta* **273** 335–48

[215] Abu-Sharkh S and Doerffel D 2004 Rapid test and non-linear model characterisation of solid-state lithium-ion batteries *J. Power Sources* **130** 266–74

[216] Heenan T M M, Jnawali A, Kok M D R, Tranter T G, Tan C, Dimitrijevic A, Jervis R, Brett D J L and Shearing P R 2020 An Advanced Microstructural and Electrochemical Datasheet on 18650 Li-Ion Batteries with Nickel-Rich NMC811 Cathodes and Graphite-Silicon Anodes *J. Electrochem. Soc.* **167** 140530

[217] Bloom I, Jansen A N, Abraham D P, Knuth J, Jones S A, Battaglia V S and Henriksen G L 2005 Differential voltage analyses of high-power, lithium-ion cells *J. Power Sources* **139** 295–303

[218] Sørensen D R, Heere M, Zhu J, Darma M S D, Zimnik S M, Mühlbauer M J, Mereacre L, Baran V, Senyshyn A, Knapp M and Ehrenberg H 2020 Fatigue in High-Energy Commercial Li Batteries while Cycling at Standard Conditions: An In Situ Neutron Powder Diffraction Study *ACS Appl. Energy Mater.* **3** 6611–22

[219] Qi Y, Guo H, Hector L G and Timmons A 2010 Threefold Increase in the Young's Modulus of Graphite Negative Electrode during Lithium Intercalation *J. Electrochem. Soc.* **157** A558

[220] Louli A J, Li J, Trussler S, Fell C R and Dahn J R 2017 Volume, Pressure and Thickness Evolution of Li-Ion Pouch Cells with Silicon-Composite Negative Electrodes *J. Electrochem. Soc.* **164** A2689–96

[221] Yin S C, Rho Y H, Swainson I and Nazar L F 2006 X-ray/neutron diffraction and electrochemical studies of lithium De/Re-intercalation in Li1-xCo1/3Ni1/3Mn 1/3O2 (x = 0 → 1) *Chem. Mater.* **18** 1901–10

[222] Markervich E, Salitra G, Levi M D and Aurbach D 2005 Capacity fading of lithiated graphite electrodes studied by a combination of electroanalytical methods, Raman spectroscopy and SEM *J. Power Sources* **146** 146–50

[223] Liu H, Wolf M, Karki K, Yu Y S, Stach E A, Cabana J, Chapman K W and Chupas P J 2017 Intergranular Cracking as a Major Cause of Long-Term Capacity Fading of Layered Cathodes *Nano Lett.* **17** 3452–7

[224] Horn B K P and Schunck B G 1981 Determining optical flow *Artif. Intell.* **17** 185–203

[225] Wadhwa N, Rubinstein M, Durand F and Freeman W T 2013 Phase-based video motion processing *ACM Trans. Graph.* **32**

[226] Nishijima M, Ootani T, Kamimura Y, Sueki T, Esaki S, Murai S, Fujita K, Tanaka K, Ohira K, Koyama Y and Tanaka I 2014 Accelerated discovery of cathode materials with prolonged cycle life for lithium-ion battery *Nat. Commun.* **5** 1–7

[227] Reddy M V., Mauger A, Julien C M, Paolella A and Zaghib K 2020 Brief History of Early Lithium-Battery Development *Materials (Basel).* **13** 1884

[228] Chen Y, CHEN R, Tang Z and Wang L 2009 Synthesis and characterization of Zn-doped LiCo0.3Ni0.4(xMn0.3ZnxO2 cathode materials for lithium-ion batteries *J. Alloys Compd.* **476** 539–42

[229] Guo J, Sun A, Chen X, Wang C and Manivannan A 2011 Cyclability study of silicon-carbon composite anodes for lithium-ion batteries using electrochemical impedance spectroscopy *Electrochim. Acta* **56** 3981–7

[230] Martin L, Martinez H, Ulldemolins M, Pecquenard B and Le Cras F 2012 Evolution of the Si electrode/electrolyte interface in lithium batteries characterized by XPS and AFM techniques: The influence of vinylene carbonate additive *Solid State Ionics* **215** 36–44

[231] Takei K, Kumai K, Kobayashi Y, Miyashiro H, Terada N, Iwahori T and Tanaka T 2001 Cycle life estimation of lithium secondary battery by extrapolation method and accelerated aging test *J. Power Sources* **97–98** 697–701

[232] Holloway J, Maddar F, Lain M, Loveridge M, Copley M, Kendrick E and Greenwood D 2020 Determining the Limits and Effects of High-Rate Cycling on Lithium Iron Phosphate Cylindrical Cells *Batteries* **6** 57

[233] Zilberman I, Ludwig S and Jossen A 2019 Cell-to-cell variation of calendar aging and reversible self-discharge in 18650 nickel-rich, silicon–graphite lithium-ion cells *J. Energy Storage* **26** 100900

[234] Fan J and Tan S 2006 Studies on Charging Lithium-Ion Cells at Low Temperatures *J. Electrochem. Soc.* **153** A1081

[235] Waldmann T, Wilka M, Kasper M, Fleischhammer M and Wohlfahrt-Mehrens M 2014 Temperature dependent ageing mechanisms in Lithium-ion batteries - A Post-Mortem study *J. Power Sources* **262** 129–35

[236] Novák P, Joho F, Lanz M, Rykart B, Panitz J C, Alliata D, Kötz R and Haas O 2001 The complex electrochemistry of graphite electrodes in lithium-ion batteries *J. Power Sources* **97–98** 39–46

[237] Dolotko O, Senyshyn A, Mühlbauer M J, Nikolowski K and Ehrenberg H

2014 Understanding structural changes in NMC Li-ion cells by in situ neutron diffraction *J. Power Sources* **255** 197–203

[238] Zhao K, Pharr M, Cai S, Vlassak J J and Suo Z 2011 Large plastic deformation in high-capacity lithium-ion batteries caused by charge and discharge *J. Am. Ceram. Soc.* **94** s226–35

[239] Kurfer J, Westermeier M, Tammer C and Reinhart G 2012 Production of large-area lithium-ion cells – Preconditioning, cell stacking and quality assurance *CIRP Ann.* **61** 1–4

[240] Ryu H-H, Park K-J, Yoon C S and Sun Y-K 2018 Capacity Fading of Ni-Rich Li[Ni x Co y Mn 1– x – y]O 2 (0.6 ≤ x ≤ 0.95) Cathodes for High-Energy-Density Lithium-Ion Batteries: Bulk or Surface Degradation? *Chem. Mater.* **30** 1155–63

[241] Samba A, Omar N, Gualous H, Capron O, Van Den Bossche P and Van Mierlo J 2014 Impact of tab location on large format lithium-ion pouch cell based on fully coupled tree-dimensional electrochemical-thermal modeling *Electrochim. Acta* **147** 319–29

[242] Osswald P J, Erhard S V., Wilhelm J, Hoster H E and Jossen A 2015 Simulation and Measurement of Local Potentials of Modified Commercial Cylindrical Cells *J. Electrochem. Soc.* **162** A2099–105

[243] Zhang G, Shaffer C E, Wang C-Y and Rahn C D 2013 Effects of Non-Uniform Current Distribution on Energy Density of Li-Ion Cells *J. Electrochem. Soc.* **160** A2299–305

10 APPENDIX

10.1 APPENDIX FOR CHAPTER 5

10.1.1 Masking and Sobel Filtering

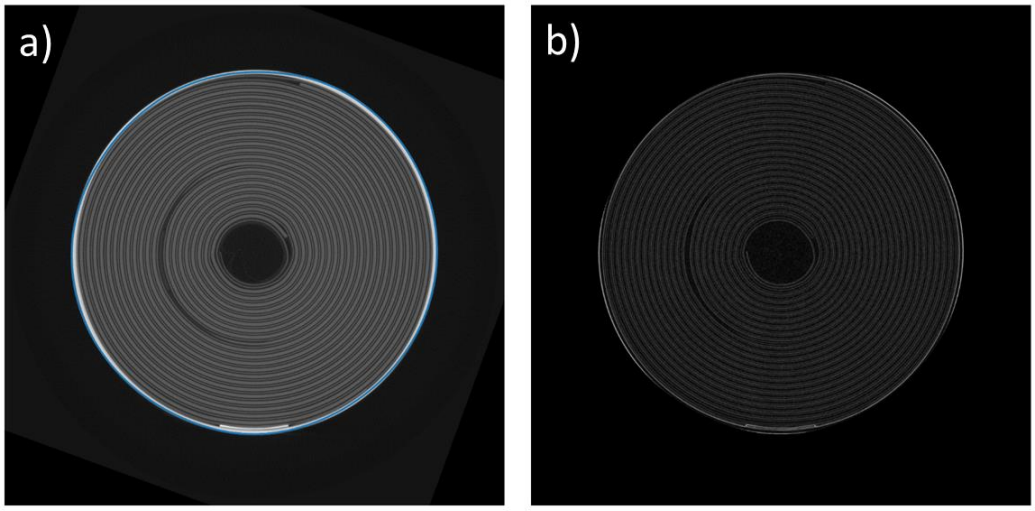

Figure A 1: An illustrative 'masked' frame of M50-P where the blue line is the outline of the cell casing from the last frame of the video, used to mask any elements outside of its perimeter, b) an illustrative Sobel filtered frame of M50-P.

10.1.2 Cell Charging Data

All the cells were charged to their upper voltage cut-off limit in four separate charging steps. In the figures below, the different steps have been combined into one graph for visual purposes.

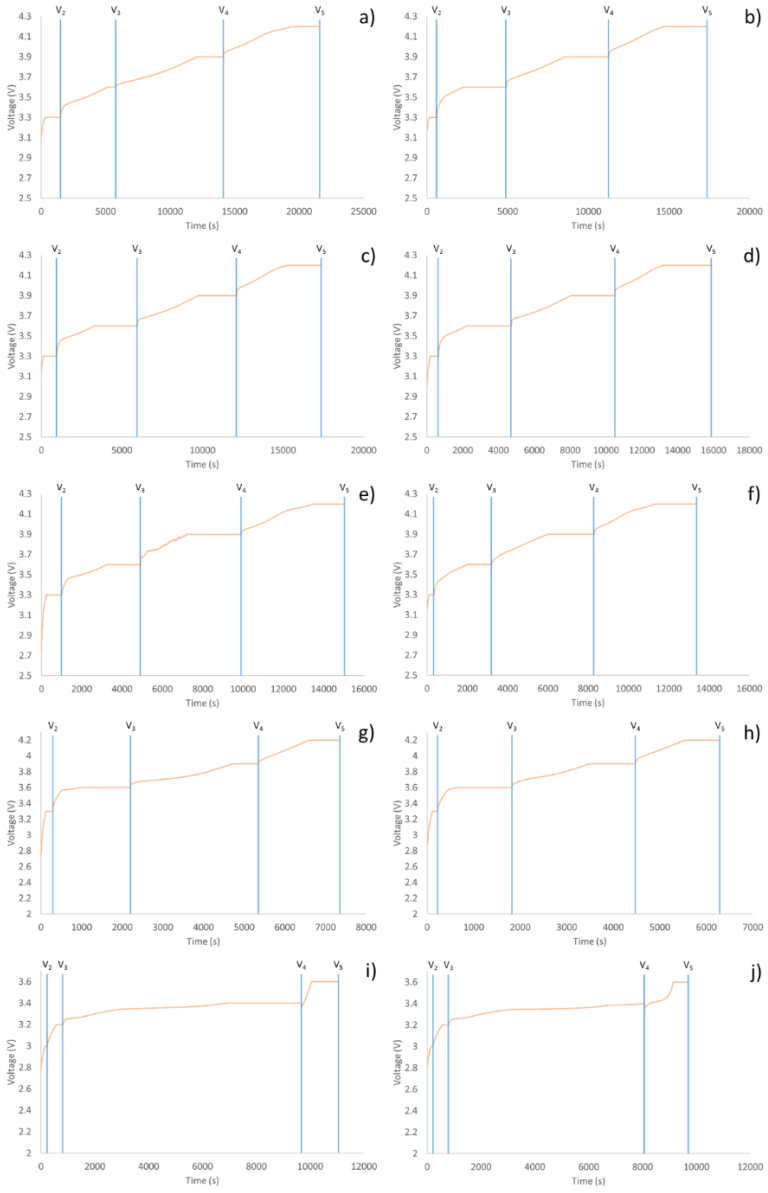

Figure A 2: Combined voltage profile during charging of: (a) M50-P, (b) M50-C, (c) MJ1-P, (d) MJ1-C, (e) VTC6-P, (f) VTC6-C, (g) HB6-P, (h) HB6-C, (i) LPC-P, (j) LPC-C.

10.1.3 Pristine and Motion Enhanced Videos of the Cells

Source videos of the pristine cells


SI_Video_1_M50_P_Source.avi


SI_Video_2_MJ1_P_Source.avi


SI_Video_3_VTC6_P_Source.avi


SI_Video_4_HB6_P_Source.avi


SI_Video_5_LPC_P_Source.avi

Enhanced videos of the pristine cells


SI_Video_6_M50_P_Enhanced.avi


SI_Video_7_MJ1_P_Enhanced.avi


SI_Video_8_VTC6_P_Enhanced.avi


SI_Video_9_HB6_P_Enhanced.avi


SI_Video_10_LPC_P_Enhanced.avi

Source videos of the cycled cells


SI_Video_11_M50_C_Source.avi


SI_Video_12_MJ1_C_Source.avi


SI_Video_13_VTC6_C_Source.avi


SI_Video_14_HB6_C_Source.avi


SI_Video_15_LPC_C_Source.avi

Enhanced videos of the cycled cells


SI_Video_16_M50_C_Enhanced.avi


SI_Video_17_MJ1_C_Enhanced.avi


SI_Video_18_VTC6_C_Enhanced.avi


SI_Video_19_HB6_C_Enhanced.avi


SI_Video_20_LPC_C_Enhanced.avi

10.2 APPENDIX FOR CHAPTER 6

10.2.1 SOH and Deformation Summaries

Table A 1: SOH and number of deformations observed in the thirty MH1 cells. Nominal capacity of the MH1 cells is 3.2 Ah.

CELL	# OF CYCLES	FINAL CHARGE CAPACITY (AH)	SOH (%)	# OF DEFORMATIONS
01	438	2.69	83.9	-
02	395	2.56	80.0	-
03	443	2.57	80.3	-
04	387	2.56	80.0	1
05	374	2.56	80.1	-
06	436	2.66	83.2	-
07	419	2.56	80.1	-
08	256	2.56	80.1	-
09	313	2.56	80.1	-
10	440	2.58	80.6	-
11	409	2.56	80.0	-
12	353	2.57	80.2	-
13	430	2.57	80.2	-
14	431	2.59	81.1	-
15	321	2.56	80.0	-
16	222	2.56	80.0	-
17	438	2.61	81.5	-
18	388	2.56	80.1	-
19	298	2.57	80.4	-
20	409	2.56	80.1	-
21	426	2.56	80.1	-
22	290	2.56	80.1	-
23	344	2.56	80.1	-
24	180	2.56	80.1	-
25	215	2.56	80.1	-
26	436	2.41	75.3	-

27	352	2.56	80.1	-
28	423	2.62	81.8	1
29	218	2.56	80.0	-
30	432	2.66	83.2	-

Table A 2: SOH and number of deformations observed in the thirty two MJ1 cells, sorted from highest to lowest in terms of SOH. Nominal capacity of the MJ1 cells is 3.5 Ah and they were all cycled for 1200 cycles.

CELL	FINAL CHARGE CAPACITY (AH)	SOH (%)	# OF DEFORMATIONS
101	2.83	80.9	1
102	2.84	81.2	2
103	2.85	81.5	3
104	2.84	81.2	1
105	2.82	80.6	3
106	2.82	80.6	0
107	2.84	81.1	2
108	2.83	80.9	3
109	2.83	81.0	2
110	2.83	80.8	1
111	2.85	81.4	3
112	2.74	78.4	2
113	2.83	80.8	3
114	2.82	80.7	2
115	2.83	80.8	2
116	2.83	80.8	3
117	2.77	79.2	2
118	2.76	78.9	1
119	2.78	79.4	2
120	2.52	71.9	3
121	2.78	79.4	0
122	2.79	79.7	2
123	2.76	78.9	2
124	2.79	79.7	2
125	2.79	79.7	2
126	2.69	76.7	3
127	2.79	79.6	3
128	2.79	79.6	1
129	2.41	69.0	2
130	2.79	79.7	2
131	2.79	79.8	0
132	2.77	79.2	1

Table A 3: Summary of the number of deformations observed for the MJ1 and MH1 cell

# OF DEFORMATIONS	# OF MJ1 CELLS	# OF MH1 CELLS
0	3	28
1	6	2
2	14	-
3	9	-

10.2.2 Consideration of Deformation

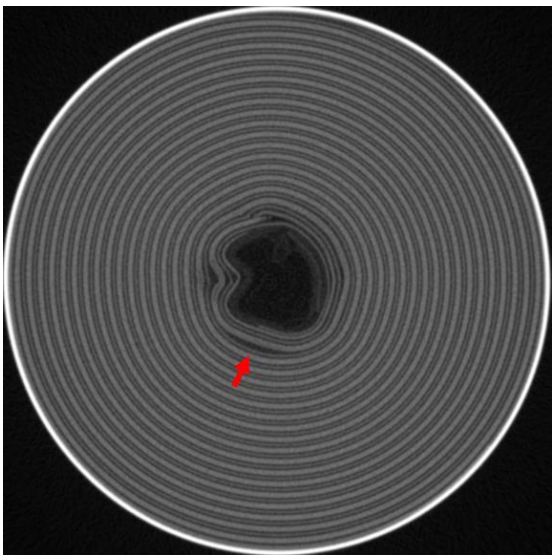

Figure A 3: A slice showing delamination of the electrode winding, as highlighted by the red arrow. In this study this is considered a deformation.

10.2.3 Virtual Unrolling of Selected Cells

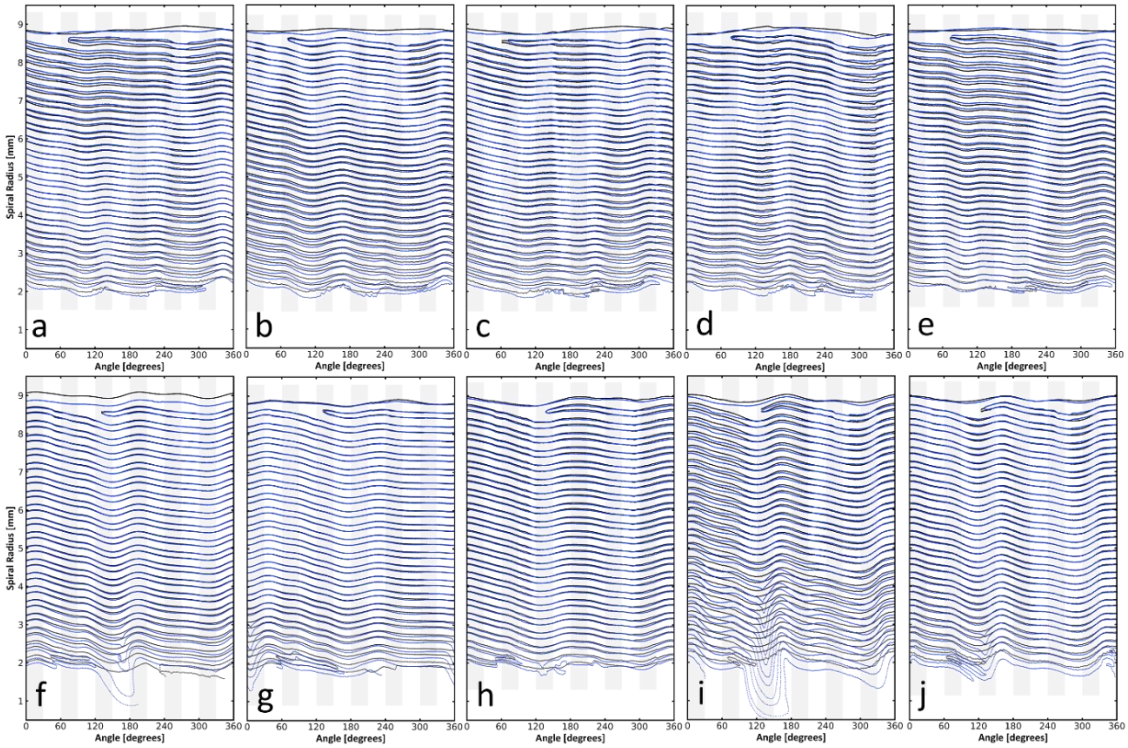

Figure A 4: Virtual unrolling of (a-e) MH1-105, 110, 115, 120, and 125, respectively, and, (f-j) MJ1-105, 110, 115, 120, and 125, respectively, showing the change in the electrode position before (black lines) and after (blue lines) cycling.

10.3 APPENDIX FOR CHAPTER 7

10.3.1 X-ray Computed Tomography

What follows are XCT slices of the 45 cells from batch A showing that 30 of those cells contain deformations where the peaks (most severe) of those deformations are located the region where the negative tab is present. As discussed in the main report, a single pair of positive and negative tabs create an uneven current distribution, which might be contributing to the formation of deformations more in the negative region.

Since the cells have been cycled for almost 2000 cycles, and have accrued heavy damage, they also contain deformations in the positive region, however, from previous works, it is believed that in most cases the deformations nucleate at the negative region [146]. X-ray slices of all the cells in batch B and batch A in their pristine state are also provided.

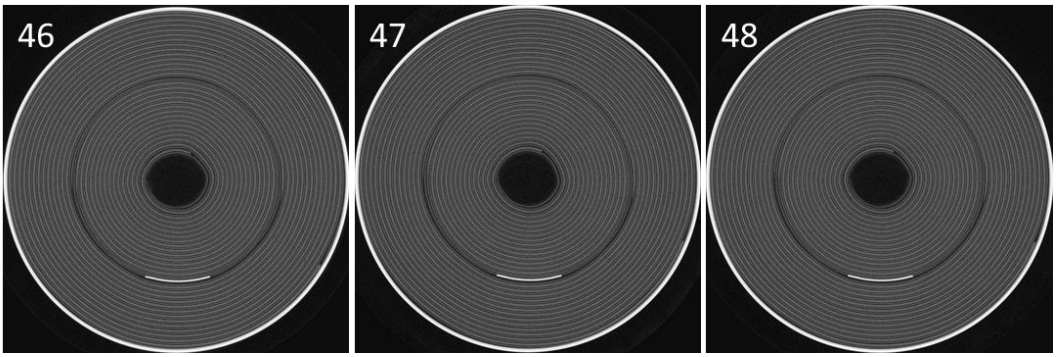

Figure A 5: XCT slices of all cells from batch B (46-48) in their pristine state.

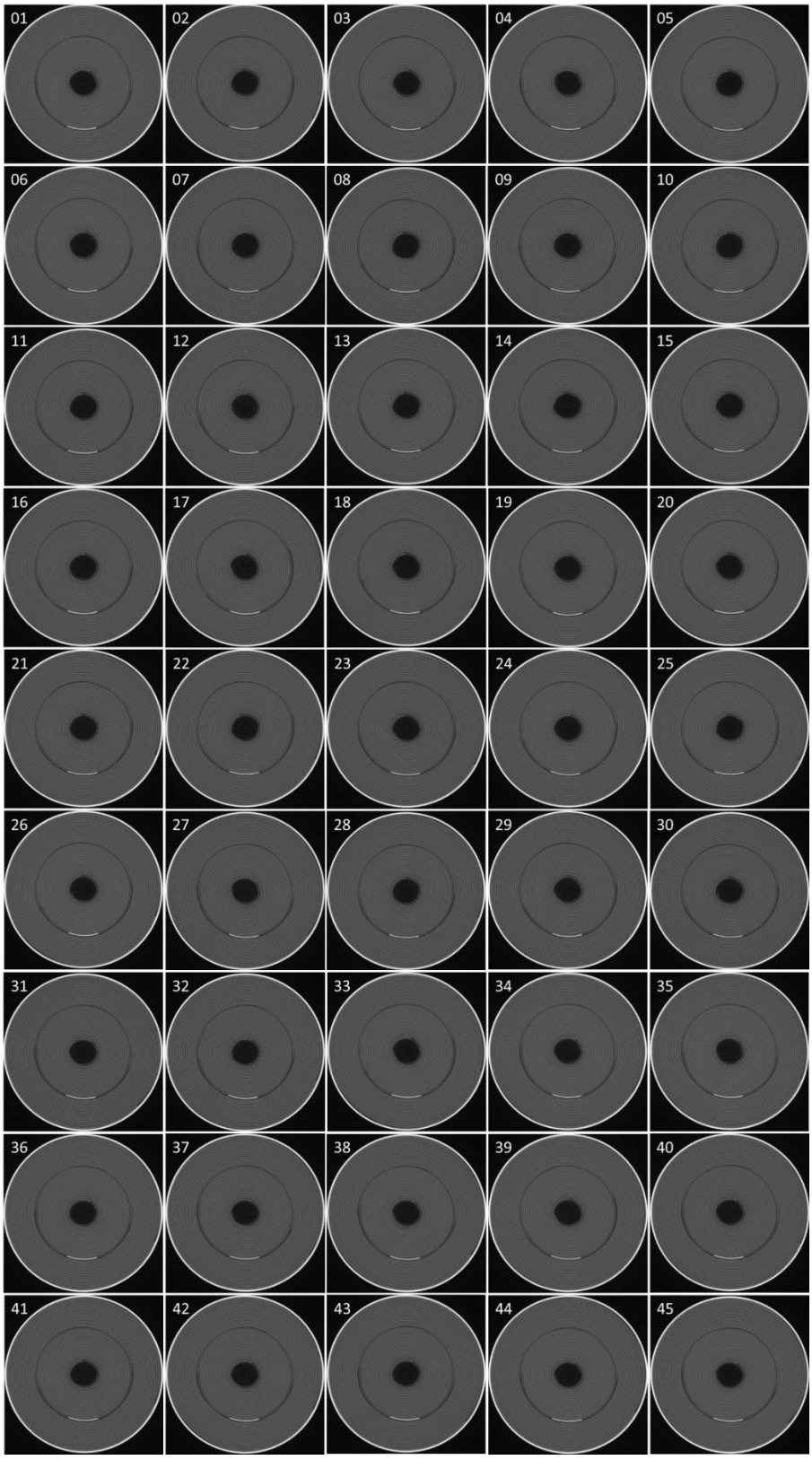

Figure A 6: XCT slices of all 45 cells in batch A before cycling.

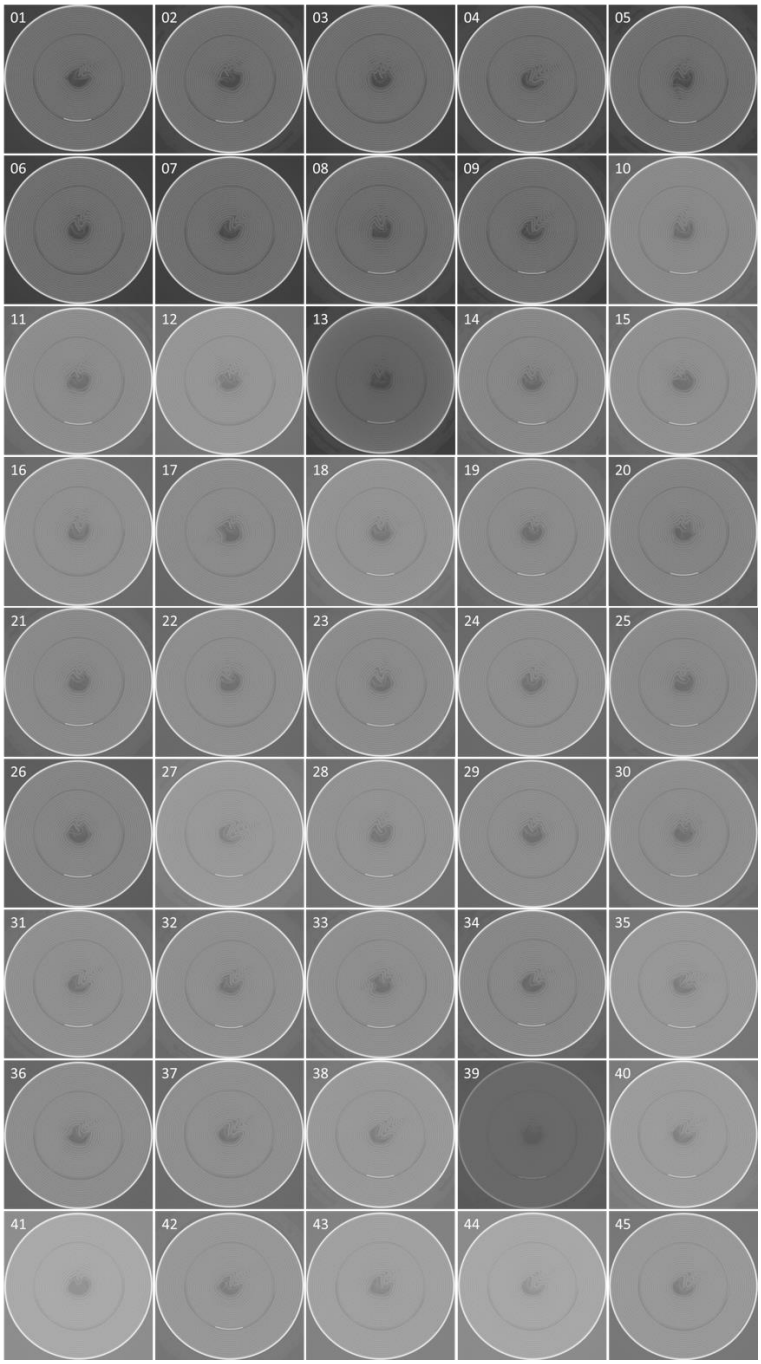

Figure A 7: XCT slices of all 45 cells in batch A.

10.3.2 Electrode Displacements

The below show the strain distributions at different voltages for the other cells in batch B that were no reported in the main chapter.

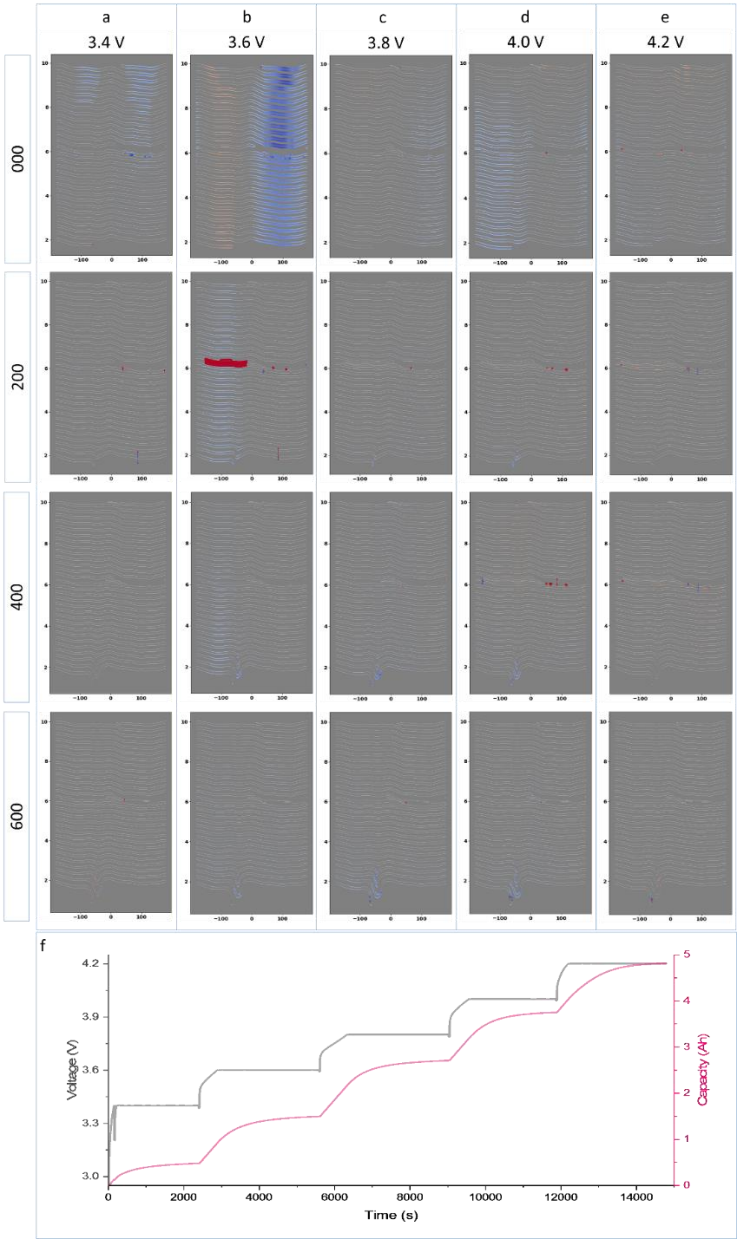

Figure A 8: Electrode displacements for cell-46 a) 2.5 V to 3.4 V, b) 3.4 V to 3.6 V, c) 3.6 V to 3.8 V, d) 3.8 V to 4.0 V, and e) 4.0 V to 4.2 V. The voltage profile at the pristine state (000) is shown in (f).

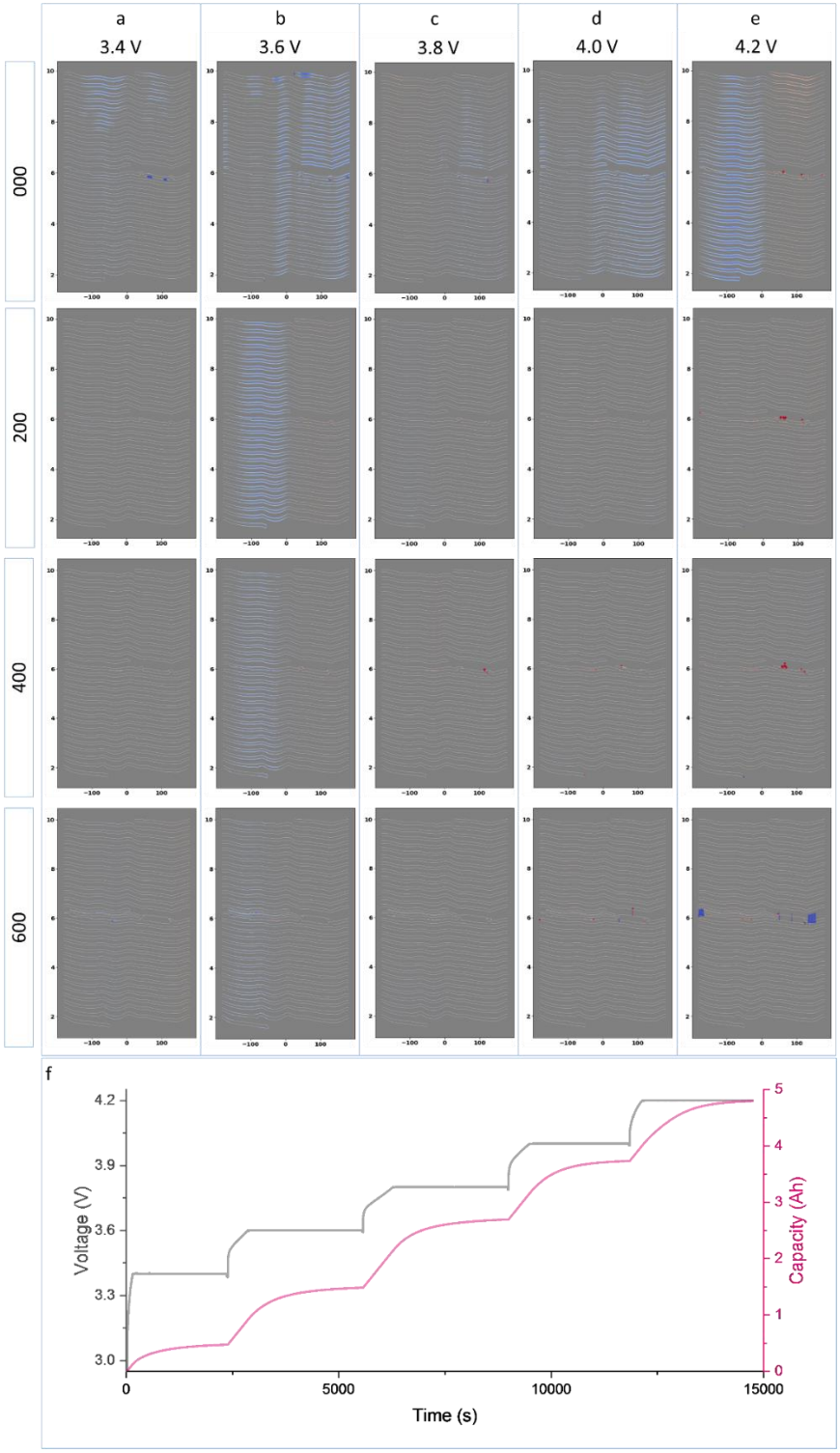

Figure A 9: Electrode displacements for cell-47 a) 2.5 V to 3.4 V, b) 3.4 V to 3.6 V, c) 3.6 V to 3.8 V, d) 3.8 V to 4.0 V, and e) 4.0 V to 4.2 V. The voltage profile at the pristine state (000) is shown in (f).